CR-72338
PWA-3161

DEVELOPMENT OF MAIN SHAFT SEALS FOR ADVANCED AIR BREATHING PROPULSION SYSTEMS

BY

A. J. PARKS, A. H. McKIBBIN, AND C. C. W. NG

FINAL REPORT — PHASE I
25 JUNE 1965 THROUGH 25 JULY 1967

GPO PRICE $ ________

CFSTI PRICE(S) $ ________

Hard copy (HC) 3.00

Microfiche (MF) .65

ff 653 July 65

PREPARED FOR
NASA-LEWIS RESEARCH CENTER CLEVELAND, OHIO 44135
UNDER CONTRACT NAS 3-7609

FACILITY FORM 602

(ACCESSION NUMBER)	(THRU)
232 (PAGES)	1 (CODE)
NASA CR 72338 (NASA CR OR TMX OR AD NUMBER)	15 (CATEGORY)

Pratt & Whitney Aircraft DIVISION OF UNITED AIRCRAFT CORPORATION

FINAL REPORT - PHASE I

DEVELOPMENT OF MAINSHAFT SEALS FOR ADVANCED AIR BREATHING PROPULSION SYSTEMS

Prepared for

NATIONAL AERONAUTICS AND SPACE ADMINISTRATION

14 August 1967

CONTRACT NAS3-7609

Technical Management
NASA Lewis Research Center
Cleveland, Ohio
Airbreathing Engine Division
D. P. Townsend
Project Manager
L. P. Ludwig
Research Advisor

Prepared by:

R. M. Slayton
Project Manager

A. J. Parks
Assistant Project Manager

A. H. McKibbin
Assistant Project Engineer

Dr. C. W. Ng
Assistant Project Engineer

Approved by:

R. P. Shevchenko
Senior Project Engineer

Pratt & Whitney Aircraft DIVISION OF UNITED AIRCRAFT CORPORATION

UA®

EAST HARTFORD, CONNECTICUT

#13

PREFACE

This report describes the work conducted during Phase I of contract NAS3-7609 by the Pratt & Whitney Aircraft Division of United Aircraft Corporation, East Hartford, Connecticut. The work was performed for the Lewis Research Center of the National Aeronautics and Space Administration.

Alton J. Parks was Project Manager for Pratt & Whitney Aircraft for this program.

The following National Aeronautics and Space Administration personnel were assigned to this project:

Contracting Officer	J. H. DeFord
Contract Administrator	T. J. Charney
Project Manager	D. P. Townsend
Research Advisor	L. P. Ludwig

The authors wish to express their appreciation to Messrs. V. P. Povinelli, Jr., M. E. Keefer, L. Alesandro, P. E. Nicolich, and H. L. Northu[illegible]p, for their assistance in the preparation of material for this report.

Appreciation is also expressed to the Stein Seal Co. for their assistance in the design, manufacture and test of the majority of these seal types.

SUMMARY

This report covers the work accomplished during Phase I of contract NAS3-7609, which was initiated on 25 June 1965 and continued to 25 July 1967. Briefly, the objective of Phase I was to analyze, design, procure, and test four types of mainshaft seals for advanced gas-turbine applications.

The work accomplished during Phase I is outlined below:

1. Four seal configurations including a rubbing-contact seal with a piston ring secondary seal, a rubbing-contact seal with bellows secondary seal, an orifice-compensated hydrostatic seal, and an orifice-compensated externally pressurized seal were analyzed, designed, procured, and tested.

2. A hybrid (combined hydrostatic and hydrodynamic) seal configuration was tested under a subsequent contract amendment.

   Posttest interface

3. ~~Post inface~~ deformation ~~test~~ analyses of the orifice-compensated hydrostatic seal and the hybrid seal were made and correlation to experimental results was obtained.

The experimental results and analysis of the two general types of seals under study, (the rubbing-contact type and the gas-film-riding seals) are high-lighted below:

1. Under the wide range of pressure differentials and the high sliding velocity at high temperature conditions, the standard rubbing contact face seal exhibits a thermal instability which resulted in excessive wear and excessive leakage.

2. The inclusion of shrouded Rayleigh hydrodynamic pads on the face of the rubbing-contact face seals did reduce leakage and wear under the room-temperature test environment.

3. The shallow recessed orifice-compensated hydrostatic gas film riding seal will perform satisfactorily up to 550°F at 200 ft/sec and a pressure differential of 100 psig when used in conjunction with a noncooled spring-loaded floating seal plate. The gas film has a converging film at 100°F and an almost perfectly parallel film at 365°F and an increasingly divergent film at higher temperatures. At these higher temperatures the thermal distortion of the seal plate

and shaft created a severely ~~severly~~ divergent film which resulted in rubbing contact and wear at the inner lip of the carbon seal's nosepiece. The degree of tilting resulting from the thermal distortion was predicted through equilibrium gas film analysis.

4. The cooling scheme used in the oil-cooled seal-plate design was inadequate with the hybrid seal. The film-stiffness characteristics of the hybrid seal imposed severe operating limitations on this seal design. In fact, the hybrid seal failed at larger nominal film thicknesses and leakage levels than the hydrostatic seal because of its inferior tolerance to divergent film operation.

5. The externally pressurized orifice-compensated seal exhibited no improvement in performance compared with the plain orifice-compensated seal.

FINAL REPORT - PHASE I

DEVELOPMENT OF MAINSHAFT SEALS FOR ADVANCED AIR BREATHING PROPULSION SYSTEMS

by

R. M. Slayton, A. J. Parks
Dr. C. C. W. Ng and A. H. McKibbin

ABSTRACT

Four mainshaft seals for advanced gas-turbine applications were designed, tested and analyzed. The seals studied were a rubbing-contact face seal with piston-ring secondary seal, a rubbing-contact face seal with bellows secondary seal, an orifice-compensated hydrostatic seal, and an orifice-compensated externally pressurized seal. In addition, a hybrid seal was tested and analyzed. Results of the testing and analysis indicated that the gas-film seals appeared to have the potential to accommodate these environments while rubbing-contact seals lacked the development potential to operate at elevated temperature levels, high relative speeds, and a wide range of pressure differentials.

TABLE OF CONTENTS

	Page
PREFACE	ii
SUMMARY	iii
ABSTRACT	v
LIST OF ILLUSTRATIONS	ix
LIST OF TABLES	xx
I. INTRODUCTION	1
II. CONCLUSIONS	2
III. RECOMMENDATIONS	3
IV TASK I	4
A. INTRODUCTION	4
B. RUBBING-CONTACT FACE SEALS	5
1. Rubbing-Contact Face Seal with Piston-Ring Secondary Seal	5
2. Rubbing-Contact Hydrodynamic Pad Face Seal with Bellows Secondary Seal	11
C. ORIFICE-COMPENSATED GAS-FILM FACE SEALS	15
1. Hydrostatic and Hybrid Seal Configurations	15
2. Externally Pressurized Seal Configuration	15
3. Force Balance and Leakage Calculation	15
4. Spring Force Calculations	22
5. Seal-Ring Distortion Because of Pressure Loading	28
6. Deflection of the Seal Assembly Because of Pressure Loading	30
7. Stress on the Seal Support and Seal Nosepiece Because of Shrinkage	32
8. Piston-Ring Stress	32
9. Stress in the Shroud and Windback	33
10. Thermal Analysis	35

TABLE OF CONTENTS (Contd)

Page

V. TASK II 40

A. INTRODUCTION 40

B. RUBBING-CONTACT FACE SEAL WITH PISTON-RING SECONDARY SEAL 49

1. Build 1 49
2. Build 2 49
3. Build 3 52
4. Build 4 52
5. Build 5 57
6. Build 6 57
7. Build 7 60

C. RUBBING-CONTACT HYDRODYNAMIC PAD FACE SEAL WITH BELLOWS SECONDARY SEAL 64

1. Builds 1 through 3 64
2. Build 4 66

D. ORIFICE-COMPENSATED HYDROSTATIC SEAL 69

1. Builds 1 through 4 69
2. Builds 5 through 7 69
3. Build 8 73
4. Build 9 76

E. ORIFICE-COMPENSATED SPIRAL-GROOVE HYBRID SEAL 83

1. Build 1 83
2. Build 2 83

F. ORIFICE-COMPENSATED EXTERNALLY PRESSURIZED SEAL 94

G. POSTTEST SEAL INTERFACE ANALYSIS OF THE ORIFICE-COMPENSATED HYDROSTATIC SEAL 98

1. Gas-Film Analytical Model 98
2. Rotation of the Seal Because of Pressure Loading 106
3. Thermal Analysis 113

TABLE OF CONTENTS (Contd)

	Page
H. POSTTEST SEAL INTERFACE ANALYSIS OF THE HYBRID SEAL	128
1. Gas-Film Analytical Model	128
2. Analysis of Build 1	136
3. Analysis of Build 2	144
I. TEST RIGS	159
1. Rig Instrumentation	160
2. Inert Gas Test	160
3. Rig Analysis	160
4. Instrumentation Validation Rig	177
APPENDIX A DEFLECTION ANALYSIS OF SEAL HOUSING FOR RUBBING CONTACT SEAL	181
1. Deflection of Body 1	181
2. Deflection of Body 2	184
3. Deflection of Body 3	184
4. Deflection of Body 4	186
5. Deflection of Body 5	186
6. Relations Between P_2, P_4, and P_5	188
7. Slopes and Deflections	188
APPENDIX B THERMAL ANALYSIS	191
1. Heat-Transfer Coefficients	191
2. Energy Balance at Interface of Seal and Seal Plate for Sheared-Film Concept	197
REFERENCES	206
BIBLIOGRAPHY	208
DISTRIBUTION LIST	209

LIST OF ILLUSTRATIONS

Figure	Title	Page
1	Schematic of the Rubbing-Contact Face Seal with Piston-Ring Secondary Seal	7
2	Simplified Model of Seal and Carrier Subassembly	7
3	Calculated Temperature Field for Rubbing-Contact Seal with Piston-Ring Secondary Seal When No External Surfaces Are Wetted by Oil	10
4	Calculated Temperature Field for Rubbing-Contact Seal with Piston-Ring Secondary Seal When Low-Pressure Surfaces Are Wetted by Oil	10
5	Local Seal Plate Temperature for Different Oil-Hole Locations	12
6	Rubbing-Contact Hydrodynamic-Pad Face Seal with Bellows Secondary Seal	12
7	Simplified Model of the Rubbing-Contact Hydrodynamic-Pad Face Seal	14
8	Schematic of the Orifice-Compensated Hydrostatic Face Seal	16
9	Schematic of the Externally Pressurized Face Seal	16
10	Analytical Model for Force Balance and Leakage Calculations	17
11	Characteristics of the Externally Pressurized Seal when P_A = 315 psia	21
12	Characteristics of the Externally Pressurized Seal when P_A = 215 psia	23
13	Characteristics of the Externally Pressurized Seal when P_A = 115 psia	23
14	Characteristics of the Externally Pressurized Seal when P_A = 75 psia	24

LIST OF ILLUSTRATIONS (Continued)

Figure	Title	Page
15	Characteristics of the Hydrostatic Seal when $P_A = 315$ psia	24
16	Characteristics of the Hydrostatic Seal when $P_A = 215$ psia	25
17	Characteristics of the Hydrostatic Seal when $P_A = 115$ psia	25
18	Characteristics of the Hydrostatic Seal when $P_A = 75$ psia	26
19	Freebody Diagram of the Piston Ring	26
20	Dimensions and Center of Gravity of the Seal Support	29
21	Cross Section of the Seal Plate	31
22	Dimensions of the Large and Small Piston Rings	34
23	Dimensions of the Shroud and Windback	34
24	Temperature Pattern for the Orifice-Compensated Hydrostatic Face Seal with High-Pressure Air Cooler than Low-Pressure Air	36
25	Temperature Pattern for the Orifice-Compensated Hydrostatic Face Seal with High-Pressure Air Hotter Than Low-Pressure Air	37
26	Rubbing-Contact Face Seal with Piston-Ring Secondary Seal 1. Transducer to Measure Generated Torque at Seal Interface 2. Accelerometers 3. Seal Housing and Carbon Thermocouples (XP-63615)	50
27	Results of Preliminary Dynamic Checkout on Build 1 of the Rubbing-Contact Face Seal with Piston-Ring Secondary Seal	51
28	Results of Preliminary Dynamic Checkout on Build 2 of the Rubbing-Contact Face Seal with Piston-Ring Secondary Seal	53
29	Effect of Temperature on Leakage of Rubbing-Contact Face Seal with Piston Ring Secondary Seal (Build 2)	54

LIST OF ILLUSTRATIONS (Continued)

Figure	Title	Page
30	Effect of Surface Speed on Leakage of Rubbing-Contact Face Seal with Piston Ring Secondary Seal (Build 2)	54
31	Results of Tests on Build 3 of the Rubbing-Contact Face Seal with Piston-Ring Secondary Seal	55
32	Results of Tests on Build 4 of the Rubbing-Contact Face Seal with Piston-Ring Secondary Seal	56
33	Results of Tests on Build 5 of the Rubbing-Contact Face Seal with Piston-Ring Secondary Seal	58
34	Results of Tests on Build 6 of the Rubbing-Contact Face Seal with Piston-Ring Secondary Seal	59
35	Effect of Oil Temperature on the Performance of Build 7 of the Rubbing-Contact Face Seal with Piston-Ring Secondary Seal with Air at 800 Degrees Fahrenheit and 100 psig	61
36	Effect of Oil Temperature on the Performance of Build 7 of the Rubbing-Contact Face Seal with Piston-Ring Secondary Seal with Air at 1200 Degrees Fahrenheit and 100 psig	62
37	Seal and Carrier from Build 7 after 57.08 Hours of Operation at Severe Test Conditions. Note Deterioration of the Springs and Carbon Seal (CN-8023)	63
38	Carbon Wear Track on the Seal Plate from Build 7 after 57.08 Hours of Operation at Severe Test Conditions (CN-8019)	63
39	Build 1 of the Rubbing-Contact Hydrodynamic Pad Face Seal with Bellows Secondary Seal	65
40	Static Leakage Calibration of the Rubbing-Contact Hydrodynamic Pad Face Seal with Bellows Secondary Seal	65
41	Build 4 of the Rubbing-Contact Hydrodynamic Pad Face Seal with Bellows Secondary Seal	67

LIST OF ILLUSTRATIONS (Continued)

Figure	Title	Page
42	Preliminary Dynamic Checkout of Build 4 of the Rubbing-Contact Hydrodynamic Pad Face Seal with Bellows Secondary Seal	68
43	Orifice-Compensated Hydrostatic Seal 1. Carrier 2. Seal-Ring Assembly 3. Assembly Guard (XP-66913)	70
44	Components of the Orifice-Compensated Hydrostatic Seal 1. Carrier 2. 18 Springs 3. Piston Ring 4. 3 Antirotation Lock Pins 5. Carrier 6. Carbon Seal Ring 7. Assembly Guard (XP-66914)	70
45	Results of Testing on Build 5 of the Orifice-Compensated Hydrostatic Seal	71
46	Spring-Loaded Floating Seal Plate	72
47	Results of Testing on Build 5 of the Orifice-Compensated Hydrostatic Seal	74
48	Results of Testing on Build 7 of the Orifice-Compensated Hydrostatic Seal	75
49	Preliminary Dynamic Checkout of Build 8 of the Orifice-Compensated Hydrostatic Seal	77
50	Effect of Oil Temperature on Air Leakage in the Orifice-Compensated Hydrostatic Seal at a Pressure Differential of 100 psi	77
51	Effect of Oil Temperature on Air Leakage in the Orifice-Compensated Hydrostatic Seal at a Pressure Differential of 200 psi	78
52	Dimensions of the Carbon Seal Lip for Build 9 of the Orifice-Compensated Hydrostatic Seal	78
53	Preliminary Dynamic Checkout of the Orifice-Compensated Hydrostatic Seal Tests Made with Ambient Air	79

LIST OF ILLUSTRATIONS (Continued)

Figure	Title		Page
54	Preliminary Dynamic Checkout of the Orifice-Compensated Hydrostatic Seal. Tests Made with Air at 250 Degrees Fahrenheit		80
55	Effect of Air Temperature on Air Leakage in Build 9 of the Orifice-Compensated Hydrostatic Seal		80
56	Carbon Seal from Build 9 of the Orifice-Compensated Hydrostatic Seal	(CN-8229)	81
57	Seal Plate from Build 9 of the Orifice-Compensated Hydrostatic Seal	(CN-8231)	82
58	Front View of the Spiral-Grooved Seal Plate Used in the Hybrid Seal	(CN-8280)	84
59	Rear View of the Spiral-Grooved Seal Plate Used in the Hybrid Seal	(CN-8281)	84
60	Dimensions of the Carbon Seal Lip for Build 1 of the Hybrid Seal		85
61	Dimensions of the Carbon Seal Lip for Build 2 of the Hybrid Seal		87
62	First Dynamic Checkout of Build 2 of the Hybrid Seal		88
63	Second Dynamic Checkout of Build 2 of the Hybrid Seal		90
64	Third Dynamic Checkout of Build 2 of the Hybrid Seal		91
65	Final Dynamic Checkout of Build 2 of the Hybrid Seal		92
66	Seal Plate after Termination of Testing on Build 2 of the Hybrid Seal	(CN-9342)	93
67	Components of the Orifice-Compensated Externally Pressurized Seal	(CN-7466)	95

LIST OF ILLUSTRATIONS (Continued)

Figure	Title	Page
68	Seal Carrier from the Orifice-Compensated Externally Pressurized Seal Showing the Three Inlet Holes for the Pressurizing Air Supply (CN-7467)	95
69	External Pressurizing Air Flow	96
70	Leakage of External Pressurizing Air Flow to High-Pressure Compartment	97ρ
71	Orifice Discharge Coefficient (C_D) for the Orifice-Compensated Hydrostatic Seal	101
72	Experimental and Analytical Values for Static Leakage Flow	105
73	Experimental and Analytical Values For Mean Film Thickness	105
74	Seal Retaining Band of Build 9 of the Orifice-Compensated Hydrostatic Seal	107
75	Dimensionless Load as a Function of Film Thickness at a Pressure Differential of 100 psi	109
76	Dimensionless Load as a Function of Film Thickness at a Pressure Differential of 200 psi	109
77	Leakage as a Function of Film Thickness at a Pressure Differential of 100 psi	110
78	Leakage as a Function of Film Thickness at a Pressure Differential of 200 psi	110
79	Seal Tilt as a Function of Mean Film Thickness with a Geometric Imbalance of 0.6935	111
80	Leakage as a Function of Seal Tilt Angle	111
81	Experimental Values for Leakage in Builds 7 and 9	112
82	Analytical Values for Piston-Ring Leakage	112

LIST OF ILLUSTRATIONS (Continued)

Figure	Title	Page
83	Rotation of the Seal Ring in Build 7	114
84	Rotation of the Seal Ring in Build 9	114
85	Thermal Map of the Orifice-Compensated Hydrostatic Seal (See Case 1, Table XIV)	118
86	Thermal Map of the Orifice-Compensated Hydrostatic Seal (See Case 2, Table XIV)	119
87	Thermal Map of the Orifice-Compensated Hydrostatic Seal (See Case 3, Table XIV)	120
88	Thermal Map of the Orifice-Compensated Hydrostatic Seal (See Case 4, Table XIV)	121
89	Thermal Map of the Orifice-Compensated Hydrostatic Seal (See Case 5, Table XIV)	122
90	High-Temperature Test of the Orifice-Compensated Hydrostatic Seal	124
91	Seal Tilt Angle as a Function of Mean Film Thickness for the High-Temperature Test	124
92	Leakage as a Function of Seal Tilt Angle for the High-Temperature Test	125
93	Film Thickness as a Function of Temperature	125
94	Change in Film Thickness	127
95	Geometry of the Hybrid Seal	129
96	Discharge Coefficients Single Orifice	134
97	Test Results for Build 1 of the Hybrid Seal with Ambient Air	138

LIST OF ILLUSTRATIONS (Continued)

Figure	Title	Page
98	Analytical Prediction of Dimensionless Load for a Groove Depth of 0.6 Mils at Static Conditions	138
99	Analytical Prediction of Dimensionless Load for a Groove Depth of 0.6 Mils and a Speed of 200 ft/sec	139
100	Analytical Prediction of Dimensionless Load for a Groove Depth of 0.3 Mils and a Speed of 200 ft/sec	139
101	Analytical Prediction of Static Leakage with a Groove Depth of 0.6 Mils	140
102	Analytical Prediction of Leakage with a Groove Depth of 0.6 Mils and a Speed of 200 ft/sec	140
103	Analytical Prediction of Leakage with a Groove Depth of 0.3 Mils and a Speed of 200 ft/sec	141
104	Dimensionless Load for Three Spiral-Groove Configurations at a Pressure Differential of 100 psi	141
105	Dimensionless Load for Three Spiral-Groove Configurations at a Pressure Differential of 200 psi	142
106	Film Stiffness for Three Spiral-Groove Configurations at a Pressure Differential of 100 psi	142
107	Film Stiffness of Three Spiral-Groove Configurations at a Pressure Differential of 200 psi	143
108	Analytical Prediction of Dimensionless Load for a Pressure Differential of 50 psi and a Temperature of 90 Degrees Fahrenheit	146
109	Analytical Prediction of Dimensionless Load for a Pressure Differential of 100 psi and a Temperature of 90 Degrees Fahrenheit	146

LIST OF ILLUSTRATIONS (Continued)

Figure	Title	Page
110	Analytical Prediction of Dimensionless Load for a Pressure Differential of 200 psi and a Temperature of 90 Degrees Fahrenheit	147
111	Analytical Prediction of Dimensionless Load Pressure Differential of 30 psi and a Temperature of 90 Degrees Fahrenheit	147
112	Analytical Prediction of Leakage at Static Conditions with a Temperature of 90 Degrees Fahrenheit	148
113	Analytical Prediction of Leakage at a Speed of 200 ft/sec and a Temperature of 90 Degrees Fahrenheit	148
114	Analytical Prediction of Leakage at a Speed of 400 ft/sec and a Temperature of 90 Degrees Fahrenheit	149
115	Analytical Prediction of Dimensionless Load at a Pressure Differential of 100 psi and a Temperature of 400 Degrees Fahrenheit	149
116	Analytical Prediction of Dimensionless Load at a Pressure Differential of 200 psi and a Temperature of 400 Degrees Fahrenheit	150
117	Analytical Prediction of Dimensionless Load at a Pressure Differential of 300 psi and a Temperature of 400 Degrees Fahrenheit	150
118	Analytical Prediction of Leakage at Static Conditions with a Temperature of 400 Degrees Fahrenheit	151
119	Analytical Prediction of Leakage at a Speed of 200 ft/sec and a Temperature of 400 Degrees Fahrenheit	151
120	Mean Film Thickness at a Temperature of 90 Degrees Fahrenheit and Pressure Differentials of 50 and 100 psi	152
121	Mean Film Thickness at a Temperature of 90 Degrees Fahrenheit and Pressure Differentials of 200 and 300 psi	152

LIST OF ILLUSTRATIONS (Continued)

Figure	Title	Page
122	Leakage at a Temperature of 90 Degrees Fahrenheit	153
123	Mean Film Thickness at a Temperature of 400 Degrees Fahrenheit	153
124	Leakage at a Temperature of 400 Degrees Fahrenheit	154
125	Measured Leakage with Room-Temperature Air	154
126	Modified Leakage with Air at 400 Degrees Fahrenheit	155
127	Method of Measuring Generated Torque at Seal Interface	161
128	The Shaded Areas Illustrate the Changes to the Rig which Permitted Testing the Seals with a Layer of Nitrogen on the Oil Sump	162
129	Pressure-Vessel Summary	163
130	Rig Temperatures at an Oil Flow of 24 ppm	170
131	System Model for Analyses of Critical Speeds	170
132	Moment and Deflection Diagrams	175
133	Method of Dividing Shaft for Vibration Analysis	176
134	Schematic of Analytical Model for Rig	176
135	Test Seal Assembled in the Instrumentation Validation Rig Cover. 1. Transducers to Measure Torque Generated at Seal Face 2. Accelerometers 3. Seal Housing and Carbon Thermocouples (XP-66908)	180
136	Division of the Seal and Housing Assembly	182
137	Freebody Diagram of the Seal	183
138	Freebody Diagram of Body 1	183

LIST OF ILLUSTRATIONS (Continued)

Figure	Title	Page
139	Freebody Diagram of Body 2	185
140	Freebody Diagram of Body 3	185
141	Freebody Diagram of Body 4	187
142	Freebody Diagram of Body 5	187
143	Oil Flow in Coolant Passages	195
144	Analytical Element for Seal-Temperature Calculations Based on Film-Riding Assumption	198
145	Electrical Analog of Heat-Transfer Analysis	203

LIST OF TABLES

Table	Title	Page
I	Plating Combinations	6
II	Force Balance Summary	14
III	Leakage and Restoring Force Results	20
IV	Required Spring Loadings	27
V	Thermal Properties of the Orifice -Compensated Hydrostatic Face Seal	38
VI	Rubbing-Contact Face Seal with Piston-Ring Secondary Seal Test Summary	41
VII	Rubbing-Contact Hydrodynamic Pad Face Seal with Bellows Secondary Seal Test Summary	42
VIII	Orifice-Compensated Hydrostatic Seal Test Summary	43
IX	Orifice-Compensated Externally Pressurized Seal Test Summary	44
X	Rubbing-Contact Face Seal with Piston-Ring Secondary Seal Inspection Summary	45
XI	Rubbing-Contact Hydrodynamic Pad Face Seal with Bellows Secondary Seal Inspection Summary	46
XII	Orifice-Compensated Hydrostatic Seal Inspection Summary	47
XIII	Orifice-Compensated Externally Pressurized Seal Inspection Summary	48
XIV	Comparison of Experimentally Measured and Analytically Derived Temperatures	116
XV	Parameters Used in Computer Program	117

LIST OF TABLES (Continued)

Table	Title	Page
XVI	Operating Mean Film Thickness and Seal Tilt Angle at 90°F	157
XVII	Operating Mean Film Thickness and Seal Tilt Angle at 400°F	158

I. INTRODUCTION

Development of seals to accommodate the increasingly severe environments of temperature, relative velocity and range of pressure differential required by the advanced air-breathing gas turbines, and to meet the performance improvements of decreased leakage and weight will require extensive effort. The labyrinth seals used on some present engines become unacceptably heavy, bulky, and have excessive leakage at the high pressure differentials and with large leakage areas imposed by large shaft diameters. Development testing of advanced gas-turbine engines in recent years has demonstrated the limited development potential of rubbing-contact seals. Subsequent analysis of the spiral-groove configuration revealed that the expected improvement in film-stiffness characteristics had not been realized. Testing of rubbing contact seals under this contract has confirmed these limitations.

A seal concept which has received increasing attention for severe seal environments is the gas-film seal. Because of the inherent reduced heat generation of this seal concept, it has the development potential to meet the increasingly severe environments of the advanced air-breathing gas turbine. Several types of gas-film seals were designed and tested during Phase I of the contract. Two types of orifice-compensated hydrostatic seals were tested. One was pressurized by the high pressure of the compartment to be sealed, and the other type was externally pressurized, using a higher pressure source. In addition, a hybrid configuration was evaluated. The hybrid configuration utilized the orifice-compensated hydrostatic configuration and incorporated a spiral groove on the seal plate to increase gas film stiffness. This increased film stiffness decreased the seal's sensitivity to thermal distortion. These seals were designed to operate with a nominal gas-film thickness of approximately 0.0004 inches separating the rotating from the nonrotating seal members.

II. CONCLUSIONS

Considerable experience and information relative to the problems of turbine engine face seals operating at elevated temperature and pressure conditions was obtained from this test series. The conclusions reached as a result of this Phase I work are as follows:

1. The advancement of the state of the art for mainshaft seal applications in air-breathing propulsion systems requires continued research and development to satisfy performance criteria.

2. Rubbing-contact seals have exhibited limitations and would require undue development effort to improve seal thermal stability and find adequate materials and/or cooling schemes to operate at the required combination of environments specified in the contract.

3. Gas-film seals have exhibited the potential to be developed for advanced gas-turbine mainshaft seals.

4. The materials combination tested under Phase I of the contract for gas-film seals would not tolerate rubbing contact between seal and seal plate at the contract environments.

5. The most critical factor affecting gas-film seal operation is the thermal distortion of the seal plate over the range of operating conditions.

6. A successful gas-film seal requires a detailed accounting of all thermal and mechanical distortions with corresponding design features to maintain parallellism of sealing members at the seal interface.

7. Inclusion of hydrodynamic pads on the rubbing contact seal showed promise of extending the range of successful operation.

8. A hydrostatic seal design has greater inherent tolerance to divergent film conditions than other gas-film seal designs tested.

9. The orifice-compensated externally pressurized seal offered no improvement in comparison with the plain orifice-compensated hydrostatic seal.

10. The hybrid seal has superior film stiffness while operating with a convergent or parallel film. However, the hybrid seal is inferior to the hydrostatic seal for divergent film operation because of the influence of the hydrodynamic effect.

III. RECOMMENDATIONS

Based on the experience obtained during the Phase I tests, the contractor recommends the following:

1. A research and development program of sufficient scope to develop an operative gas-film seal to fulfill the requirements of contemplated advanced air-breathing propulsion systems should be pursued.

2. Major development effort should be directed into minimizing thermally induced distortions in seal plates and maximizing the conformance capability of the seal and seal plate.

3. A materials-compatibilities evaluation development program should be considered to develop a gas-film seal which will withstand momentary high-speed rubbing over the full range of operating conditions.

4. No further development effort should be expended on rubbing-contact seals to meet operating conditions as severe as those specified in this contract.

IV. TASK I
MAINSHAFT SEAL DESIGN

A. INTRODUCTION

The objective of this task was to analyze and design four mainshaft seals capable of operating at the following conditions:

- Seal sliding speed: 0 to 500 ft/sec
- Seal pressure differential: 0 to 300 psi
- Gas temperature: ambient to 1300°F
- Oil-sump temperature: ambient to 500°F

The four seals designed were a rubbing-contact face seal with piston-ring secondary seal, a rubbing-contact hydrodynamic pad face seal with bellows secondary seal, an orifice-compensated hydrostatic seal, and an orifice-compensated externally pressurized seal. In additon, the contractor analyzed and tested a hybrid seal which consisted of the basic orifice-compensated hydrostatic seal running against a spiral-groove seal plate supplied by NASA. All five seals were designed for flight applications.

The seal design concepts were related to the particular operating conditions and the problems generated by those conditions. The central design problem was the fact that the seal assemblies must be kept within very close dimensional tolerances in order to operate successfully, yet the thermal distortions, pressure distortions, and wear caused by the operating conditions all tend to degrade the designed tolerances. High sliding speeds affect the design in many ways, the most important of which is heat generation by friction. Heat generation can be countered by increasing the coolant flow and by reducing the face loading on the seal. The latter approach was tried in the three film-riding seals, where the face load is supported by a thin gas film. Cooling oil was used in some seal plates to keep thermal gradients to a minimum.

B. RUBBING-CONTACT FACE SEALS

The contract dealt with two rubbing-contact face seals: a conventionally designed face seal with a piston-ring secondary seal, and a face seal with hydrodynamic pads and a bellows secondary seal. The latter seal was designed and built by the Stein Seal Company. The thermal analysis of the face seal with piston-ring secondary seal is included in this report.

1. RUBBING-CONTACT FACE SEAL WITH PISTON RING SECONDARY SEAL

The design of the rubbing-contact seal required that close attention be given to many details such as closing forces, deflections, and operating temperatures. A sketch of a seal assembly which meets these requirements is shown in Figure 1. The seal is shown installed in the test rig in which it was run. Also shown in the figure are the bore diameter and the carbon dimensions which were used to calculate the seal's pressure balance.

The seal assembly contains the seal subassembly and the seal holder. The seal subassembly consists of a CDJ-83 seal ring shrunk in the seal housing. Secondary sealing is accomplished by two piston rings housed in the seal holder. The piston rings seal against the inner surface of the seal housing, which is flame-plated with Linde ~~LC1C~~ LA2 coating ~~(chrome carbide).~~ (aluminum oxide) Twenty-four springs are used to keep the carbon seal in contact with the seal plate, which is mounted on a simulated turbine shaft. The seal plate is flame-plated with Linde LC1C coating on the rubbing face and is oil cooled.

a. Force Calculations

The spring force F_s must be designed to overcome the frictional forces F_f and the inertial forces F_a. The friction force in a typical seal design is the result of the piston-ring secondary seals and the torque pins rubbing on the housing. If an undamped bellows design were employed, this force would not exist. The diametral tension for a standard piston ring should be approximately 2 to 3 pounds for 4 - to 8-inch diameter rings, and the ring should be pressure-balanced to keep the normal forces low. In addition, the choice of piston ring and housing materials and platings should be made with the coefficient of friction in mind. Several satisfactory plating combinations from a wear point of view are listed, with their coefficients of friction, in Table I.

TABLE I

PLATING COMBINATIONS

Plating Combinations	Coefficient of Friction
chrome on chrome	0.225
chrome on LC1C (chrome carbide)	0.218
chrome on LC1A (chrome carbide)	0.145
chrome on LA2 (aluminum oxide)	0.165

The frictional force on the piston ring is the sum of the diametral tension and pressure forces times the coefficient of friction:

$$F_f = \left[N\ T_d\ C_1 + (1-K)\Delta P A\right]\alpha$$

where T_d = diametrial tension = 3.4
N = number of pistion rings = 2
C_1 = constant to give the normal load from the diametrial tension = 2.76
K = equivalent pressure-balancing coefficient = 0.652
ΔP = 300 psi
A = $\pi(6.799)\ (0.05)$ = 1.067 in.^{2}
α = coefficient of friction = 0.145

$$F_f = 18.96 \text{ lb.}$$

The inertial forces are more complicated and involve motion with several degrees of freedom in following the runout of a seal plate. The analysis used was that of angular motion of the seal and carrier following the axial runout of the seal plate (0.001 inch FIR). The simplified model shown in Figure 2 was used for this analysis.

Summing moments of inertia about the carbon face for the four bodies shown in Figure 2 (taken to be hollow circular cylinders) gives -

$$\Sigma I = I_1 + I_2 + m_2 \ell_1^2 + I_3 + m_3(\ell_1 + \ell_2)^2 + I_4$$

$$= \frac{m_1}{12}\left(\frac{R_4^2 + R_5^2}{4} + \frac{\ell_1^2}{12}\right) + \frac{m_2}{12}\left[\left(\frac{R_4^2 + R_1^2}{4} + \frac{\ell_2^2}{12}\right) + \ell_1^2\right] + \frac{m_3}{12}\left[\left(\frac{R_3^2 + R_2^2}{4} + \frac{\ell_3^2}{12}\right)\right.$$

$$\left. + (\ell_1 + \ell_2)^2\right] + \frac{m_4}{12}\left(\frac{R_5^2 + R_1^2}{4} + \frac{\ell_1^2}{12}\right)$$

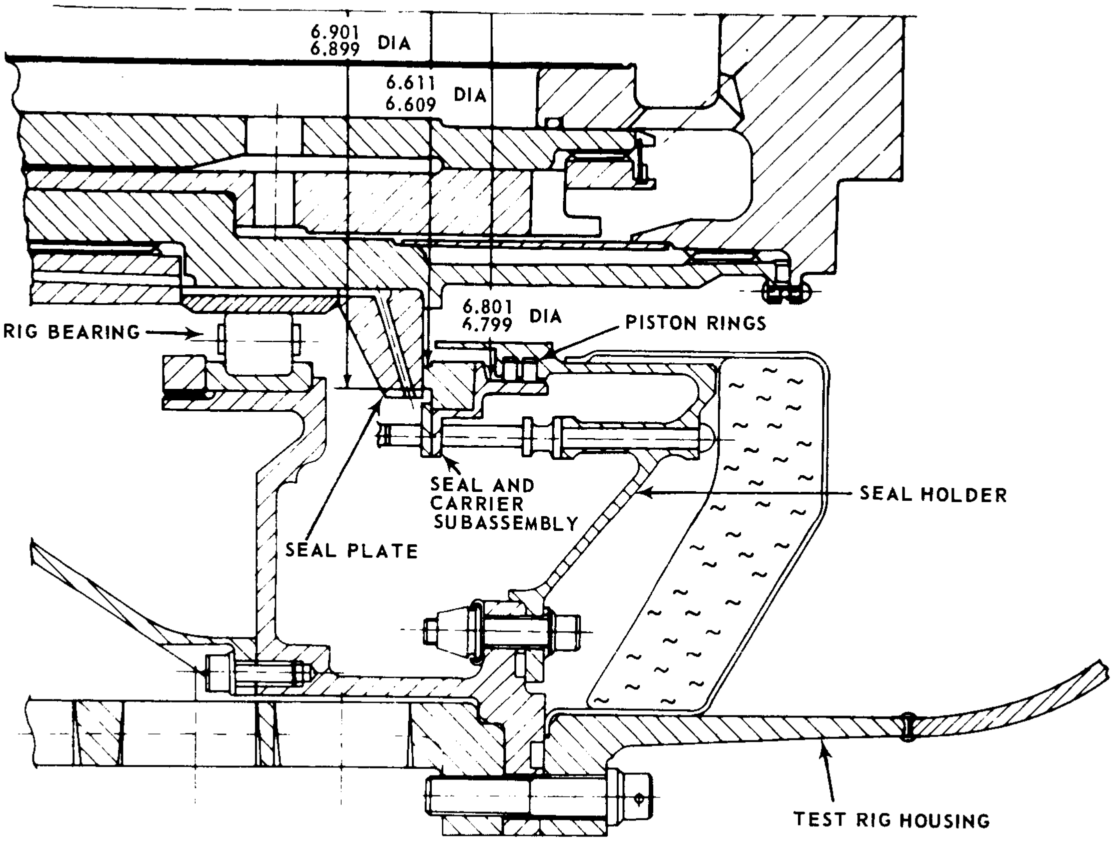
6.901
6.899 DIA
6.611
6.609 DIA
6.801
6.799 DIA
PISTON RINGS
RIG BEARING
SEAL AND
CARRIER
SUBASSEMBLY
SEAL PLATE
SEAL HOLDER
TEST RIG HOUSING

Figure 1 Schematic of the Rubbing-Contact Face Seal with Piston-Ring Secondary Seal

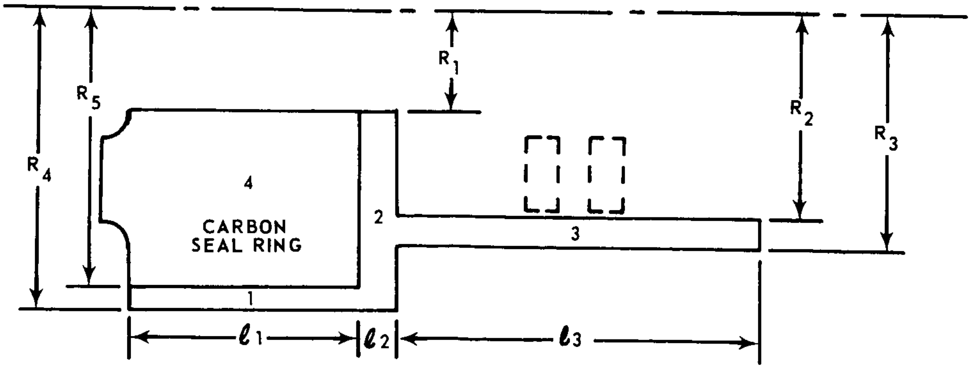
R_1
R_5
R_4
R_2
R_3
4
CARBON
SEAL RING
2
3
1
ℓ_1
ℓ_2
ℓ_3

Figure 2 Simplified Model of Seal and Carrier Subassembly

where
$$m_1 = \rho_s \pi \ell_1 \left(R_4^2 - R_5^2\right)/g$$
$$m_2 = \rho_s \pi \ell_2 \left(R_4^2 - R_1^2\right)/g$$
$$m_3 = \rho_s \pi \ell_3 \left(R_3^2 - R_2^2\right)/g$$
$$m_4 = \rho_c \pi \ell_1 \left(R_5^2 - R_1^2\right)/g$$

Units of inches for R_i, ℓ_i

ρ_s = density of steel
ρ_c = density of carbon

Since $\Sigma M = \Sigma I \cdot \alpha$ and for simple harmonic motion of the seal plate, the angular acceleration

$$\alpha = \frac{r\omega^2}{2R_5}$$

r = runout of the seal

Finally, $$F_a = \frac{\Sigma M}{R_5}$$

For a speed of 17,000 rpm, a runout of 0.001 inch FIR, and the given geometry, the inertial force is equal to 3.68 pounds. (Reference Semi Annual Report No. 1 - PWA-2683).

The spring force is therefore represented by $F_s \geqslant (F_f + F_a)$, the total net closing force by

$$F_c = F_s \pm (F_f + F_a) + \left(\frac{A_1}{A} - K\right) A \Delta P$$

where:

K = Equivalent pressure balancing coeffecient = 0.652

A_H = Area bounded by the secondary cylinder diameter and high pressure side of seal face

A_T = Total area of seal face

Consequently this development yields a spring force of (18.96 + 3.68) = 22.64 pounds for the design. (Reference Semi Annual Report No. 1 - PWA-2683).

b. Deflection Analysis

For the rubbing-contact seal, the deflection analysis by means of computer solution yielded the following results:

Deflections of the rubbing-contact seal carbon ring and carrier assembly have been calculated with the aid of a digital computer. The methods used are described in Appendix A page 181 and the results of the analysis are summarized below.

The angular deflection of the carbon seal face due to the interference fit between the carbon ring and the steel carrier is 0.011 radians (the positive sense denotes a diverging leakage path). Following installation of the carbon ring into the carrier, the seal face is lapped flat. The elevated temperature present during seal operation reduces the interference fit and imparts an angular displacement to the seal face in the negative or convergent direction. At the maximum operating temperature the angular displacement of the seal face is -0.0094 radians. The angular displacement of the seal face due to a 300 psi pressure differential is 0.004 radians. The rotation of the seal face at maximum operating conditions, therefore, is -0.0054 radians.

The net convergence or divergence of the leakage path through the seal interface is the difference between the angular deflections of the carbon seal face and the seal plate. Seal plate deflection due to pressure loading is numerically less than -0.0001 radians. Thermal deflection of the seal plate, however, is significant and is caused by thermal gradients in the shaft and seal plate. A discussion of seal plate thermal analysis follows.

c. Temperature Maps

Preliminary analysis was based on the assumption that the heat generation at the seal and seal plate interface was due to the friction of carbon-to-metal contact. The analysis utilized the TOSS computer program from the SHARE General Program Library. A coefficient of friction 0.3 was assumed. This value is slightly lower than published friction coefficients of carbon brushes.

A thermal analysis was performed to determine the effects of keeping the exterior surface of the seal plate and the seal carrier dry rather than cooling them by oil-jet impingement. A nominal heat-transfer coefficient of 50 Btu/hr ft^2°F was assumed for the oil splashing on the surfaces. The bulk temperatures of the carbon seal and seal carrier were markedly reduced, but the seal plate temperatures were essentially unchanged. The derived temperature maps for the dry and oil wetted conditions are shown in Figures 3 and 4, respectively. The heat-generation input for these two maps was based on theoretical film-shear considerations. The analytical methods used are outlined in Appendix B.

d. Optimum Coolant Hole Location in Seal Plate

The thermal effects associated with the internal cooling of a seal plate were analyzed. Temperatures were computed for three possible configurations: a seal plate without internal coolant, a seal plate with coolant holes parallel to

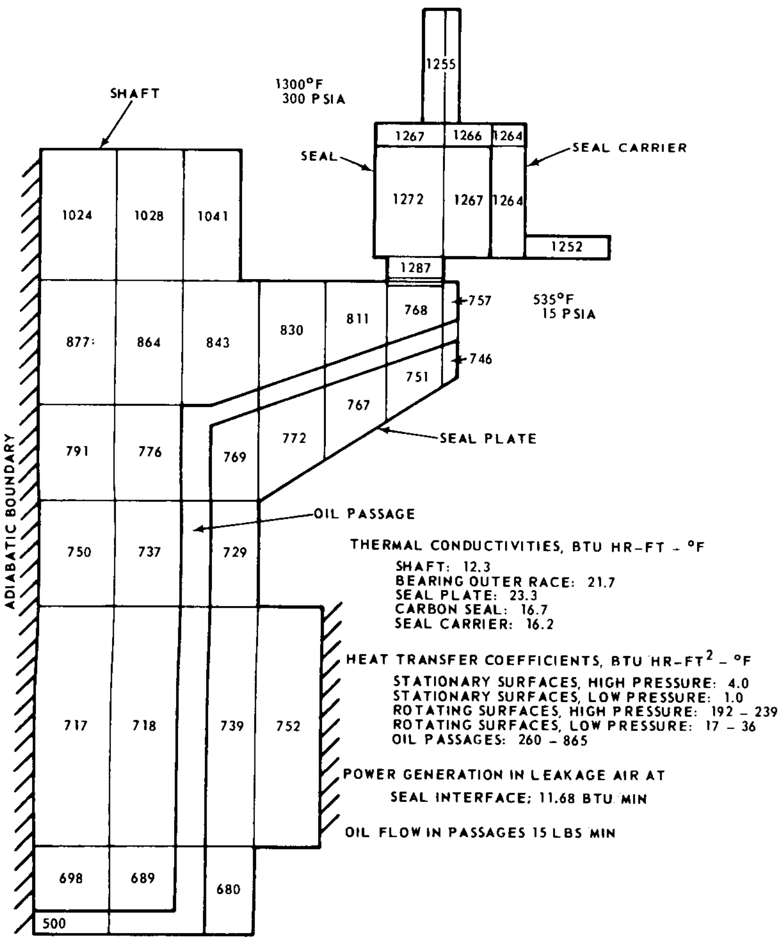
SHAFT
1300°F
300 PSIA
SEAL
SEAL CARRIER
1255
1267
1266
1264
1272
1267
1264
1252
1287
1024
1028
1041
877:
864
843
830
811
768
757
746
751
767
772
769
791
776
750
737
729
717
718
739
752
698
689
680
500
535°F
15 PSIA
SEAL PLATE
OIL PASSAGE
ADIABATIC BOUNDARY

THERMAL CONDUCTIVITIES, BTU HR-FT - °F
SHAFT: 12.3
BEARING OUTER RACE: 21.7
SEAL PLATE: 23.3
CARBON SEAL: 16.7
SEAL CARRIER: 16.2

HEAT TRANSFER COEFFICIENTS, BTU HR-FT^2 - °F
STATIONARY SURFACES, HIGH PRESSURE: 4.0
STATIONARY SURFACES, LOW PRESSURE: 1.0
ROTATING SURFACES, HIGH PRESSURE: 192 - 239
ROTATING SURFACES, LOW PRESSURE: 17 - 36
OIL PASSAGES: 260 - 865

POWER GENERATION IN LEAKAGE AIR AT
SEAL INTERFACE; 11.68 BTU MIN

OIL FLOW IN PASSAGES 15 LBS MIN

Figure 3 Calculated Temperature Field for Rubbing-Contact Seal with Piston-Ring Secondary Seal When No External Surfaces are Wetted by Oil

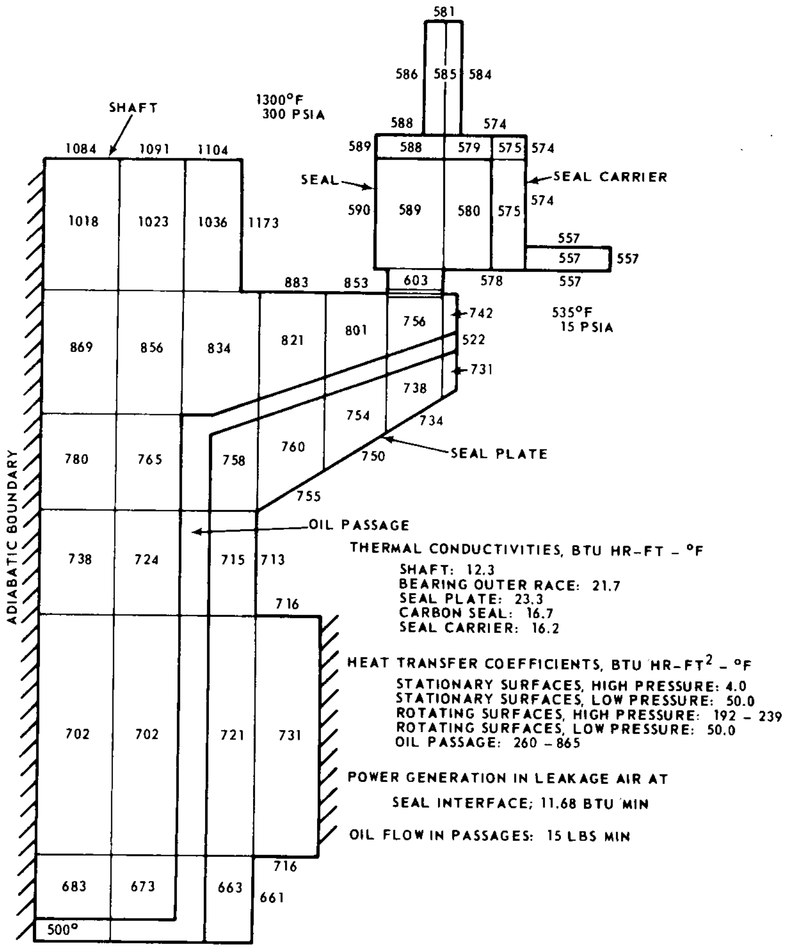
581
586
585
584
SHAFT
1300°F
300 PSIA
588
574
1084
1091
1104
589
588
579
575
574
SEAL
SEAL CARRIER
574
1018
1023
1036
1173
590
589
580
575
557
557
557
557
883
853
603
578
869
856
834
821
801
756
742
522
731
535°F
15 PSIA
738
754
734
760
750
SEAL PLATE
780
765
758
755
OIL PASSAGE
738
724
715
713
716
702
702
721
731
683
673
663
716
661
500°
ADIABATIC BOUNDARY

THERMAL CONDUCTIVITIES, BTU HR-FT - °F
SHAFT: 12.3
BEARING OUTER RACE: 21.7
SEAL PLATE: 23.3
CARBON SEAL: 16.7
SEAL CARRIER: 16.2

HEAT TRANSFER COEFFICIENTS, BTU HR-FT^2 - °F
STATIONARY SURFACES, HIGH PRESSURE: 4.0
STATIONARY SURFACES, LOW PRESSURE: 50.0
ROTATING SURFACES, HIGH PRESSURE: 192 - 239
ROTATING SURFACES, LOW PRESSURE: 50.0
OIL PASSAGE: 260 - 865

POWER GENERATION IN LEAKAGE AIR AT
SEAL INTERFACE; 11.68 BTU MIN

OIL FLOW IN PASSAGES: 15 LBS MIN

Figure 4 Calculated Temperature Field for Rubbing-Contact Seal with Piston-Ring Secondary Seal When Low-Pressure Surfaces Are Wetted by Oil

and near the interface (source of heat), and a seal plate with coolant holes diagonal to and far from the interface. The coolant holes have a nominal inside diameter of 0.060 inch and are located every 10 degrees circumferentially. The radial temperature distribution of the rubbing surface (contact face), for each of the three configurations is shown in Figure 5. The corresponding temperatures located 0.079 inches below the rubbing surface are also shown in the figure.

It can be seen from the curves corresponding to the oil-cooled plate that moving the coolant holes closer to the source of heat has little effect on either the temperature level or on the local axial temperature gradient.

It is apparent that near the interface, the plate with no internal coolant has a lower local thermal gradient axially, radially, and circumferentially, but it has the highest temperature level. The local high-temperature region in each curve is due to the presence of heat generation at the interface between the seal and seal plate. The interface lies between 3.29 and 3.47 inches from the shaft's axis of rotation.

To obtain a seal plate with more uniform interface temperatures circumferentially and lower temperatures near the surface, a coolant annulus approximately the width of the seal lip might be incorporated near the face of the plate. The annulus would reduce the circumferential temperature variations which are characteristic of discrete hole designs.

2. RUBBING-CONTACT HYDRODYNAMIC PAD FACE SEAL WITH BELLOWS SECONDARY SEAL

a. Description

Figures 39 and 41 show sketches of the rubbing-contact hydrodynamic pad face seal. This seal consists of a carbon primary seal and a bellows secondary seal. The high-pressure air is at the inner edge of the seal.

Leakage air flows radially outward though grooves in the carbon face and the full pressure drop across the seal occurs over a 0.05-inch wide circumferential land or seal "dam". Hydrodynamic separation of the seal interface is produced by 12 pads on the carbon face located adjacent to the inner radius of the seal dam. The surface of each pad is tapered in the circumferential direction so that the rotational velocity of the seal plate produces a local increase in air pressure on the surface of each pad.

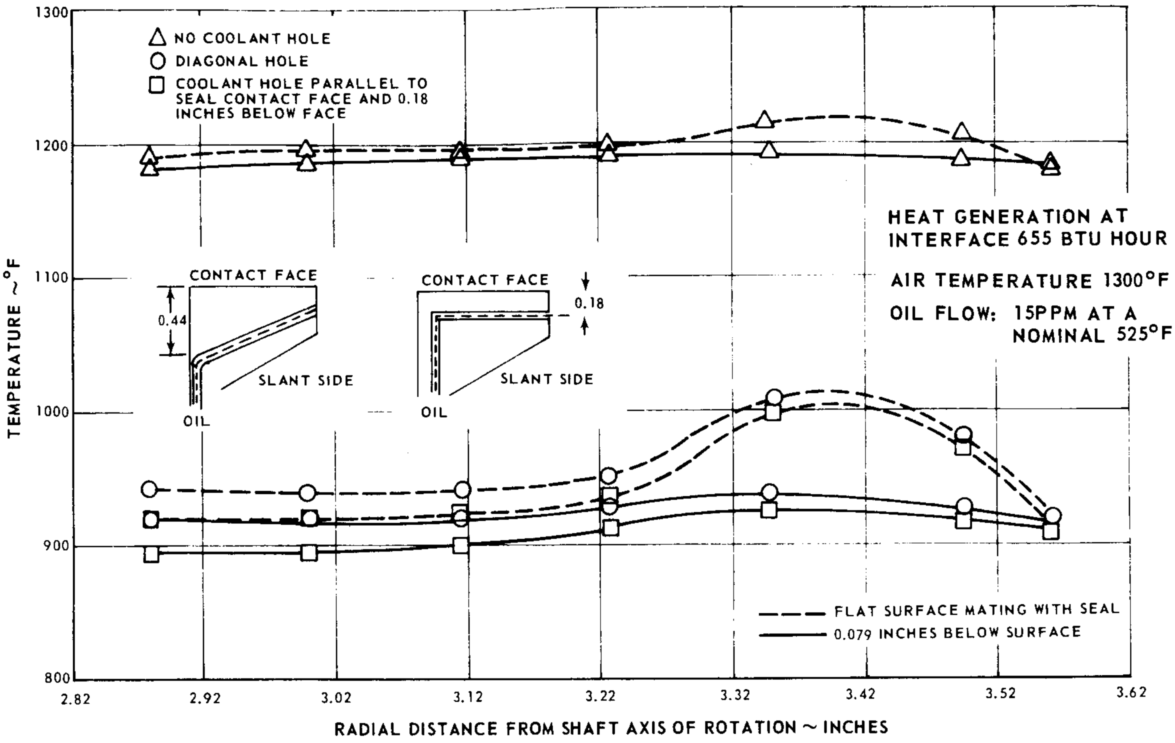

Figure 5 Local Seal Plate Temperature for Different Oil-Hole Locations

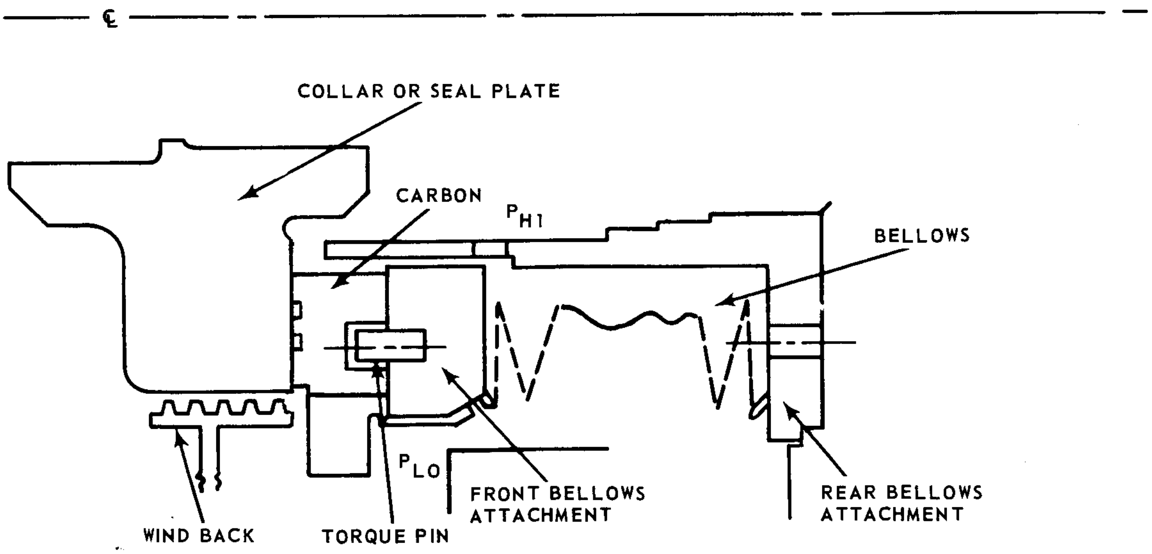
℄
COLLAR OR SEAL PLATE
CARBON
P_{HI}
BELLOWS
P_{LO}
FRONT BELLOWS ATTACHMENT
REAR BELLOWS ATTACHMENT
WIND BACK
TORQUE PIN

Figure 6 Rubbing-Contact Hydrodynamic-Pad Face Seal with Bellows Secondary Seal

b. Deflection Analysis

The deflection analysis of this seal was based on the equations of R. T. Roark (Reference 1). For purposes of the analysis, the seal was assumed to be composed of the section shown in Figure 7. The radial deflection of the carbon (δ carbon) was represented by Roark's equation for a thick-walled cylinder subject to pressure loading, Equation 1.

$$\delta_{\text{carbon}} = \frac{aP_1}{E_1} \; \frac{2b^2}{a^2-b^2} - \frac{aP_o}{E_1}\left(\frac{b^2+a^2}{a^2-b^2} - \nu_1\right) \qquad (1)$$

where:

P_o = Pressure associated with the press fit between the carbon and the carrier
P_1 = 300 psia
E_1 = 3×10^6 (Young's modulus of elasticity for carbon)
ν_1 = 0.25 (Poisson's ratio for carbon)
a = 3.75 inches
b = 3.1 inches

Similarly, the radial deflection of the carrier is represented by Equation 2,

$$\delta_{\text{carrier}} = \frac{aP_o}{E_2}\left(\frac{a^2 + c^2}{c^2 - a^2} + \nu_2\right) \qquad (2)$$

where:

E_2 = 30×10^6 (Young's modulus of elasticity for steel)
ν_2 = 0.3 (Poisson's ratio for steel)
c = 4.1 inches

To ensure continuity, the deflection of the carbon and carrier must be equal. The increase in P_o is 208.35 psi, and the radial deflections of the carbon and carrier are 0.00030 inch.

c. Force Calculations

The inertial loadings were calculated using the procedure described for the rubbing-contact face seal with piston-ring secondary seal. The total weight of the bellows (including the front end fitting) is 3.2053 pounds, or 0.1457 pounds per inch of circumference. G-loadings were calculated for sliding speeds of 200, 400, and 500 ft/sec, and multiplied by the bellows' weight per inch of circumference to obtain the inertial forces of the bellows on the seal face. To ensure good tracking, the spring force was set equal to the maximum inertial force. This means that the force supplied by the air-pressure differential is always in excess of the required amount. The results of these calculations are shown in Table II.

TABLE II

FORCE BALANCE SUMMARY

Pressure gradient (psig)	100	100	200	300
Velocity (ft/sec)	200	332*	400	500
G-loading	0.3646	1.0	1.458	2.28
Inertial force on seal face (lb/in)	0.0531	0.146	0.2124	0.3321
Spring Force (lb/in)	0.3321	0.3321	0.3321	0.3321
Required Pressure Force (lb/in)	-0.2790	-0.1861	-0.1197	0
Pressure Seat Force Supplied (lb/in)	0.1150	0.1150	0.0600	0
Excess Pressure Seat Force (lb/in)	0.3940	0.3011	0.1797	0

*Under condition of Δp=100 psig, 200 ft/sec, G=0.3646, it is intended that G $\geq$ 1 for design requirements, set G=1, thus inertia force is calculated to be equal to 0.146 lb/in and additional column is tabulated as shown.

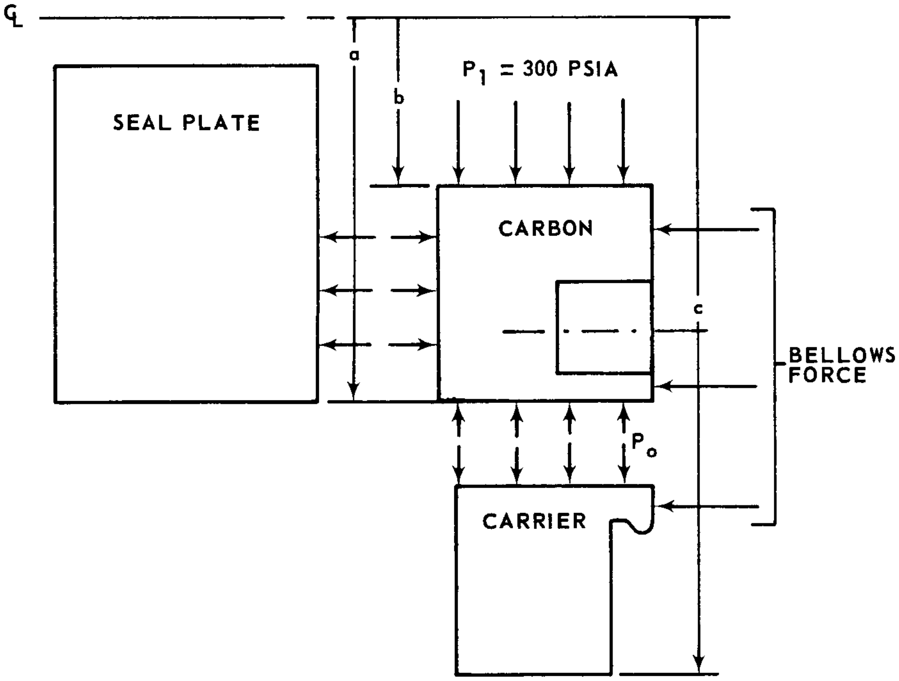

Figure 7 Simplified Model of the Rubbing-Contact Hydrodynamic-Pad Face Seal

C. ORIFICE-COMPENSATED GAS-FILM FACE SEALS

Originally, the contract dealt with two gas-film seals: an orifice-compensated hydrostatic seal and an orifice-compensated externally pressurized seal. A hybrid seal consisting of a hydrostatic seal running against a spiral-groove seal plate was added to the program in May 1967. These three seals are discussed jointly in the following sections. The original seal types were designed and manufactured by the Stein Seal Co.

1. HYDROSTATIC AND HYBRID SEAL CONFIGURATIONS

Figure 8 is a sketch of the orifice-compensated hydrostatic face seal mounted in the test rig. Figure 8 and the discussion below also apply to the hybrid seal, since the only difference between the two seals is that the seal plate of the hybrid seal has spiral grooves etched in it by NASA-Lewis.

The sealed high-pressure air is ducted through three holes to an annular groove (1) in the carbon face. Each of the holes contains an assembly of four orifices in series (2). The leakage flow through the orifice produces a pressure drop from the sealed pressure to the recess (annular groove in the carbon) pressure (P_r), and the sealing gap height is controlled by compensations in this recess pressure. If the sealing gap height is closed down for some reason the following occurs: (a) the seal leakage out is reduced, (b) the pressure drop across the orifices is reduced because of reduced leakage flow, thus the recess pressure increases and (c) the increased recess pressure acts as a restoring force to maintain design gap height. If the seal gap opens beyond the design point the inverse process takes place, therefore the design gap is maintained by compensations in the recess pressure.

2. EXTERNALLY PRESSURIZED SEAL CONFIGURATION

Figure 9 is a schematic drawing of the externally pressurized face seal. This seal is a film-riding seal which allows high-pressure gas to be introduced to the annular groove in the carbon from an external source. The addition of the external source is the principal difference between this seal and the other two film-riding seals. Like the other two seals, the gas is introduced to the annular groove through three holes, each of which contains four orifices in series. This gas and the leakage air creates the gas film for the seal to ride on.

3. FORCE BALANCE AND LEAKAGE CALCULATIONS

The procedure described in this section is for the externally pressurized seal. Calculations for the hydrostatic seal were similar, but somewhat simpler. The analysis requires that all axial forces on the seal carbon nosepiece are balanced. The analytical model on which the calculations are based is shown

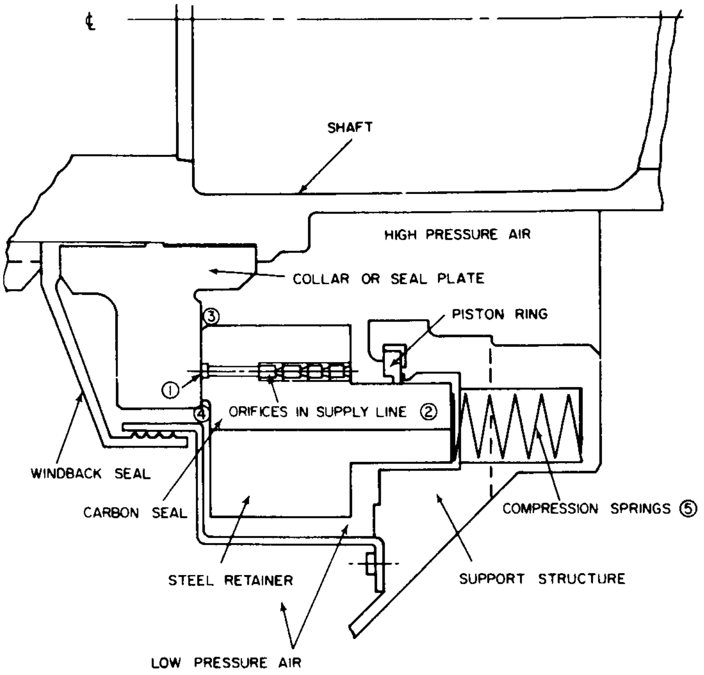
℄
SHAFT
HIGH PRESSURE AIR
COLLAR OR SEAL PLATE
③
PISTON RING
①
④
ORIFICES IN SUPPLY LINE ②
WINDBACK SEAL
CARBON SEAL
COMPRESSION SPRINGS ⑤
STEEL RETAINER
SUPPORT STRUCTURE
LOW PRESSURE AIR

Figure 8 Schematic of the Orifice-Compensated Hydrostatic Face Seal

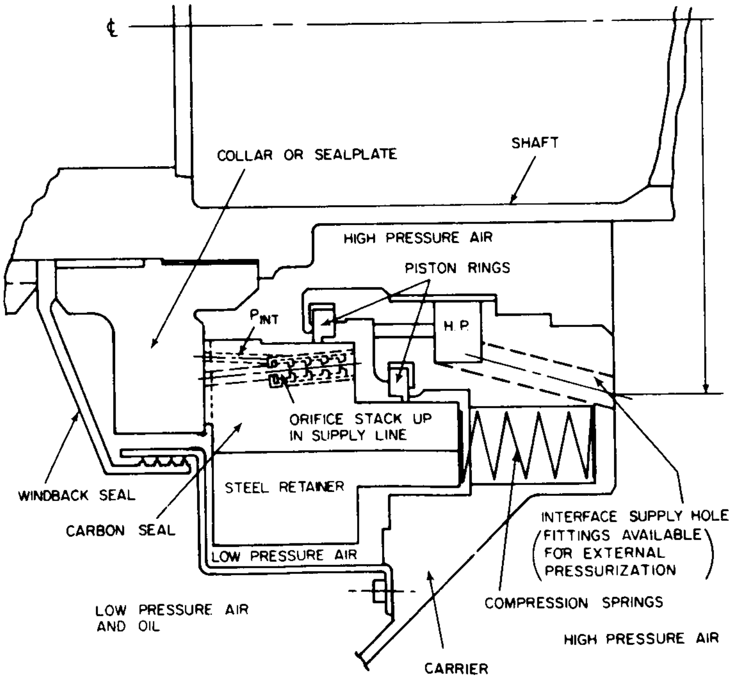
℄
COLLAR OR SEALPLATE
SHAFT
HIGH PRESSURE AIR
PISTON RINGS
P_{INT}
H P
ORIFICE STACK UP IN SUPPLY LINE
WINDBACK SEAL
STEEL RETAINER
CARBON SEAL
LOW PRESSURE AIR
INTERFACE SUPPLY HOLE (FITTINGS AVAILABLE FOR EXTERNAL PRESSURIZATION)
LOW PRESSURE AIR AND OIL
COMPRESSION SPRINGS
HIGH PRESSURE AIR
CARRIER

Figure 9 Schematic of the Externally Pressurized Face Seal

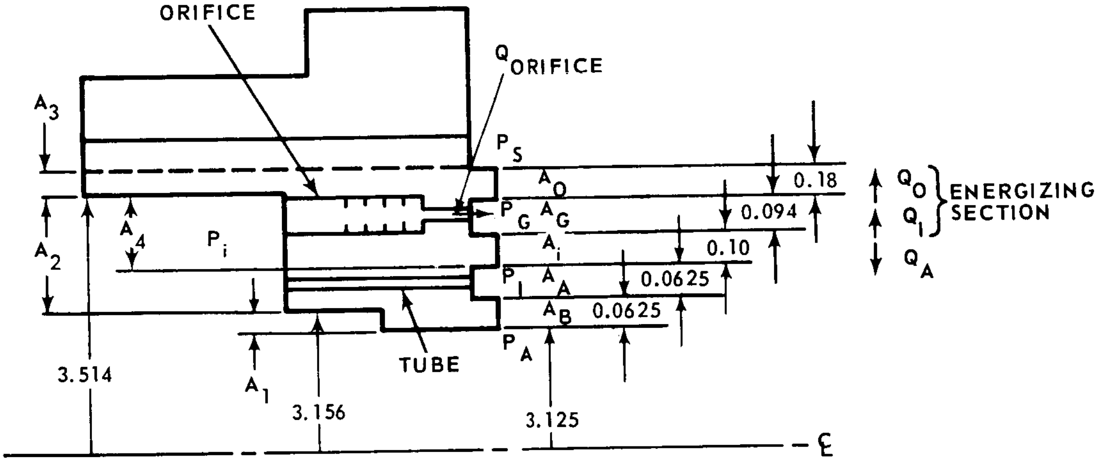
ORIFICE
$Q_{ORIFICE}$
A_3
P_S
A_O
0.18
Q_O
ENERGIZING SECTION
P_G
A_G
0.094
Q_I
A_2
A_4
P_i
A_i
0.10
Q_A
P_I
A_A
0.0625
A_B
0.0625
P_A
TUBE
3.514
A_1
3.156
3.125
℄

Figure 10 Analytical Model for Force Balance and Leakage Calculations

in Figure 10. The energizing section consists of three equally spaced orifice assemblies (one of which is shown in Figure 10). Each orifice assembly contains four orifice plates, each with a well-rounded 0.0225-inch or 0.0290-inch diameter orifice, depending upon whether the orifice-compensated externally pressurized or hydrostatic seal is used. The annular areas (A_o, A_G, etc.) are listed below:

$A_o = \pi(3.624^2 - 3.444^2) = 3.9947 \text{ in}^2$
$A_G = 2.0052 \text{ in}^2$,
$A_i = 2.0724 \text{ in}^2$,
$A_A = 1.2635 \text{ in}^2$,
$A_B = 1.2390 \text{ in}^2$,

$A_1 = 0.6114 \text{ in}^2$
$A_2 = 7.4980 \text{ in}^2$
$A_3 = 2.4655 \text{ in}^2$
$A_4 = 5.6100 \text{ in}^2$

To make the calculations, the following values were assumed as the conditions of operation:

Pressurizing gas	$P_i = 335$ psia	$T_i = 200°F$
Sump gas	$P_S = 15$ psia	$T_S = 500°F$
Ambient air	$P_A = 315$ psia	$T_A = 1300°F$
Viscosity	$\mu = 240$ micropoise	

For continuity of the flow

$$Q_{total} = Q_{orifice} + Q_{inner\ dam} = Q_{outer\ dam}$$

where:

$$Q_{orifice} = C_D\, P_i\, A_{Oi}\, C_1\, C_2\, K_r$$

C_D = Orifice discharging coefficient = 0.85
A_{Oi} = Area of three orifices
C_1 = Conversion factor to scfm = $(P_i/P_{st})\,(T_{st}/T_i)$
$C_2 = 60g/\rho\sqrt{RT}) = (60 \times 386)/(7.64 \times 10^{-2} \times \sqrt{245{,}000 \times 760\#}) = 87.6$
$K_r = f\,(P_i/P_G) = f(r)$

and

$$f(r) = \sqrt{\frac{2k}{k-1}}\left(r^{1}/k\right)\left[1-r^{\frac{k-1}{k}}\right]^{\frac{1}{2}} \quad \text{for } r > \left(\frac{2}{k+1}\right)^{\frac{k}{k-1}}$$

$$= \sqrt{\frac{2k}{k+1}}\left(\frac{2}{k+1}\right)^{\frac{1}{k-1}} \quad \text{for } r \leq \left(\frac{2}{k+1}\right)^{\frac{k}{k-1}}$$

where

$k = C_p/C_v = 1.4$ for air
$r = P_i/P_G$

then

$$*Q_{\text{inner dam}} = 2\pi R_{mi} \frac{h_o^3}{24 \mu L_i} \quad \frac{(P_i^2 - P_G^2)}{P_{st}} \quad \frac{T_{st}}{T}$$

$$*Q_{\text{outer dam}} = 2\pi R_{mo} \frac{h_o^3}{24 \mu L_o} \quad \frac{(P_G^2 - P_S^2)}{P_{st}} \quad \frac{T_{st}}{T}$$

where

R_m = the mean radius of the inner or outer dams

L_i and L_o = the differences between the inner and outer radii of the areas A_i and A_o, respectively.

T_{st} and P_{st} = temperature and pressure at standard conditions.

h_o = film thickness.

With the substitution of Q_{orifice}, $Q_{\text{inner dam}}$, and $Q_{\text{outer dam}}$ into the continuity equation, we have

$$5.604\, K_r + 4.0336 \times 10^{+6}\, h_o{}^3\, (P_i^2 - P_G^2) = 2.4 \times 10^{+6}\, h_o{}^3\, (P_G^2 - P_S^2)$$

Since K_r is a function of P_G, P_G can be determined from this equation with a given value of h_o.

It is to be noted that K_r is a function of P_G, with given value of h_o, P_G can be determined through nomograph or computer iteration from the above equation.

The total force generated in the seal face is the summation of all the pressure force from the areas A_O, A_G, A_i, A_A and A_B. Since P_i has the same order as P_A, the total force can be approximated by summing the pressure forces from A_O, A_G and A_i only. Thus

$$F_{\text{total}} = F_O + F_G + F_i$$

where

$$F_O = K_O A_O (P_G - P_S)$$

$$F_G = A_G (P_G - P_S)$$

$$F_i = K_i A_i (P_I - P_G) + A_i (P_G - P_S)$$

K_O and K_i are the equivalent pressure balancing coefficients.

* See Reference 2

With the calculated P_G for a given thickness h_o, K_o and K_i can be determined from the formula of pressure distribution; which is function a film thickness, pressure gradient across the seal width, downstream pressure, and the seal width. F_{total} is the summation of F_o, F_G, and F_i, and is given in Table III below with the corresponding K_o and K_i values.

TABLE III

LEAKAGE AND RESTORING FORCE RESULTS

$h_o x10^{-4}$ (in)	P_G, (psia)	K_o	K_i	F_{tot} (lb)
2	310	0.651	0.5065	1997.3
3	289	0.650	0.512	1874.43
4	275	0.6495	0.516	1798.9
5	271	0.6485	0.5175	1777.1
7	267.5	0.648	0.5185	1756.7

At equilbrium,

$$F_{seat} = F_{total}$$

At openings other than equilbrium

$$F_{restoring} = F_{total} - F_{seat}, \text{ where } F_{seat} = P_i A_4$$

Q_{FL} = face leakage to sump = $2.4 \times 10^{+6} h_o^3 (P_G^2 - P_S^2)$. Substitute values of h_o and P_G calculated for face leakage. Face leakage to sump is then plotted in Figure 11 for the 300-psi (P_A-P_S) condition.

Q_A = face leakage to ambient = $6.173 \times 10^{+6} H_o^3 (P_i^2 - P_S^2)$. Leakage to the ambient side was controlled by face opening. These results are plotted as a dotted line in Figure 11 for the same operating condition.

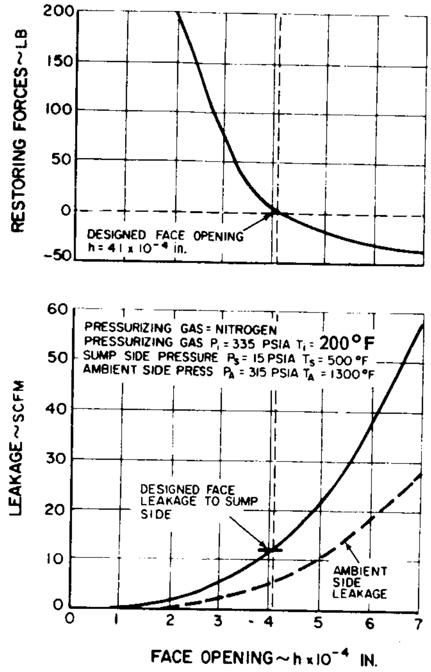

Figure 11 Characteristics of the Externally Pressurized Seal When P_A = 315 psia

Results of calculations at other conditions are illustrated in Figures 12 through 14.

Results of calculations for the Hydrostatic Seal are illustrated in Figures 15 through 18.

4. SPRING FORCE CALCULATIONS

The inertial forces on the seal assembly and the friction force on the piston ring were calculated in order to estimate the required spring force. The weight of the steel band which contains the carbon seal is 2.71 pounds and the weight of the seal itself is 0.772 pounds, for a total weight of 3.48 pounds, or a weight per inch of circumference of 0.158 lb/in. At the condition of $\Delta P=300$ psi, the sliding velocity is 500 ft/sec, which corresponds to a speed of 16,371 rpm, or 1712 rad/sec. Assuming a runout of 6×10^{-4} inch total indicator reading, and simple harmonic motion, then

$$X = \sin \omega t$$
$$\ddot{X} = -\omega^2 \sin \omega t = -\omega^2 X$$

where X = axial displacement and X_{max} = 1/2 runout.

then,

$$G = \frac{\omega^2 X_{max}}{g} = \frac{2.93\times10^{6}(3\times10^{-4})}{3.86\times10^{2}} = 2.28$$

The equivalent force on the seal's face (F_I) is equal to the seal's weight per inch of circumference times the G-loading. For this case, $F_I = 0.158 \times 2.28 = 0.36$ lb/in. The results of these calculations are tabulated below:

ΔP (psi)	Velocity (ft/sec)	Weight (lb/in)	G	F_I (lb/in)
100	200	0.158	0.3646	0.0576
200	400	0.158	1.458	0.230
300	500	0.158	2.28	0.36

Frictional forces on the piston ring were calculated using the freebody diagram shown in Figure 19. Definitions of the parameters used in the calculations are shown below:

F_{rp} = Force per inch of circumference on the piston ring in the radial direction due to $\Delta P = \Delta P\,(1-K)\,(0.019)$.

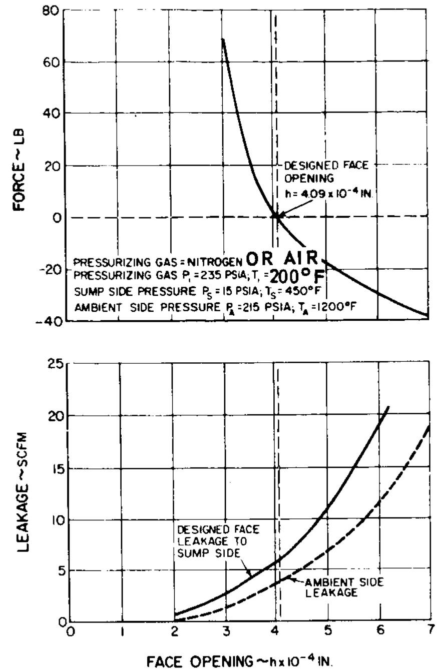

Figure 12 Characteristics of the Externally Pressurized Seal When $P_A = 215$ psia

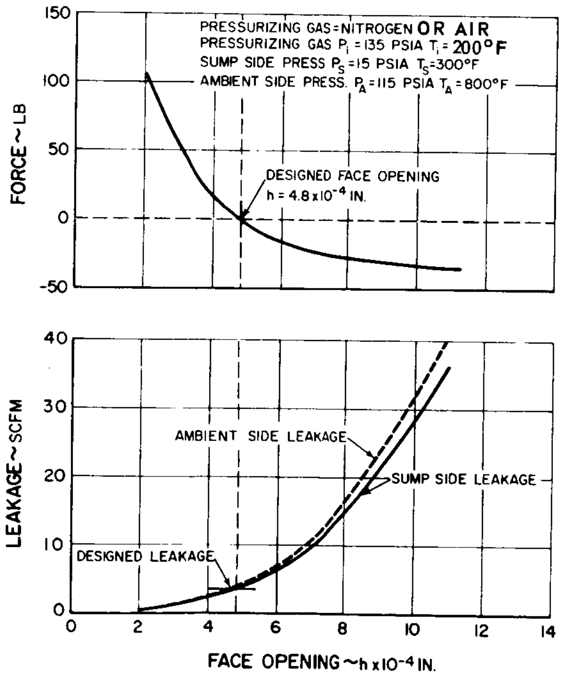

Figure 13 Characteristics of the Externally Pressurized Seal When $P_A = 115$ psia

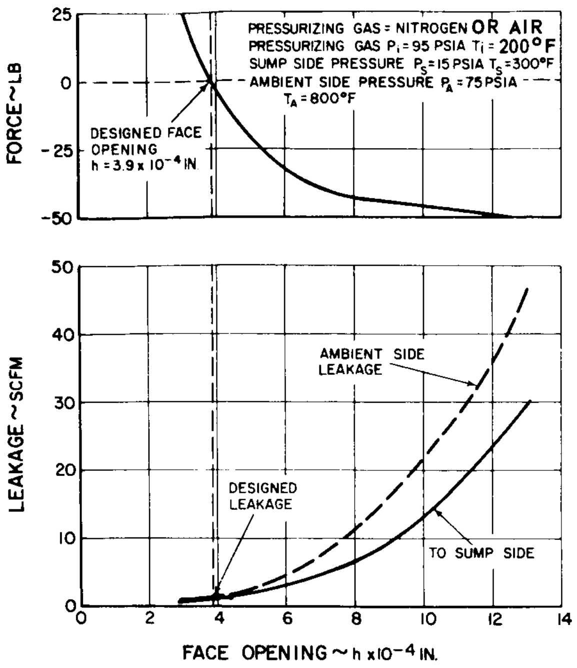

Figure 14 Characteristics of the Externally Pressurized Seal When P_A = 75 psia

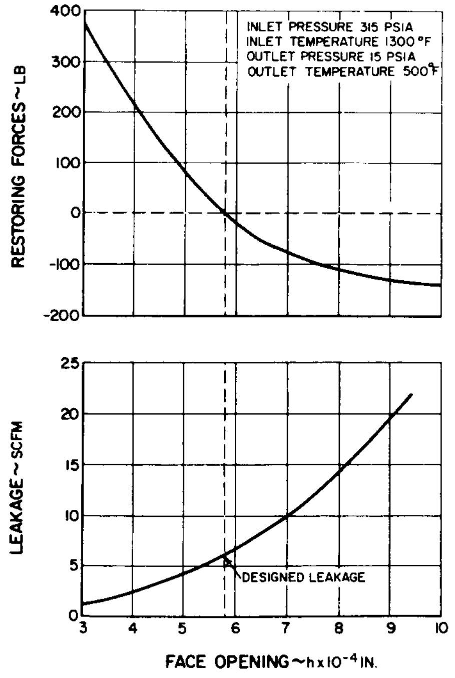

Figure 15 Characteristics of the Hydrostatic Seal When P_A = 315 psia

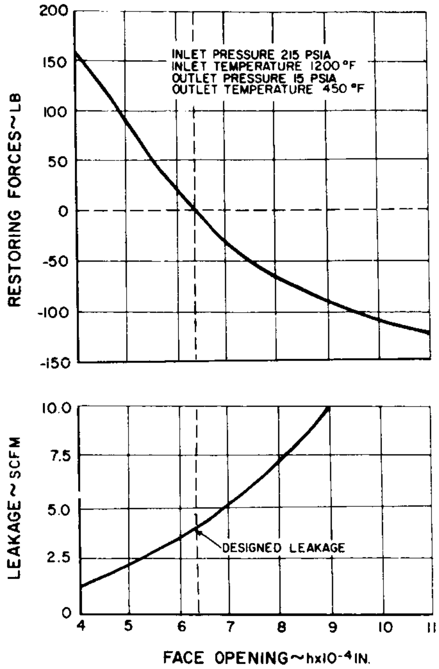

Figure 16 Characteristics of the Hydrostatic Seal When P_A = 215 psia

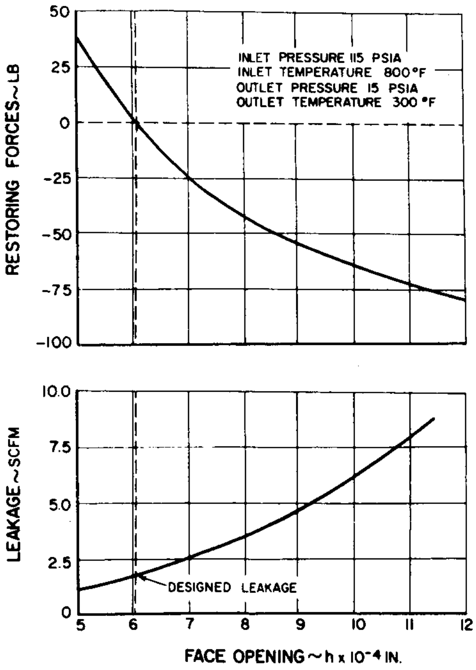

Figure 17 Characteristics of the Hydrostatic Seal When P_A = 115 psia

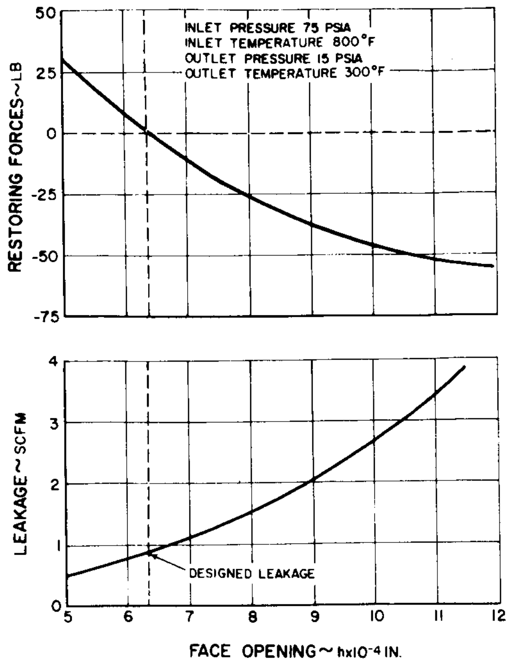

Figure 18 Characteristics of the Hydrostatic Seal When P_A = 75 psia

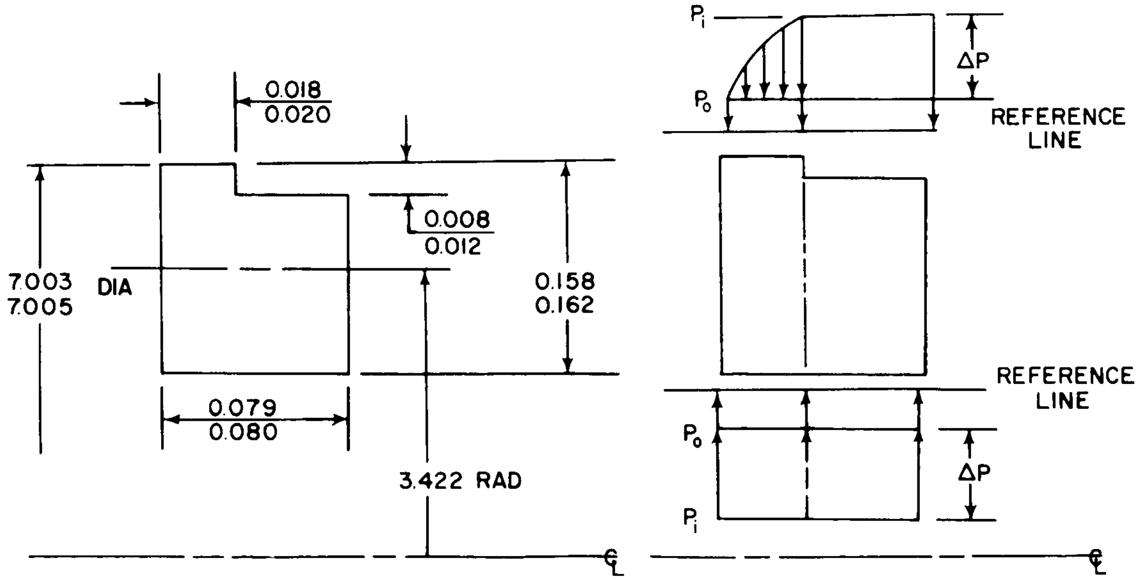
0.018
0.020
0.008
0.012
7.003
7.005
DIA
0.158
0.162
0.079
0.080
3.422 RAD
℄
P_i
P_o
ΔP
REFERENCE LINE
REFERENCE LINE
P_o
P_i
ΔP
℄

Figure 19 Freebody Diagram of the Piston Ring

F_{rs} = Force per inch of circumference on the piston ring in the radial direction due to its tendency to restore itself to its original shape = 0.15 lb/in.

F_{rt} = Total force per inch of circumference on the piston ring in the radial direction = $F_{rp} + F_{rs}$

C_f = Coefficient of friction = 0.2

F_{pr} = Force on the piston ring in the axial direction due to friction = $F_{rt} \times C_f$

K = Equivalent pressure balancing coefficient: the fraction of ΔP acting over the dam area.

The calculations are summarized in the tabulation below:

ΔP (psi)	Velocity (ft/sec)	K	F_{rp} (lb/in)	F_{rt} (lb/in)	F_{pr} (lb/in)
100	200	0.629	0.705	0.85	0.1710
200	400	0.646	1.344	1.494	0.2988
300	500	0.652	1.98	2.13	0.426

The total force on the piston ring is the sum of the inertial and friction forces. In calculating the required loading, however, one is interested in G-loadings greater than or equal to 1.0. Therefore, in calculating the required loading, F_I was taken to be 0.158 at a velocity of 200 ft/sec., despite the fact that the G-loading at that velocity is only 0.3646. The total forces calculated in this way were divided by a factor of 0.85 to obtain the required loading. This value is a safety factor to overcome the locking-pin friction, and is based on past experience. The results of the calculations are shown in Table IV.

TABLE IV

REQUIRED SPRING LOADINGS

ΔP (psi)	Velocity (ft/sec)	F_I (lb/in)	F_{pr} (lb/in)	Total Force (lb/in)	Required Loading (lb/in)
100	200	0.158	0.171	0.329	0.388
200	400	0.230	0.2988	0.5288	0.621
300	500	0.36	0.426	0.786	0.925

The average seal operating pressure was 200 psi. At this condition, the required loading is 0.621 lb/in. It was assumed that nearly half of this force would be taken up by the spring: consequently 0.3 lb/in in axial spring force was required. The total spring force was then $0.3 \times 2\pi \times 3.502$, or 6.6 pounds.

Since the design required 18 springs, the force per spring was 0.367 pounds. The characteristics of the spring are listed below:

Material - Inconel X
Operating temp. - 900°F (heat-treat accordingly)
Ends to be ground flat and square
Wire diameter - 0.03 in.
Mean coil diameter - 0.450 in.
Total coils - 18
Active coils - 16
Scale - 0.8 lb/in
Free length - 1.336 in
Normal operating length - 0.877 in
Load at operating length - 2.367 lb/spring
Stress at operating length - 15,500 psi

5. SEAL RING DISTORTION BECAUSE OF PRESSURE LOADING

The tilting of the seal face because of pressure loading was approximated by considering only the tilting of the seal support, since the steel support has a higher modulus of elasticity than the carbon seal. The height of the extruded section of the steel seal support was determined by matching the position of the centroid in the x-direction with that of the carbon seal. Thus, the resultant radial forces pass through the centroids of both pieces. The dimensions of the seal support and its center of gravity are shown in Figure 20.

To calculate the moment of inertia, it was assumed that the surfaces of A and B in Figure 20 were plane surfaces,

$$I = \frac{bh^3}{12} + A\ell^2$$

$$\begin{array}{lll} \text{Member A:} & 1/12\,(0.225)\,(0.6)^3 + 0.245\,(0.178)^2 & = 0.01181 \\ \text{B:} & 1/12\,(0.613)\,(0.4)^3 + 0.135\,(0.322)^2 & = \underline{0.01725} \\ & I & = 0.02906 \text{ in}^4 \end{array}$$

$F_r = \Delta P\ell$ where $\ell \equiv$ distance from face of collar to land face of piston ring

$= 300\ (0.9) = 270$ lb/in of circumference.

$M = F_r\,(\frac{0.9}{2} - 0.438) = 270\ (0.012) = 3.24$ lb-in/in of circumference.

$$\theta = \frac{MR^2}{EI} = \frac{(3.24)\,(4.07)^2}{30 \times 10^6 \times .029} = 61.9\text{x}10^{-6} \text{ radian}$$

The moment is in the clockwise direction, and the tilting of the steel seal support will create a converging gas film for the carbon seal nosepiece. This converging

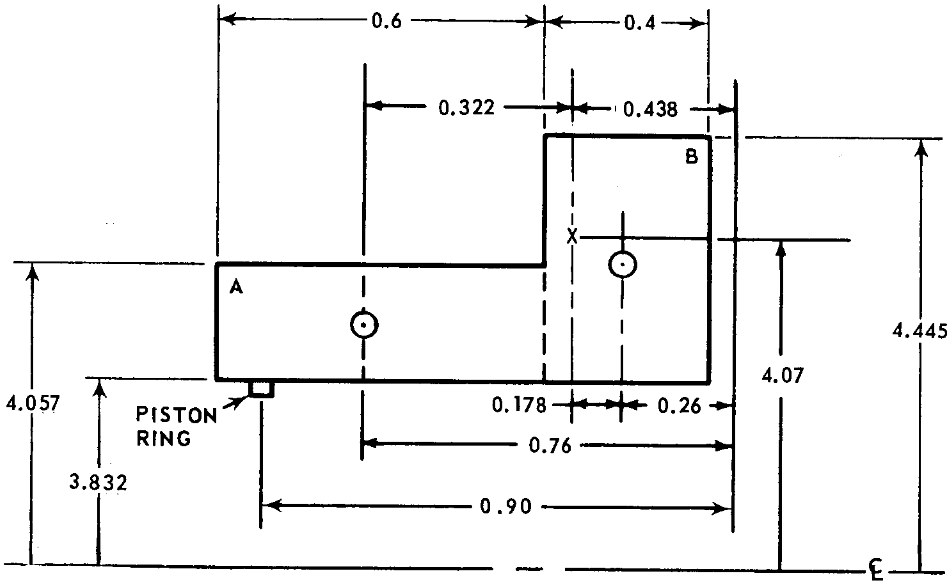
0.6
0.4
0.322
0.438
B
X
A
4.057
3.832
PISTON
RING
0.178
0.26
0.76
0.90
4.07
4.445
℄

Figure 20 Dimension and Center of Gravity of the Seal Support

film (that is one in which the clearance decrease with flow) gives rise to a positive stiffness and hence stability.

6. DEFLECTION OF THE SEAL ASSEMBLY BECAUSE OF PRESSURE LOADING

The deflection of the seal support was calculated by using the standard formula for a thick-walled cylinder subject to internal and external loading. The radial deflections of the hydrostatic seal and the externally-pressurized hydrostatic seal were determined to be 0.00016 inch and 0.00028 inch respectively, for a pressure loading of 300 psig. The deflection of the clamped seal plate was estimated from the formula for a uniformly loaded ring fixed at its inner edge. The deflection amounts to 0.0000295 inch under an axial pressure load of 300 psig. The unclamped seal-plate design was also analyzed as described below.

The cross section of the seal plate is shown in Figure 21. The radius of the centroid was found to be 3.07 inches from the centerline, and its distance from the right side was found to be 0.726 inch. The moment of inertia about the radial axis through the centroid was found to be 0.1162 inch^4. The calculations for the moment due to axial loading are summarized in the tabulation below:

			F (lb/in)		R (in)		M_a (in-lb. /in.)
F_p = 1315 lb.	/ 2π(3.07)	=	68.2	x	3.052	=	208.
F_i = 1115 lb.	/ 2π(3.07)	=	57,9	x	3.269	=	189.2
F_G = 490 lb.	/ 2π(3.07)	=	25.4	x	3.416	=	86.6
F_o = 544 lb.	/ 2π(3.07)	=	28.2	x	3.563	=	100.6
F_R = -3464lb.	/ 2π(3.07)	=	-179.9	x	2.945	=	-530.
							M_a = 54.4

The moment per inch of circumference at the centroid's radius is therefore 54.4 in-lb/in. in a clockwise direction.

The pressure load of 300 psig gives a radial force per inch of circumference of 97 lb/in at the radius of the centroid (3.07 inches). This force acts at 0.547 inch from the centroid, producing a moment due to radial loading (M_r) of # -53.0 in-lb/in.

The angular displacement of the seal plate is then,

$$\theta = \frac{(M_a+M_r)R_c^2}{EI} = 3.8\text{x}10^{-6} \text{ radians}$$

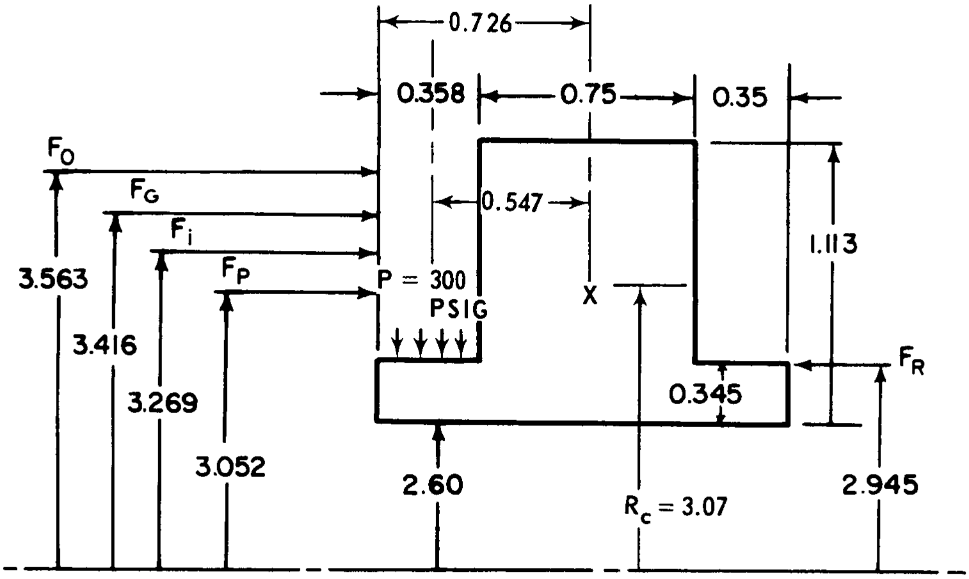
0.726
0.358
0.75
0.35
F_O
F_G
F_i
F_P
0.547
1.113
P = 300 PSIG
X
3.563
3.416
3.269
3.052
0.345
F_R
2.60
$R_c = 3.07$
2.945

Figure 21 Cross Section of the Seal Plate

7. STRESS ON THE SEAL SUPPORT AND SEAL NOSEPIECE BECAUSE OF SHRINKAGE

For shrinkage allow

$$\delta_{min} = 18 \times 10^{-3} \text{ (radial) inch}$$

$$\delta_{max} = 20 \times 10^{-3} \text{ (radial) inch}$$

$$A_{carbon} = 0.5186 \text{ in}^2$$

$$A_{steel} = 0.3802 \text{ in}^2$$

$$F_{max} = \frac{\delta_{max}}{R^2} \times \frac{(EA)_{steel} \cdot (EA)_{carbon}}{(EA)_{steel} + (EA)_{carbon}}$$

$$= \frac{20 \times 10^{-3}}{(3.832)^2} \times \frac{30 \times 10^6 \times 0.3802 \times 3 \times 10^6 \times 0.5186}{30 \times 10^6 \times 0.3802 + 3 \times 10^6 \times 0.5186} = 1859 \text{ lb/in}$$

$$T = F_{max} \times R$$

$$= 1859 \times 3.832 = 7123.68 \text{ pounds}$$

$$\sigma_{steel} = \frac{T}{A} = \frac{7123.68}{0.3802} = 18736.66 \text{ psi}$$

$$\sigma_{carbon} = \frac{7123.68}{0.5186} = 13736.36 \text{ psi}$$

8. PISTON-RING STRESS

The dimensions of the large and small piston rings are shown in Figure 22. The large piston ring was used in both the plain hydrostatic seal and the externally pressurized seal, while the small ring was used only in the externally pressurized seal. For both the large and small rings, the stress was calculated by assuming a uniformly distributed load on the ring to calculate the gap closure, and calculating the stress from the gap closure.

$$\text{gap closure} = \frac{9.43 F_{rs} \, R_m^{\;4}}{EI}$$

where F_{rs} = 0.15 lb/in
R_m = mean radius
E = modulus of elasticity
I = moment of inertia

For the large ring, the gap closure was found to be 0.2368 inch for the plain hydrostatic seal and 0.2401 inch for the externally pressurized seal. For the small ring, the gap closure was 0.1546 inch. Given the gap closure, the stress in the ring can be expressed as:

$$\sigma_{Pr} = \frac{d(E)\ (\text{gap closure})}{9.43\ R_m^2}$$

where

σ_{Pr} = stress in piston ring due to closing it the amount of the gap closure.

d = radial wall thickness of the ring.

For the large piston ring, the stress was found to be 10,200 psi in the plain hydrostatic seal and 10,359 psi in the externally pressurized seal. The stress was 8304 psi in the small piston ring.

9. STRESS IN THE SHROUD AND WINDBACK

To calculate the stress in the shroud and windback, the assembly was divided into four parts, as shown in Figure 23.

Part 1:

$$\text{Volume of ring} = \frac{\pi}{4}\ (5.6^2 - 5.152^2)\ (0.15) = 0.565\ \text{inch}^3$$

$$\text{Weight of ring} = 0.278 \times 0.565 = 0.157\ \text{pound}$$

$$\text{Centrifugal force, } F_1 = 28.416 \times 10^{-6}\ W_1\ R_{m1}\ n^2$$

$$= 28.416 \times 10^{-6} \times 0.157 \times 2.688\ n^2 = 12.\ 10^{-6}\ n^2$$

Part 2:

$$W_2 = \frac{\pi}{4}\ (6.658^2 - 5.6^2)\ (0.10)\ (0.278) = 0.2827\ \text{pound}$$

$$F_2 = 28.416 \times 10^{-6}\ W_2\ R_{m2}\ n^2$$

$$= 28.416 \times 10^{-6} \times 0.2827 \times 3.0645\ n^2 = 24.61 \times 10^{-6}\ n^2$$

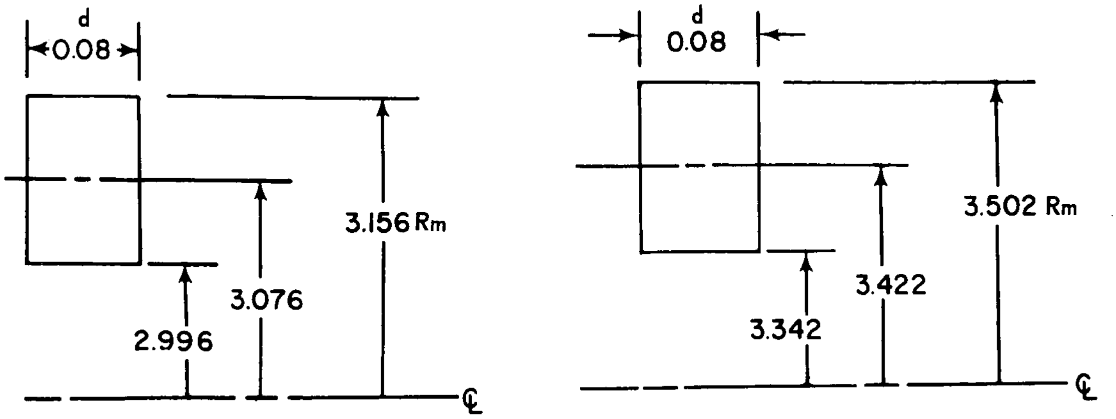
d
0.08
3.156 Rm
3.076
2.996
℄
d
0.08
3.502 Rm
3.422
3.342
℄

Figure 22 Dimension of the Large and Small Piston Rings

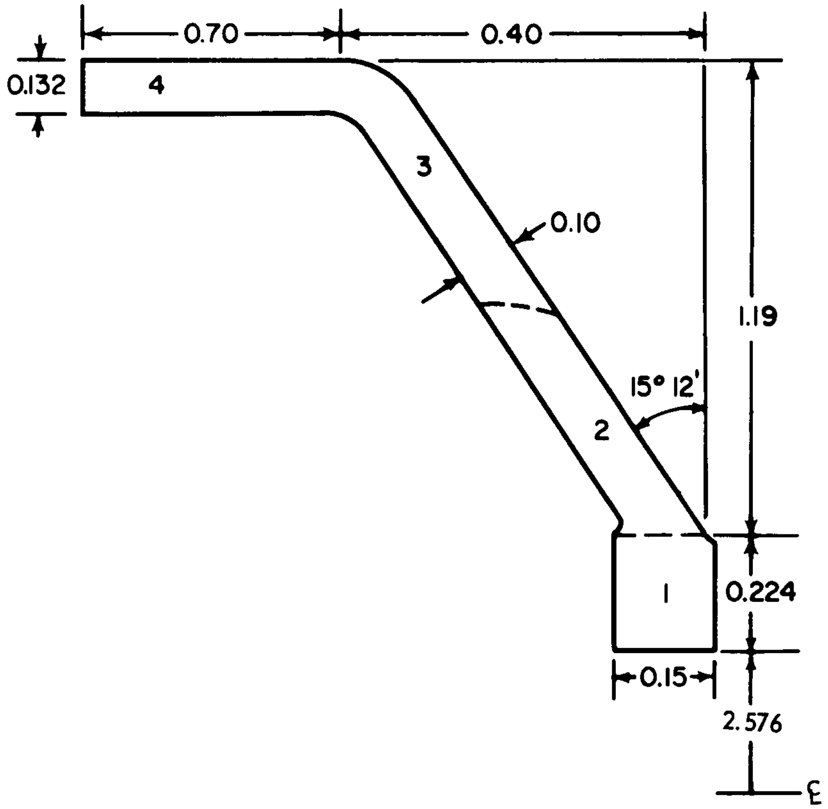
0.70
0.40
0.132
4
3
0.10
1.19
15° 12'
2
0.224
1
0.15
2.576
℄

Figure 23 Dimensions of the Shroud and Windback

Part 3:

$$W_3 = \frac{\pi}{4} (7.716^2 - 6.658^2) (0.10) (0.278) = 0.3319 \text{ pound}$$

$$F_3 = 28.416 \times 10^{-6} W_3 R_{m_3} n^2$$

$$= 28.416 \times 10^{-6} \times 0.3319 \times 3.5935 n^2 = 33.89 \times 10^{-6} n^2$$

Part 4:

$$W_4 = \frac{\pi}{4} (7.98^2 - 7.716^2) (0.70) (0.278) = 0.6335 \text{ pound}$$

$$F_4 = 28.416 \times 10^{-6} \times 0.6335 \times 3.924 n^2 = 70.63 \times 10^{-6} n^2$$

The results of the calculations are summarized in the tabulation below:

Speed (ft/sec)	n (rpm)	F_1 (lb)	F_2 (lb)	F_3 (lb)	F_4 (lb)	ΣF (lb)
500	16,350	3223.6	6516.7	9061.5	18895.0	37,696.8
450	14,700	2605.0	5266.0	7322.4	15269.0	30,462.4
400	13,100	2069.5	4183.6	5817.0	12130.0	24,200.0
200	6,550	517.4	1046.0	1454.3	3032.6	6050.3

As shown in the tabulation, the maximum total force is approximately 37,700 pounds. Therefore, the maximum force per inch of circumference is 2235 lb/in and the maximum stress is 22,350 psi per inch of circumference.

10. THERMAL ANALYSIS

Thermal analysis of the orifice-compensated hydrostatic face seal shows that the distortion of the seal plate depends largely on the relative temperatures of the high- and low-pressure air. Temperature distributions were determined analytically for two situations which differed only in the temperatures of the high- and low-pressure air.

The temperature pattern shown in Figure 24 is based on typical test conditions of environmental temperatures, pressures, and air leakage rates. The temperature pattern shown in Figure 25, was calculated on the same basis, except that the temperature of the high-pressure air was increased to its design value of 1300 degrees Fahrenheit. When the high-pressure air is cooler than the low-pressure air, as shown in Figure 24, there will be a convergent film at the primary seal interface. When the high pressure air is hotter than the low pressure air, see Figure 25, a divergent film will be present.

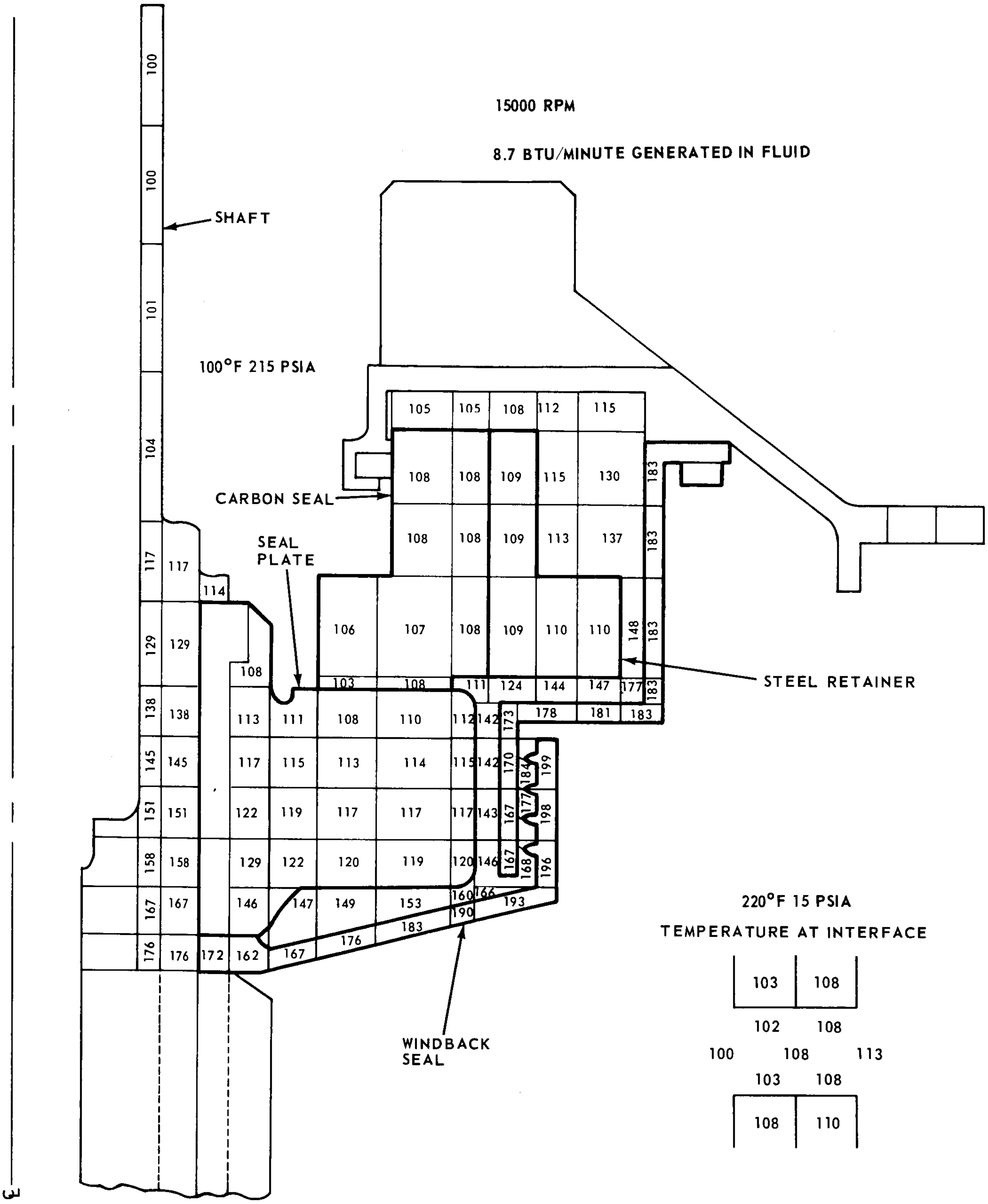
15000 RPM
8.7 BTU/MINUTE GENERATED IN FLUID
SHAFT
100°F 215 PSIA
CARBON SEAL
SEAL PLATE
STEEL RETAINER
WINDBACK SEAL
220°F 15 PSIA
TEMPERATURE AT INTERFACE
103 108
102 108
100 108 113
103 108
108 110
100 100 101 104 117 129 138 145 151 158 167 176
117 129 138 145 151 158 167 176
114 172 162
105 105 108 112 115
108 108 109 115 130 183
108 108 109 113 137 183
106 107 108 109 110 110 148 183
108 113 111 103 108 111 124 144 147 177 183
108 110 112 142 173 178 181 183
117 115 113 114 115 142 170 184 199
122 119 117 117 117 143 167 177 198
129 122 120 119 120 146 167 168 196
146 147 149 153 160 166 193 190
167 176 183
3

Figure 24 Temperature Pattern for the Orifice-Compensated Hydrostatic Face Seal with High-Pressure Air Cooler than Low-Pressure Air

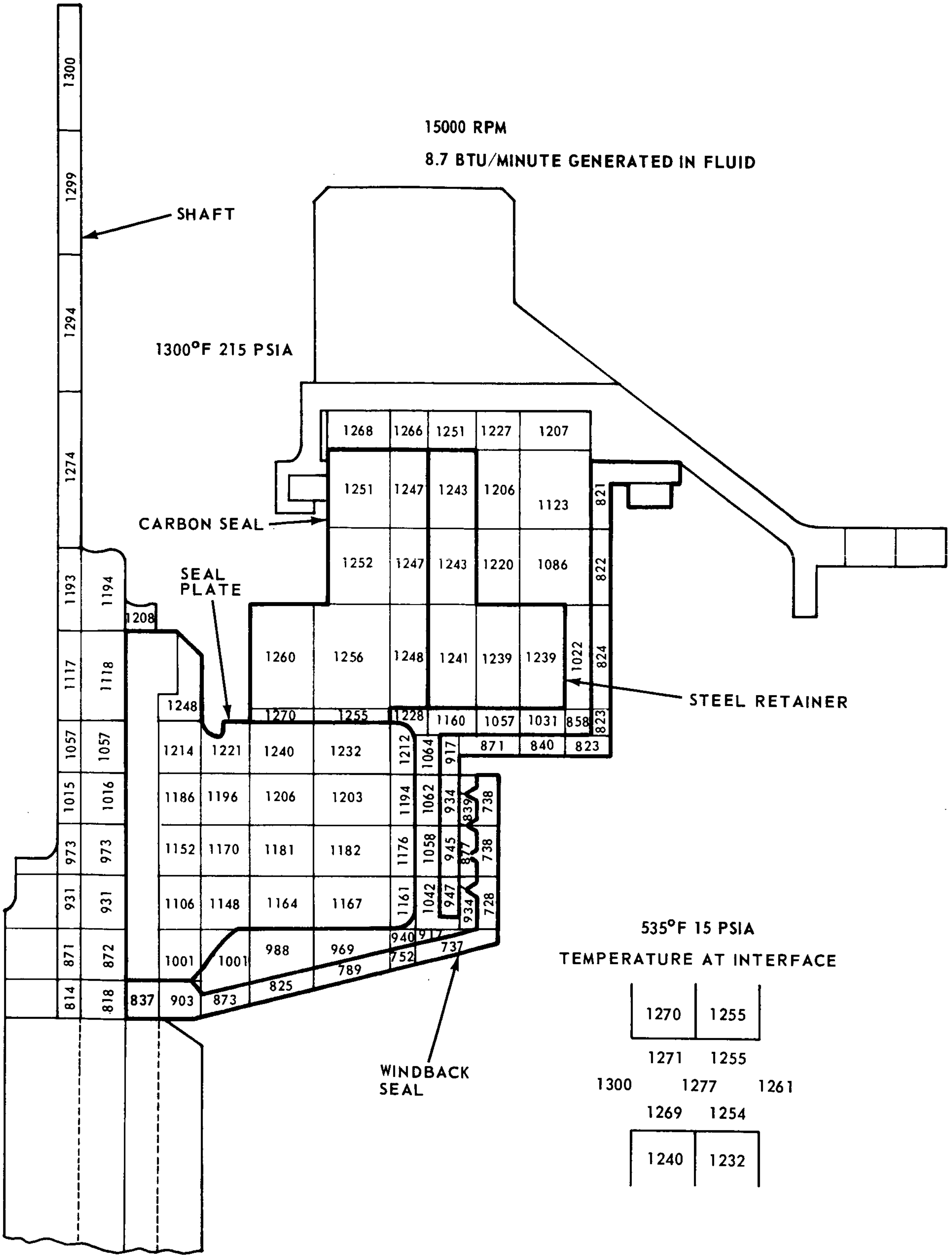
15000 RPM
8.7 BTU/MINUTE GENERATED IN FLUID
SHAFT
1300°F 215 PSIA
CARBON SEAL
SEAL PLATE
STEEL RETAINER
WINDBACK SEAL
535°F 15 PSIA
TEMPERATURE AT INTERFACE
1270
1255
1271
1255
1300
1277
1261
1269
1254
1240
1232
1300
1299
1294
1274
1193
1194
1117
1118
1057
1057
1015
1016
973
973
931
931
871
872
814
818
1208
1248
1214
1221
1186
1196
1152
1170
1106
1148
1001
1001
837
903
873
1268
1266
1251
1227
1207
1251
1247
1243
1206
1123
821
1252
1247
1243
1220
1086
822
1260
1256
1248
1241
1239
1239
1022
824
1270
1255
1228
1160
1057
1031
858
823
1240
1232
1212
1064
917
871
840
823
1206
1203
1194
1062
934
839
738
1181
1182
1176
1058
945
877
738
1164
1167
1161
1042
947
934
728
988
969
940
917
752
737
789
825

Figure 25 Temperature Pattern for the Orifice-Compensated Hydrostatic Face Seal with High-Pressure Air Hotter than Low-Pressure Air

Heat-transfer coefficients for the rotating external surfaces were calculated by the method in Appendix B. Heat-transfer coefficients for the stationary surfaces were calculated using the free-convection correlation in Reference 3. Heat-transfer coefficients for all internal surfaces were calculated from equations in References 4 and 5. The coefficients for these internal surfaces were then converted to effective thermal conductivities of the air on the surfaces. Table V shows the thermal properties of the components included in the analysis and the effective thermal conductivities of the air.

TABLE V

THERMAL PROPERTIES OF THE ORIFICE-COMPENSATED HYDROSTATIC FACE SEAL

(Reference Figures 24 & 25)

THERMAL CONDUCTIVITIES (Btu/hr-ft-°F)	
Shaft	12.3
Seal Plate	18.0
Carbon	8.0
Carrier	16.7
Air in windback	0.40
Air between plate and fixed guard	0.40
Air between plate and rotating guard	0.68
Air between carrier and fixed guard	0.016
HEAT TRANSFER COEFFICIENTS, (Btu/hr-ft^2-°F)	
High-pressure rotating surfaces	236.0
High-pressure stationary surfaces	4.0
Low-pressure stationary surfaces	1.0
Rotating guard surface	30.0 - 39.0
Fixed guard, "flat plate" surface	18.0

Heat generation at the interface of the seal and seal plate was calculated by the method shown in Appendix B. This equation is based on air-film shearing considerations. The temperatures of the surfaces and leakage air at the interface of the seal and plate are also based on the methods of Appendix B. The enthalpy of the leakage air at the interface increases downstream for the low-temperature case and decreases downstream for the high-temperature case.

V. TASK II
MAINSHAFT SEAL EVALUATION

A. INTRODUCTION

Task II had three objectives: the procurement of four seal assemblies of each of the four seal designs after they were approved by the NASA project manager, the design and procurement of test equipment capable of testing the seals at the design conditions, and an experimental evaluation program for each seal design. The NASA project manager approved all four of the following seal designs:

- Rubbing-contact face seal with piston-ring secondary seal
- Rubbing-contact hydrodynamic pad face seal with bellows secondary seal*
- Orifice-compensated hydrostatic seal
- Orifice-compensated externally pressurized seal

In addition, the contractor tested a hybrid seal which consisted of the basic orifice-compensated hydrostatic seal running against a spiral-groove seal plate supplied by NASA.

A brief summary of the various builds and test results is shown on Table VI through IX. Tables X through XIII show the results of the pretest and post-test inspections.

---

* This includes the hydrodynamic ramped-pad primary seal required by a NASA technical directive.

TABLE VI

RUBBING-CONTACT FACE SEAL WITH PISTON RING SECONDARY SEAL TEST SUMMARY

Build No.	Seal Plate	Carbon Seal	Other Special Features	Test		Reason for Test Termination	Condition After Test		Test Hours
				PCO	SEO		Seal Plate	Carbon Seal	
1	New	New - wide carbon lip.	19.5 lb. Spring Load	X		Excessive air leakage - amb. air temp.		0.0002 in wear	16.00
2*	New	Carrier from Bld 1 with new carbon 0.150 in. lip.	Enlarged inlets to seal plate oil holes	X	X	Excessive air leakage - amb. air temp.	Excessive wear	Excessive wear 0.0256 in. wear	50.00
3*	Relapped plate from Bld 1 with enlarged holes	New - incorrect seal lip width.	Oil jet manifold in seal area		X	Excessive air leakage - 800F air		0.0060 in. wear	5.75
4*	Used plate from Bld 3	Used - from Bld 3 reworked to correct lip width - relapped			X	Excessive air leakage - 800 & 1000F air temp.	Very sl. wear	0.0020 in. wear	9.75
5*	Relapped plate from Bld 4	Used - from Bld 4	Increased oil flow to roller brg & seal plate oil scoop. Additional jet to roller brg.		X	Excessive air leakage - 800 & 1000F air temp.	O.K.	Carbon deposits on seal. 0.0025 in. wear	14.75
6*	Used plate from New Bld 5				X	Completed limited running of SEO with 250°F oil	Polished - Small am't carbon varnish - slight depression in wear track.	0.0022 in. wear good condition	101.75
7*	Refaced seal plate from Bld 2	Recarboned Seal From Bld 2	Same as Bld 6		X	Apparent fire while running at 350F oil, 1200F air and 100 psi air conditions.	Seal plate was 0.0005 to 0.0006 in. out of flat and coned 0.0003 - 0.0004 in. with the outer edge high.	Carbon lip 0.011 in. out of flat and coned 0.007 in. with outer edge high.	57.08

Note: Unless stated otherwise, all carbon lips are 0.155 in. wide, all springs 30 lb. load.
PCO = Preliminary Check Out
SEO = Simulated Engine Operation

* Seal revision - different than original design approval.

TABLE VII

RUBBING-CONTACT HYDRODYNAMIC PAD FACE SEAL WITH BELLOWS SECONDARY SEAL TEST SUMMARY

Build No.	Seal Plate	Carbon Seal	Other Special Features	Preliminary Checkout	Reason for Test Termination	Condition After Test Seal Plate	Condition After Test Carbon Seal	Test Hours
1**	New oil cooled seal plate	New, hydrodynamic ramped pads on ID	Background accelerometer on guard ass'y	X	Carbon to bellows anti rotation pin disengaged	Good	Good	0.00
2**	Used - from Bld. 1	Build 1 seal with vent passages on back of bellows end fitting enlarged. Vent holes enlarged	Background accelerometer on guard ass'y	X	Same as Bld. 1	Good	Good	0.05
3**	Used - from Bld. 1	Build 2 seal with further enlarged vent passages and additional vent holes. Heatshield installed	Background accelerometer on guard ass'y	X	Rubbing occurred between heatshield and seal support	Good	Lightly scored	0.01
4**	Used - from Bld. 1	New hydrodynamic ramped pad carbon with sides	Background accelerometer on guard ass'y	X	Seal failed while attempting to run 100 psig and 400 ft/sec.	Severe burn marks	Worn	11.00

5 (Cancelled - seal plate reworked for use in Bld. 11, orifice-compensated seal)

* Seal revision - different than original design approval

**Technical directive

TABLE VIII

ORIFICE COMPENSATED HYDROSTATIC SEAL TEST SUMMARY

Build No.	Seal Plate	Carbon Seal	Other Special Features	Tests PCO	Tests SEO	Reason for Test Termination	Condition After Test Seal Plate	Condition After Test Carbon Seal	Test Hours
1	New	New - carbon lip design incorrect	T/C's connected to seal	X		Excessive leakage	Slight rubbing on outer lip	Good	1.50
2	Used - from Bld. 1	Used - from Bld. 1 carbon lip design incorrect	No T/C's connected to seal	X		Excessive leakage	Good	Good	0
3	Used - from Bld. 2	Used - from Bld. 2 carbon lip design incorrect	No T/C's connected to seal	X		Excessive leakage	Good	Good	4.25
4*	Used - from Bld. 3	New - correct carbon lip design	No T/C's connected to seal	X		Excessive leakage	Good	Good	6.50
5*	New	New - correct carbon lip design	No T/C's connected to seal	X		Rub at 320 ft/sec and 80 ΔP	Severe burn marks	Severe wear	6.00
6*	New spring loaded plate	New - correct carbon lip design	No T/C's connected to seal	X		Rub at 400 ft/sec and 60 ΔP	Severe burn marks	Severe wear	7.30
7*	Used - relapped Bld. 6 spring loaded plate	Used - ex. Bld. 6 relapped	No T/C's connected to seal	X		Rub at 400 ft/sec and 80 ΔP	Severe burn marks	Severe wear	5.41
8*	New spring loaded plate	Carbon retainer lightened by 1/3. Narrower outer lip. (Larger I.D. radius) 1/3 less spring load	1 axial and 1 radial accelerometer and 1 background	X		Removed for inspection after low leakage and instability	Good	Lightly scored	54.00
9**	Used - same as Bld. 8	Bld. 8 seal reworked to 0.12 in. deep annulus	2 axial, 1 radial and 1 background accelerometer. 4 T/C's in carbon and carbon retainer	X	X	Seal failed at an air temp. of 825°F	Severe burn marks on inner wear track	Severe wear on inner lip	49.25
			HYBRID SEAL						
1**	New oil-cooled plate reworked for 0.003-in. deep spiral grooves by NASA. Heat shield installed	Build 1 carbon reworked to give .100 in. outer lip and .010 - .012 in. deep annulus. Spring load and weight same as Bld. 8.	2 axial and 1 background accelerometer 6 T/C's in carbon and carbon retainer	X		Seal failed while attempting to run 100 psi and 400 ft/sec	Severe burn marks	Severe wear	13.50
2***	New oil-cooled plate reworked for 0.006 in. deep spiral grooves by NASA. Heat shield installed	New - Build 4 type carbon reoperated to 0.444 in face width and 0.012-in. deep annulus	2 axial and 1 background accelerometer 4 T/C's in carbon and carbon retainer	X	X	Excessive leakage	Slight rubbing marks on inner wear track	Lightly scored	48.41

PCO = Preliminary Check Out
SEO = Simulated Engine Operation

* Seal revision-different than original design approval
** Technical directive
***Contract Modification No. 2

TABLE IX

ORIFICE-COMPENSATED EXTERNALLY PRESSURIZED SEAL TEST SUMMARY

Build No.	Seal Plate	Carbon Seal	Other Special Features	Preliminary Checkout	Reason for Test Termination	Condition After Test		Test Hours
						Seal Plate	Carbon Seal	
1*	New spring loaded plate	New, 1 small ID chip; several very light radial scratches	No T/C's	X	Seal failed 400 ft/sec 80 Psi	Severe burn marks	Severe wear	11.75

TABLE X

RUBBING-CONTACT FACE SEAL WITH PISTON RING SECONDARY SEAL INSPECTION SUMMARY

Build No.		1	1	2	2	3	3	4	4	5	5	6	6	7	7
Test Condition	Units	Pre	Post	Pre	Post	Pre	Post	Pre	Post	Pre	Post	Pre	Post	Pre	Post
Static Seal Leakage															
At assembly - 80 psig	SCFM	0.13	0.56	0.05	-	1.2	4.0	1.6	4.0	1.6	5.8	1.1	2.9	1.8	-
At test stand - 20 psig	SCFM	1.2	1.2	1.2	Excessive	1.2	-	1.2	26.6	1.2	11.5	1.2	Data	.54	44.
40	SCFM	1.5	1.5	1.5	Excessive	1.6	27.3	1.5	45.8	1.3	21.2	1.5	Not	1.2	44.
60	SCFM	1.8	1.9	1.8	Excessive	1.9	48.6	2.4	68.1	1.9	27.5	1.8	Taken	1.9	44.
80	SCFM	1.9	3.0	1.9	Excessive	3.3	70.0	3.6	85.4	2.6	33.7	2.3		2.9	44.
100	SCFM	2.2	3.6	2.4	Excessive	11.2	94.6	4.8	107.5	3.4	41.1	2.9		4.3	44.
120	SCFM	2.7	3.9	3.1	Excessive	24.8	132.0	6.2	130.8	3.9	46.6	4.3		5.6	44.
140	SCFM	3.4	3.4	3.6	Excessive	39.4	132.0	7.9	153.5	4.9	51.0	4.1		6.7*	44.
160	SCFM	4.1	3.8	4.0	Excessive	55.5	132.0	9.2	153.5	5.3	58.9	6.7		6.4	44.
180	SCFM	4.9	4.6	4.5	Excessive	70.7	132.0	11.7	153.5	6.0	67.2	11.8		7.6	44.
200	SCFM	5.4	6.1	5.1	Excessive	94.3	132.0	12.9	153.5	6.8	72.9	14.3		9.4	44.
220	SCFM	5.6	7.5	5.7	Excessive	-	-	-	-	-	-	-	-	-	-
240	SCFM	5.7	9.0	6.3	Excessive	-	-	-	-	-	-	-	-	-	-
260	SCFM	7.0	10.2	6.6	Excessive	-	-	-	-	-	-	-	-	-	-
Spring Rate in Assembly	lb/in.	52.3*	34.7*	30.0*	50.7	52.3	51.6	53.8	53.5	55.0	50.9	47.9	47.9	56.6	Springs Damaged
Total Spring Force (no piston rings)															
Tare wt (seal face assy)	lb	1.85	1.77	1.74	1.73	1.7	1.7	1.8	1.8	1.8	1.8	1.9	1.9	1.82	
Total Load (normal assembled length)	lb	13.35	26.33	26.33	26.98	26.0	26.0	26.5	27.2	25.6	26.5	28.5	28.5	25.0	
Total Load (operating length)	lb	19.60	18.20	32.2	-	32.2	32.7	33.3	34.0	33.0	33.5	34.0	33.7	34.0	
Total Load (fully compressed)	lb	29.50	24.50	36.49	44.69	42.0	43.0	43.5	44.5	44.0	43.3	42.5	42.3	42.7	
Carbon Dam Height															
0°	in.	0.1014	0.1014	0.0953	0.0664	0.0972	0.0911	0.0941	0.0920	0.0895	0.0870	0.0972	0.0953	.1024	*
90°	in.	0.1011	0.1009	0.0953	0.0690	0.0972	0.0912	0.0957	0.0938	0.0895	0.0871	0.0967	0.0938	.1021	*
Avg		0.1013	0.1011	0.0954	0.0698	0.0971	0.0911	0.0953	0.0933	0.0900	0.0875	0.0970	0.0948	.1023	*
Flatness															
Seal plate	He lt. bands	2	9	1	too rough	4	on rig	5	too rough	5	on rig	on rig	too rough	2	Seal
Carbon	He lt. bands	1	9	3	too rough	4	too rough	4 to 5	too rough	4 to 5	too rough	3	too rough	2	Failed
Remarks		(19 lb spring load)		(32 lb spring load)											

*Questionable data

TABLE XI

RUBBING-CONTACT HYDRODYNAMIC PAD FACE SEAL WITH BELLOWS SECONDARY SEAL INSPECTION SUMMARY

Build No. Test Condition	Units	1 Pre	1 Post	2 Pre	2 Post	3 Pre	3 Post	4 Pre	4 Post
Static Seal Leakage									
At assembly - 80 psig	SCFM	FIXTURE NOT AVAILABLE							
At test stand - 20 psig	SCFM	0.6	50	0.6	50	0.1	9.2	0.2	10.8
40 psig	SCFM	0.6	50	1.3	50	0.2	16.4	0.4	18.3
60 psig	SCFM	0.6	50	1.9	50	0.3	22.5	0.9	25.0
80 psig	SCFM	0.7	50	2.9	50	0.6	27.9	1.7	30.6
100 psig	SCFM	1.0	50	4.0	50	0.7	34.9	2.0	37.9
120 psig	SCFM	1.2	50	5.1	50	1.0	42.4	3.0	44.0
140 psig	SCFM	2.0	50	5.9	50	1.5	50.2	3.6	50.4
160 psig	SCFM	2.3	50	7.4	50	2.1	56.9	4.7	58.8
180 psig	SCFM	2.6	50	8.7	50	2.5	63.7	5.1	64.0
200 psig	SCFM	3.6	50	9.9	50	3.1	72.6	5.7	71.0
220 psig	SCFM	-	-	-	-	-	-	-	-
240 psig	SCFM	-	-	-	-	-	-	-	-
260 psig	SCFM	-	-	-	-	-	-	-	-
Spring Rate in Assembly	lb/in.	252	252	Same as Build #1				197	Same as Bld. 4
Total Spring Force									
Tare wt.	lb.	1.06	1.06	Same as Build #1				1.0	Same as Bld. 4
Total Load (Normal assembled length)	lb.	0.0	0.0	Same as Build #1 Same as Build #1				0.0	Same as Bld. 4
Total Load (Operating Length)	lb.	9.0	9.0	Same as Build #1				11.0	Same as Bld. 4
Total Load (Fully compressed)	lb.	31.5	31.5	Same as Build #1				30.5	Same as Bld. 4
Carbon Dam Height									
0°	in.	0.0424	0.0427	0.0420	0.0420	0.0366	Seal Failed	0.0300	0.0263
90°	in.	0.0424	0.0426	0.0420	0.0419	0.0374		0.0292	0.0364
Avg.	in.	0.0429	0.0424	0.0421	0.0419	0.0371		0.0391	0.0275
Flatness									
Seal plate	He lt. bands	15		Not Removed From Rig				9	Seal Failed
Carbon	He lt. bands	8	-	2	-	2	2	3	Seal Failed

TABLE XII

ORIFICE-COMPENSATED HYDROSTATIC SEAL INSPECTION SUMMARY

Build No. Test Condition	Units	1 Pre	1 Post	2 Pre	2 Post	3 Pre	3 Post	4 Pre	4 Post	5 Pre	5 Post	6 Pre	6 Post	7 Pre	7 Post	8 Pre	8 Post	9 Pre	9 Post	Hybrid 1 Pre	Hybrid 1 Post	Hybrid 2 Pre	Hybrid 2 Post
Static Seal Leakage																							
At assembly - 80 psig	SCFM	--	D	--	D	--	D	--	D	2.8	--	2.8	--	3.92	--	3.9	--	4.25	--	4.6	--	4.0	8.0 at 60 psi
At test stand - 20 psig	SCFM	29.4	A	32.6	A	3.4	A	1.8	A	1.7	2.6	1.1	9.2	1.0	13.2	1.1	0.9	1.2	6.2	3.2	--	2.5	
40 psig	SCFM	52.1	T	54.0	T	7.1	T	5.2	T	3.4	13.2	2.6	26.0	1.9	32.8	2.3	1.1	2.6	10.6	6.3	--	5.2	25.2 at 50 psig
60 psig	SCFM	72.2	A	73.1	A	12.7	A	7.5	A	5.3	36.0	4.5	52.0	2.5	56.2	3.2	1.7	3.9	15.7	9.5	--	8.1	
80 psig	SCFM	95.5		95.5		18.2		11.0		6.9	48.6	5.8	80.0	4.7	87.8	4.3	2.3	7.1	20.3	12.8	--	12.0	
100 psig	SCFM	121.5	N	125.0	N	28.5	N	17.2	N	10.5	82.6	7.5	106.3	5.9	102.0	6.5	3.0	8.9	26.5	16.3	40.5	16.7	44.2
120 psig	SCFM	139.2	O	125.0	O	37.5	O	24.0	O	13.0	108.8	8.7	119.0	7.6	119.0	6.6	3.7	12.4	31.8	19.7	51.5	21.2	
140 psig	SCFM	139.2	T	125.0	T	45.8	T	28.2	T	19.0	126.6	10.4	119.0	9.3	119.0	8.0	4.7	16.2	37.2	22.8	64.8	24.9	
160 psig	SCFM	139.2		125.0		51.0		33.0		24.0	126.6	13.6	119.0	10.8	119.0	10.1	5.2	19.0	43.1	25.8	79.4	28.2	91.7 at 150 psig
180 psig	SCFM	139.2	T	125.0	T	59.3	T	38.0	T	27.8	126.6	15.2	119.0	12.0	119.0	10.7	6.2	23.7	49.0	29.2	96.5	31.0	117 at 250 psig
200 psig	SCFM	139.2	A	125.0	A	67.3	A	44.2	A	34.0	126.6	17.2	119.0	14.4	119.0	11.0	7.2	28.6	53.5	31.6	110.4	36.4	134 at 280 psig
220 psig	SCFM	--	K	--	K	--	K	--	K	--	--	--	--	--	--	--	--	--	--	--	--	--	140 at 290 psig
240 psig	SCFM	--	E	--	E	--	E	--	E	--	--	--	--	--	--	--	--	--	--	--	--	--	
260 psig	SCFM	--	N	--	N	--	N	--	N	--	--	--	--	--	--	--	--	--	--	--	--	--	
Spring Rate in Assembly	lb/in.	16.75				16.75		13.35								9.1	9.1	9.1	9.1	9.5	9.5	8.8	S B 9 U
Total Spring Force (no piston rings)								3.4	Same as Build 4	3.42	Same as Builds 4 and 5	3.43	3.43	Same as Builds 4, 5 and 6	Same as Builds 4,5 and 6	2.48	2.48	2.46	2.46	2.44	2.44	2.49	M 1
Tare wt (Seal face assembly)	lb.	3.44	Same as Build 1	Same as Build 1	Same as Build 1 and 2	3.44	Same as Builds 1 and 2	4.7		Same as Build 4		Same as Builds 4 and 5	Same as Builds 4 and 5			2.9	2.9	2.9	2.9	2.8	2.8	2.8	e L
Total Load (Normal assembled length)	lb.	4.25				4.25		5.6								3.4	3.4	3.0	3.0	3.2	3.2	3.2	a D S 11
Total Load (Operating length)	lb.	5.3				5.3		7.7								5.1	5.1	5.1	5.1	5.2	5.2	5.2	
Total Load (Fully compressed)	lb.	8.4				8.4																	
Carbon Dam Height																						*	
0°	in.	0.0550	--	Same Seal as Build 1	0.0550	0.0550	0.0551	0.0599	--	0.0613	Seal Failed	0.0597	Seal Failed	0.462	Seal Failed	0.0528	0.0522	0.0118	0.0112	0.0118	0.0008	0.0160	.0144
90°	in.	0.0549	--		0.0547	0.0547	0.0550	0.0598	--	0.0614		0.0596		0.461	-	0.0530	0.0522	0.0115	0.0110	0.0117	0.0010	0.0157	.0136
Avg	in.	0.0549	--		0.0549	0.0549	0.0550	0.0598	--	0.0613		0.0596		0.461									
Flatness																							
Seal plate	He lt. bands	--	--	--	--	--	--	--	--	8	Seal Failed	2 to 10	Seal Failed	Checked by Vendor	Seal Failed	4	in rig	in rig	severely worn	7	severely worn	9	27
Carbon	He lt. bands	11	--	--	--	5	4	5	--	1		2				2	5	1		1		1	140
																						* after lapping	* after lapping .0153 .0149

*Data not taken - await validation rig study

TABLE XIII

ORIFICE-COMPENSATED EXTERNALLY PRESSURIZED SEAL INSPECTION SUMMARY

Build No.			1	2
Test Condition			Pre	Post
		Units		
Static Seal Leakage				
At Assembly	80 psig	SCFM	Fixture	Not Available
At Test Stand	20 psig	SCFM	6.7	--
	40 psig	SCFM	9.5	20.6
	60 psig	SCFM	11.8	26.1
	80 psig	SCFM	15.0	32.8
	100 psig	SCFM	17.3	38.8
	120 psig	SCFM	19.8	43.6
	140 psig	SCFM	21.3	75.0
	160 psig	SCFM	23.3	75.0
	180 psig	SCFM	26.2	75.0
	200 psig	SCFM	28.3	75.0
Spring Rate in Assembly		lb/in	13.3	13.3
Total Spring Force				
Tare Wt.		lb.	4.25	4.25
Total Load (Normal Assembled Length)		lb.	7.2	7.2
Total Load(Operating Length)		lb.	7.7	7.7
Total Load (Fully Compressed)		lb.	8.6	8.6
Carbon Dam Height				
	0°	in.	0.0252	Not Recorded
	90°	in.	0.0248	
	Avg.	in.		
Flatness				
Seal Plate		He lt. bands	1 1/2 -3 1-1 1/2	Unable to Measure

B. RUBBING-CONTACT FACE SEAL WITH PISTON-RING SECONDARY SEAL

This seal design is similar to the rubbing-contact seals used in the turbines of many Pratt & Whitney Aircraft gas-turbine engines. Current practice has been to use these seals at conditions not exceeding 350 ft/sec, 125 psi, and 800 degrees Fahrenheit gas temperature. At these conditions, the seals have been found to be reliable. It was desirable, however, to include a seal of this type in the contract in order to determine the limits of its successful operation and to serve as a comparison to more unconventional seals.

Seven builds of this seal were tested and are described in separate sections below. In general, it appears that these seals could be improved to a limited extent by improvements in materials and minor changes in design. Major improvements in performance are not likely, however, without major changes to the basic design concept. Figure 26 is a photograph of the seal with its instrumentation.

1. Build 1

The objective of Build 1 was to evaluate a standard rubbing-contact seal in order to establish a performance level to which the other seals in this program could be compared. The seal lip was 0.200 inch wide, designed with an unbalanced geometric area ratio of 65 percent. In the operating position, the spring load was 19 pounds.

The preliminary dynamic checkout program was terminated because leakage rose above 50 scfm. The seal had been tested at rubbing speeds of 200 and 300 fps, air pressures from 20 to 100 psig, using air at ambient temperatures and oil at 250 degrees Fahrenheit throughout the tests. The increase in leakage was caused by insufficient spring load on the seal, resulting in a low pressure loading. This condition decreases wear, but also sacrifices some sealing ability at high pressures. The seal assembly was in good condition after the test, although the seal plate had sludge deposits on the outer surface of its internal scoop. The results of the test are summarized in Figure 27.

2. Build 2

The objective of this build was to decrease the dynamic leakage experienced with Build 1 and to decrease the amount of sludge deposited on the internal scoop of the seal plate. The sludge problem was reduced by enlarging the inlets to the seal plate's cooling-oil holes.

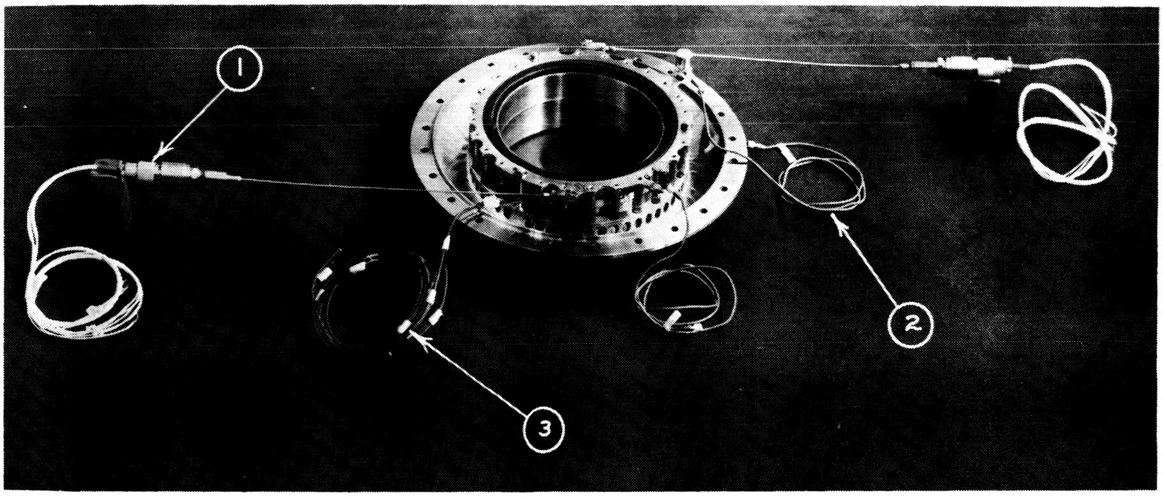

Figure 26 Rubbing-Contact Face Seal with Piston-Ring Secondary Seal
1. Transducer to Measure Generated Torque at Seal Interface
2. Accelerometers 3. Seal Housing and Carbon
Thermocouples (XP-63615)

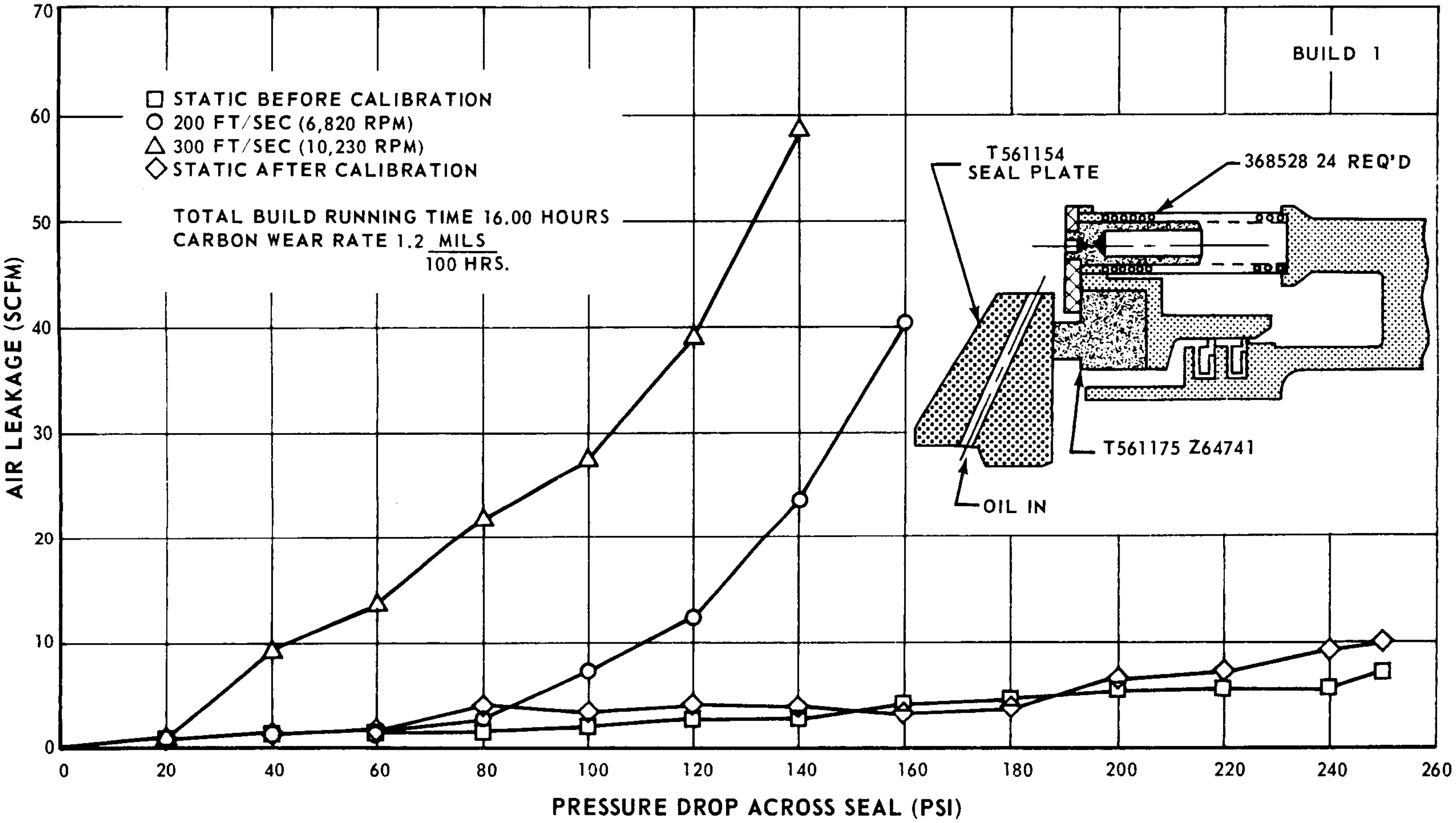

Figure 27 Results of Preliminary Dynamic Checkout on Build 1 of the Rubbing-Contact Face Seal with Piston-Ring Secondary Seal

In order to decrease leakage, the spring loading on the seal was increased to approximately 30 pounds and the carbon lip width was reduced to 0.150 inch. These changes enabled the seal to complete the dynamic checkout program with significantly reduced leakage as shown in Figure 28.

Simulated engine operation tests were run on Build 2 using oil at 250 degrees Fahrenheit and gas at 800 degrees Fahrenheit. The tests were performed at static conditions and at surface speeds of 200 and 300 ft/sec. The effect of temperature on leakage at a rubbing speed of 300 ft/sec was negligible, as shown in Figure 29. The effect of speed on leakage is shown in Figure 30. The effect is negligible for low pressure differentials, but significant at higher pressure differentials.

An attempt was made to test with a rubbing speed of 400 ft/sec at an air temperature of 800 degrees Fahrenheit, but the test was terminated because of excessive leakage. This test pointed out the need for increased cooling to enable the seal to operate at high temperatures and speeds.

3. Build 3

The objective of this build was to decrease the wear experienced in Build 2 at high speeds and temperatures. To this end, an oil-spray manifold was incorporated in this build to direct cooling oil at the rear side of the carbon seal carrier.

The build was run for 5.75 hours, but excessive seal leakage occurred at pressure differentials above 120 psig, as shown in Figure 31. Inspection revealed that the carbon lip's outer diameter was 0.036 inch above the required size, giving a geometric area-ratio imbalance of 0.57 instead of the required 0.65.

4. Build 4

For this build, the Build 3 carbon seal lip was machined to the proper dimensions, lapped, reinstalled in the rig and testing was resumed. Results of the preliminary dynamic checkout are shown in Figure 32. The seal had performed well for 9.75 hours when an abnormal increase in air leakage caused the breather temperature and pressure to increase excessively. At the time of the increase, the seal was being tested at a rubbing speed of 400 ft/sec, a pressure differential of 160 psi, air at 1000 degrees Fahrenheit, and oil at 325 degrees Fahrenheit.

Inspection showed that the carbon had worn 2 mils in the 9.75 hours of operation and that the seal plate had worn slightly in the carbon lip's wear track. The combination of high speed, high temperature, and high pressure had caused the carbon seal lip to deteriorate.

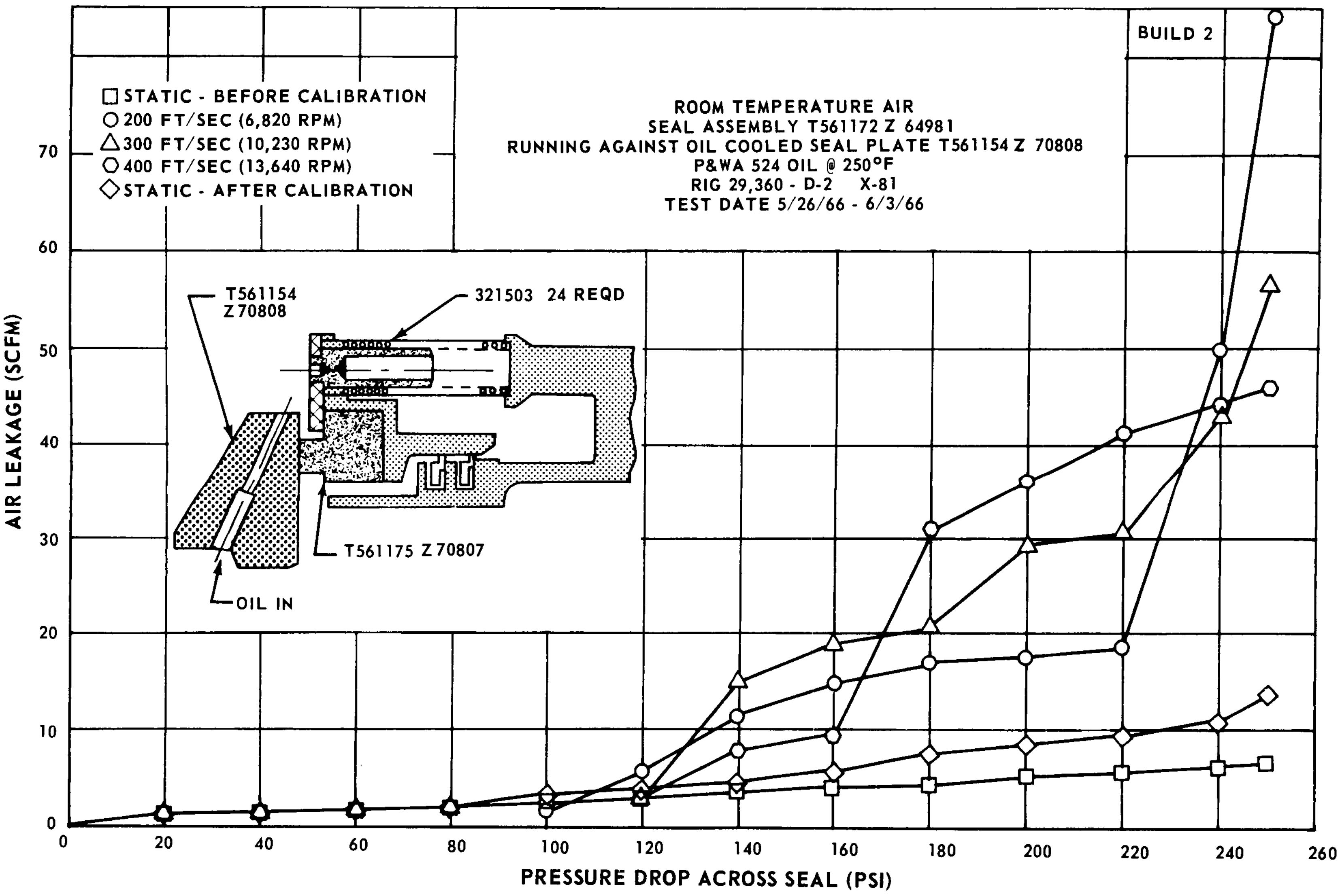

Figure 28 Results of Preliminary Dynamic Checkout on Build 2 of the Rubbing - Contact Face Seal with Piston-Ring Secondary Seal

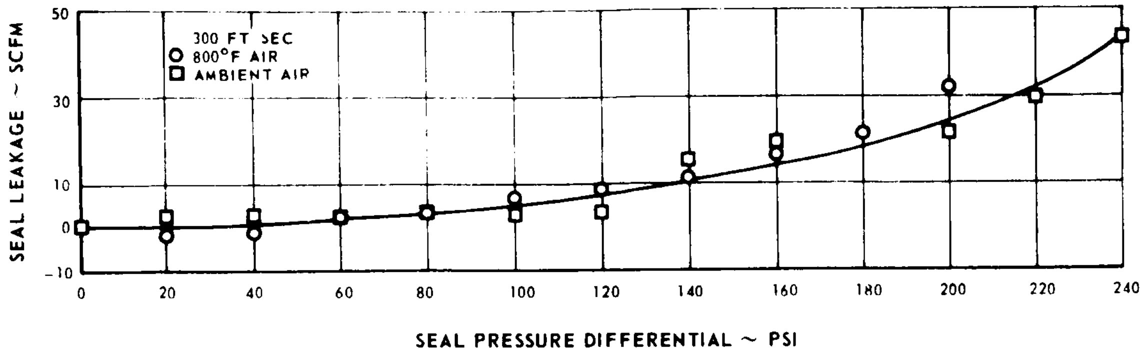

Figure 29 Effect of Temperature on Leakage of Rubbing-Contact Face Seal with Piston Ring Secondary Seal (Build 2)

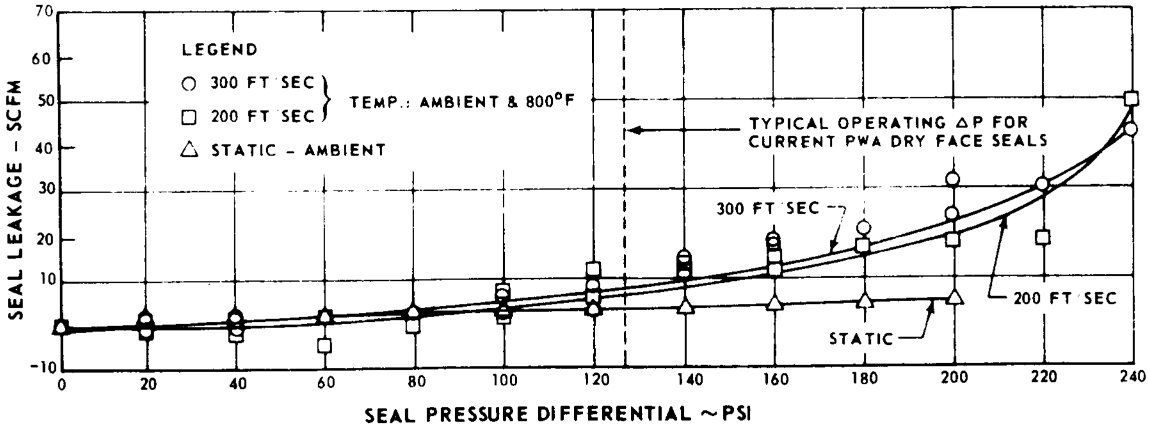

Figure 30 Effect of Surface Speed on Leakage of Rubbing-Contact Face Seal with Piston Ring Secondary Seal (Build 2)

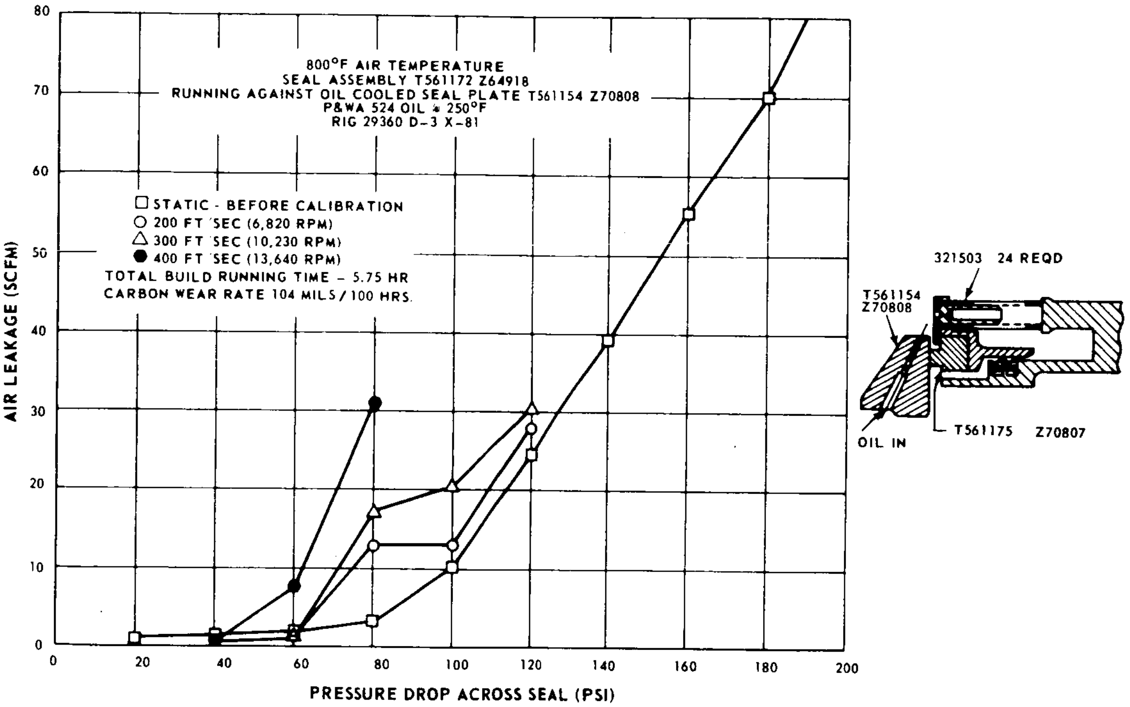

Figure 31 Results of Tests on Build 3 of the Rubbing-Contact Face Seal with Piston-Ring Secondary Seal

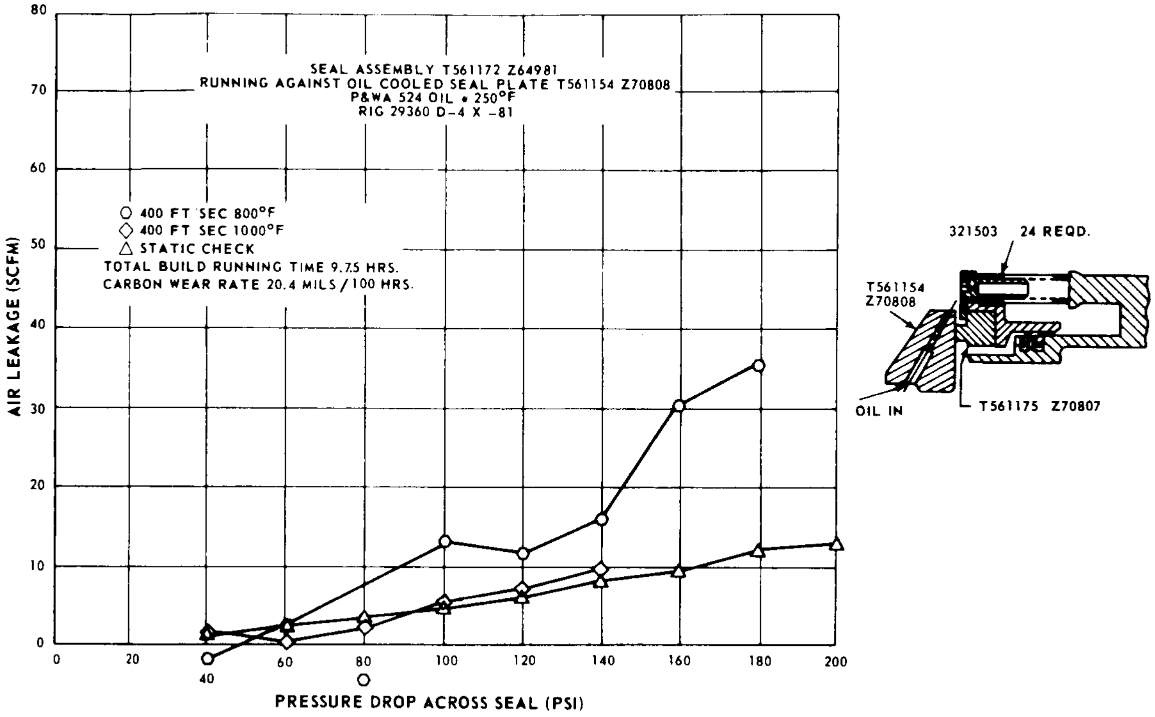

Figure 32 Results of Tests on Build 4 of the Rubbing-Contact Face Seal with Piston-Ring Secondary Seal

5. Build 5

In an attempt to extend the operating range of the seal beyond 1000 degrees Fahrenheit at 400 fps and to prevent deterioration of the carbon seal lip, the cooling oil flow was increased from 15 ppm to 24 ppm. The build was tested with a nominal inlet air temperature of 1200 degrees Fahrenheit, accumulating 14.75 hours of operation before the test was terminated by excessive air leakage. Results of the testing are shown in Figure 33. The conditions at the last point tested were a rubbing speed of 300 ft/sec, a pressure differential of 40 psi, inlet air temperature of 1230 degrees Fahrenheit, and oil at 215 degrees Fahrenheit. Air leakage was 32.2 scfm.

Inspection revealed that the carbon lip had worn approximately 2.5 mils for the 14.75 hours of test time. The wear was not even, however, the surface had assumed a conical shape with the outside edge an average of 0.00045 inch higher than the inside edge. The seal plate was in good condition, although the carbon lip's wear track was polished with small amounts of carbon-varnish deposits.

The results of the testing indicated that the additional oil had not alleviated the deterioration of the carbon lip. The coning of the seal was caused by the fact that the seal wears in while running to conform to the surface of the seal plate.

6. Build 6

The object of this build was to investigate more thoroughly the effects of temperature on the seal's performance. For this series of tests, rubbing speed was held constant at 300 ft/sec and oil temperature was held at 250 degrees Fahrenheit. Air-pressure differentials up to 200 psi were used, and the air temperature was increased from 800 to 1200 degrees Fahrenheit during testing at each pressure level. Build 6 employed a new carbon seal assembly and the seal plate from Build 5. The results of the 101.75 hours of testing are shown in Figure 34.

As shown in Figure 34, leakage increased sharply when the temperature was increased from 800 to 1200 degrees Fahrenheit at pressures above 100 psi. At 800 degrees Fahrenheit, the seal's performance was marginal at pressures of 200 psi and above. At 1000 degrees Fahrenheit, performance became marginal at 140 psi, and at 1200 degrees Fahrenheit, performance became marginal at 120 psi. Post-test inspection showed that the seal had only worn 2.2 mils in the 101.75 hours of operation. The wear track on the seal plate was polished, with small amounts of carbon-varnish deposits and a slight depression (0.0005 inch deep) was found in part of the carbon wear track.

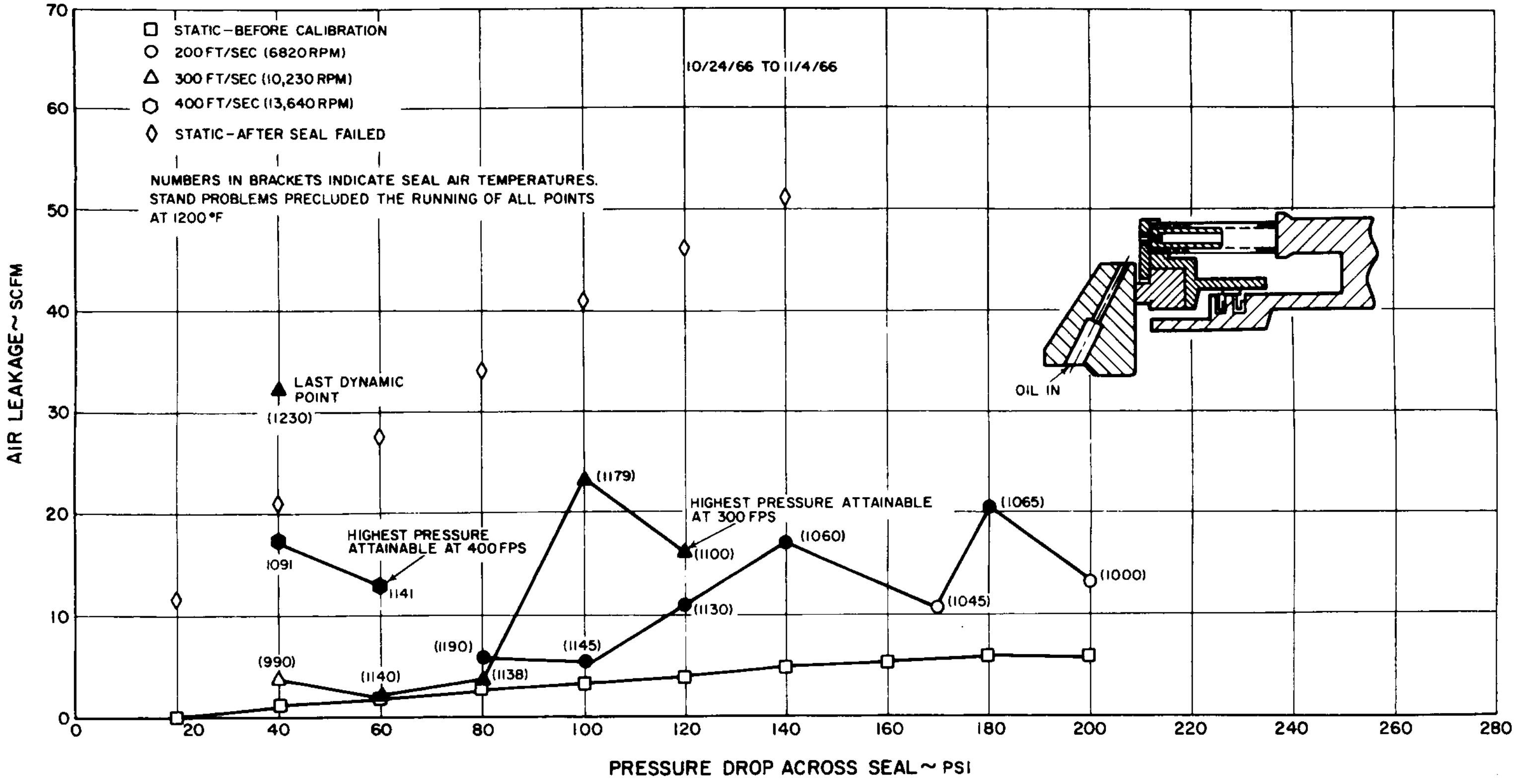

Figure 33 Results of Tests on Build 5 of the Rubbing-Contact Face Seal with Piston-Ring Secondary Seal

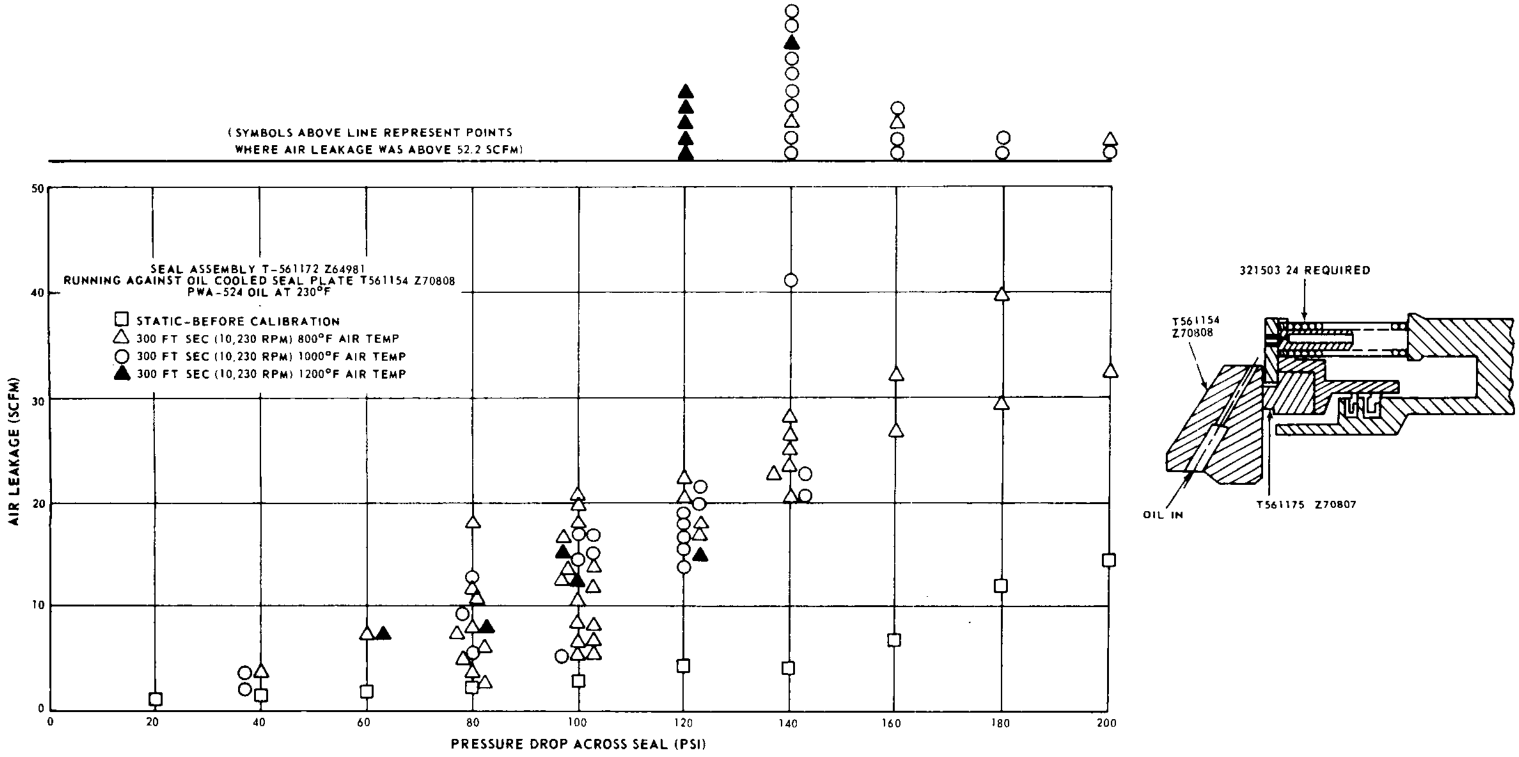

Figure 34 Results of Tests on Build 6 of the Rubbing-Contact Face Seal with Piston-Ring Secondary Seal

These test results indicate that thermal distortion of the seal and seal plate is a decisive factor in performance. They also indicate that if questions of material integrity are left aside, the operational limits of the seal are inherent in the basic design.

7. Build 7

The objective of this build was to investigate more thoroughly the effects of increasing oil temperature on the seal's performance. Testing was conducted at a pressure differential of 100 psi, since test results in Build 6 pointed to unstable operation at high air pressures and temperatures. Tests were conducted at 200, 300, and 400 ft/sec. At each of these rubbing speeds, the oil temperature was increased from 250 to 350 degrees Fahrenheit in 25-degree increments. This procedure was completed for air temperatures of 800 and 1200 degrees Fahrenheit.

When the seal had successfully completed the above tests with oil temperatures to 350 degrees Fahrenheit, similar tests were run at air temperatures of 800 degrees Fahrenheit and oil temperatures up to 450 degrees Fahrenheit. The seal failed when an attempt was made to continue the tests at an air temperature of 1200 degrees Fahrenheit. At the time of failure, Build 7 had undergone 57.08 hours of operation. A summary of the test results is presented in Figures 35 and 36. Figures 37 and 38 show the effect of the excessive air leakage at 1200°F on the seal and seal plate.

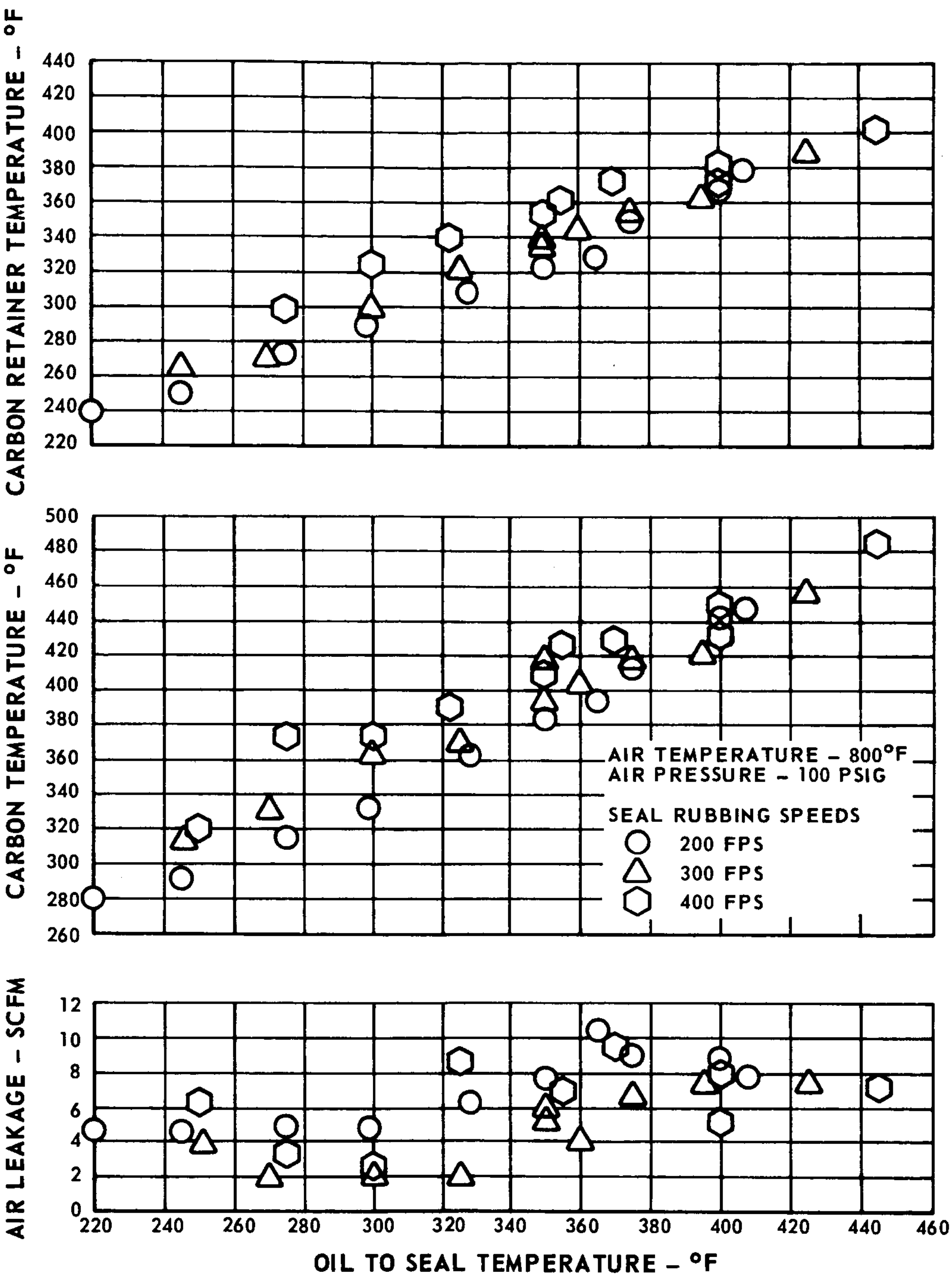

Figure 35 Effect of Oil Temperature on the Performance of Build 7 of the Rubbing-Contact Face Seal with Piston-Ring Secondary Seal with Air at 800 Degrees Fahrenheit and 100 psig

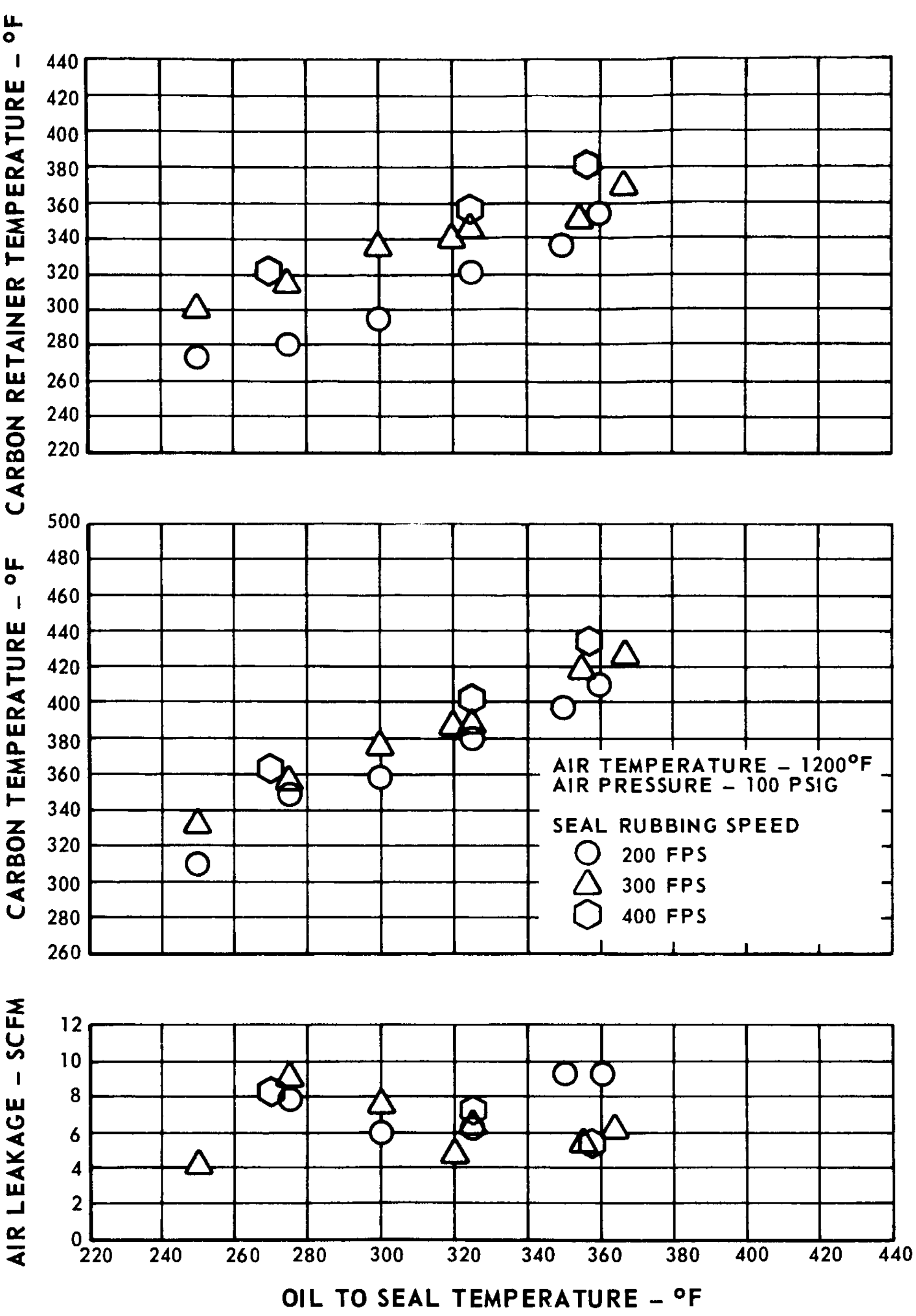

Figure 36 Effect of Oil Temperature on the Performance of Build 7 of the Rubbing-Contact Face Seal with Piston-Ring Secondary Seal with Air at 1200 Degrees Fahrenheit and 100 psig

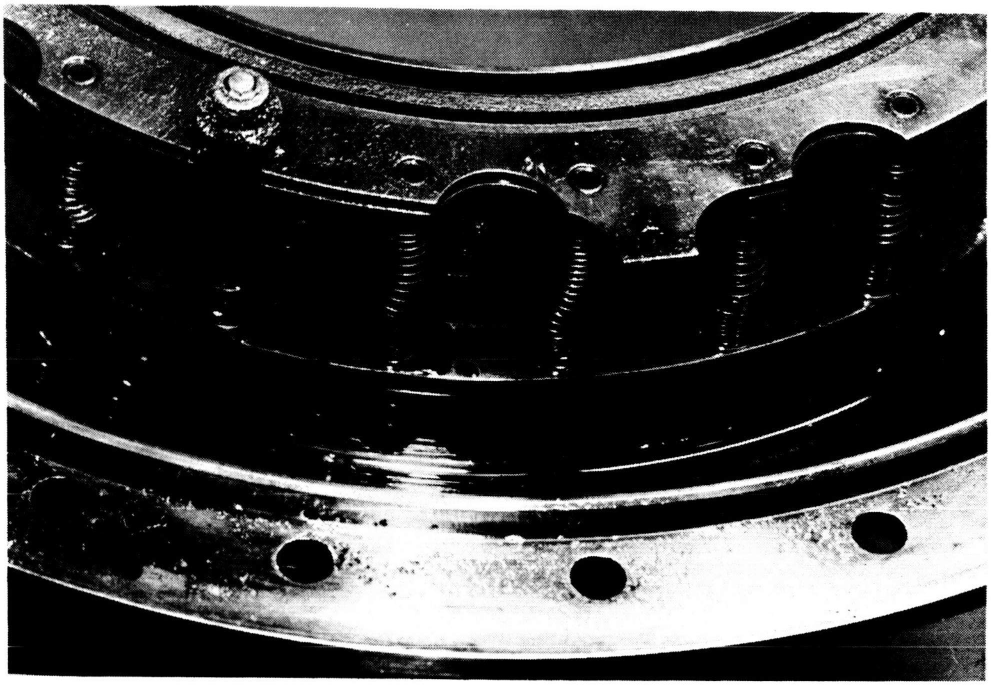

Figure 37 Seal and Carrier from Build 7 after 57.08 Hours of Operation at Severe Test Conditions. Note Deterioration of the Springs and Carbon Seal (CN-8023)

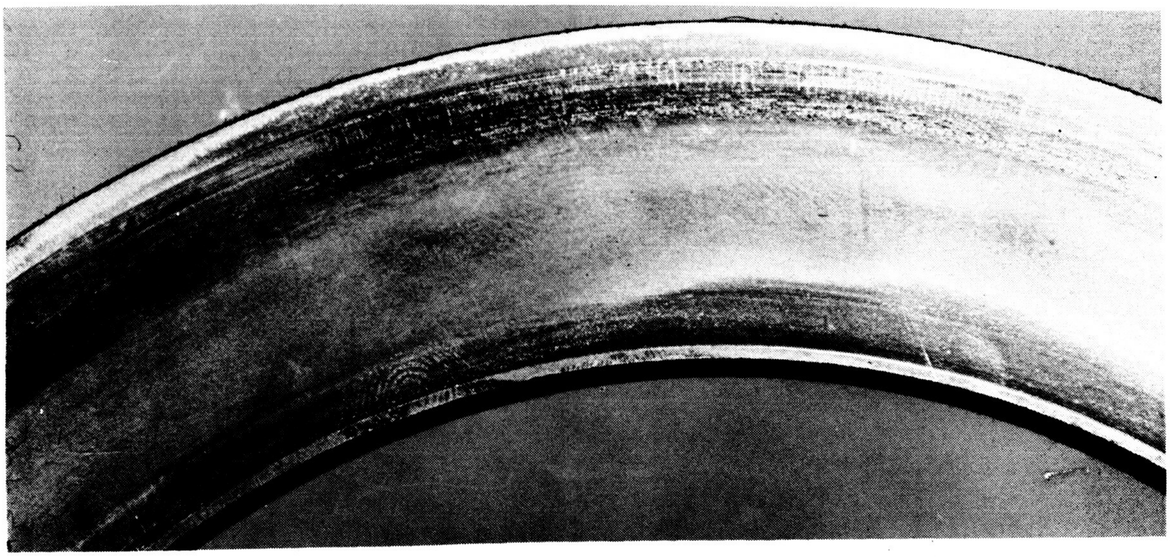

Figure 38 Carbon Wear Track on the Seal Plate from Build 7 after 57.08 Hours of Operation at Severe Test Conditions (CN-8019)

C. RUBBING-CONTACT HYDRODYNAMIC PAD FACE SEAL WITH BELLOWS SECONDARY SEAL

The rubbing-contact hydrodynamic pad face seal with bellows secondary seal was designed and manufactured by the Stein Seal Company. The main objective of the testing of this seal was to determine whether hydrodynamic pads machined on the seal face could produce lower leakage and wear than can be attained with the more standard rubbing-contact face seals. While not entirely successful, the tests which were performed showed low leakage and low wear.

1. Builds 1 through 3

The dimensions of the Build 1 seal are shown in Figure 39. The results of the static pressure check on the seal are shown in Figure 40. After the static check, prior to start-up, the leakage increased suddenly above 50 scfm at 20 psig. Turning the shaft did not reduce the air leakage. Inspection revealed that the wafer had lifted off the bellows end fitting and antirotation pin. The wafer was not damaged, and the rear side only lightly scored by the antirotation pin.

Build 2 used the seal and seal plate from Build 1. The carbon wafer was relapped on both sides to a flatness within two helium light bands. The depth of the 12 bleed grooves in the bellows end fitting was increased to approximately 0.020 inch. The diameter of the 12 bleed holes in the centering band was increased to 0.094 inch.

A static test on Build 2 yielded approximately the same results on the static test of Build 1. The dynamic test was started at a rubbing speed of 200 ft/sec and with a 100-psi pressure differential across the seal. The dynamic leakage varied between 0.6 and 1.1 scfm. After three minutes of testing, the leakage suddenly increased to a quantity in excess of 50 scfm. Inspection revealed the same type of malfunction as that experienced in Build 1. The seal assembly was returned to the Stein Seal Company for their inspection and rework as required.

To ensure that the carbon wafer would not lift off the end fitting in Build 3, the volume of the pressure-relief grooves on the bellows end fitting was increased and a metal band was installed to hold the wafer in position. In addition, a heat shield for the hot-air side of the seal plate and hub was installed in the test rig.

A static leakage calibration showed slightly lower leakage than had been experienced on Builds 1 and 2. Immediately after the start of the preliminary dynamic checkout, leakage increased rapidly and the rig was stopped. A repeat of the static check showed significantly increased leakage. Disassembly revealed that the sleeve of the seal support had rubbed on the heat shield. The carbon wafer did not separate from the end fitting as in previous builds.

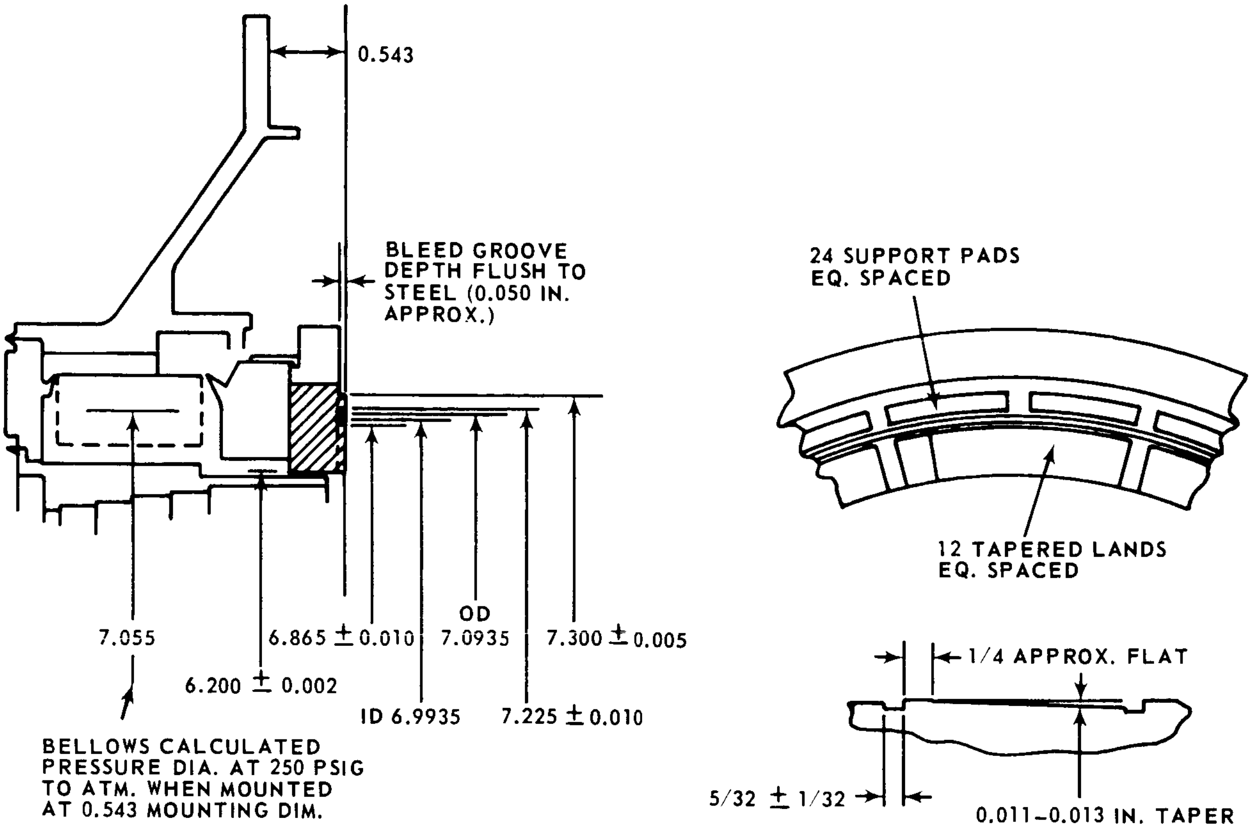
0.543
BLEED GROOVE DEPTH FLUSH TO STEEL (0.050 IN. APPROX.)
24 SUPPORT PADS EQ. SPACED
12 TAPERED LANDS EQ. SPACED
7.055
6.865 ± 0.010
OD 7.0935
7.300 ± 0.005
6.200 ± 0.002
ID 6.9935
7.225 ± 0.010
BELLOWS CALCULATED PRESSURE DIA. AT 250 PSIG TO ATM. WHEN MOUNTED AT 0.543 MOUNTING DIM.
1/4 APPROX. FLAT
5/32 ± 1/32
0.011-0.013 IN. TAPER

Figure 39 Build 1 of the Rubbing-Contact Hydrodynamic Pad Face Seal with Bellows Secondary Seal

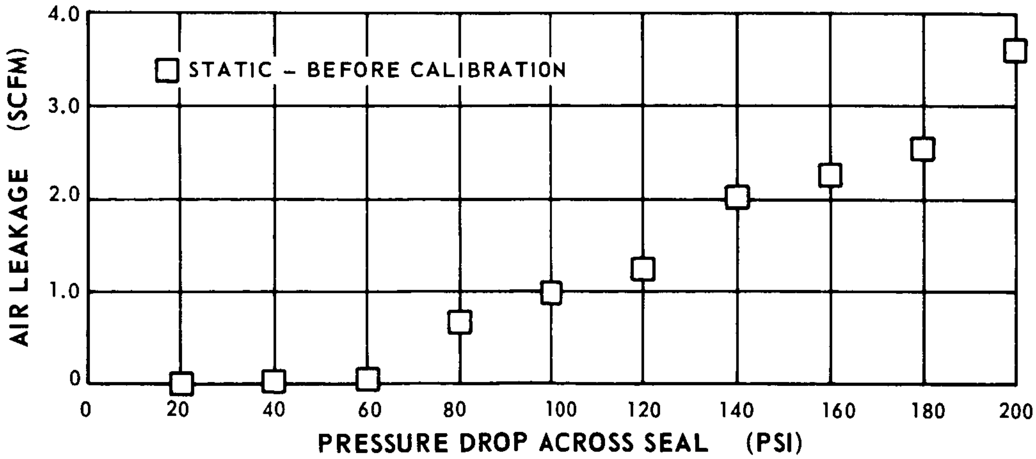

Figure 40 Static Leakage Calibration of the Rubbing-Contact Hydrodynamic Pad Face Seal with Bellows Secondary Seal

2. Build 4

An alternate seal design was tested in Build 4. The major difference between this build and previous builds was in the hydrodynamic pads, as shown in Figure 41. Some minor dimensional changes were also incorporated.

A static check of the seal gave an air leakage of 2.0 scfm at 100 psig and 5.7 scfm at 200 psig. The preliminary dynamic checkout program was run at rubbing speeds of 200 and 300 ft/sec and air pressures of 100 tp 200 psi. When the 400 ft/sec, 100-psig point was set, the air leakage increased sharply and fluctuated erratically. The leakage remained erratic when the 300 ft/sec, 100-psig point was reset. The test program was then terminated. A static leakage check resulted in a 10- to 15-fold increase in air leakage over the initial static check. The results of the dynamic checkout are shown in Figure 42.

Teardown of the rig showed that the carbon was polished and lightly scored on the pad tops. The carbon wear track on the seal plate showed evidence of severe seal chattering.

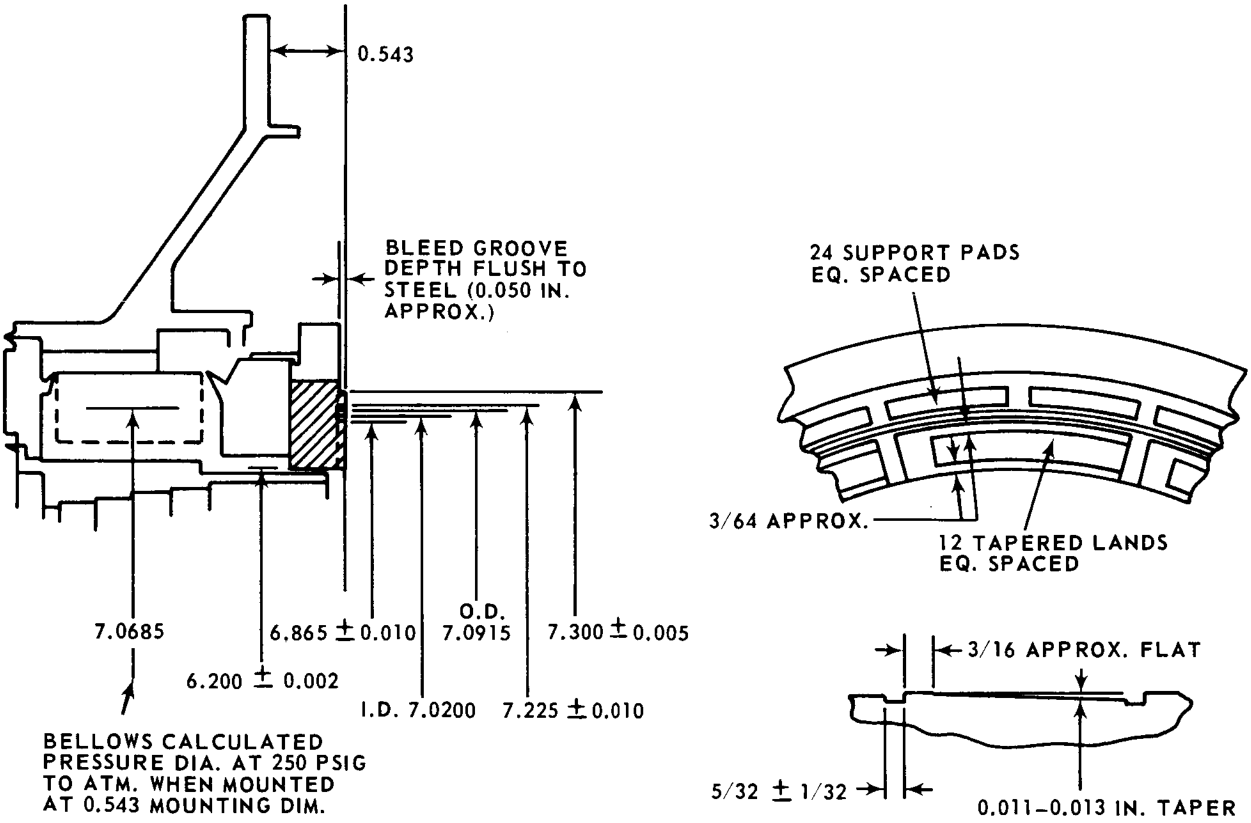
0.543
BLEED GROOVE DEPTH FLUSH TO STEEL (0.050 IN. APPROX.)
7.0685
6.865 ± 0.010
O.D. 7.0915
7.300 ± 0.005
6.200 ± 0.002
I.D. 7.0200
7.225 ± 0.010
BELLOWS CALCULATED PRESSURE DIA. AT 250 PSIG TO ATM. WHEN MOUNTED AT 0.543 MOUNTING DIM.
24 SUPPORT PADS EQ. SPACED
3/64 APPROX.
12 TAPERED LANDS EQ. SPACED
3/16 APPROX. FLAT
5/32 ± 1/32
0.011-0.013 IN. TAPER

Figure 41 Build 4 of the Rubbing-Contact Hydrodynamic Pad Face Seal with Bellows Secondary Seal

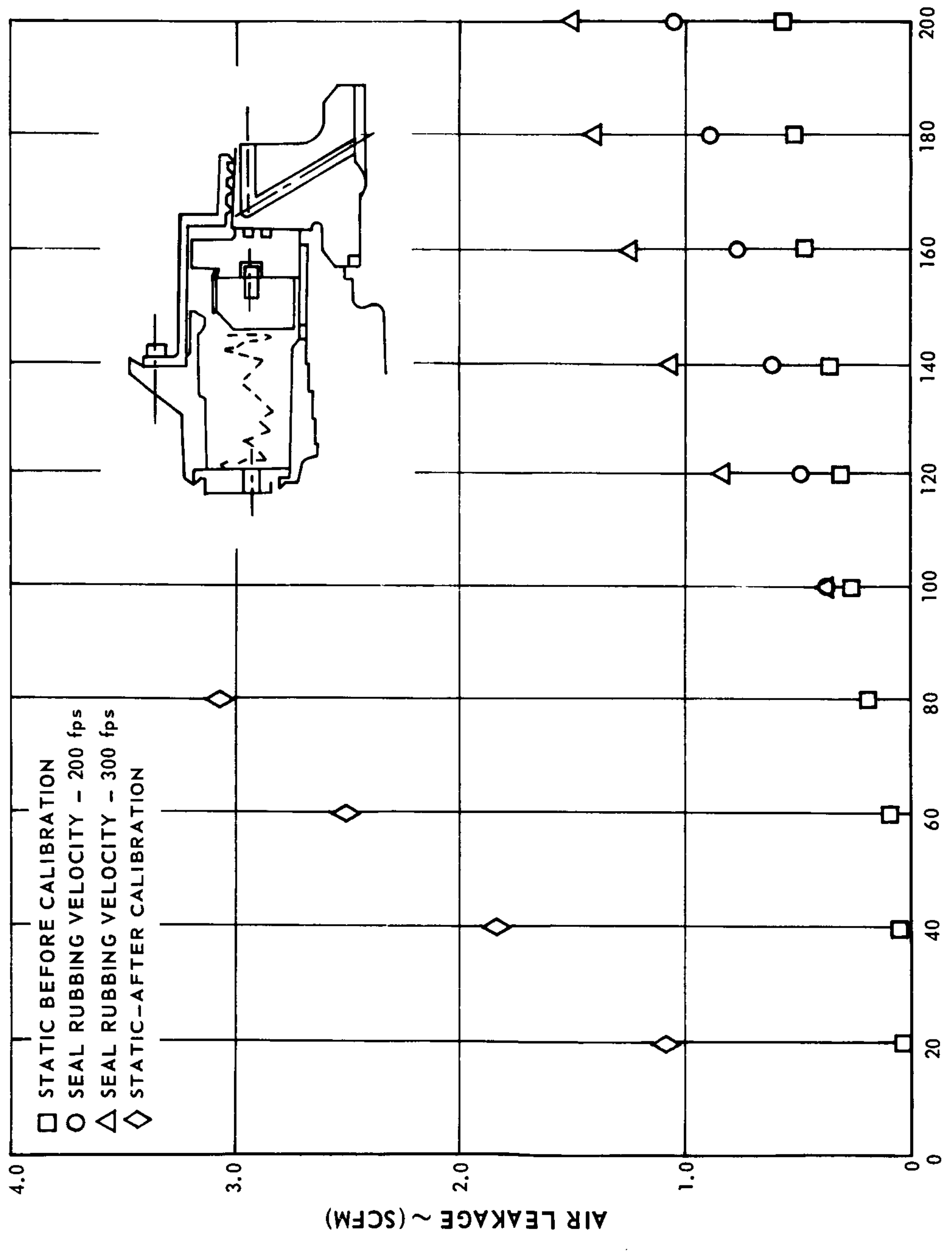

Figure 42 Preliminary Dynamic Checkout of Build 4 of the Rubbing-Contact Hydrodynamic Pad Face Seal with Bellows Secondary Seal

D. ORIFICE-COMPENSATED HYDROSTATIC SEAL

The objective of this part of Task II was to evaluate a new type of film-riding seal, a design in which the seal does not contact the carbon, but rides on a film of air. Nine builds of the orifice-compensated seal were tested. In general, the performance of the orifice-compensated hydrostatic seal indicated that extremely careful control of tolerances and thermal gradients is required for successful operation. This seal was manufactured by the Stein Seal Company. Figures 43 and 44 show the seal assembled and disassembled.

1. BUILDS 1 THROUGH 4

In the first four builds, leakage on the test stand was much in excess of the analytically predicted values. Several solutions to this problem were tried, including a changed seal-face design, included in Build 4. The new design included a revised carbon lip which produced an improved restoring force characteristic when the seal moved from the designed face-opening clearance.

During the posttest inspection of Build 4, the cause of the high-leakage problem was traced to the assembly procedure for installing the seal in the test rig. The assembly procedure called for the hub nut to be torqued to the design requirements of 2000 inch-pounds plus 30 to 35 degrees of rotation. This procedure warped the seal plate so that it was out of flat by 0.0008 to 0.0010 inch and conical, with the outer edge 0.000040 to 0.000080 inch higher than the inner edge.

2. BUILDS 5 THROUGH 7

In Build 5, the torque on the hub nut was reduced to 2000 inch-pounds plus 5 to 10 degrees of rotation in an attempt to reduce the distortion of the seal plate. With this procedure, static leakage was reduced to approximately half of the amount experienced in the first four builds.

Dynamic leakage tests were run on Build 5 at 160, 240, and 320 ft/sec. The seal failed and the test was terminated at a rubbing speed of 320 ft/sec and a pressure differential of 80 psi. Test results are shown in Figure 45. Inspection revealed that the outer lip of the seal was smooth, while the inner lip was worn and rough. The outer edge of the seal plate was polished, but the inner edge showed four equidistant burn marks.

In Build 6, a new spring-loaded floating seal plate was used to eliminate distortion from torque on the hub nut. The new design is shown schematically in Figure 46. Static testing with a pressure differential of 200 psi at the ambient air temperature produced an air leakage of 17.2 scfm, about half that experienced in Build 5.

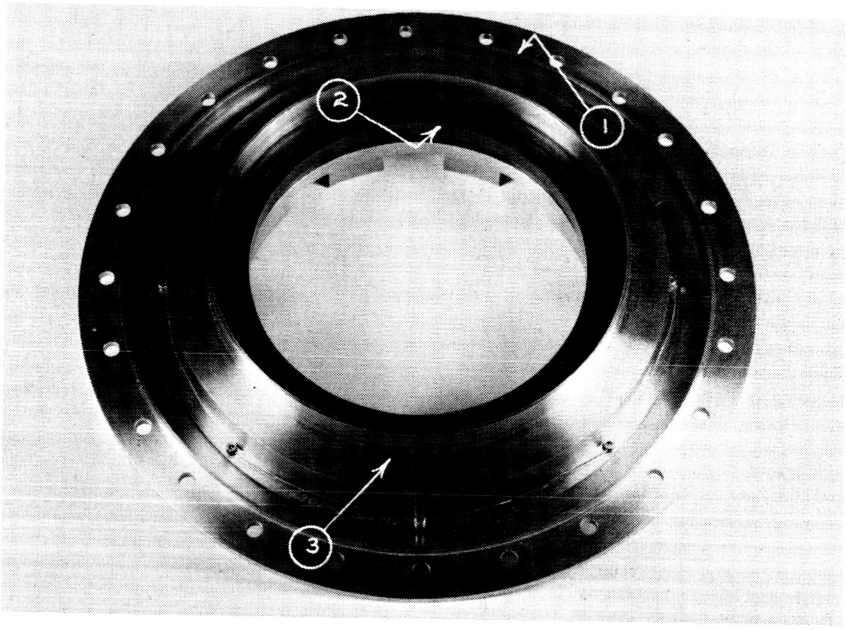

Figure 43 Orifice - Compensated Hydrostatic Seal 1. Carier 2. Seal-Ring Assembly 3. Assembly Guard (XP-66913)

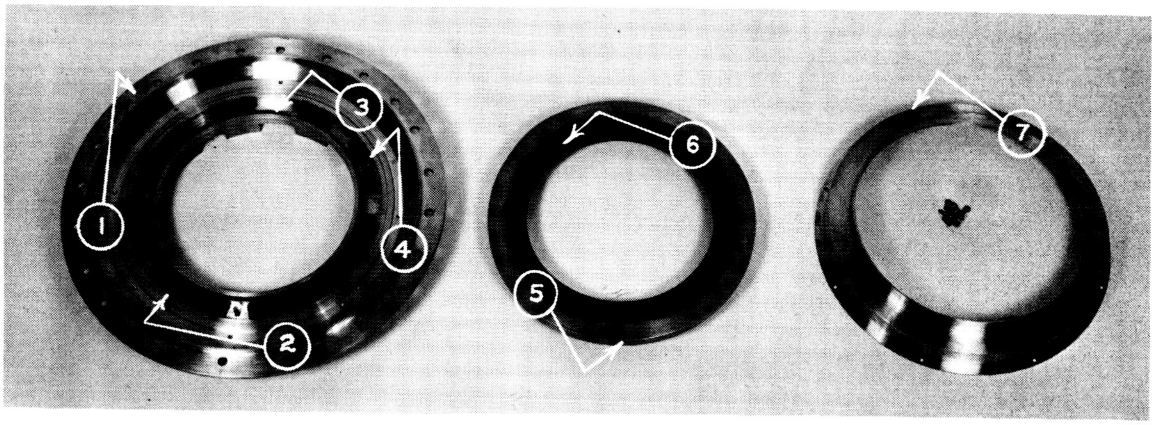

Figure 44 Components of the Orifice-Compensated Hydrostatic Seal 1. Carrier 2. 18 Springs 3. Piston Ring 4. 3 Antirotation Lock Pins 5. Carrier 6. Carbon Seal Ring 7. Assembly Guard (XP-66914)

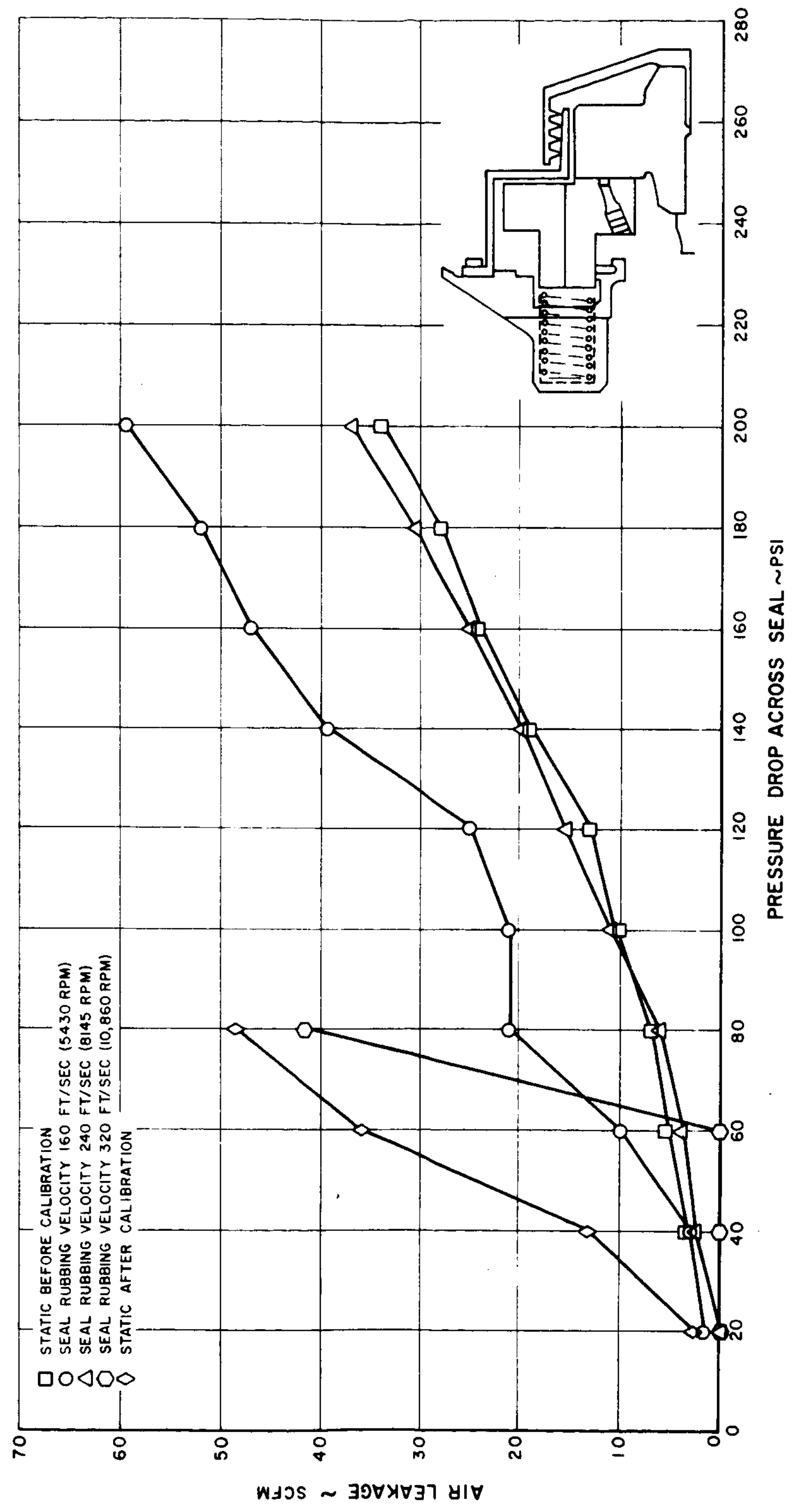

Figure 45 Results of Testing on Build 5 of the Orifice-Compensated Hydrostatic Seal

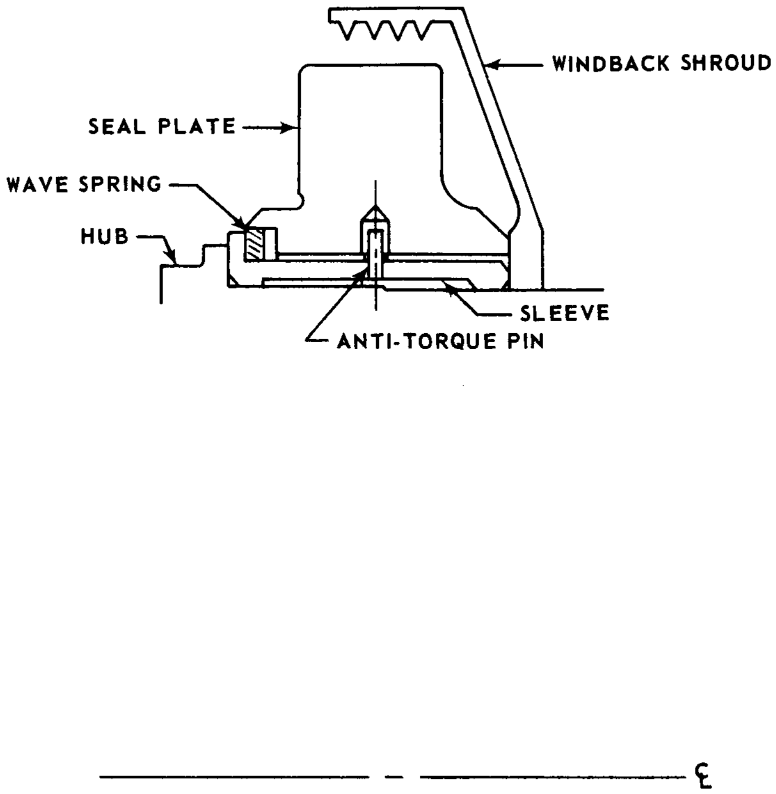
WINDBACK SHROUD
SEAL PLATE
WAVE SPRING
HUB
SLEEVE
ANTI-TORQUE PIN
℄

Figure 46 Spring-Loaded Floating Seal Plate

Dynamic testing was conducted at rubbing speeds of 160, 200, and 300 ft/sec. As the speed was being set for testing at 400 ft/sec with a 60-psi pressure differential, the seal failed. Inspection revealed that the seal failed in a similar manner to Build 5. The inner lip was worn and the inner edge of the seal plate showed four equidistant burn marks. Results of the tests are shown in Figure 47.

Static leakage in Build 7 was about the same as that for Build 6. Build 7 was tested at a rubbing speed of 400 ft/sec at pressure differentials from 200 psi to 80 psi. After about eight minutes of running at 80 psi, the leakage increased suddenly and the dynamic test was stopped. A second static check showed that the leakage for this condition was also excessive. Inspection revealed that the seal had failed. The seal was found to have a smooth lapped wear path on the outer lip of the carbon, but the inner lip was worn and rough. The outer edge of the seal plate's face was polished but the inner edge showed four, equidistant burn marks. Results of the tests are shown in Figure 48.

3. BUILD 8

For Build 8 the carbon retainer band was lightened by removing material at the outer surface. This was done to reduce possible inertial loads at higher speeds. In addition, the annular groove in the seal lip was widened to increase the stiffness of the gas film between the seal and the seal plate.

Inspection of the spring-loaded seal plate assembly in the free condition revealed that the face of the seal plate was conical, with the inner edge 2 to 2 1/2 helium light bands (one helium light band = 0.0000116 in) higher than the outer edge. After some difficulty with seal-plate distortion when the plate was assembled on the rig hub, an acceptable flatness of 4 helium light bands was obtained. The carbon seal assembly was instrumented with two accelerometers, one in the axial direction and one in the radial direction, to monitor seal vibration during the test program.

The preliminary dynamic checkout program was discontinued because of a large reduction in the seal's air leakage characteristics at 400 ft/sec. (see Figure 49). Inspection revealed that the seal and seal plate were both in good condition. The carbon seal face was lightly scored on both inner and outer lips, but was flat within five helium light bands. The rear side of one orifice was partially blocked with some carbon particles. The seal plate showed little evidence of rubbing.

Before the seal was removed from the rig, it had been tested at air-pressure differentials ranging from 100 to 200 psi at ambient air temperatures and with speeds of 200, 300, and 400 ft/sec. A total running time of 54.00 hours was accumulated at these conditions. The seal air leakages recorded at these conditions were above acceptable limits. For example, the dynamic leakage was 67 to 82 scfm at 200 psi, compared to a static leakage of only 11.0 scfm at the same pressure. The curve of seal air leakage is shown in Figure 49.

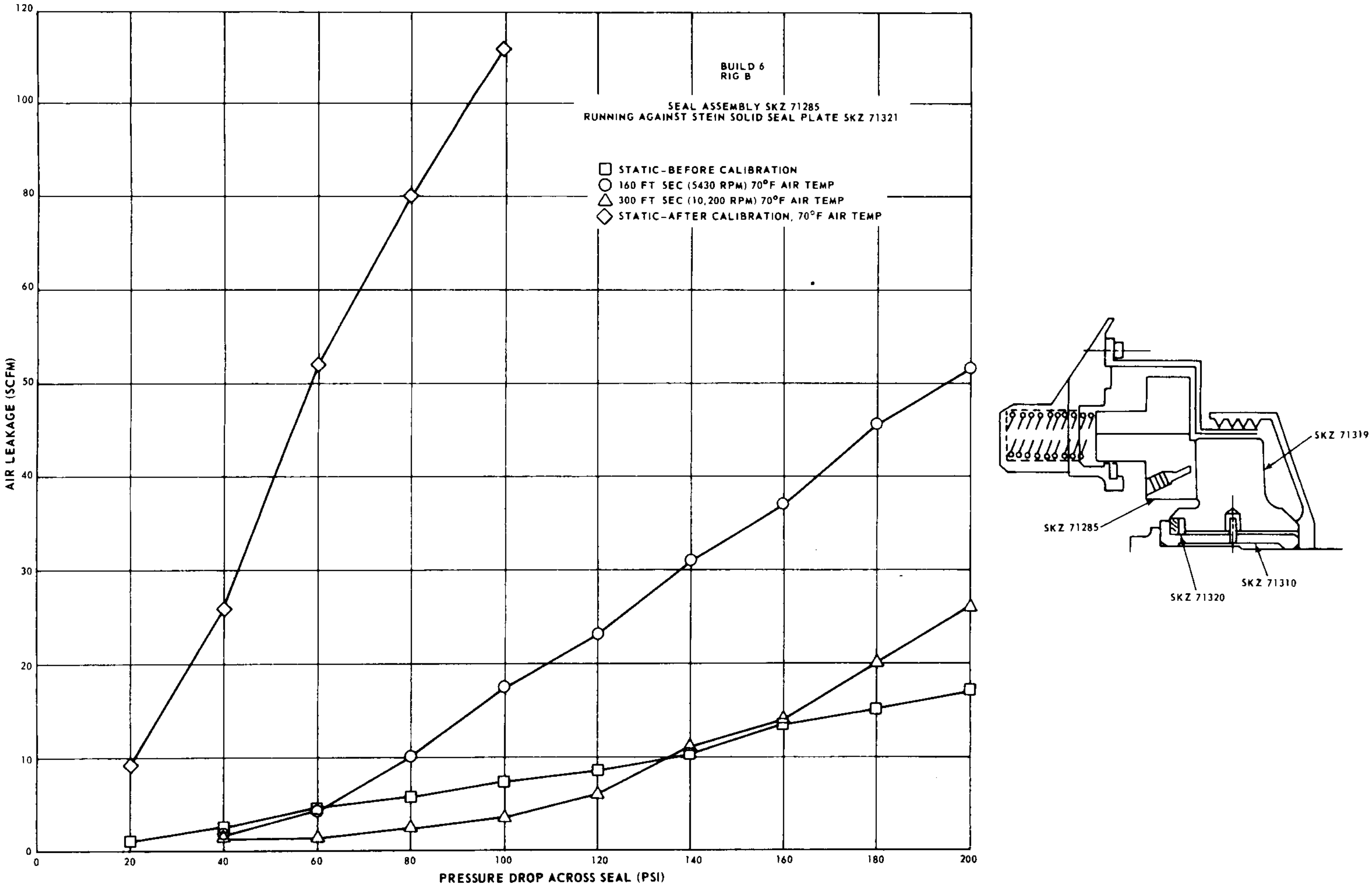

Figure 47 Results of Testing on Build 5 of the Orifice-Compensated Hydrostatic Seal

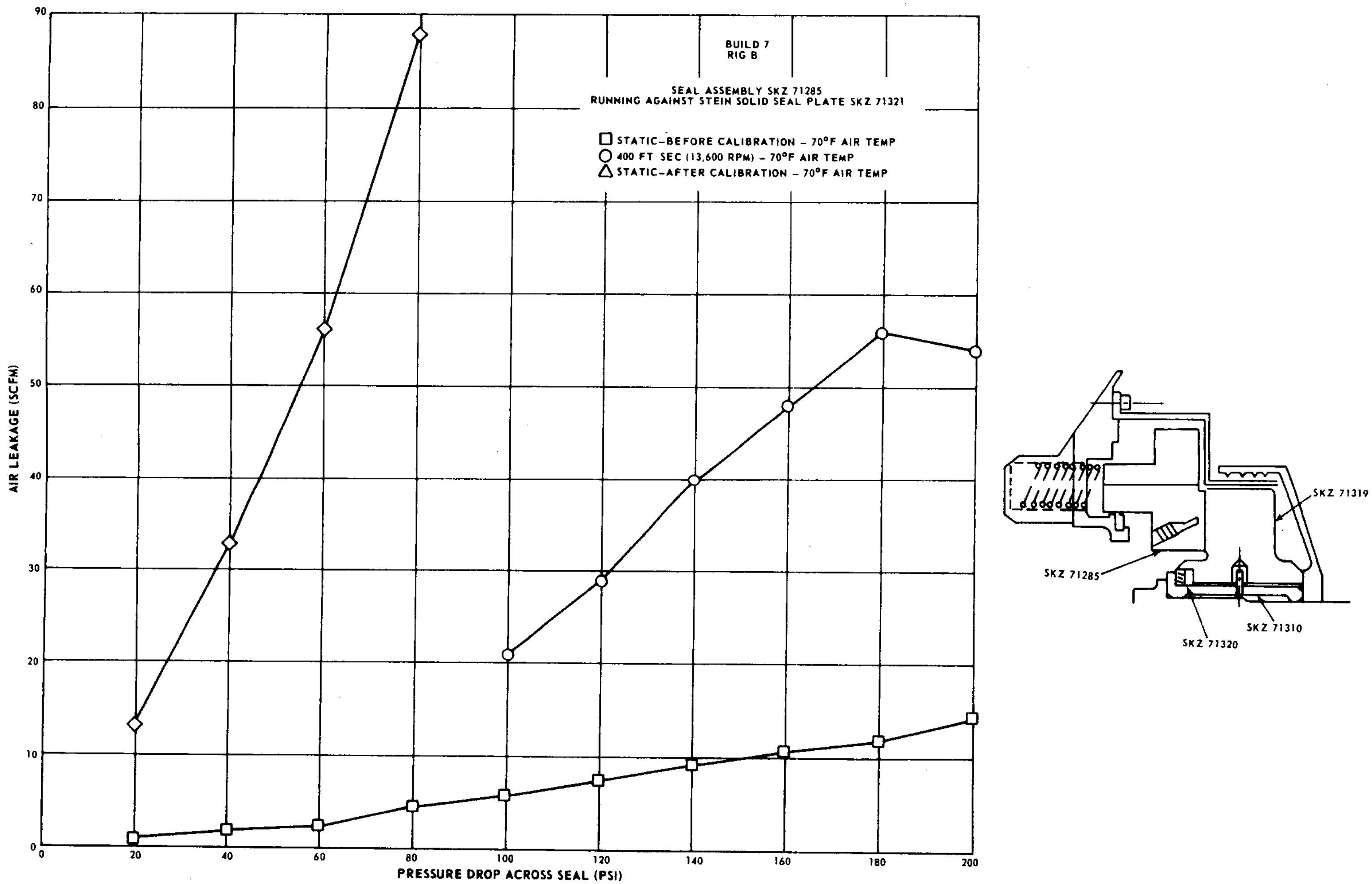

Figure 48 Results of Testing on Build 7 of the Orifice-Compensated Hydrostatic Seal

Testing the seal at air-pressure differentials of 100 and 200 psi and sliding speeds of 200, 300, and 400 feet per second revealed that oil temperature has a significant effect on seal performance. A decrease in oil temperature from 250 degrees Fahrenheit to 150 degrees Fahrenheit reduced air leakage by approximately a factor of five for both pressure conditions. The effect of oil temperature on air leakage is shown in Figures 50 and 51.

4. BUILD 9

Build 9 was assembled with the reoperated seal from Build 8. The carbon seal lip height was decreased to reduce the depth of the annular groove from 0.053 to 0.012 inches in order to reduce the susceptibility of the seal to air hammering. The final seal lip dimensions are shown in Figure 52.

The seal was instrumented with two accelerometers in the axial direction, 90 degrees apart, one in the radial direction and one for a background reference accelerometer. The seal was also instrumented with thermocouples to monitor the carbon and carbon-carrier temperatures.

The high-pressure part of the preliminary dynamic checkout program was completed with both ambient air and 250-degree Fahrenheit air. The low-pressure part of the checkout was completed with ambient air only. Prior to this test, the seal had never been run successfully at pressures below 100 psig with the seal rotating at 400 ft/sec. Results of the preliminary dynamic checkout are shown in Figures 53 and 54.

During the preliminary dynamic checkout, the output of the accelerometers was recorded at steady-state conditions. Data were taken at a pressure differential of 100 psi at 0, 6,800, and 13,600 rpm rig speeds. The over-all acceleration level recorded on the axial accelerometer was ±0.5 g's at 0 rpm, ±2.2 g's at 6,800 rpm, and ±4.6 g's at 13,600 rpm. Data were also recorded at lower pressures. The highest acceleration levels recorded were found at 60 psi at all speeds, and at the 40-psi, 13,600-rpm test point, where the over-all acceleration level on the axial accelerometer was ±18.4 g's.

After 42.25 hours of testing, the seal was removed from the test rig for inspection, and the carbon seal face was found to be flat within 5 helium light bands. The inner carbon lip had no evidence of contact with the seal plate, while the outer lip was only lightly scored in some areas. The seal plate was in excellent condition, with no evidence of prolonged rubbing.

In the simulated engine operation program, the seal was started at an air pressure of 100 psig and a sliding speed of 200 ft/sec (6,800 rpm), using ambient air. As the temperature was increased, the seal's air leakage decreased (see Figure 55). This trend continued to a seal air temperature of 550 degrees Fahrenheit. On

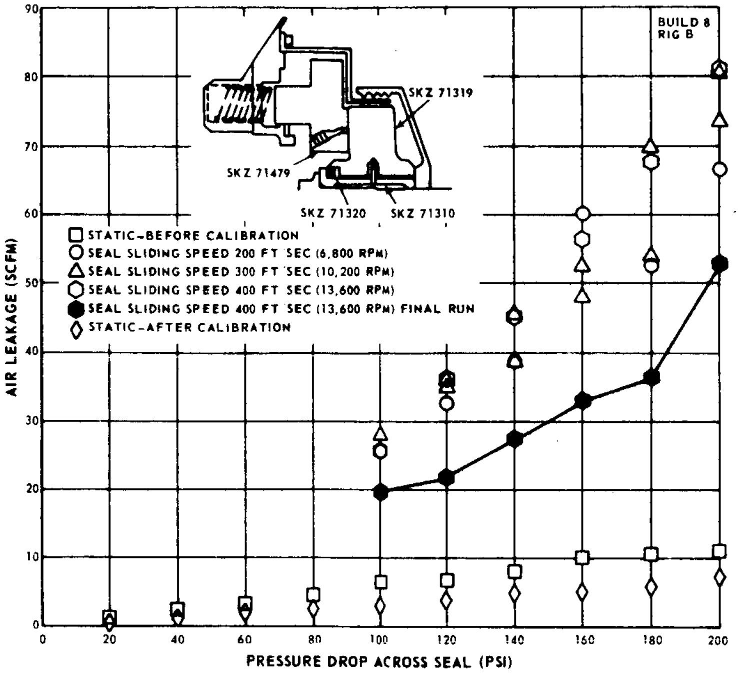

Figure 49 Preliminary Dynamic Checkout of Build 8 of the Orifice-Compensated Hydrostatic Seal

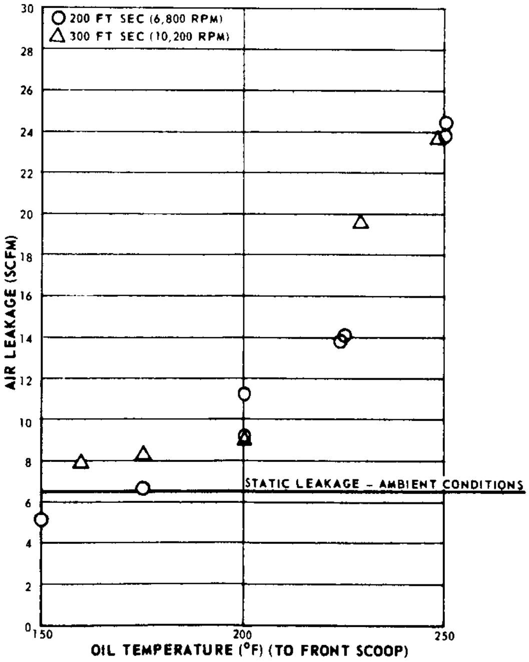

Figure 50 Effect of Oil Temperature on Air Leakage in the Orifice- Compensated Hydrostatic Seal at a Pressure Differential of 100 psi

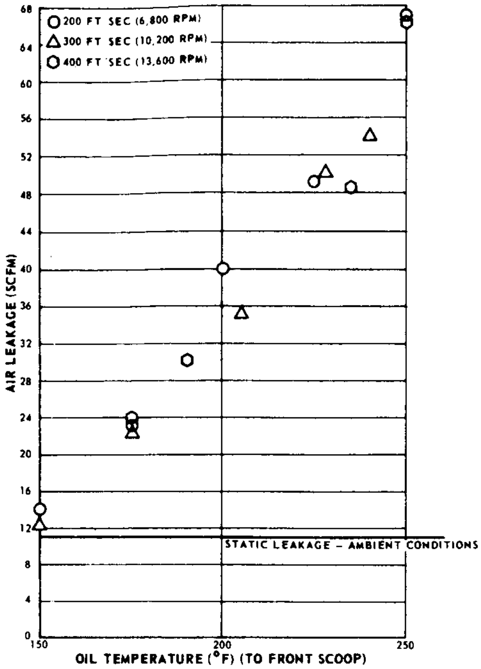

Figure 51 Effect of Oil Temperature on Air Leakage in the Orifice-Compensated Hydrostatic Seal at a Pressure Differential of 200 psi

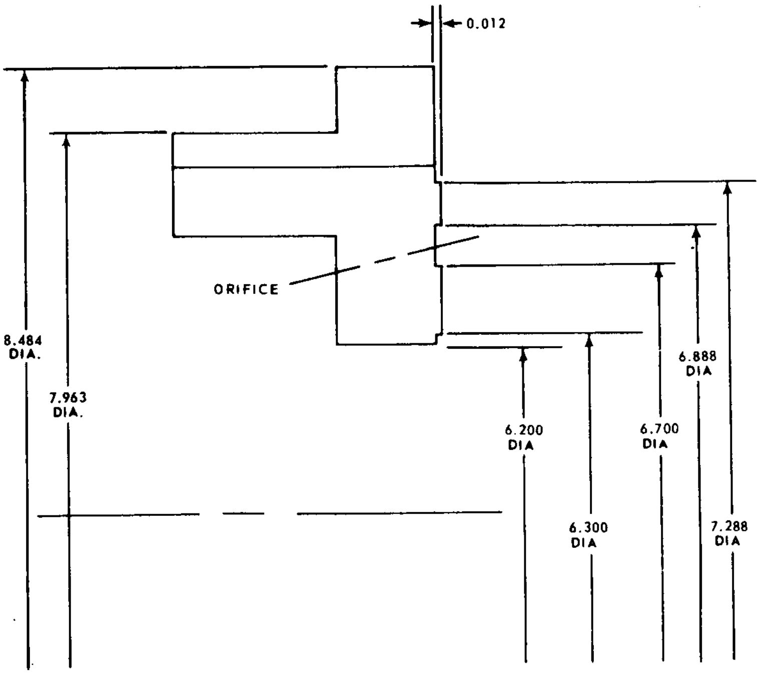
0.012
ORIFICE
8.484 DIA.
7.963 DIA.
6.200 DIA
6.300 DIA
6.700 DIA
6.888 DIA
7.288 DIA

Figure 52 Dimensions of the Carbon Seal Lip for Build 9 of the Orifice-Compensated Hydrostatic Seal

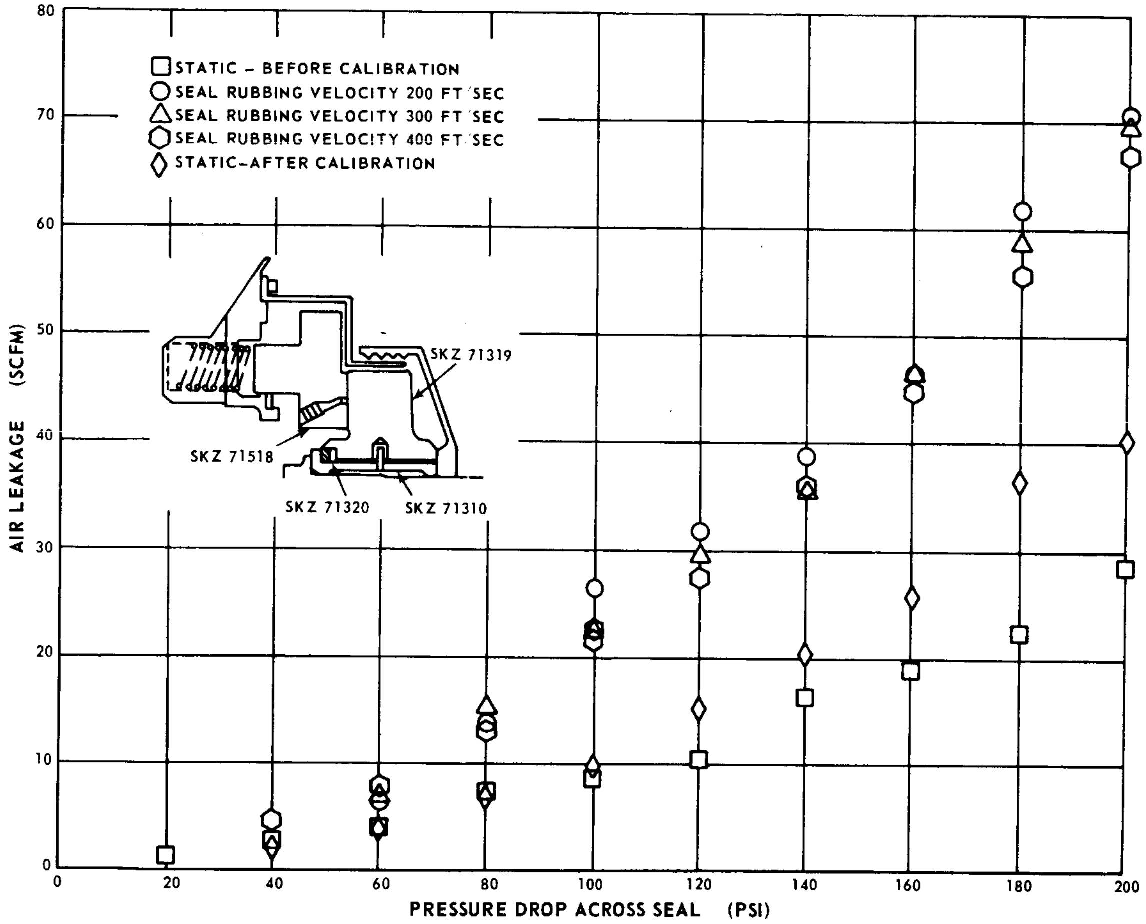

Figure 53 Preliminary Dynamic Checkout of the Orifice-Compensated Hydrostatic Seal Tests Made with Ambient Air

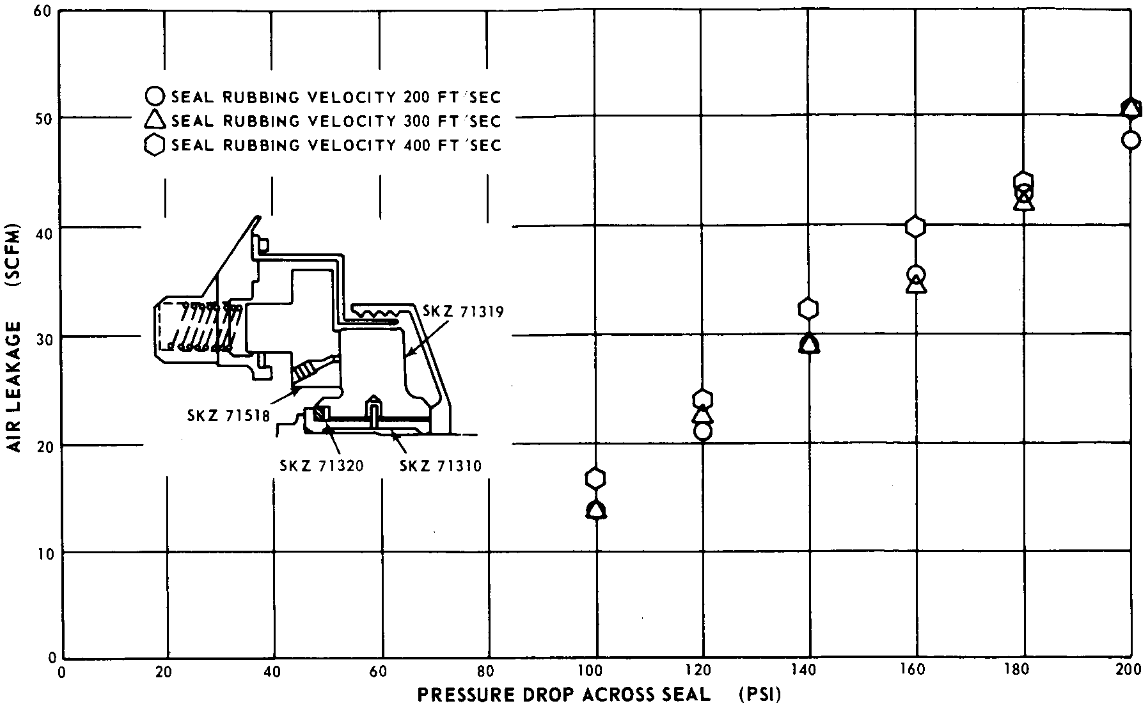

Figure 54 Preliminary Dynamic Checkout of the Orifice-Compensated Hydrostatic Seal Tests Made with Air at 250 Degrees Fahrenheit

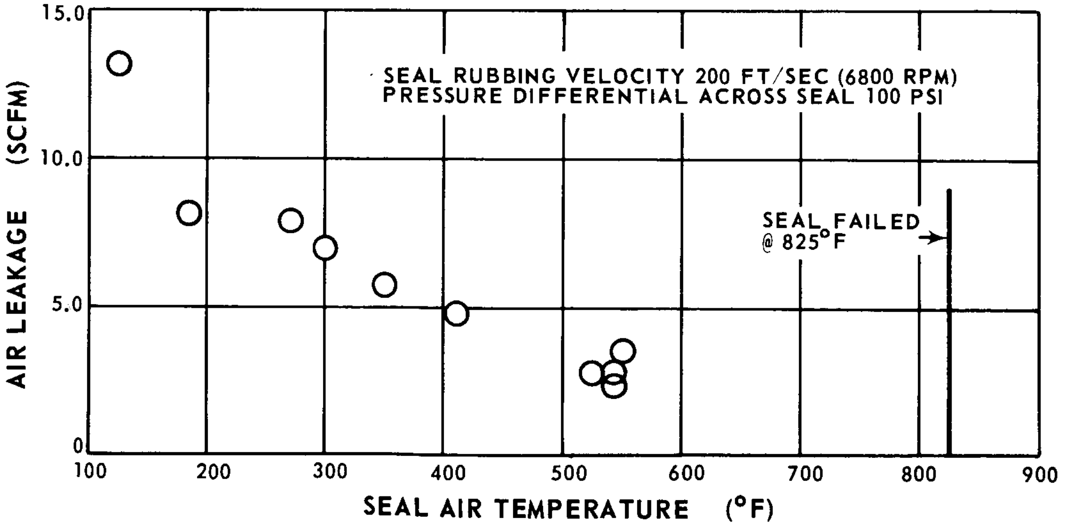

Figure 55 Effect of Air Temperature on Air Leakage in Build 9 of the Orifice-Compensated Hydrostatic Seal

shutdown, an air-temperature control valve was opened, leading to a sudden rise of air temperature to 825 degrees Fahrenheit, when the seal failed because of rubbing.

Inspection revealed that the rubbing had occurred at the inside lip of the seal. The inner carbon lip was severely scored and radially tapered 0.0012 to 0.0017 inch, with the inner edge lower. The outer lip was flat, although scored. The coating on the seal plate was worn through at the wear path of the seal's inner lip. Figures 56 and 57 are close-up posttest reviews of the seal and seal plate respectively.

Both Build 8 and Build 9 demonstrated the importance of keeping the seal plate and seal parallel to each other. In Build 9, the effect of the increased air temperature was to set up a diverging gas film, which became more divergent as temperature increased and finally caused a catastrophic failure.

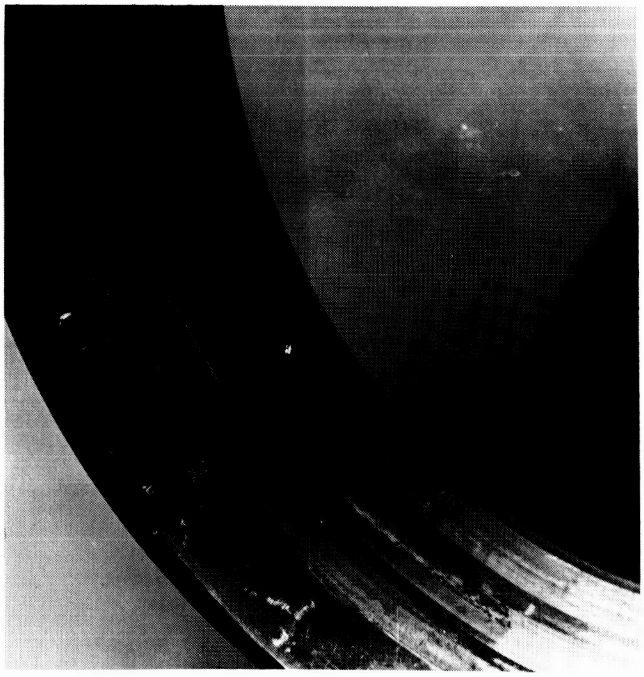

Figure 56 Carbon Seal from Build 9 of the Orifice-Compensated Hydrostatic Seal (CN-8229)

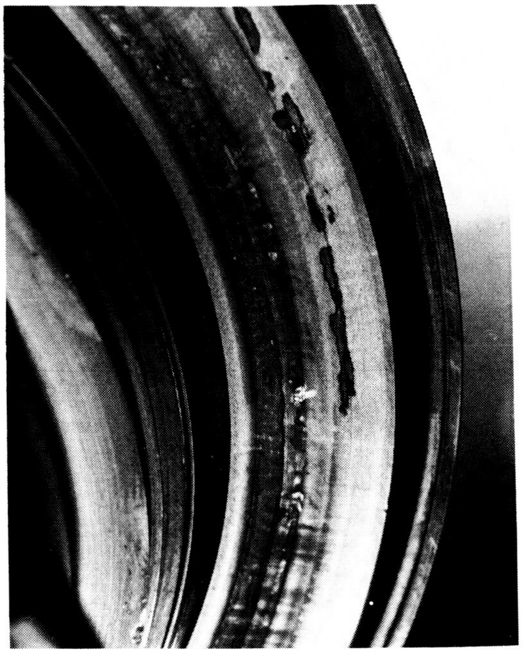

Figure 57 Seal Plate from Build 9 of the Orifice-Compensated Hydrostatic Seal (CN-8231)

E. ORIFICE-COMPENSATED SPIRAL GROOVE HYBRID SEAL

The hybrid seal consisted of the carbon seal from the orifice-compensated hydrostatic seal running against a spiral-grooved seal plate supplied by NASA. The seal was tested to investigate the effect on performance of combining the hydrostatic action of the seal with the hydrodynamic action of the spiral-grooved seal plate. In general, the hybrid seal performed somewhat better than the orifice-compensated seal, but the seal was still extremely sensitive to thermal distortions and to nonparallel operation.

1. BUILD 1

The seal plate used in Build 1 was oil-cooled to obtain an improved thermal gradient across the plate. The spiral grooves in the plate were etched 0.00025 to 0.00045 inch deep into the face to a diameter of 6.660 inches to support the inner carbon lip should the seal plate cone. The grooves (etched by NASA) are illustrated in Figure 58. The back side of the plate is shown in Figure 59. The carbon seal assembly from Build 1 of the orifice-compensated hydrostatic seal was reworked to the dimensions shown in Figure 60 for use in the hybrid seal.

After some difficulity with seal-plate distortion when the plate was assembled on the rig hub, an acceptable flatness of seven helium light bands was obtained by reducing the locking torque from 14,000 to 5,700 inch-pounds. In order to insulate the front shoulder of the seal plate, a heat shield for the hot-air side of the seal plate and hub was installed in the rig. The carbon seal assembly was instrumented with two accelerometers, 90 degrees apart, which monitored the seal's axial vibration during the test program.

A static leakage calibration resulted in an air leakage of 13.1 scfm at 100 psig and 28.7 scfm at 200 psig. The high-pressure part of the preliminary dynamic checkout program was performed at sliding velocities of 200 ft/sec (6,800 rpm) and 300 ft/sec (10,200 rpm) with ambient air at pressures ranging from 100 to 200 psig. It revealed no major changes in seal air leakage from the static results.

Testing was terminated by a seal failure at the start of the 400 ft/sec (13,600 rpm) run with a pressure differential of 100 psig. Disassembly of the rig revealed that the seal had rubbed against the entire face of the seal plate. Test results are presented and discussed in Section H.

2. BUILD 2

A reoperated spiral-grooved seal plate was used for Build 2 of the hybrid seal. The spiral grooves varied in depth from 0.0002 inch to 0.0010 inch, with an average depth of approximately 0.0006 inch. The outer diameter of the grooves was 6.664

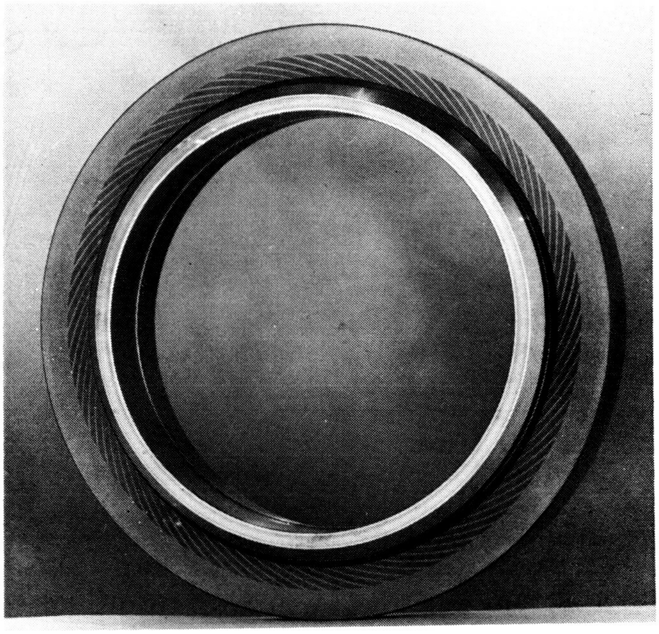

Figure 58 Front View of the Spiral-Grooved Seal Plate Used in the Hybrid Seal (CN-8280)

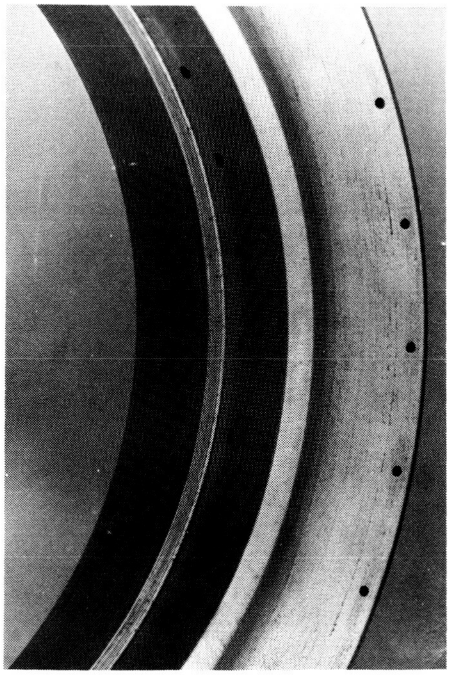

Figure 59 Rear View of the Spiral Grooved Seal Plate Used in the Hybrid Seal (CN-8281)

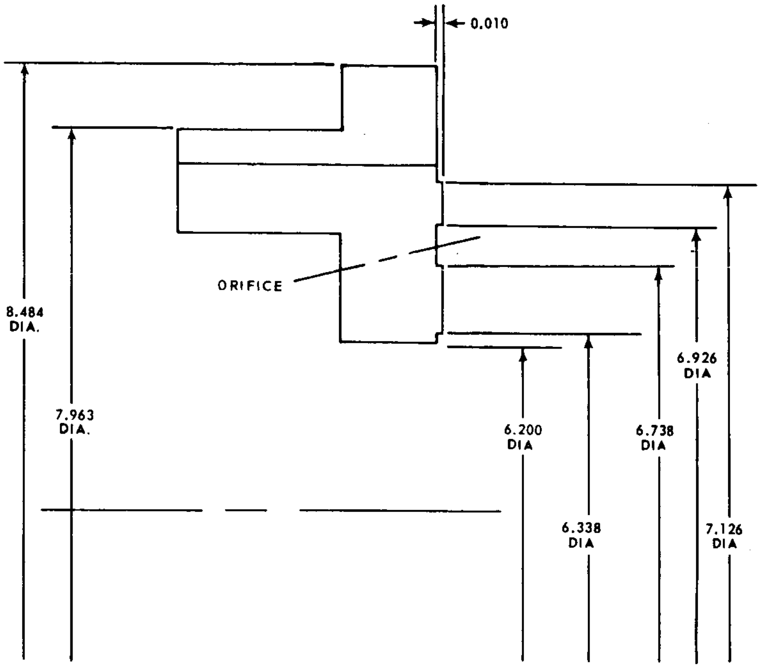
0.010
ORIFICE
8.484
DIA.
7.963
DIA.
6.200
DIA
6.338
DIA
6.738
DIA
6.926
DIA
7.126
DIA

Figure 60 Dimensions of the Carbon Seal Lip for Build 1 of the Hybrid Seal

inches. The Build 1 carbon seal dimensions were revised for Build 2. A new carbon seal assembly of the type used in Build 4 of the orifice-compensated hydrostatic seal was reoperated to the dimensions shown in Figure 61.

Initial attempts to assemble the seal and the rig produced a waviness of 0.000200 to 0.000250 inch in the seal plate face. Inspection of the seal plate in the unassembled condition revealed that the face was out-of-flat by 0.000080 to 0.000120 inch, and conical, with the outer edge higher than the inner edge 0.000075 to 0.000120 inch. The seal plate face was then lapped flat to within 0.000010 inch, but was still conical within 0.000030 inch. The spiral groove depth was not changed significantly, as most of the material removed during the lapping was from the outer edge of the face. When the hub was reassembled with the relapped seal plate, inspection of the seal plate face revealed the face to be flat within 0.000110 inch and conical by 0.000080 inch, with the outer edge higher than the inner edge.

A static leakage calibration gave the results tabulated below:

Pressure Differential (psi)	Leakage (scfm)
80	12.0
100	16.7
200	36.4
300	52.2

In the preliminary dynamic checkout program, the seal was successfully operated at sliding speeds of 200 ft/sec (6,800 rpm) and 300 ft/sec (10,200 rpm) using ambient air at pressures ranging from 50 to 300 psig. The dynamic leakages recorded were generally higher than the static leakage, as expected. The leakage at 300 fps was generally 1 to 3 scfm lower than the leakage at 200 fps for the same pressure. Several points in the dynamic checkout were run more than once to detect any appreciable change in the seal's performance. Up to the 400-ft/sec point there appeared to be no change, however, when a pressure differential of 100 psi was set at 400 ft/sec, the dynamic leakage dropped below the static value. Leakage remained below the static value for checks at 120 psi and 140 psi, so the rig was shut down and the seal was removed for inspection. A summary of the dynamic testing to this point is shown in Figure 62.

Inspection of the seal plate showed light scattered rubbing on the outer lip's wear track, with one burn mark in the track. The carbon face showed signs of rubbing in an area between the two seal axial accelerometers mounted on the carbon carrier and another area approximately opposite it. The areas were approximately 20 helium light bands low and were confined to the outer lip.

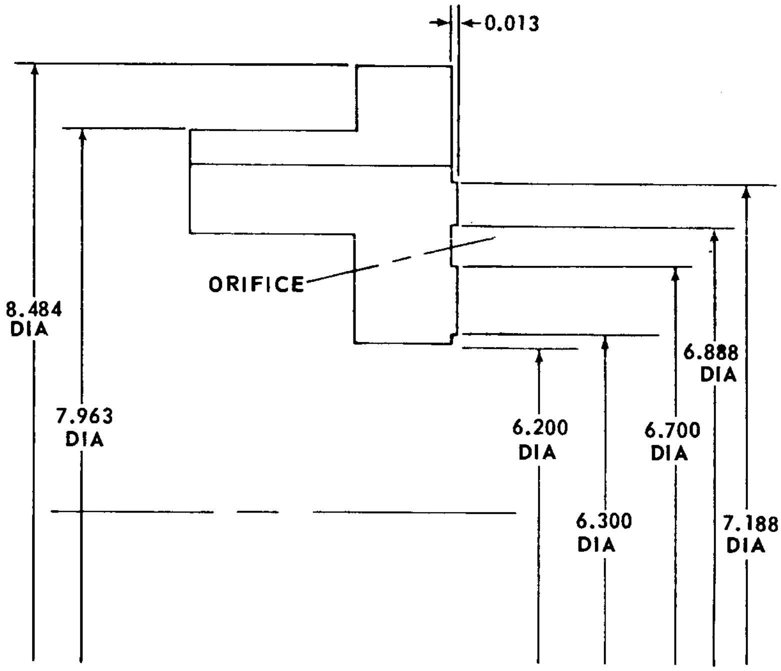
0.013
ORIFICE
8.484
DIA
7.963
DIA
6.200
DIA
6.300
DIA
6.700
DIA
6.888
DIA
7.188
DIA

Figure 61 Dimensions of the Carbon Seal Lip for Build 2 of the Hybrid Seal

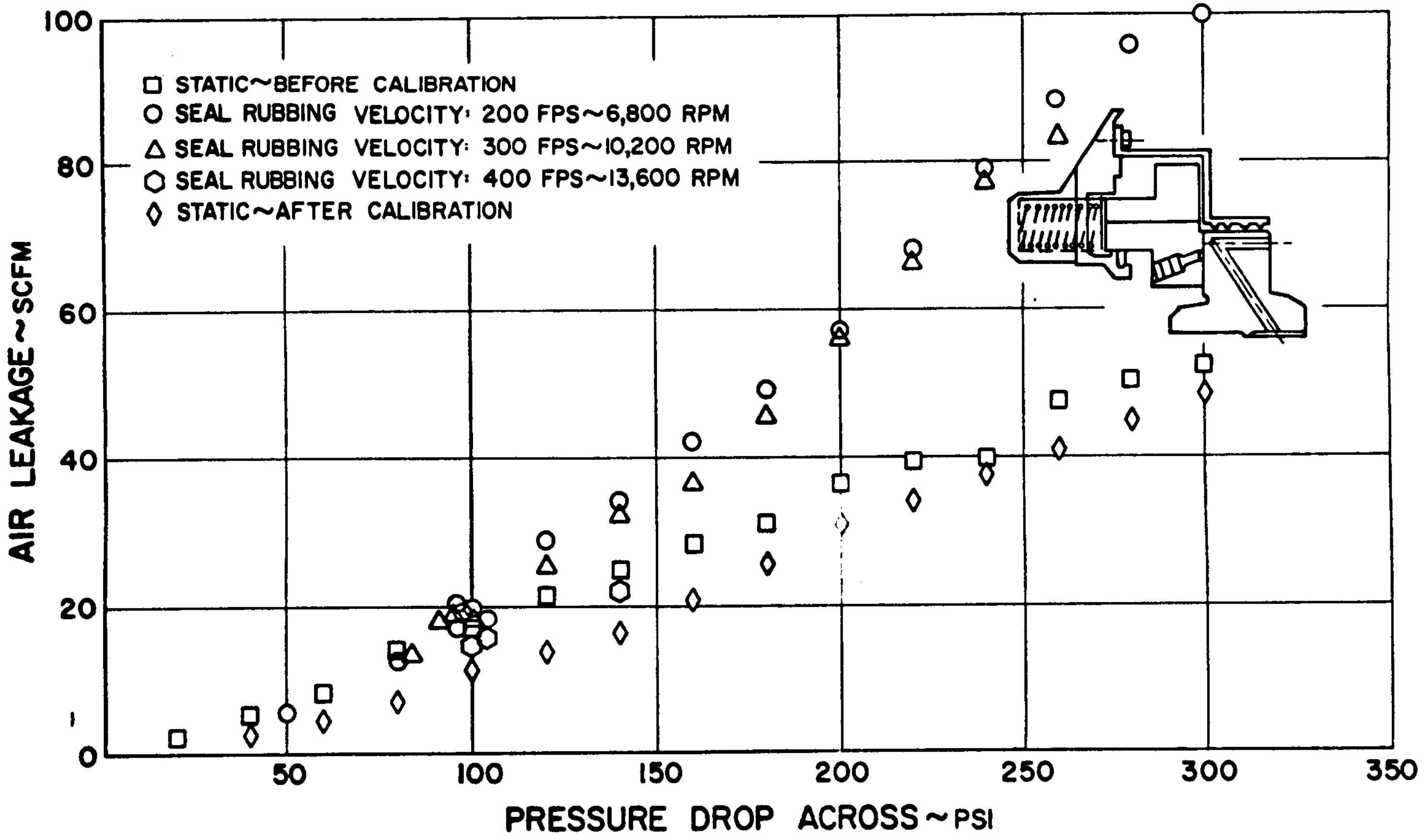

Figure 62 First Dynamic Checkout of Build 2 of the Hybrid Seal

After inspection, the seal was reinstalled in the rig and a second test series was performed. The results of the second series are shown in Figure 63.

Another inspection of the seal plate showed additional light rubbing although the carbon seal face remained essentially unchanged. The accelerometers were removed from the seal at this time before a temperature higher than their design limit of 350 degrees Fahrenheit was reached. The results of the third series of tests are shown in Figure 64.

The third inspection of the seal plate showed evidence of rubbing in both the inner and outer lip-wear tracks. Another area, approximately 120 degrees clockwise from the previously mentioned burn mark showed signs of light rubbing on both the inner and outer wear tracks. A check on the seal plate's runout showed an increase from less than 0.0005 inch to 0.0013 inch. The carbon seal was restored to its original condition by lapping to a flatness of four helium light bands for the conclusion of the test. The depth of the annular groove was reduced to 0.011 inch from its original depth of 0.013 inch.

Static tests were performed on the reassembled seal at ambient temperatures and at 400 degrees Fahrenheit. These tests compared favorably with earlier static tests. At 600 degrees Fahrenheit, the static leakage was less than the leakage at 400 degrees Fahrenheit.

Brief dynamic tests were conducted at 200 ft/sec with air temperatures of 400 and 600 degrees Fahrenheit. Leakage increased to an excessive level when the seal was started at 200 ft/sec with air at 300 psi and 600 degrees Fahrenheit, and remained excessive when pressures of 250 psi and 200 psi were tried. Static calibration with 800-degree Fahrenheit air and ambient air also revealed excessive leakage. Results of the final series of tests are shown in Figure 65.

Posttest inspection revealed that both the inner and outer lips had rubbed on the seal plate. The outer lip of the seal was 0.0002 to 0.0016 inch higher than the inner lip. The average wear was 0.0011 inch on the outer lip and 0.0021 inch on the inner lip. The outer lip was 0.00015 inch out of flat and the inner lip was 0.00150 inch out of flat. The seal plate showed intermittent rubbing on the lands between the spiral grooves and one prominent burn area in the wear track of the outer carbon lip. The seal plate was 0.0004 inch out of flat. The appearance of the seal plate is shown in Figure 66.

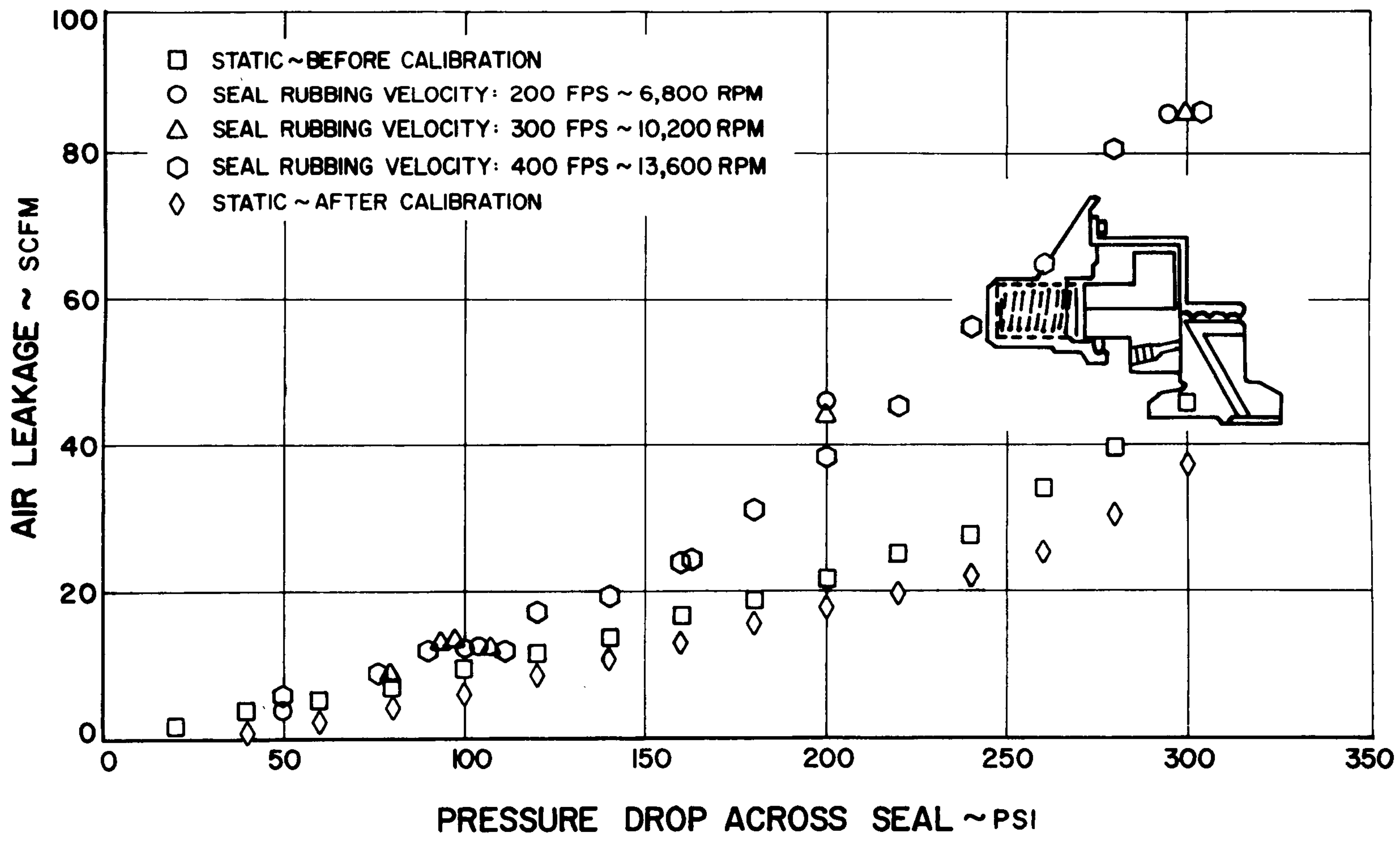

Figure 63 Second Dynamic Checkout of Build 2 of the Hybrid Seal

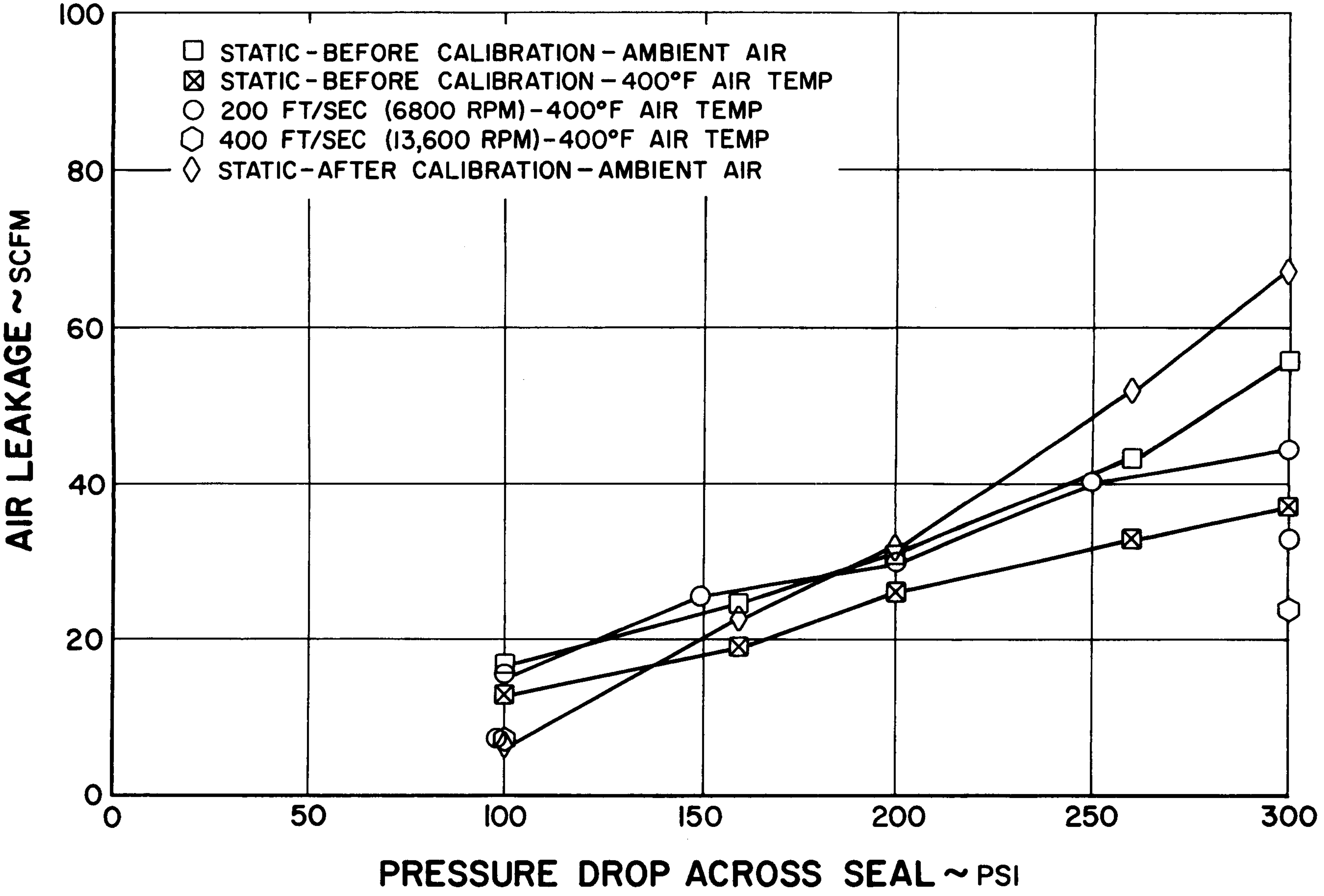

Figure 64 Third Dynamic Checkout of Build 2 of the Hybrid Seal

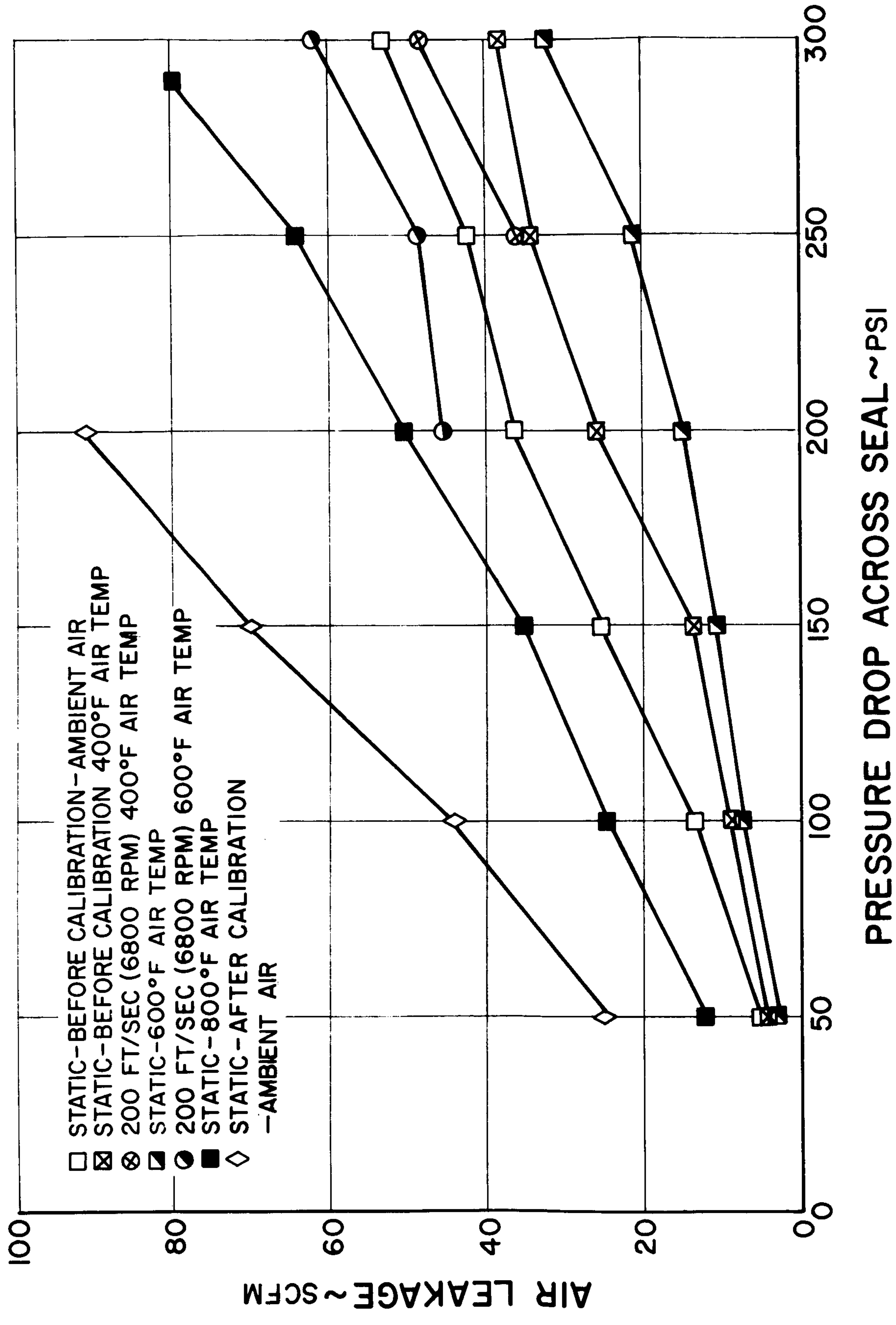

Figure 65 Final Dynamic Checkout of Build 2 of the Hybrid Seal

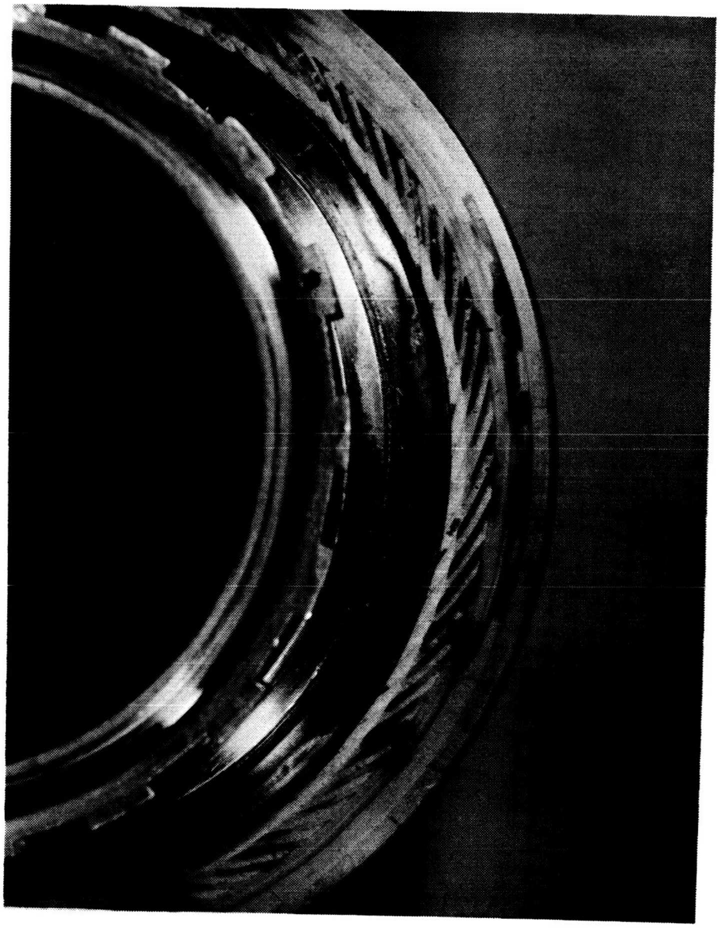

Figure 66 Seal Plate after Termination of Testing on Build 2 of the Hybrid Seal (CN-9342)

F. ORIFICE-COMPENSATED EXTERNALLY PRESSURIZED SEAL

The orifice-compensated externally pressurized seal was tested to see whether the addition of an external source for the annular groove in the orifice-compensated hydrostatic seal would improve the stability of the seal. Only one build of this seal was tested, and the external pressurizing source did not prove to be particularly helpful: the seal failed in the same manner as Builds 5, 6, and 7 of the orifice-compensated hydrostatic seal. The outer lip of the seal was smooth, while the inner lip was worn and rough. The outer edge of the seal plate was polished, but the inner edge showed four equidistant burn marks. The seal had completed 11.75 hours of testing before failure.

The components of the orifice-compensated externally pressurized seal are shown in Figures 67 and 68. In addition to the external source, this design incorporated the spring-loaded floating seal-plate design which was also used in Builds 5 through 9 of the orifice-compensated hydrostatic seal.

For the dynamic checkout, the external pressure was kept 20 psi higher than the pressure at the inner surface of the seal. At each speed condition, testing was started at an external air pressure of 100 psig. Then the pressure was increased to 220 psig, and reduced in 20-psi increments to its original value. The external pressurizing air flow and the ambient side leakage were recorded at each test point.

At 200 ft/sec rubbing velocity, the external air pressure was lowered from 100 to 60 psi at 300 ft/sec from 100 to 60 psi; and at 400 ft/sec from 100 to 80 psi, when failure appeared to be imminent. At this condition, the external pressurizing air flow decreased from 12.0 to 9.5 scfm after 0.15 hours at this condition. The test was terminated, and a static leakage calibration indicated excessive air leakage. The seal had completed the following points before shutdown.

Seal Sliding Speed (feet per second)	External Air Pressure (pounds per square inch)
200	220 to 60
300	220 to 60
400	220 to 100

The test seal assembly and the seal plate were removed from the test unit for inspection. The seal had failed in the same manner as the orifice-compensated hydrostatic seal. The inner carbon lip was ~~severly~~ severely scored and the plate coating was worn at the inner lip contact diameter.

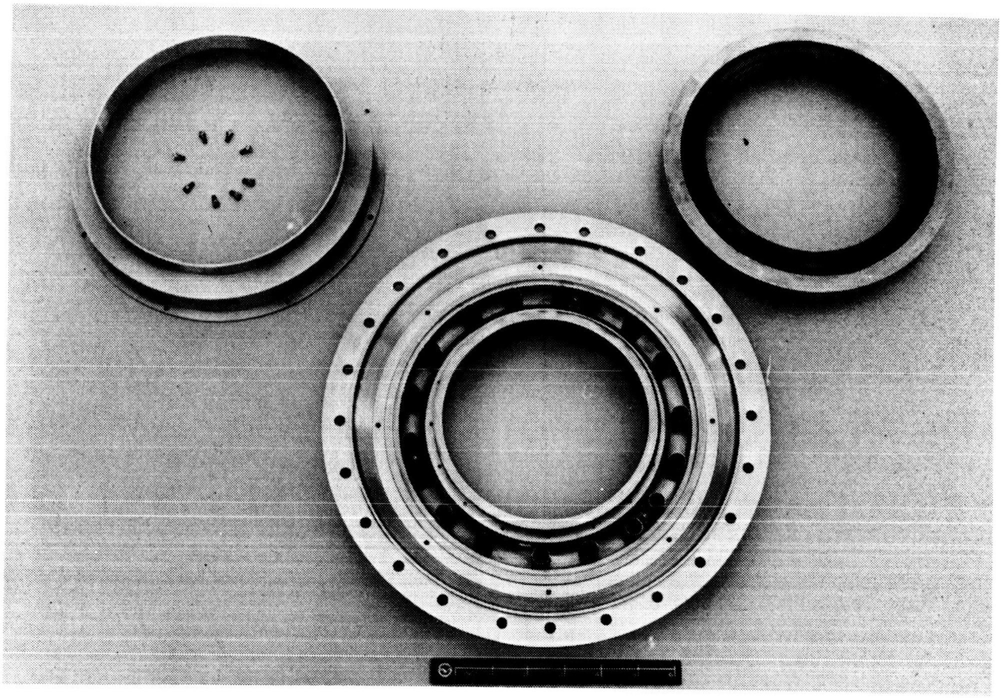

Figure 67 Components of the Orifice-Compensated Externally Pressurized Seal (CN-7466)

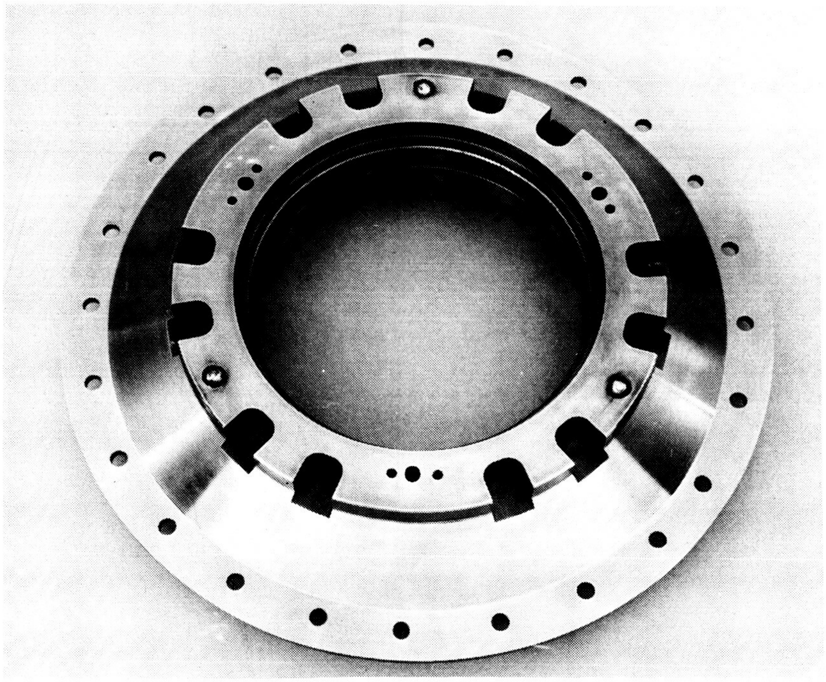

Figure 68 Seal Carrier from the Orifice-Compensated Externally Pressurized Seal Showing the Three Inlet Holes for the Pressurizing Air Supply (CN-7467)

Figure 69 shows the external pressurizing air flow supplied to the seal, and Figure 70 shows that portion of the external pressurizing air flow which leaks to the inner surface of the seal. Note that the total external pressurizing air flow divides itself into leakage to the inner (high-pressure) and leakage to the outer (low-pressure) compartment of the seal.

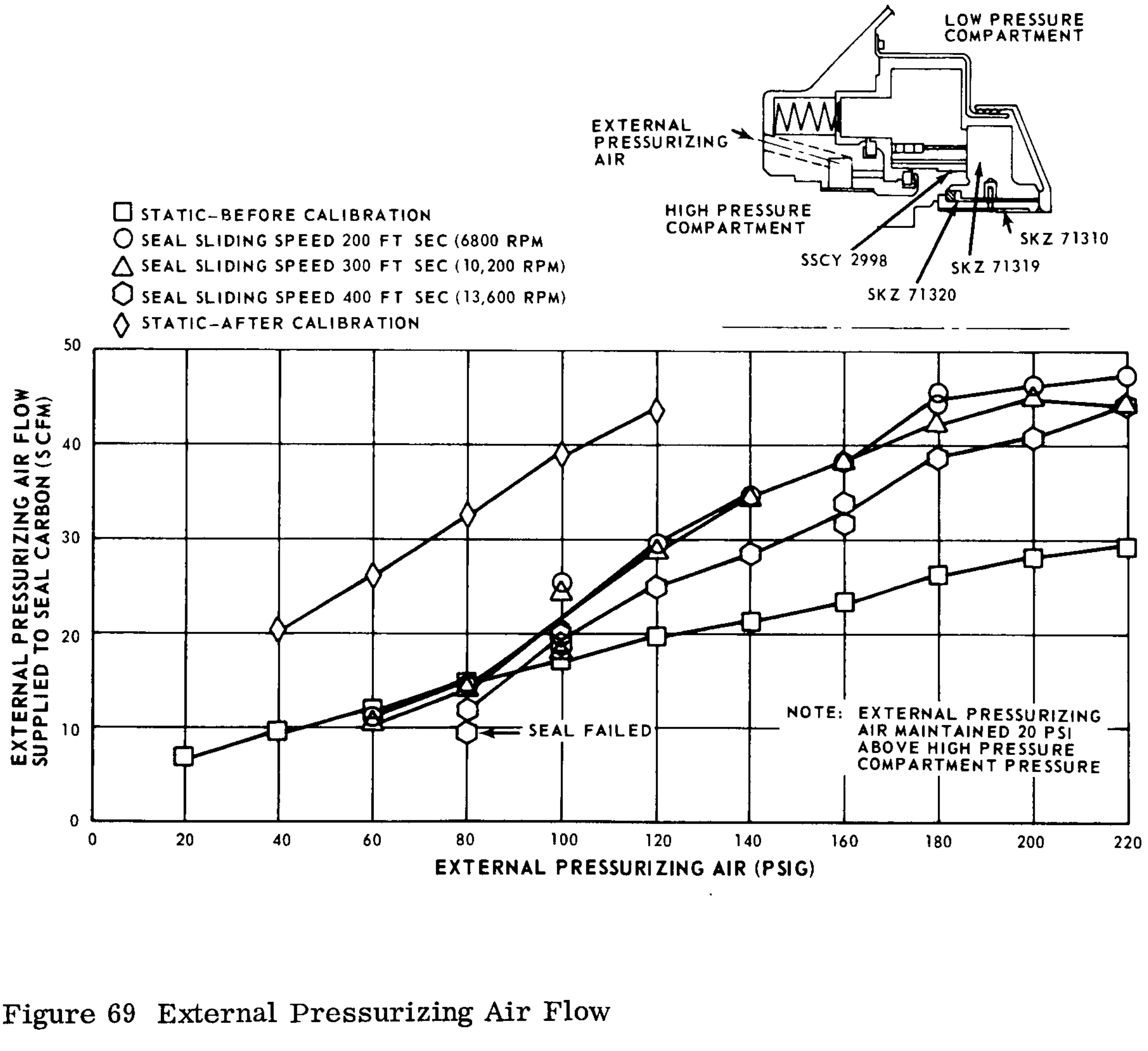

Figure 69 External Pressurizing Air Flow

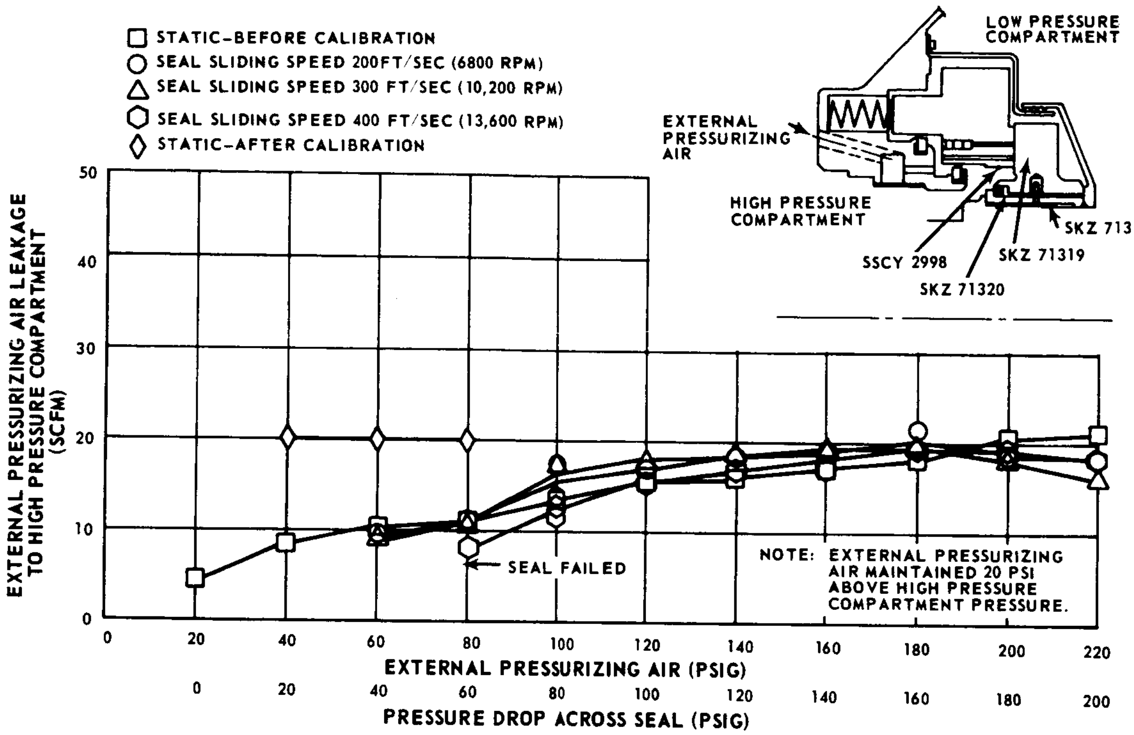

Figure 70 Leakage of External Pressurizing Air Flow to High-Pressure Compartment

G. POSTTEST SEAL INTERFACE ANALYSIS OF THE ORIFICE-COMPENSATED HYDROSTATIC SEAL

The contractor developed gas-film analytical models for the orifice-compensated hydrostatic seal and the hybrid seal to verify and improve the performance of the seal configurations being tested. Agreement between the analysis and experimental results was very good. The three types of analyses performed for the orifice-compensated hydrostatic seal were the formulation of a gas-film analytical model, estimates of seal face rotation caused by pressure loading, and estimates of seal face rotation caused by thermal distortion.

Because the best experimental results were obtained on Build 9, it was used as the basis for the analytical work. The single feature of Build 9 which improved its stability was the shallower annular groove. The depth of the groove in Build 9 was only 12 mils, much less than the 55-mil depth used in Build 7. As a result of this change, the area of the piston-ring bore exposed to high pressure was increased, shifting the pressure loading on the seal. Thus, the initial tilt from pressure loading introduced a converging film of a reasonable order of magnitude, which is extremely desirable for stable operation over a wide temperature range.

1. GAS-FILM ANALYTICAL MODEL

The analytical model of this seal consisted of an annular flat plate with inner and outer radii R_2 and R_1, respectively. The high pressure was located at the inner edge of the seal and was also used to provide high-pressure air to the annular groove at radius R_c through three feeding holes. Each hole contained four orifices in series. The model took account of the fact that the area of the seal ring is finite, and treated the individual annular feed grooves with equivalent inherent compensation. The fact that dishing and crowning of the seal face with respect to the seal plate results in converging and diverging gas films was also considered.

a. Parallel Film

For static load and uniform film thickness, the dimensionless Reynolds equation on both sides of the feeding plane can be written as

$$\frac{1}{r}\frac{\partial}{\partial r}\left[r\frac{\partial P^2}{\partial r}\right] + \frac{\partial^2 P^2}{r^2 \partial \theta^2} = 0$$

where $r = R/R_c$ and $P = p/p_a$. The second term is zero because of axial symmetry. Hence, the solution for dimensionless pressure becomes:

$$P^2 = 1 + C_1(\ln r)$$

where C_1 is an integration constant. Introducing the dimensionless bearing parameters:

$$\eta = R_1/R_c\ ,\quad \gamma = R_c/R_2\ ,\quad \beta = \ln\eta/\ln\gamma$$

C_1 can be evaluated for the boundary condition to give the dimensionless pressure.

$$1 \leq r \leq \eta\ , \qquad P^2 = 1 + q_1 \ln(\eta/r) \tag{1}$$

$$1/\gamma \leq r \leq 1 \qquad P^2 = V^2 + \beta q_2 \ln(\gamma r) \tag{2}$$

By equating the orifice flow and the leakage flow at r=1, we have,

$$\left[-\frac{\partial P^2}{\partial r}\bigg|_{r \geq 1} + \frac{\partial P^2}{\partial r}\bigg|_{r \leq 1} \right]_{r=1} = \frac{12\,\mu\,N\,a^2\sqrt{RT}}{p_a h^3}\,Vm \tag{3}$$

Inserting Equations 1 and 2 into Equation 3, we get

$$(q_1 + \beta q_2) = \Lambda_t\,Vm \tag{4}$$

where $\Lambda_t = \dfrac{12\,\mu\,N\,a^2\sqrt{RT}}{p_a h^3}$, $V = p_s/p_a$

q_1 and q_2 can be evaluated in terms of the dimensionless downstream feeding pressure P_i from Equations 1 and 2 at r = 1, with P_i defined as $P_i = p_i/p_a$.

$$q_1 = (P_i^2 - 1)/\ \ln\eta$$

$$q_2 = (P_i^2 - V^2)/\ \ln\eta$$

With values of q_1 and q_2 substituted into Equation 4, the dimensionless downstream orifice pressure can be calculated through the iteration scheme in the equation given below:

$$P_i^2 = \left[\ln\eta\ \ln\gamma\ \Lambda_t Vm + \quad \ln\gamma + V^2 \ln\eta\right] / (\ln\gamma + \ln\eta) \tag{5}$$

where, m = the dimensionless orifice flow = $M\sqrt{RT}/\pi a^2 p_s$

$$= C_D\sqrt{\frac{2k}{k-1}}\,(P_i/V)^{1/k}\left(1 - (P_i/V)^{(k-1)/k}\right)^{1/2}$$

for $P_i/V > \left(\dfrac{2}{k+1}\right)^{k/(k-1)}$

$$= C_D\sqrt{\frac{2k}{k+1}}\left(\frac{2}{k+1}\right)^{1/(k-1)}$$

$$\text{for } P_i/V \le \left(\frac{2}{k+1}\right)^{k/(k-1)}$$

C_D is the orifice discharging coefficient given by Figure 71.

With P_i obtained through the iteration process from Equation 5, the leakage rates can be calculated, and pressure distribution evaluated from Equations 1 and 2.

The dimensionless load $\bar{W}$ can be found by integrating the pressure function.

$$\bar{W} = \frac{W}{\Delta p A} = \frac{W}{\pi(p_s - p_a)(R_1^2 - R_2^2)} = \frac{R_c^2 p_a}{\pi(p_s - p_a)(R_1^2 - R_2^2)}\int_0^{2\pi}\int_{1/\gamma}^{\eta} r(P-1)\,dr\,d\theta$$

b. Tilting Film

A seal supported on a gas film tends to have a converging or diverging film (dishing or crowning) due to pressure loading, thermal loading, and initial tilting of the seal plate. It is necessary to incorporate the effect of dishing and crowning in the formulation of the present analysis.

Assume that the film thickness can be represented by a linear function of r with the mean film thickness positioned at $(R_1 + R_2)/2$. The film distribution is given by

$$h = a + b\,r$$

where $a = 1 - 0.5\alpha(R_1 + R_2)/H_o$, and $b = \alpha R_c/H_o$

The governing equation is again given the simplified Reynolds equation

$$\frac{1}{r}\frac{\partial}{\partial r}\left[r\,h^3\frac{\partial P^2}{\partial r}\right] = 0$$

Equations 1 and 2 are replaced by the equations below

$$1 \le r \le \eta \qquad P^2 = 1 - q_1\int_1^r \frac{dr}{rh^3} + q_1\int_1^\eta \frac{dr}{rh^3}$$

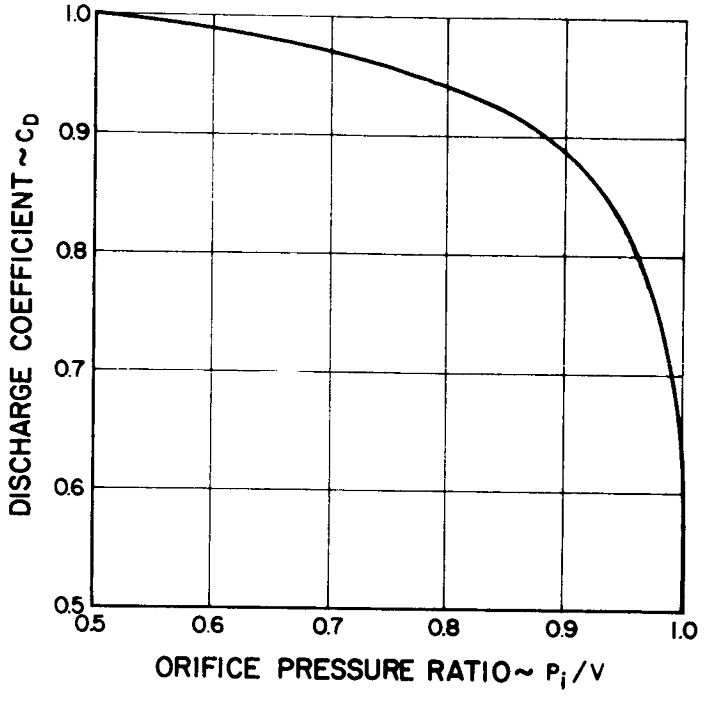

Figure 71 Orifice Discharge Coefficient (C_D) for the Orifice-Compensated Hydrostatic Seal (See Reference 14)

$$1/\gamma \leq r \leq 1 \qquad p^2 = V^2 - q_2 \int_1^{1/\gamma} \frac{dr}{rh^3} - q_2 \int_r^1 \frac{dr}{rh^3}$$

where $$\int_1^r \frac{dr}{rh^3} = \frac{-a^2 + (a + b\,r)\ (a + 2\,b\,r)}{2a^2\ b\ r\ (a + b\,r)^2} - \frac{1}{a^3} \ln\left(\frac{a + br}{r}\right)$$

where $r=1$, $$q_1 = (P_i^2 - 1)/\int_1^{\eta} \frac{dr}{rh^3}$$

$$q_2 = -(P_i^2 - V^2)/\int_1^{1/\gamma} \frac{dr}{rh^3}$$

and Equation 5 is replaced by

$$P_i^2 = (C_1\ C_2\ \Lambda_t\ Vm + C_2 + V^2 C_1)/\ (C_1 + C_2)$$

where $$C_1 = \int_1^{\eta} \frac{dr}{rh^3}, \qquad C_2 = \int_{1/\gamma}^1 \frac{dr}{rh^3}$$

c. Feeding Mechanism

Orifice feeding is treated as a line feed in this analysis. The configuration used for the orifice-compensated hydrostatic seal consists of three shallow recessed slots with four orifice in series positioned in the middle of each slot. The presence of the shallow recess relieves the pressure in the neighborhood of the orifice, so the pressure in each slot is quite uniform and equal to the downstream feeding pressure.

Three types of feeding mechanism can easily be incorporated into the present analysis. The feeding parameter Λ_t as given before applies to orifice restriction only, and its general expression is

$$\Lambda_t = \frac{12\ \mu\ Na^2 \sqrt{RT}}{\sqrt{1+\delta^2 p_a}\ h^3}$$

where $\delta = a^2/dC$
a = radius of the orifice (in)
d = diameter of the circular recess (in)
C = clearance at the end of the recess (in)

The feeding parameter Λ_t can be redefined as the restrictor parameter Λ_s

$$\Lambda_s = \Lambda_t / V = \frac{12 \mu Na^2 \sqrt{RT}}{\sqrt{1+\delta^2}\, p_s h^3} \qquad (6)$$

for a restricted orifice with $\delta \approx 0$

$$Na^2 = \frac{p_s h^3}{12\mu\sqrt{RT}} \Lambda_s$$

For inherently compensated orifices with $\delta \gg 1$

$$NdC = \frac{p_s h^3}{12\mu\sqrt{RT}} \Lambda_s$$

For orifice compensated films, the general expression appearing in Equation 6 applies.

$$\frac{Na^2}{\sqrt{1+\delta^2}} = \frac{p_s h^3}{12\mu\sqrt{RT}} \Lambda_s \qquad (7)$$

This expression is used for the design of the orifice-compensated hydrostatic seal. It is to be noted that the diameter of the recess is the equivalent diameter for the area of the finite feeding-slot groove.

Since the feed hole in the present design use four orifices in series, the factor $\sqrt{1+\delta^2}$ in Equation 7 must be modified. In general, for a seal using N feed holes, each with M orifices in series, Equation 7 becomes

$$\frac{Na^2}{\sqrt{M+\delta^2}} = \frac{p_s h^3}{12\mu\sqrt{RT}} \Lambda_s$$

The annular groove was accounted for by merely expanding the line feed to an annular feed with the pressure in the annulus assumed to be uniform. If the location of the annulus is given by R_{C1} and R_{C2}, the flow must be matched at R_C, the location of the feeding hole.

d. Experimental Comparison

In order to better verify the analytical predictions, they were checked against data contained in Reference 6, which describes an experiment in which an orifice-compensated hydrostatic seal was tested to measure its static leakage and gas-film thickness.

The seal was composed of a quartz optical flat, a steel stator, and a steel head plate. The stator was positioned adjacent to the optical flat by means of an elastomer O-ring which itself was constrained by a groove in the head plate. Leakage measurements were made by means of three flow meters (covering the range from 0.03 cfm to 13 cfm) connected to a containment vessel enclosing the outlet of the seal. Gas-film thickness at three equally spaced circumferential locations was determined interferometrically using a helium light source corresponding to 11.57 microinches per light fringe.

A schematic diagram of a radial section of the test stator is shown in Figure 72. A slot was cut within the seal land and provided with twelve supply lines and orifices such that the back pressure on the orifices, p_s, is equal to the seal pressure, p_2. The average diameter of the 12 orifices was 14.2 ± 1.5 mils. The quantities ℓ_1 and ℓ_2 designate the location of the secondary seal relative to the seal land and were maintained at the values indicated on the diagram throughout the experiments. The initial coning angle was small in each case so that the stator would tend to distort into a parallel channel as the seal pressure was increased. The actual initial coning (h_2-h_1) amounts to 21 microinches in this stator. The absolute minimum film thickness was determined as a function of the seal pressure by means of the light-interference technique.

The stator for the orifice-compensated hydrostatic seal contained an initial saddle-shaped warp, despite careful preparation, which yielded circumferential variations in the film-thickness readings. The maximum variation encountered was about 170 microinches at a seal pressure of 45 psi. The variation decreased to about 70 microinches at 315 psia.

It is known that the leakage rate varies approximately as the third power of the film thickness under circumferentially uniform conditions and it is believed that the root-mean-cube value of the three readings obtained at each value of the seal pressure will best approximate the effective constant film-thickness value for the purpose of comparison with the theory.

Film-thickness data in terms of the root-mean-cube values as a function of seal pressure is given in Figure 72 with the analytically predicted results. Experimental and analytical leakage rates as a function of seal pressure are given in Figure 73. The agreement is excellent for the comparison of leakage rates and satisfactory for the comparison of film thicknesses.

The satisfactory correlation obtained with the experimental results firmly establishes the validity of the proposed analytical model for this orifice-compensated hydrostatic seal.

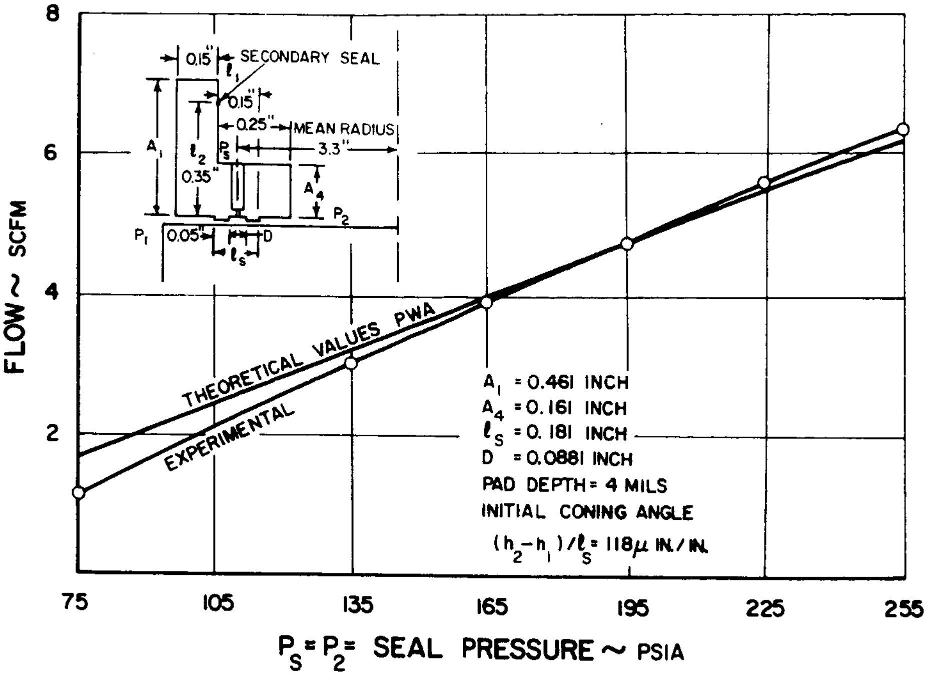

Figure 72 Experimental and Analytical Values for Static Leakage Flow

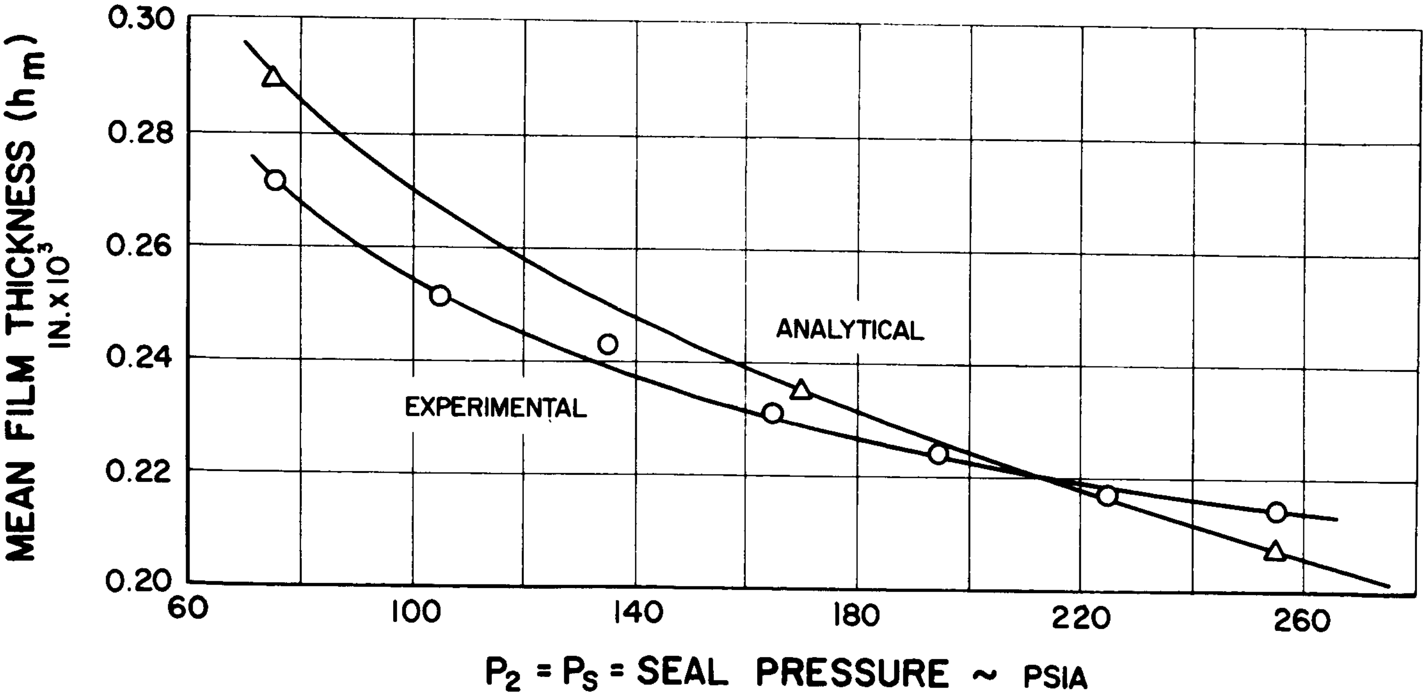

Figure 73 Experimental and Analytical Values For Mean Film Thickness

2. ROTATION OF THE SEAL BECAUSE OF PRESSURE LOADING

The seal's rotation because of pressure loading was analyzed by two methods. The first method was relatively straightforward, accounting for the angular rotation directly from considerations of the pressure differential on the steel seal support. The second method was based on the gas-film equilibrium analysis by matching the measured leakage rates to the predicted values, thus, the angular rotation and operating film thickness can be predicted. Furthermore, a refined analysis of first method was based on Kalnins' "Analysis of Shell Revolutions Subject to Symmetrical and Non Symmetrical Loads", (Reference 7). Agreement between the two methods was quite good. The positive sense denotes a diverging leakage path.

a. Direct Analysis

This analysis was performed assuming a pressure differential across the seal of 200 psi. In addition, the assumption was made that the effect of the carbon could be neglected, since its modulus of elasticity is so much less than that of the steel seal support. The centroid of the analytical model of Build 9 and its dimensions are shown in Figure 74. The plane moment of inertia of the model is 0.0194 $in.^4$.

The radial force (F_r) on the seal is the summation of pressure over the distance from the face of the seal plate to the land face of the piston ring.

$$F_r = 200\ (0.925) = 185 \text{ lb/in of circumference}$$

Then the moment (M) on the seal section due to F_r is

$$M = F_r\ (0.925/2 - 0.39) = -13.5 \text{ in-lb/in of circumference}$$

The pressure force on the back face of the seal is located at a radius of 3.326 inches, and on the front face at a radius of 3.356 inches. This gives a moment arm of 0.030 inch.

The effective area of the seal's back face is $\pi(3.502^2 - 3.15^2)$, or 7.356 in^2. This results in a load of 1471.2 pounds. The circumference of the seal's face at the center of pressure is $2\ \pi\ (3.326)$, or 20.898 inches. Therefore, the moment from that load is (1471.2) (0.03)/ 20.898, or 2.11 in-lb/in of circumference. Thus, the net moment is -13.5 + 2.11, or -11.4 in-lb/in of circumference.

The rotation of the seal is given by MR^2/EI, and is equal to -312×10^{-6} radians.

Calculations of rotation were performed for both Build 7 and Build 9 at pressure differentials of 100 and 200 psi. They are tabulated below.

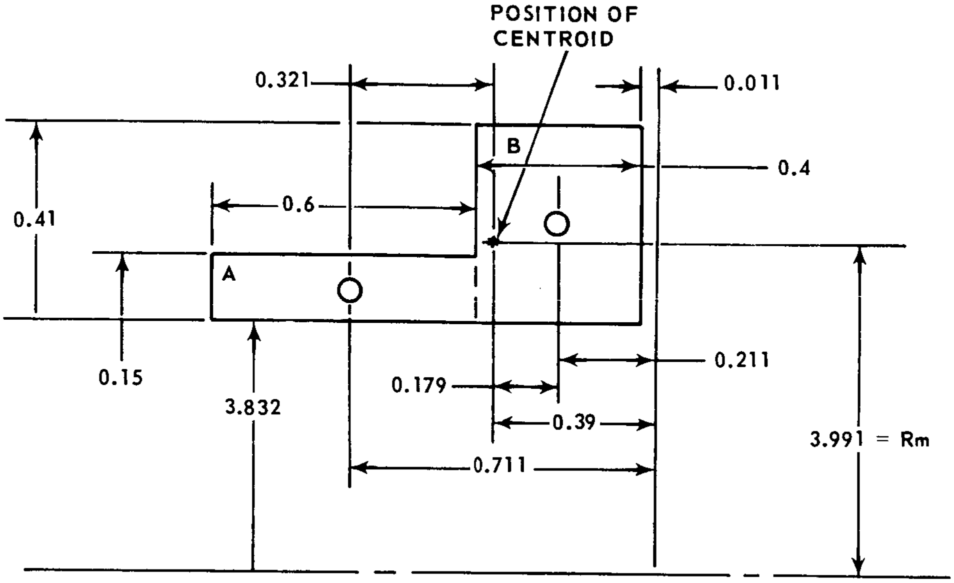
POSITION OF CENTROID
0.321
0.011
B
0.4
0.41
0.6
A
0.15
3.832
0.179
0.211
0.39
0.711
3.991 = Rm

Figure 74 Seal Retaining Band of Build 9 of the Orifice-Compensated Hydrostatic Seal

Build	P (psi)	Rotation (Radians)
7	100	-65.2×10^{-6}
7	200	-125.0×10^{-6}
9	100	-159.0×10^{-6}
9	200	-312.0×10^{-6}

b. Analysis via Gas-Film Equilibrium Considerations

Using the analysis as outlined in Section 1, curves of dimensionless load ($\overline{W}$) versus film thickness (h_m) were obtained for pressure differentials of 100 and 200 psi at an air temperature of 70 degrees Fahrenheit. These curves are shown in Figures 75 and 76. This analysis also yielded curves of leakage flow versus film thickness, shown in Figures 77 and 78.

The geometrical balance of this seal can be calculated by taking the ratio of the back area A_B to the front area A_F of the carbon seal nose-piece. We have

$$\text{Imbalance} = \frac{A_B}{A_F} = \frac{3.5^2 - 3.15^2}{3.644^2 - 3.15^2} = 0.6935$$

The dimensionless load $\overline{W}$ is defined as load per unit area per pressure gradient. $\overline{W} = W/\Delta P A_F$. When the seal is in equilibrium position, the load in the back of the seal represented by $\Delta P\ A_B$, is equal to W which is the load generated due to hydrostatic pressure. By substituting $W = \Delta P A_B$ into $\overline{W} = W/\Delta P\ A_F$ we have $\overline{W} = A_B/A_F$ = Imbalance.

For the given imbalance of 0.6935, seal tilt was plotted as a function of mean film thickness in Figure 79. Similarly, Figure 80 was obtained from Figures 77 and 78 using the relationship between seal tilt angle and mean film thickness from Figure 79. The experimental leakage for Builds 7 and 9 is shown in Figure 81, and the analytical leakage of the piston ring is shown in Figure 82.

If one has the net leakage by subtracting piston-ring leakage from experimental leakage, through matching to the analytical leakage he can find the seal's tilt angle from Figure 80. Using this information, mean film thickness can be found from Figure 79.

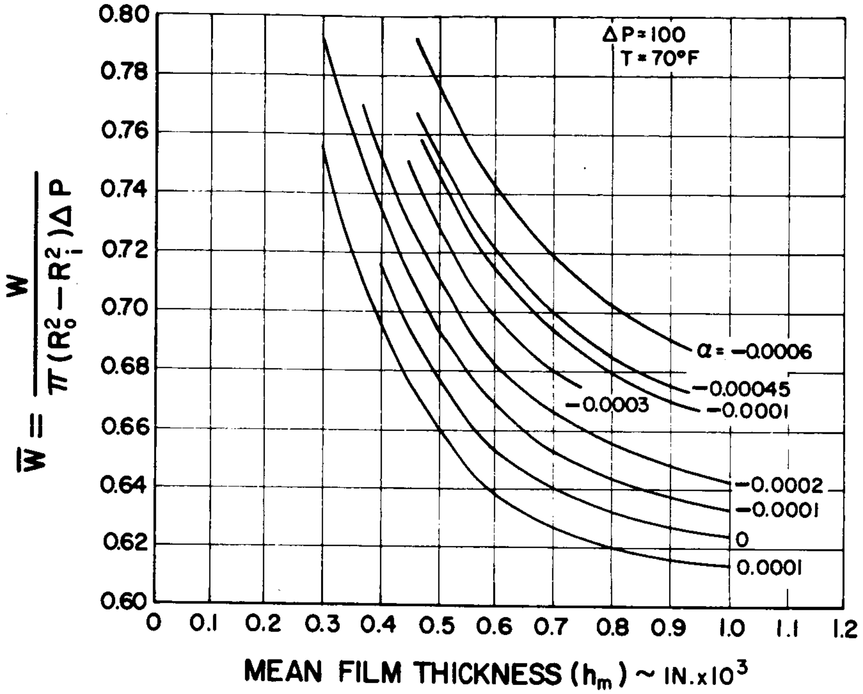

Figure 75 Dimensionless Load as a Function of Film Thickness at a Pressure Differential of 100 psi

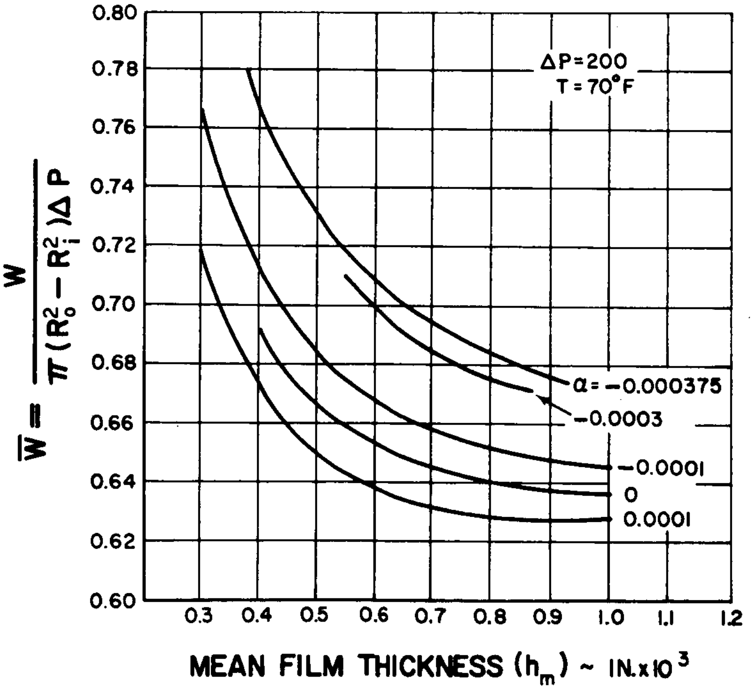

Figure 76 Dimensionless Load as a Function of Film Thickness at a Pressure Differential of 200 psi

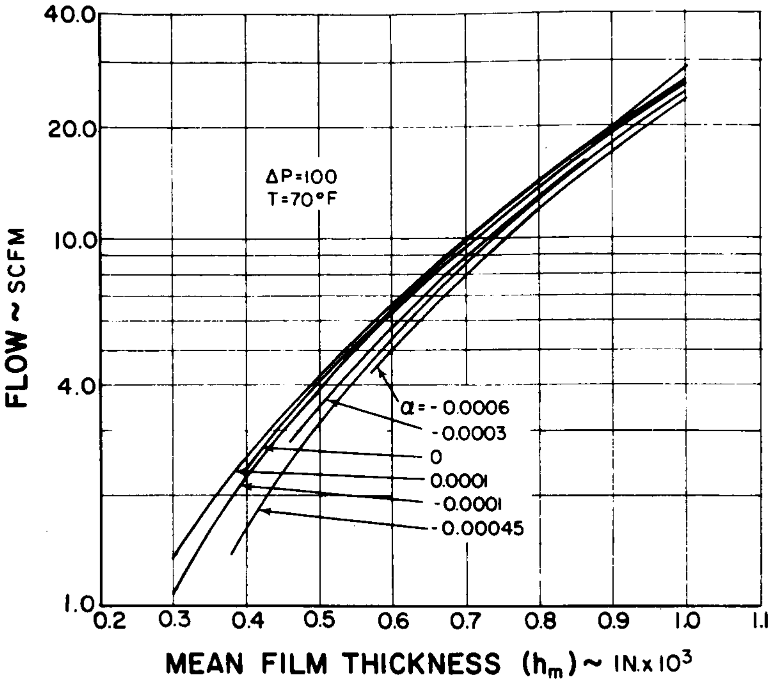

Figure 77 Leakage as a Function of Film Thickness at a Pressure Differential of 100 psi

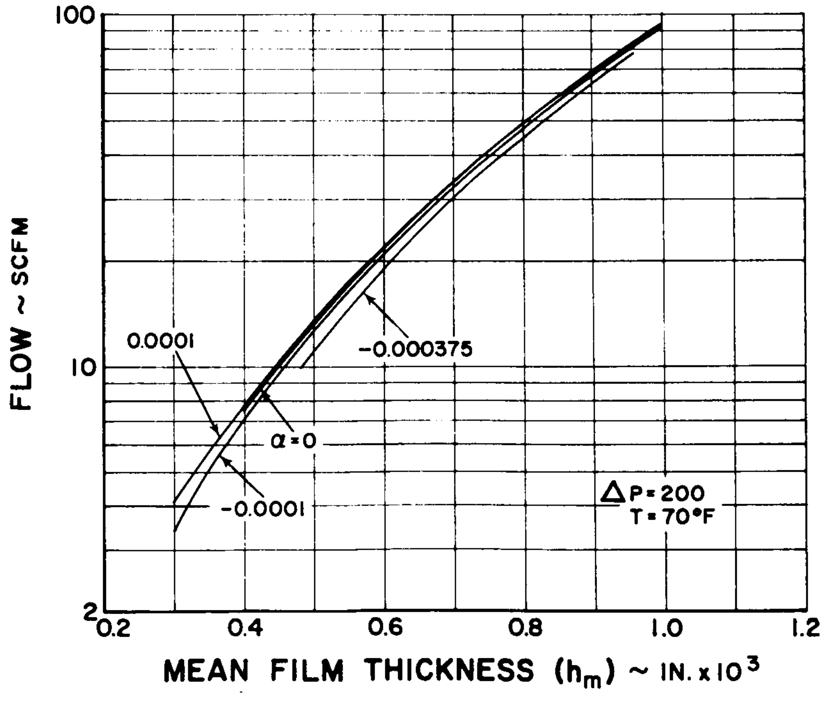

Figure 78 Leakage as a Function of Film Thickness at a Pressure Differential of 200 psi

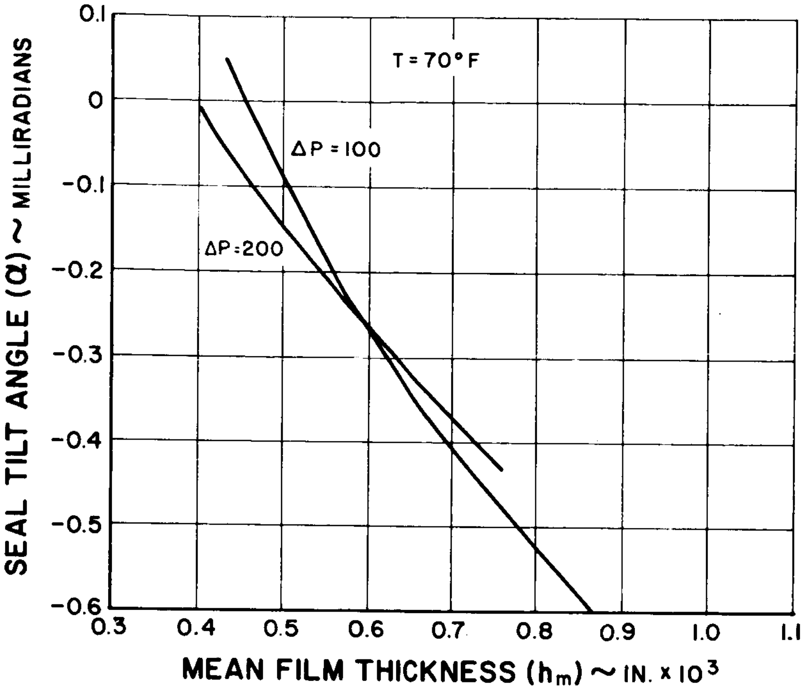

Figure 79 Seal Tilt as a Function of Mean Film Thickness with a Geometric Imbalance of 0.6935

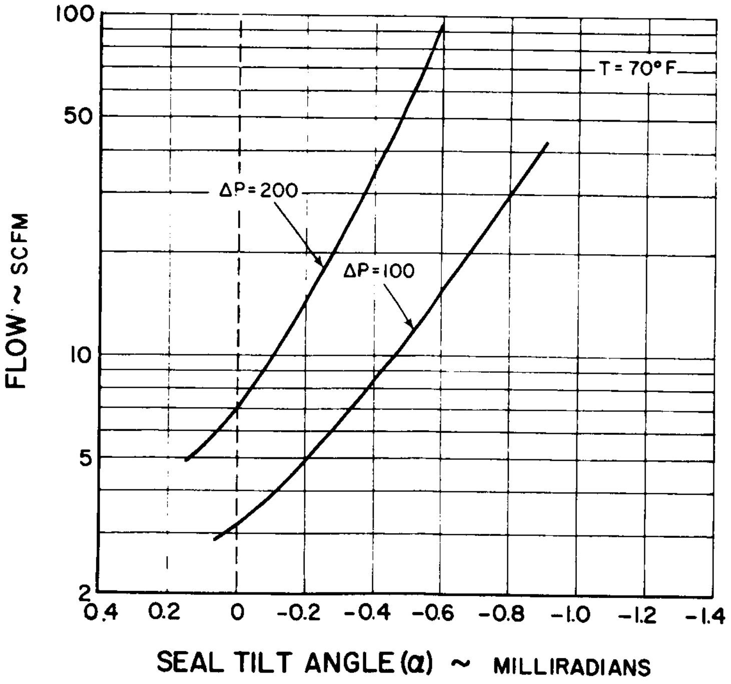

Figure 80 Leakage as a Function of Seal Tilt Angle

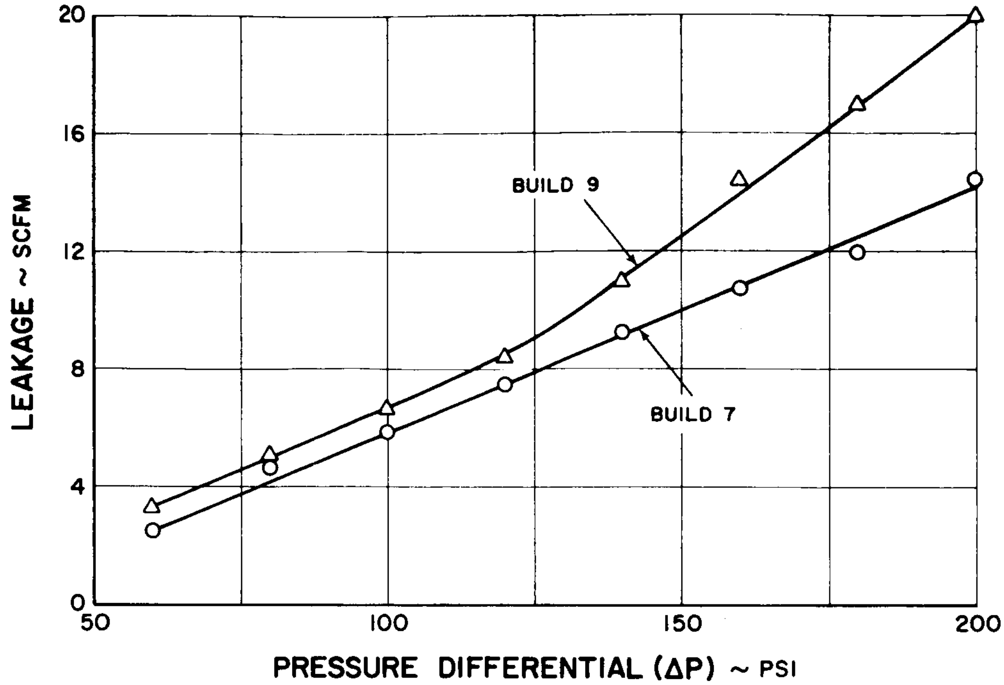

Figure 81 Experimental Values for Leakage in Builds 7 and 9

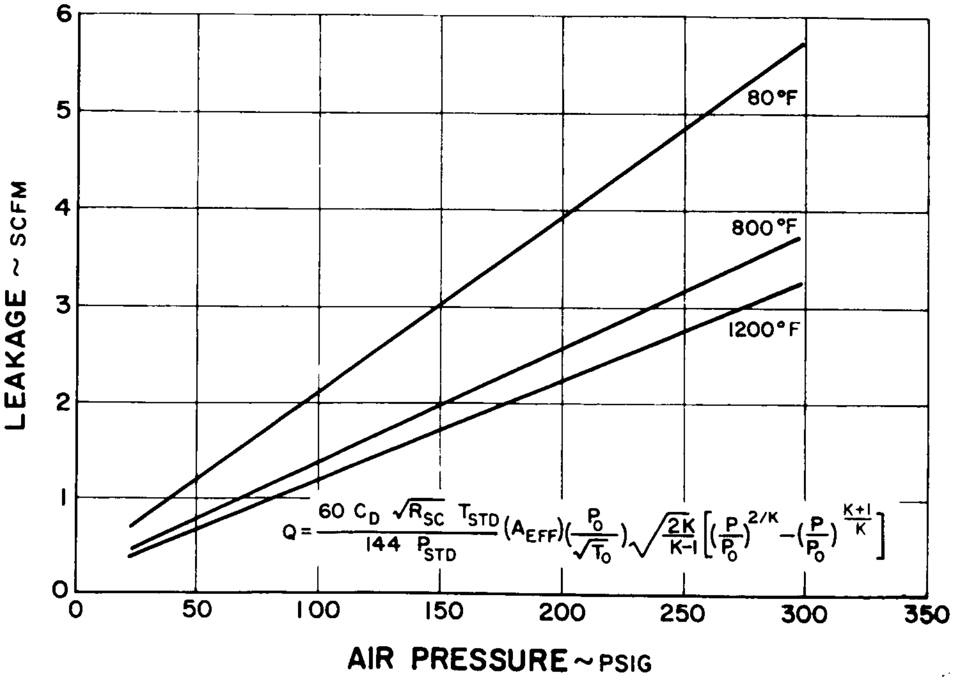

Figure 82 Analytical Values for Piston-Ring Leakage

Seal tilt angle is tabulated below with the values obtained by the elastic seal support calculation. The comparison is quite good, providing further support for the analytical model.

		Total Leakage (scfm)	Net Leakage (scfm)	Seal Tilt Angle α (gas film)	Seal Tilt Angle α (elastic)	Operating Mean Film Thickness h_m (mils)
Build 7	$\Delta P = 100$	5.9	3.8	-0.000085	-0.000065	0.495
	$\Delta P = 200$	14.5	10.6	-0.000112	-0.000125	0.469
Build 9	$\Delta P = 100$	6.85	4.75	-0.000182	-0.000159	0.547
	$\Delta P = 200$	20.4	16.5	-0.000225	-0.000312	0.554

The rotation of the combined steel seal support and carbon seal was calculated directly on the basis of Kalnins' analysis. The results of the calculations are shown in Figures 83 and 84. These values are comparable with the preliminary calculation but slightly smaller. This result was expected, since the preliminary analysis was based only on the steel support, while the values of Figures 83 and 84 include the effect of the carbon.

3. THERMAL ANALYSIS

Both direct and indirect methods were used in the thermal analysis. In the direct method, thermal distortion was calculated from the temperature map of the assembly and tilt angle was obtained from the distortion. Crowning and dishing calculated from load balance and leakage rates were then compared to the tilt angle. For the indirect method, mean film thickness was calculated from the equilibrium gas-film analysis and compared to the predicted failure temperature.

a. Direct Method

(1) Temperature Map of the Seal Assembly

In order to improve the thermal analytical model, comparisons were made between experimental data and the analytically predicted temperatures of four areas: the steel seal support, the carbon seal nose piece, the disk portion of the fixed guard, (windback shroud) and the cylindrical portion of the fixed guard.

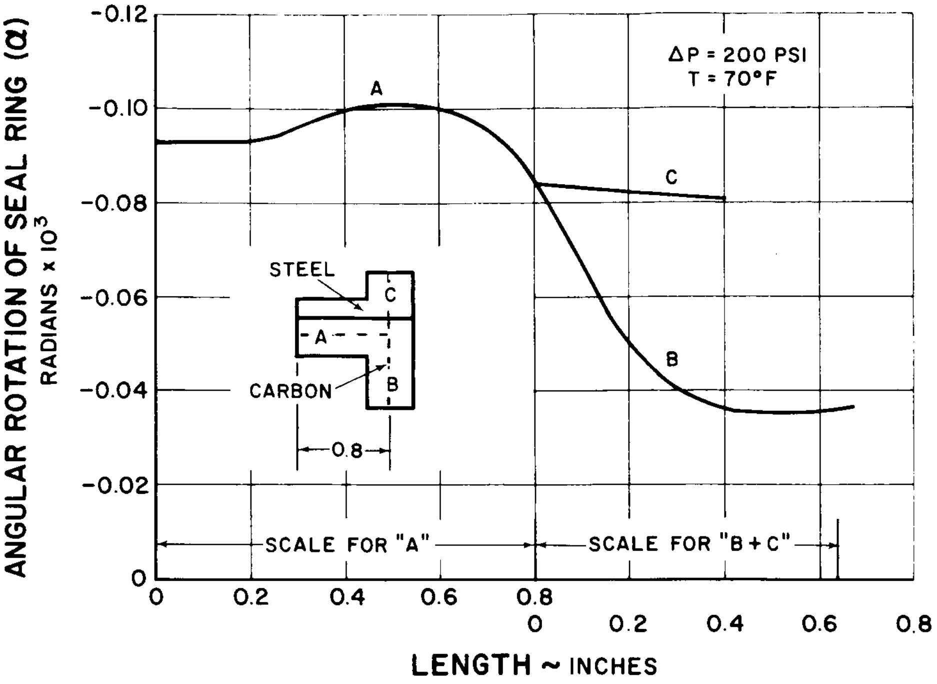

Figure 83 Rotation of the Seal Ring in Build 7

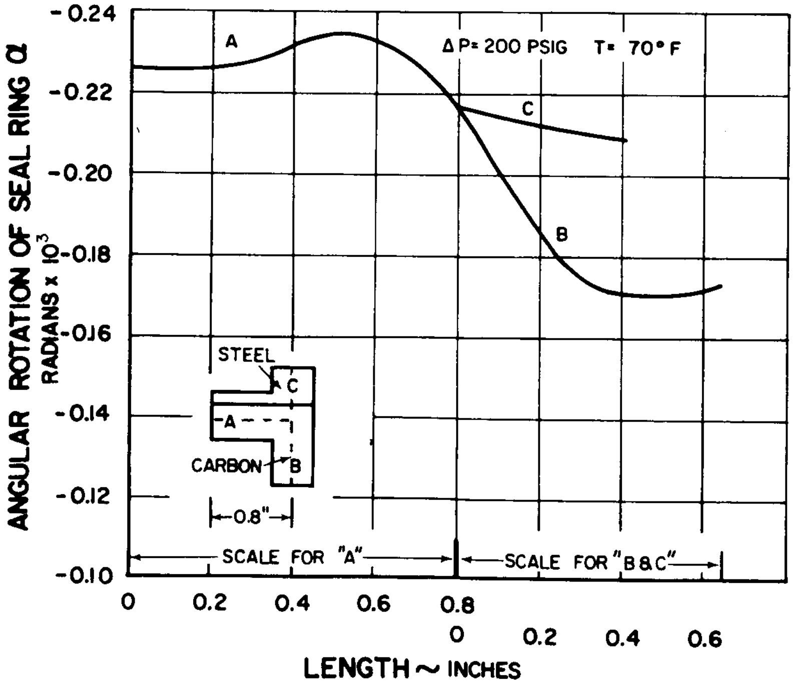

Figure 84 Rotation of the Seal Ring in Build 9

The comparison was made for a series of five test condition selected from test data on the orifice - compensated hydrostatic seal, Build 9.

To perform this comparison, the TOSS computer program which predicts the temperatures of the four areas mentioned above was used. The temperatures and pressures of the high- and low-pressure sides of the seal, the leakage past the seal, the speed of the shaft, and the heat generation at the interface between the seal and seal plate were used to generate the needed input parameters. All of the program's input parameters were taken directly from test data except for heat generation at the interface, heat-transfer coefficients, and thermal conductivities.

The heat-transfer coefficients were determined as illustrated in Appendix B. It was found that varying the heat-transfer coefficients within their range of uncertainty did not yield analytical temperatures which compared favorably with the experimentally measured ones. Therefore, the heat generation at the interface was varied until the temperatures predicted by the program agreed closely with the temperatures observed in the tests. Table XIV shows the input parameters for the computer program, the predicted temperatures, the temperatures observed in testing, and the heat generation predicted by Appendix B. The values of heat-transfer coefficients and thermal conductivities used in the computer program are shown in Table XV. Figures 85 through 89 are analytical temperature maps corresponding to test cases 1 through 5 on Table XIV.

Table XIV shows that the predicted values of heat generation are substantially lower than those values which produce good agreement between calculated and measured temperatures in the seal carrier and carbon. Heat generation calculations have considered only the tangential velocity gradients within the air film and neglect the radial gradients. The heat generation correlation, however, may not be the only explanation for the discrepancy between calculated and measured temperatures. It is possible that holes in the cylindrical portion of the fixed guard (required for clearance around the accelerometers) influenced seal temperatures. These holes may have permitted bearing compartment air to circulate around the seal freely enough to cause a significant increase in seal temperature when the bearing compartment air is hotter than the high-pressure air.

(2) Rotation of the Seal Plate

For comparison purposes, the thermal maps shown in Figures 85 and 88 were chosen, since they represent operation with ambient air at pressure differentials of 200 and 100 psi, respectively. The thermal distortion was calculated on the basis of a Raleigh-Ritz finite-element thermoelastic computer program furnished by Mr. Terry Russell of NASA. The seal's tilt angle was found by taking the slope of the face of the seal plate.

TABLE XIV

COMPARISON OF EXPERIMENTALLY MEASURED AND ANALYTICALLY DERIVED TEMPERATURES

	High Pressure Side		Low Pressure Side				Heat Generation At Interface (Lbs/Hour)	
Case	Air Temp. (°F)	Air Pres. (psia)	Oil Temp. (°F)	Air Pres. (psia)	Measured Leakage Past Seal (Lbs/Hour)	Speed of Shaft (rpm)	Input to Analytical Program	Calculated From Eq. for Half Mil Gap
1	92	215	250	15	305	13,600	5074	544
2	90	155	255	15	164	10,200	2710	300
3	85	115	260	15	103	10,200	3150	303
4	90	115	282	15	103	13,600	4520	550
5	250	215	282	15	216	13,600	2135	632

	Seal Carrier		Carbon Seal		Fixed Guard Disc Portion		Fixed Guard Cylindrical Portion	
Case	Test (°F)	Analytical (°F)	Test (°F)	Analytical (°F)	Test (°F)	Analytical (°F)	Test (°F)	Analytical (°F)
1	150	150	144	145	195	192	195	196
2	152	153	147	149	201	193	207	196
3	177	177	174	175	227	206	233	208
4	208	209	210	209	253	234	255	235
5	276	280	274	280	285	280	281	280

TABLE XV

PARAMETERS USED IN COMPUTER PROGRAM

	Case Number				
	1	2	3	4	5
THERMAL CONDUCTIVITIES (Btu/Hr Ft°F)					
Shaft	12.3	12.3	12.3	12.3	12.3
Seal Plate	18.0	18.0	18.0	18.0	18.0
Carbon	8.0	8.0	8.0	8.0	8.0
Carrier	16.7	16.7	16.7	16.7	16.7
Air In Windback	0.319	0.2755	0.2975	0.351	0.316
Air Between Plate and Fixed Guard	0.319	0.2755	0.2975	0.351	0.316
Air Between Plate and Rotating Guard	0.249	0.217	0.2340	0.276	0.261
Air Between Carrier and Fixed Guard	0.0196	0.0196	0.0196	0.0200	0.0214
HEAT TRANSFER COEFFICIENTS $\frac{\text{Btu}}{\text{hr ft}^2\ ^\circ\text{F}}$					
High Pressure, Rotating Surfaces	240-280	150-175	85-150	90-176	210-242
High Pressure, Stationary Surfaces	5.0	5.0	5.0	5.0	1.0
Low Pressure, Stationary Surfaces	0.772	0.772	0.700	0.614	0.718
Rotating Guard Surface	25-30	21-24	21-24	25-30	21-28
Fixed Guard "Flat Plate" Surface	19.1	14.2	11.4	11.46	16.9

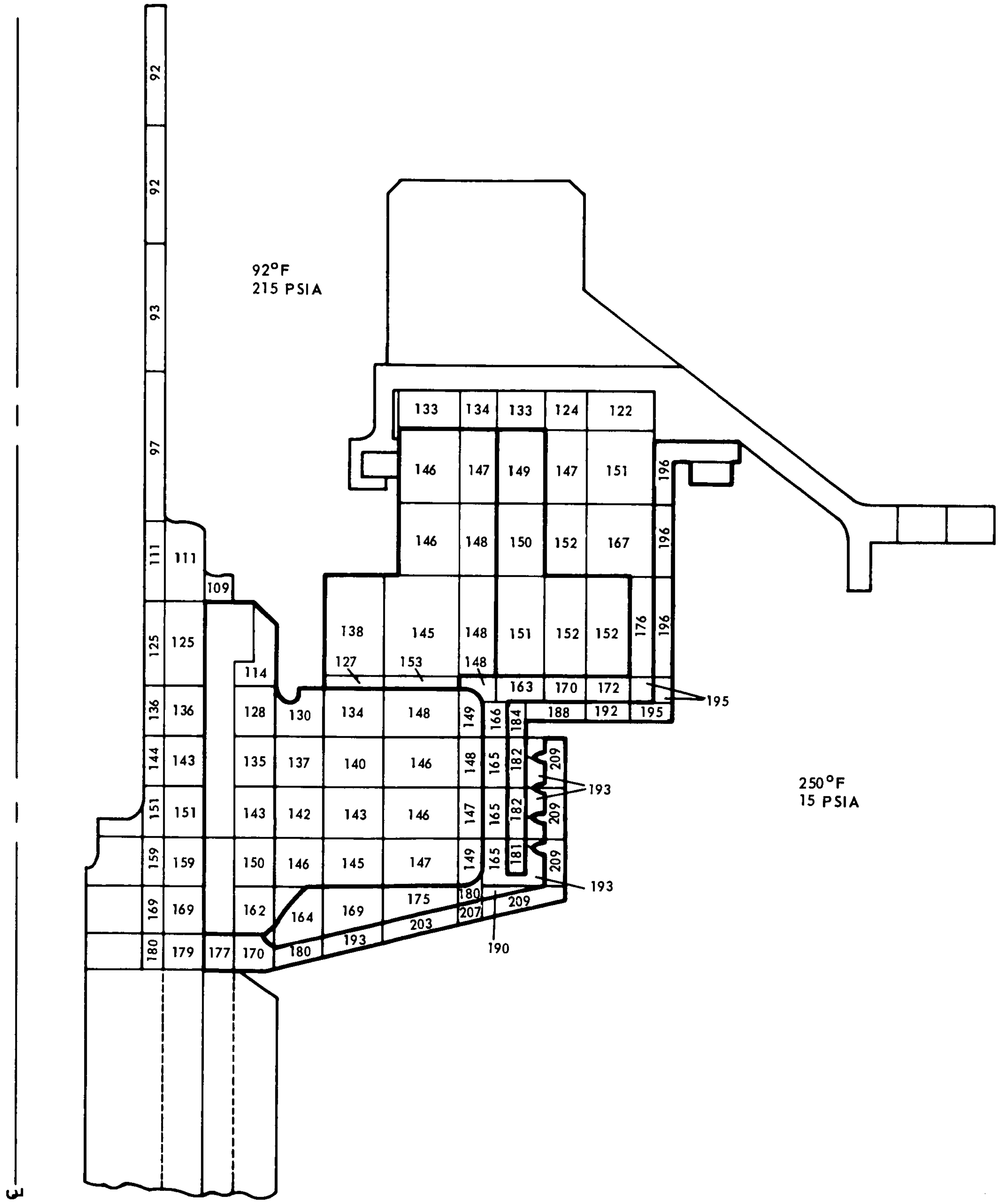
92°F
215 PSIA
250°F
15 PSIA
92
92
93
97
111
111
109
125
125
114
136
136
128
130
144
143
135
137
151
151
143
142
159
159
150
146
169
169
162
164
180
179
177
170
180
133
134
133
124
122
146
147
149
147
151
196
146
148
150
152
167
196
138
145
148
151
152
152
176
196
127
153
148
163
170
172
195
134
148
149
166
184
188
192
195
140
146
148
165
182
209
193
143
146
147
165
182
209
145
147
149
165
181
209
193
169
175
180
207
209
203
193
190

Figure 85 Thermal Map of the Orifice-Compensated Hydrostatic Seal (See

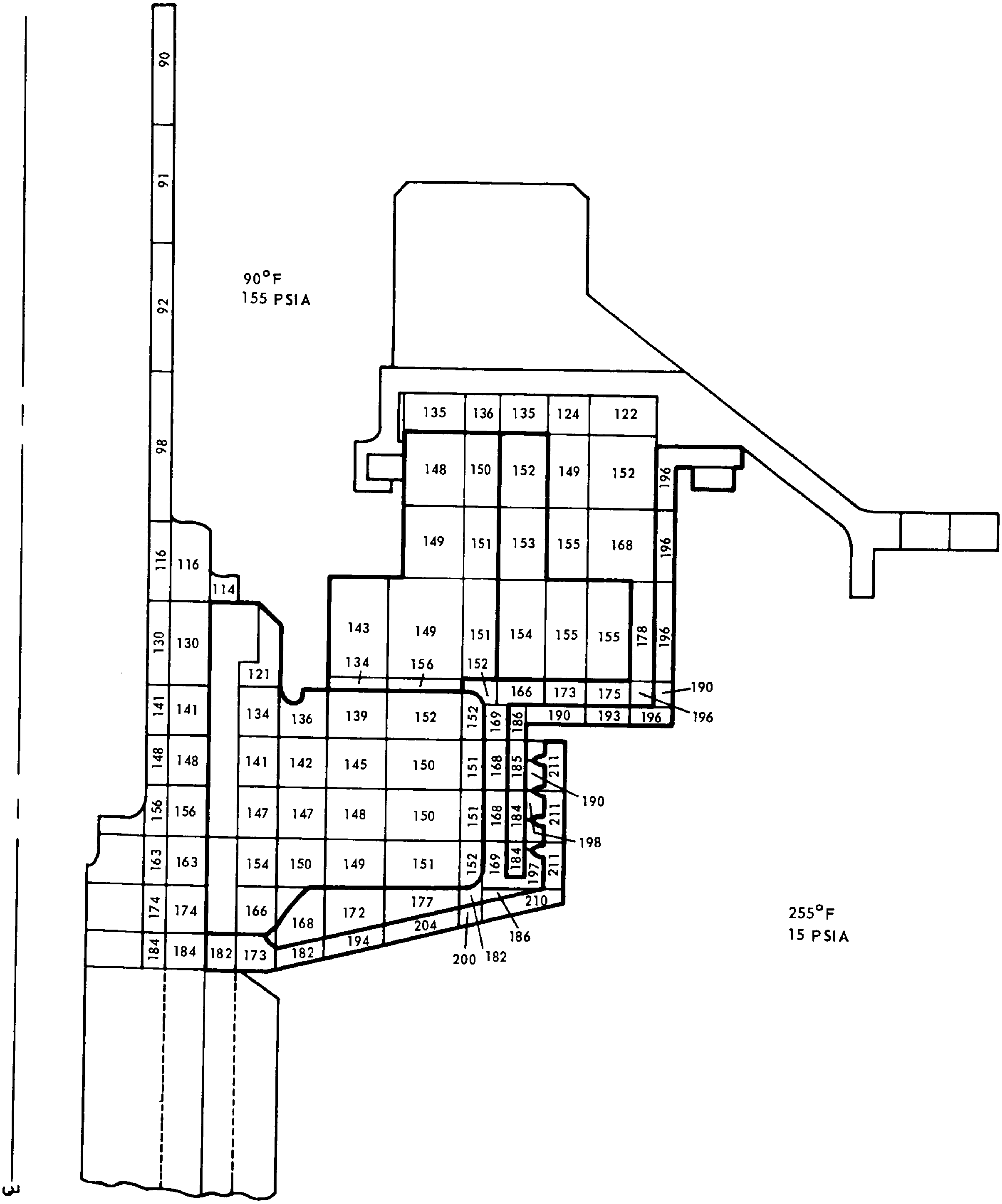
90°F
155 PSIA
255°F
15 PSIA
90
91
92
98
116
116
114
130
130
121
141
141
134
136
148
148
141
142
156
156
147
147
163
163
154
150
174
174
166
168
184
184
182
173
182
194
204
177
172
135
136
135
124
122
148
150
152
149
152
196
149
151
153
155
168
196
143
149
151
154
155
155
178
196
134
156
152
166
173
175
190
196
190
193
196
139
152
152
169
186
145
150
151
168
185
211
190
148
150
151
168
184
211
198
149
151
152
169
184
197
211
210
186
200
182

Figure 86 Thermal Map of the Orifice-Compensated Hydrostatic Seal (See Case 2, Table XIV)

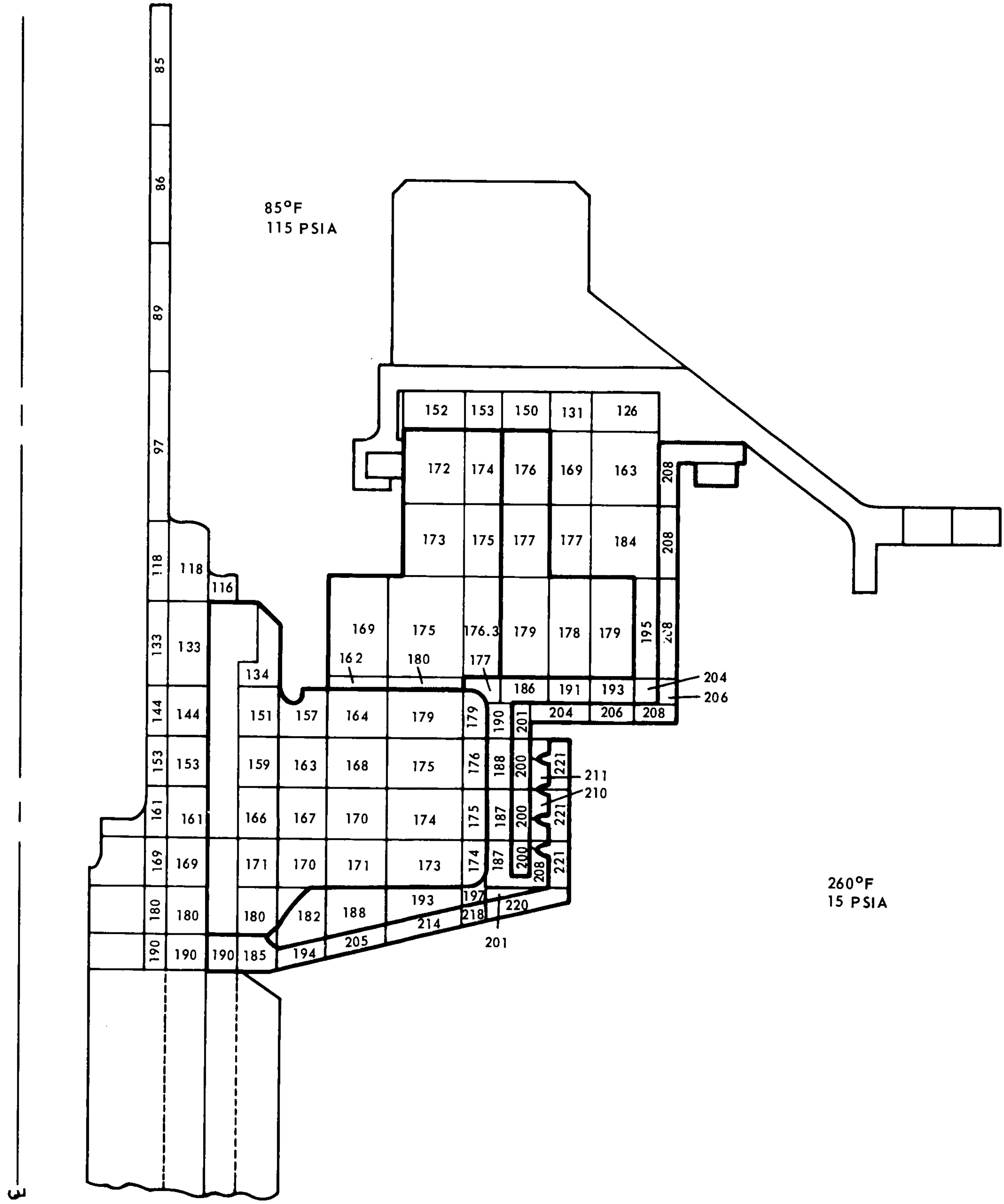
85°F
115 PSIA
85
86
89
97
118
118
116
133
133
134
144
144
151
157
153
153
159
161
161
166
169
169
171
180
180
180
190
190
190
185
152
153
150
131
126
172
174
176
169
163
208
173
175
177
177
184
208
169
162
175
180
176.3
177
179
178
179
195
208
186
191
193
204
206
204
206
208
164
179
179
190
201
168
175
176
188
200
221
211
210
163
167
170
174
175
187
200
221
170
171
173
174
187
200
208
221
182
188
193
214
197
218
220
201
194
205
260°F
15 PSIA
3

Figure 87 Thermal Map of the Orifice-Compensated Hydrostatic Seal (See Case 3, Table XIV)

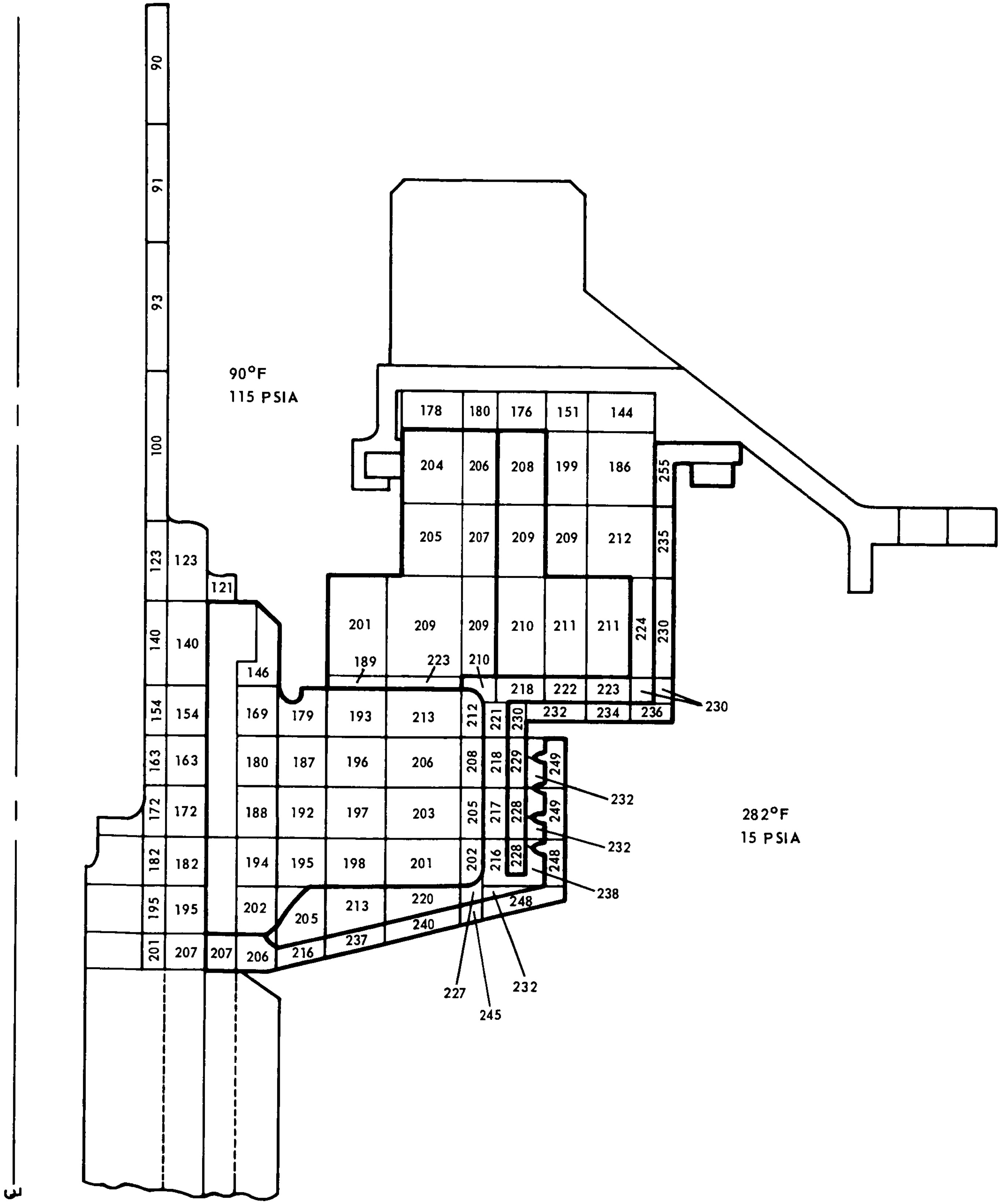
90
91
93
100
90°F
115 PSIA
178
180
176
151
144
204
206
208
199
186
255
205
207
209
209
212
235
123
123
121
201
209
209
210
211
211
224
230
140
140
189
223
210
146
218
222
223
230
154
154
169
179
193
213
212
221
230
232
234
236
163
163
180
187
196
206
208
218
229
249
232
282°F
15 PSIA
172
172
188
192
197
203
205
217
228
249
232
182
182
194
195
198
201
202
216
228
248
238
195
195
202
205
213
220
248
240
201
207
207
206
216
237
227
232
245

Figure 88 Thermal Map of the Orifice-Compensated Hydrostatic Seal (See Case 4, Table XIV)

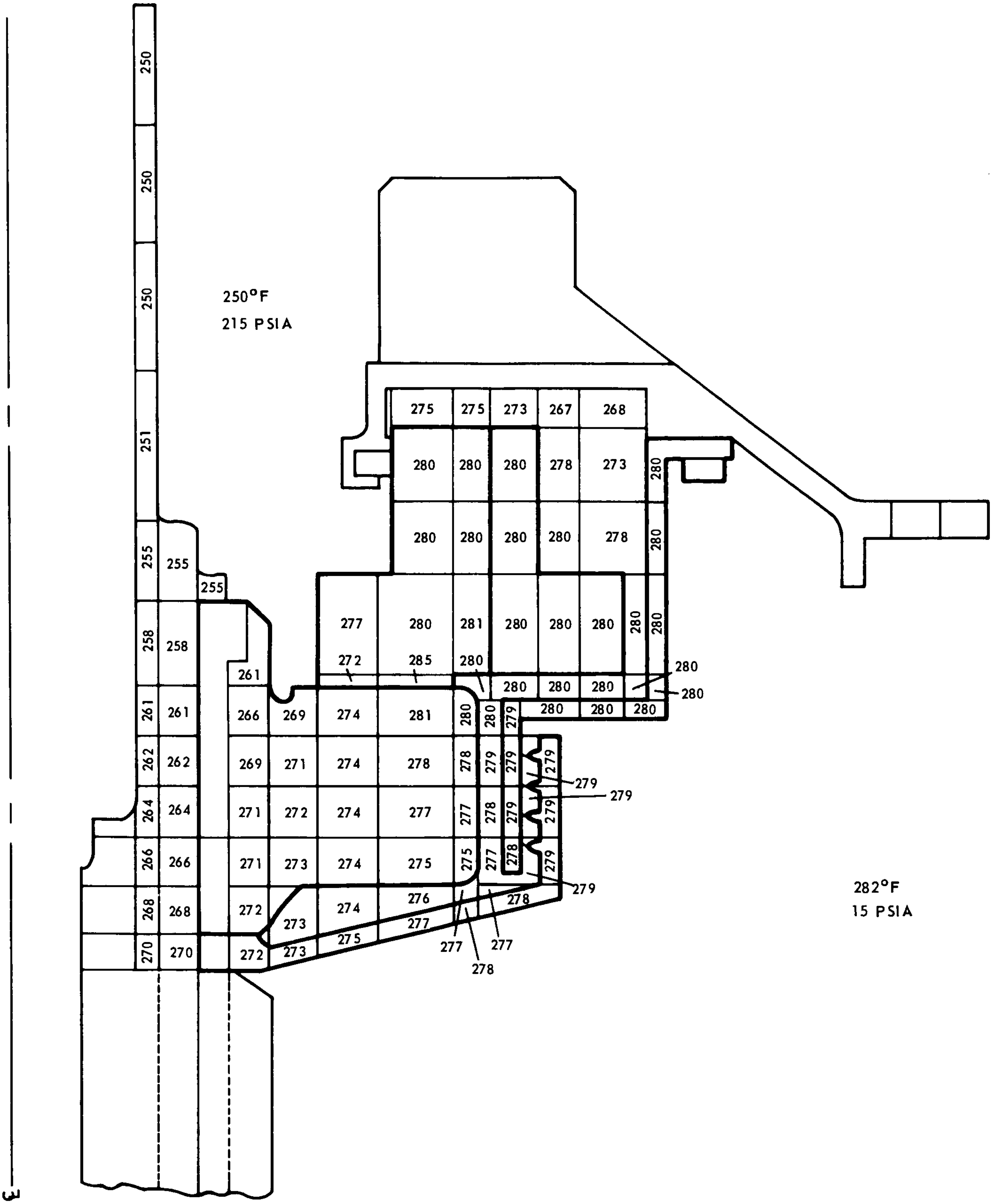
250°F
215 PSIA
282°F
15 PSIA
250
250
250
251
255
255
255
258
258
261
261
261
262
262
264
264
266
266
268
268
270
270
266
269
269
271
271
272
271
273
272
273
272
273
274
274
274
274
274
275
281
278
277
275
276
277
275
277
272
285
280
275
275
273
267
268
280
280
280
278
273
280
280
280
280
278
280
281
280
280
280
280
280
280
280
280
280
280
280
280
280
280
280
278
277
275
280
279
278
277
279
279
279
278
279
279
279
279
279
279
279
278
277
277
278

Figure 89 Thermal Map of the Orifice-Compensated Hydrostatic Seal (See Case 5, Table XIV)

With the net leakage rates, the seal's tilt angle and mean film thickness can be obtained from Figures 79 and 80. Seal tilt angles from gas-film considerations and from thermal considerations are tabulated below:

ΔP	Case	Net Leakage (scfm)	Calculated Operating Film Thickness (mils)	Seal Tilt Angle (Milliradians)	
				Temp. Map	Gas Film
100	4	20.9	0.955	- 0.92	-0.69
200	1	63.0	0.85	- 0.70	-0.52

As shown the agreement between these values is marginal.

b. Indirect Method

The high-temperature test run of the orifice-compensated hydrostatic face seal (shown in Figure 90) indicated that the failure started in the neighborhood of 600 degrees Fahrenheit and procceded to complete failure at 800 degrees Fahrenheit under the test conditions of 200 ft/sec speed and a pressure differential of 100 psi. Using the gas-film equilibrium analysis outlined in the previous section, the curves of seal tilt angle versus film thickness and seal tilt angle versus leakage were found for the conditions of the high-temperature test. The curves are shown in Figures 91 and 92. On the basis of the net leakage (found from Figure 90), the seal tilt angle and operating film thicknesses were found from Figures 91 and 92. The results of these computations are tabulated below:

Temp. (°F)	Net Leakage Rate (scfm)	Angular Rotation (radians)	Film Thickness	
			Operating (In. x 10^3)	Min (In. x 10^3)
70	13.4	-0.000553		
			0.827	0.689
250	7.7	-0.000352		
			0.711	0.623
350	4.2	-0.000042		
			0.518	0.506
500	1.9	+0.00074		
			0.326	0.141

In addition, the minimum film thickness and mean film thickness were obtained as function of temperature, as shown in Figure 93. It is to be noted that the minimum film thickness approaches zero in the neighborhood of 600 degrees Fahrenheit, which initiated the failure at the inner edge of the carbon seal. That the mean film thickness approaches zero in the neighborhood of 800 degrees Fahrenheit indicates that the seal cannot operate successfully as a gas-film-supported seal in this temperature region.

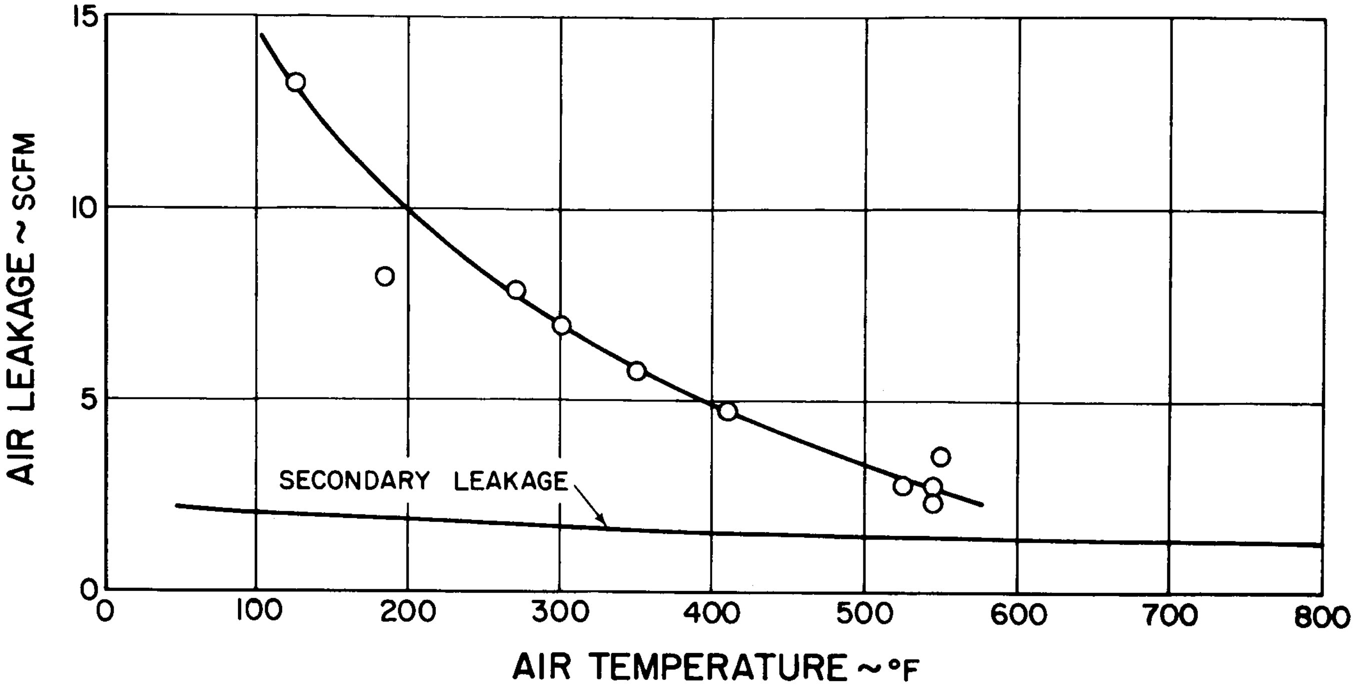

Figure 90 High-Temperature Test of the Orifice-Compensated Hydrostatic Seal

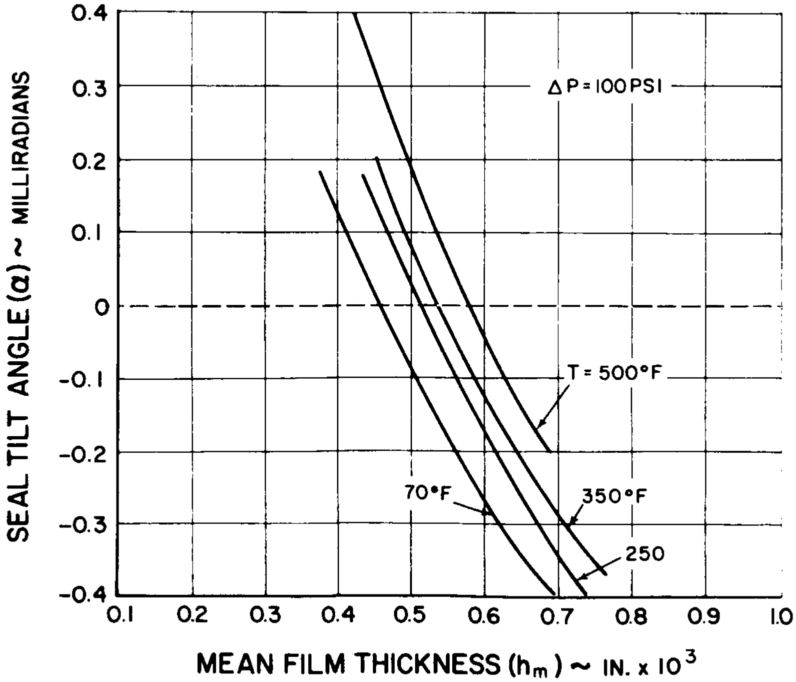

Figure 91 Seal Tilt Angle as a Function of Mean Film Thickness for the High-Temperature Test

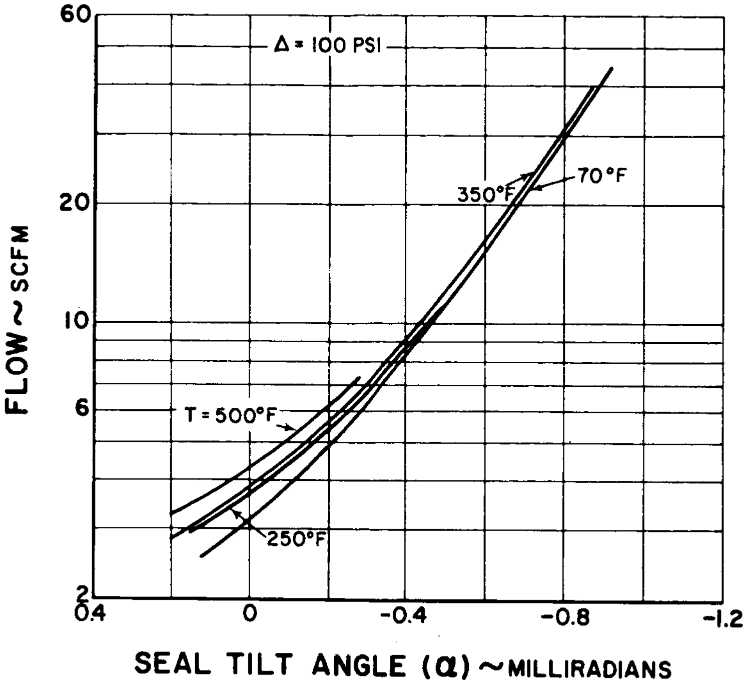

Figure 92 Leakage as a Function of Seal Tilt Angle for the High-Temperature Test

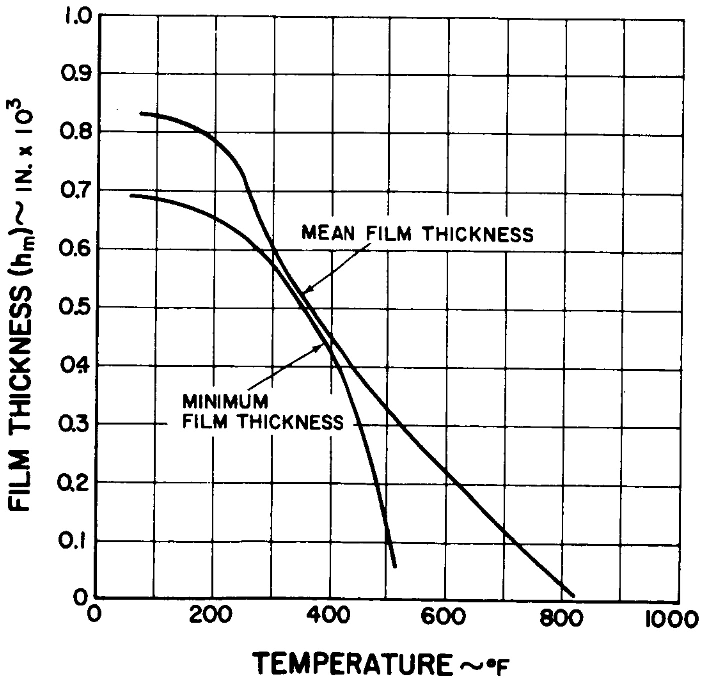

Figure 93 Film Thickness as a Function of Temperature

Finally the film thickness difference from the inner to the outer edge of the carbon seal nose-piece was plotted in Figure 94 as a function of temperature.

It is interesting to note that Δh went through a transition in sign, which implies that the gas film was converging at 100 degrees Fahrenheit, approximately parallel at 365 degrees Fahrenheit, and was diverging at 800 degrees Fahrenheit. The rate of the change of the thermal distortion can be readily seen from the slope of the curve. The higher rate of change of thermal distortion makes it extremely difficult to run a gas seal successfully at high temperature with an uncooled seal plate.

It is recommended that future seal designs incorporate an oil-cooled seal plate or a conforming-seal feature instead of the current rigid design.

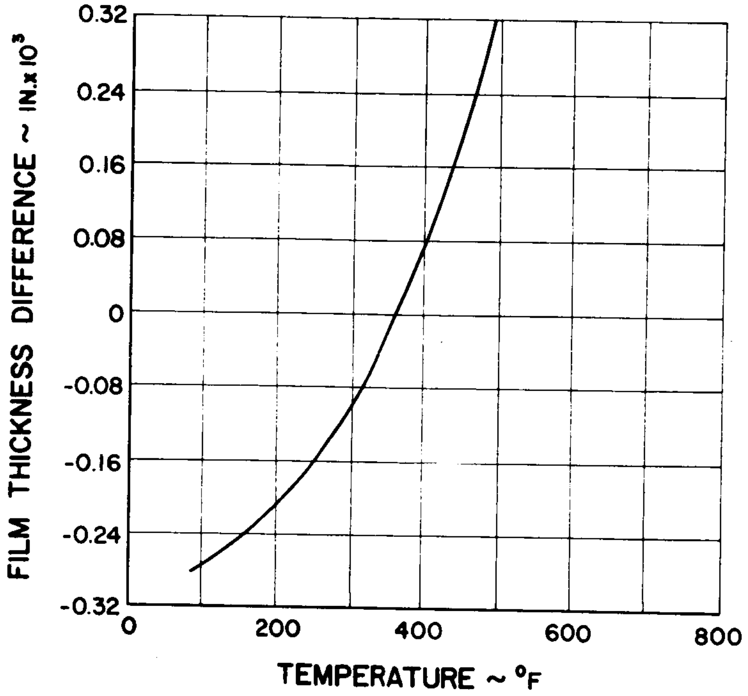

Figure 94 Change in Film Thickness

H. POSTTEST SEAL INTERFACE ANALYSIS OF THE HYBRID SEAL

The failure of Build 9 of the orifice-compensated hydrostatic seal occurred at the inner edge of the carbon seal, leading to the conclusion that the stiffness of the gas film must be increased in that location and that an oil-cooled seal plate should be incorporated in order to reduce thermal distortion. The design of the spiral-groove seal plate, intended to correct these deficiencies, contained three faults which led to the failure of Build 1 of the hybrid seal. First, the locations of the spiral-groove and the feeding slot result in a high imbalance of 84.5 percent at an operating film thickness of 0.3 mil or less, for room-temperature conditions. Second, the seal plate was not manufactured to the specified flatness of one or two helium light-band widths. For this reason, measured leakage rates were two to three times higher than the predicted values and the tracking of the seal assembly was not satisfactory. Third, at the operating speed of 400 ft/sec, the stiffness at the operating film thickness was decreasing instead of increasing, resulting in a complete failure at this condition.

The design of Build 2 of the hybrid seal was based on the analysis of Build 1. Most of the faults in Build 1 were eliminated. Build 2 had an imbalance of 78 percent with an operating film thickness of 0.5 mils or greater and an initial tilt due to pressure loading. The initial tilt was incorporated because of the satisfactory experience with Build 9 of the orifice-compensated hydrostatic face seal. Difficulties with the seal plate hampered the performance of Build 2 as well as Build 1. Because of the limited time remaining in the contract, the intended groove depth was not attained: a variation of 0.2 to 1 mil in groove depth was measured, the seal plate was not lapped flat in the circumferential direction, and flatness in the radial direction was marginal, with a dishing of at least 0.2 milliradian.

Despite these difficulties, the hybrid seal did reach its design limit. Better overall design of seal geometry will probably perform satisfactorily over the full pressure and speed range at 600 degrees Fahrenheit. To operate above this temperature, however, a flexibly mounted seal plate and seal ring will probably have to be used.

1. ANALYTICAL MODEL

The geometry of the hybrid seal is shown in Figure 95. For the purposes of simplification, it was assumed that the radius effect could be neglected, so the analysis assumes that the spiral-groove portion extends to infinity. Specifically, the infinite spiral-groove solution of Whipple (Reference 8) was used.

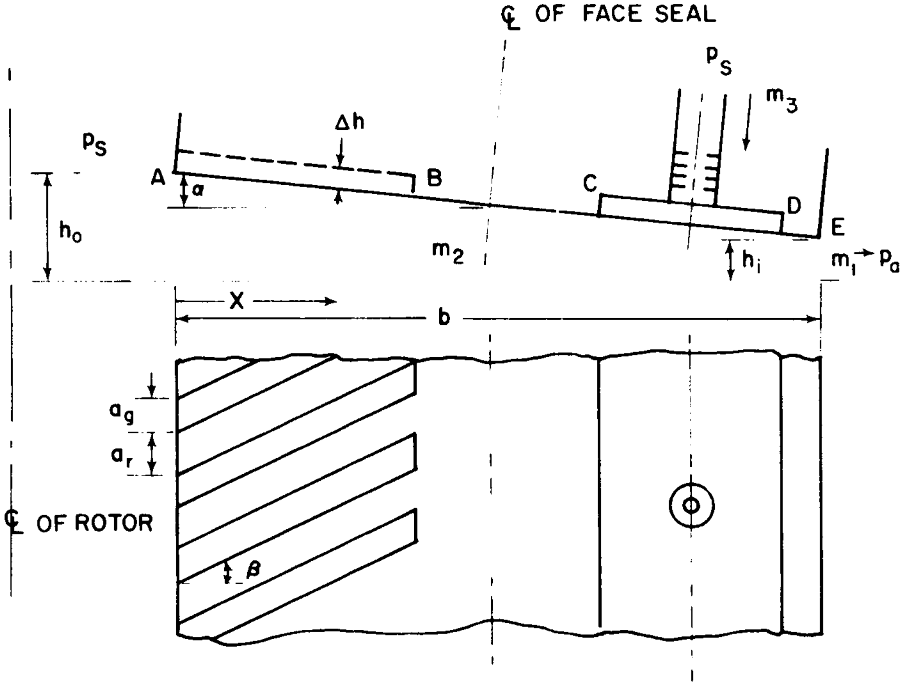
℄ OF FACE SEAL
P_s
P_s
m_3
Δh
A
B
C
D
E
a
h_o
m_2
h_i
$m_1 \rightarrow P_a$
X
b
a_g
a_r
℄ OF ROTOR
β

Figure 95 Geometry of the Hybrid Seal

The equation governing the pressure distribution in the grooved region AB is:

$$\frac{dP}{d\bar{x}} = \Lambda\left(h_m\right) \left(\frac{h_m}{h}\right)^2 K_1(h) - \frac{M_2}{2} \left(\frac{h_m}{h}\right)^3 \frac{K_2(h)}{P} \qquad (8)$$

where

$P = p/p_s$

$\bar{x} = x/b$

$$\Lambda = \frac{6\,\mu\,Ub}{p_s h_m^2}$$

$$K_1 = \frac{(H^3-1)(H-1)\sin 2\beta}{(H^3+1)^2 + 2H^3(A+A^{-1})+(H^3-1)^2 \cos 2\beta}$$

$$K_2 = \frac{2(1+A^{-1})(H^3+A)}{(H^3+1)^2 + 2H^3(A+A^{-1})+(H^3-1)^2 \cos 2\beta}$$

$$M_2 = \frac{24\,\mu\, b}{p_s h_m^3\, \rho_s}\, m_2$$

$H = \frac{\Delta h}{h} + 1$ = groove-to-ridge depth ratio

U = mean speed (in/sec)

μ = viscosity $\left(\frac{\text{lb sec}}{\text{in}^2}\right)$

m_2 = mass flow $\left(\frac{\text{lb sec}}{\text{in}^2}\right)$

ρ_s = density of upstream gas $\left(\frac{\text{lb sec}^2}{\text{in}^4}\right)$

A = groove-to-ridge width ratio = Ag/Ar

β = groove angle

$h_m = \frac{h_o + h_i}{2}$ = mean film thickness

Equation 8 can be expressed alternatively by replacing P^2 with Q giving

$$\frac{dQ}{d\bar{x}} = 2\,\Lambda\left(\frac{h_m}{h}\right)^2 K_1\,(h)\,\sqrt{Q} - M_2\left(\frac{h_m}{h}\right)^3 K_2\,(h) \qquad (9)$$

When the groove action is weak, Equation 9 is preferable, because the non-linear portion is contained in the less dominating hydrodynamic term. If the groove action is strong, Equation 8 is more useful, since the hydrodynamic term now becomes dominating.

Approximating Equations 8 and 9 by finite difference equations for each grid point, one obtains

$$P_j = P_{j-1} + f_j - M_2\,g_j \qquad (10)$$

$$Q_j = Q_{j-1} + f'_j - M_2 g'_j \qquad (11)$$

where

$$f_j = \Delta\,\bar{x}\left[\Lambda\left(\frac{h_m}{h_{j-1/2}}\right)^2 K_{1,\,j-1/2}\right]$$

for Equation 10,

$$f'_j = \Delta\,\bar{x}\left[2\,\Lambda\left(\frac{h_m}{h_{j-1/2}}\right)^2 K_{1,\,j-1/2}\;\sqrt{Q_{j-1/2}}\right] \qquad (12)$$

for Equation 11,

$$g_j = \Delta\bar{x}\left[\frac{1}{2}\left(\frac{h_m}{h_{j-1/2}}\right)^3 K_{2,\,j-1/2}\;\frac{1}{P_{j-1/2}}\right] \qquad (13)$$

for Equation 10, and

$$g'_j = \Delta \bar{x} \left[\left(\frac{h_m}{h_{j-1/2}} \right)^3 \quad K_{2,j-1/2} \right]$$

for Equation 11.

In the land region BD, Equations 10 and 11 are directly applicable if $K_1 = 0$ and $K_2 = 1$. Likewise, in region DE, Equations 10 and 11 are applicable if $K_1 = 0$, $K_2 = 1$ and M_2 is replaced by M_1, where

$$M_1 = \left(\frac{24 \mu b}{p_s h^3_m \rho_s} \right) m_1$$

In Equations 10 and 11, f_j, f'_j, g_j, and g'_j are considered to be known quantities. The nonlinearity in Equations 12 or 13 is solved by iteration.

Identifying the stations at the edge C of the feeding slot by j = JC, and adding Equations 10 or 11 from j = 2 to j = JC, one obtains

$$M_2 = \frac{\sum_{j=2}^{JC} f_j - (P_{JC} - P_1)}{\sum_{j=2}^{JC} g_j}$$

for Equation 10, and

$$M_2 = \frac{\sum_{j=2}^{JC} f'_j - (Q_{JC} - Q_1)}{\sum_{j=2}^{JC} g'_j}$$

for Equation 11. Likewise, identifying the stations at the edge D of the feeding slot by j = JD, and adding Equations 10 or 11 from j = JD to the last station j = JE, yields

$$M_1 = \frac{\sum_{j=JD}^{JE} f_j - (P_{JE} - P_{JC})}{\sum_{j=JD}^{JE} g_j}$$

for Equation 10, and

$$M_1 = \frac{\sum_{j=JD}^{JE} f'_j - (Q_{JE} - Q_{JC})}{\sum_{j=JD}^{JE} g'_j}$$

for Equation 11. The flow through the orifice is governed by

$$m_3 = \frac{\pi a^2}{RT_s} p_s G \left[(p_G/p_s)\right] \tag{14}$$

$$\text{where } G\left[(p_G/p_s)\right] = C_D \sqrt{\frac{2k}{k-1}} (p_G/p_s)^{1/k}\left[1-(p_G/p_s)^{(k-1)/k}\right]^{1/2}$$

$$\text{for } p_G/p_s > \left(\frac{2}{k+1}\right)^{k/(k-1)}$$

$$= C_D \sqrt{\frac{2k}{k+1}} \left(\frac{2}{k+1}\right)^{1/(k-1)}$$

$$\text{for } p_G/p_s \leq \left(\frac{2}{k+1}\right)^{k/(k-1)}$$

C_D is given with an approximate polynominal formula in Figure 96. It is to be noted that the values used here are smaller than the values presented for the orifice-compensated hydrostatic gas seal, since it was assumed that the orifice contour was diverging, instead of converging.

Matching the flow between the orifice and the gas film requires

$$m_1 = m_2 + m_3 \tag{15}$$

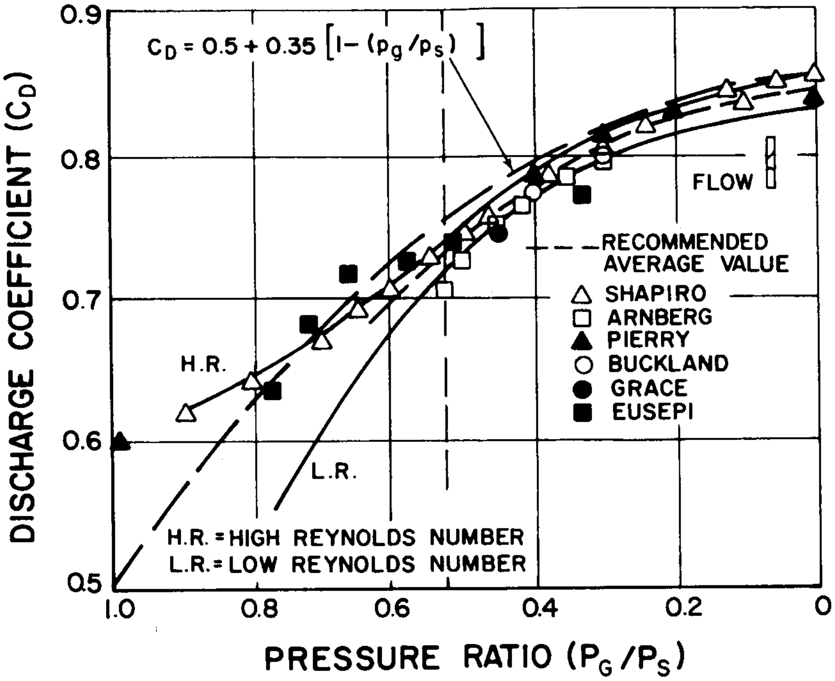

Figure 96 Discharge Coefficients of Single Orifice

Substituting Equation 14 into Equation 15 and by virtue of the definition of M_1 and M_2, one obtains,

$$M_1 = H_m \; G \left[(p_G/p_s) \right] + M_2 \tag{16}$$

where
$$H_m = \frac{24\,\mu\, b \sqrt{RT_s} \;\; \pi a^2}{\ell h_m^3 \, p_s \sqrt{M + \delta^2}} = \frac{12\,\mu\, N a^2 \;\; \sqrt{RT_s}}{\sqrt{M+\delta^2} \;\; p_s h_m^3} \;\; \frac{b}{R_m}$$
$$= \Lambda_s \; \frac{b}{R_m}$$

$N = 2\pi R_m/\ell$ = Number of feeding holes

ℓ = Distance between two feeding holes

$R_m = (R_o + R_i)/2$ = Mean radius

$$\Lambda_s = \text{Restrictor Parameter} = \frac{12\,\mu\, N a^2 \;\; \sqrt{RT_s}}{\sqrt{M + \delta^2} \;\; p_s h_m^3}$$

M = Number of orifices in series per feeding hole

$\delta = a^2/d\,h_m$

a = orifice radius

d = Equivalent diameter of the recessed area per feeding hole

The implication of the restrictor parameter is the same as was discussed in the section on the orifice-compensated hydrostatic seal.

With the values of M_1 and M_2, P_{JC} and Q_{JC}, can be found numerically from Equation 16 by the secant method. Between iterations, the pressure distributions are corrected, i.e. the values of g_j or f'_j are adjusted respectively during each iteration.

Once Q_{JC} and P_{JC} and the pressure at each station are found, the load and center of pressure can be determined as follows with the aid of Simpson's integration formula.

$$\overline{W} = \frac{W}{b\Delta p} = \left[\int_0^1 P d\bar{x} - p_a/p_s \right] \Big/ (1 - p_a/p_s)$$

$$\bar{x}_c = \left[\int_o^1 P\bar{x}d\bar{x} - \frac{1}{2}(p_a/p_s) \right] \Big/ \left[\overline{W}\ (1 - p_a/p_s) \right]$$

To take into account the end leakage of the groove, the results obtained by Muijderman (Reference 9) have been employed. According to his findings, the portion of the ineffective groove depth at the entrance is approximately equal to one half of the width of the groove.

The dishing and crowning of the seal face are incorporated by assuming that the film thickness is a linear function of tilting angle. Because the infinite solution was used in the present analysis, film thickness variation is independent of the radius.

2. ANALYSIS OF BUILD 1

The groove depth of Build 1 was equal to 0.3 mils on the average, yet it varies from 0.25 to 0.43 mils. Because of the higher measured leakage rates, the design data for a groove depth of 0.6 mils is also given. The linear imbalance for this seal design is

$$U_\ell = \frac{\ell_B}{\ell_F} = \frac{0.333}{0.394} = 0.845$$

while the area unbalance is

$$U_A = \frac{A_B}{A_F} = (3.502^2 - 3.169^2)/(3.563^2 - 3.169^2) = 0.8375$$

The linear imbalance is used here for correlation with the analytical results because the analytical model used assumed a spiral-grooved infinite strip.

Ambient-temperature test results for Build 1 are given in Figure 97. The static leakage rate was taken from the run-in value, and the dynamic leakage rates at 200 ft/sec and 300 ft/sec were taken with an oil temperature of 250 degrees Fahrenheit.

Curves of the dimensionless load versus mean film thickness are presented in Figures 98 through 100 for various speeds, groove depths, and pressure differentials. The corresponding leakage curves are presented in Figures 101 through 103. These analytical results are presented for groove depths of 0.6 and 0.3 mil to provide upper and lower bounds for the seal assembly used. Analysis of the static results is presented for a groove depth of 0.6 mil only, because the effect of the grooves is very small at static conditions.

Under static conditions at a pressure differential of 100 psi, the operating mean film thickness is 0.3 mil for a parallel film ($\alpha = 0$) and 0.35 mil for a converging film ($\alpha = -0.2$ milliradian) at the equilibrium position (see Figure 98). The corresponding leakages (found from Figure 101) are 2.1 and 3.0 scfm, respectively. If the seal plate runout of approximately 0.1 mil is accounted for, the leakages become approximately 6.5 scfm, which is in fair agreement with the experimental value of 7.4 scfm.

At 200 ft/sec and a pressure differential of 100 psig, the net measured leakage rates were equal to 11 scfm, from Figure 97. The operating film thickness is fairly close to the static value for groove depth, 0.3 mil. The predicted leakage rates with the adjusted film thickness are approximately equal to 4.5 scfm. The large difference can only be attributed to the dynamic effects of the seal plate's runout. Because of the poor correlation on the leakage measurements, no attempt at calculation of the seal's tilt angle was conducted for this particular build.

In order to find out the cause of this failure, analytical results for a parallel film were obtained for a velocity of 400 ft/sec with a pressure differential equal to 100 and 200 psig. A study of geometrical parameters was also conducted to find out whether improvements can be made in order to have the seal operating successfully at 400 ft/sec.

Curves of the dimensionless load versus mean film thickness for several variations in the spiral-groove configuration are shown in Figures 104 and 105. The corresponding stiffness curves are shown in Figures 106 and 107. Three sets of geometrical variation were considered: the variation of groove depth, the variation of groove-to-ridge width ratio, and the variation of the feeding

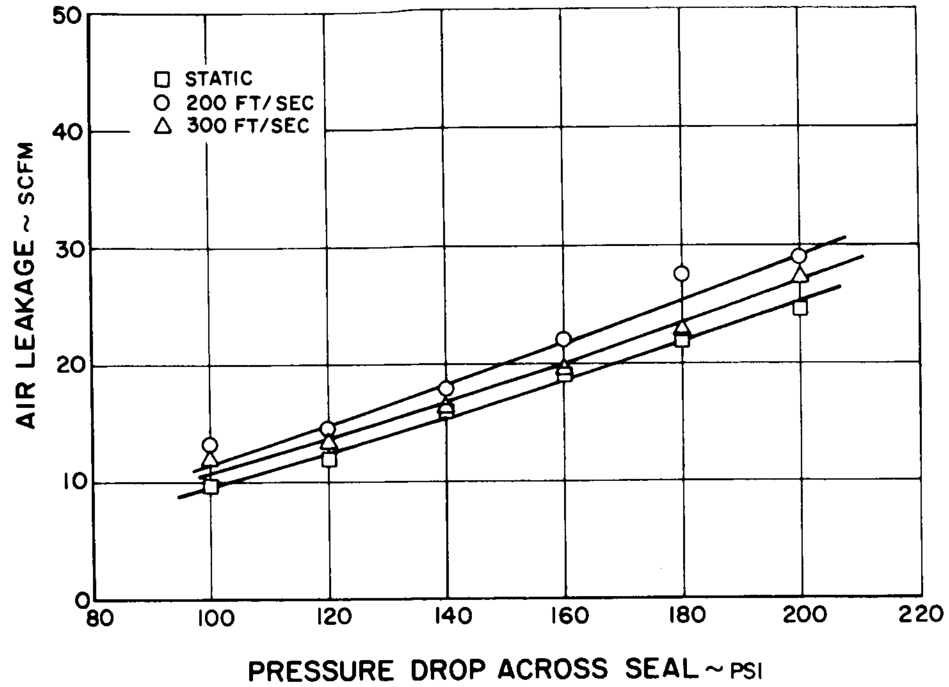

Figure 97 Test Results for Build 1 of the Hybrid Seal with Ambient Air

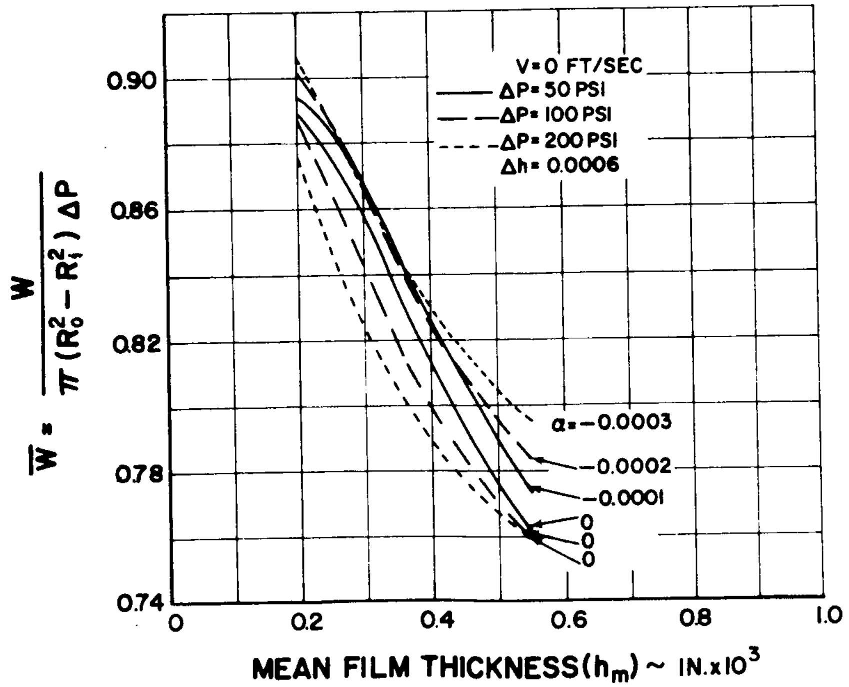

Figure 98 Analytical Prediction of Dimensionless Load for a Groove Depth of 0.6 Mils at Static Conditions

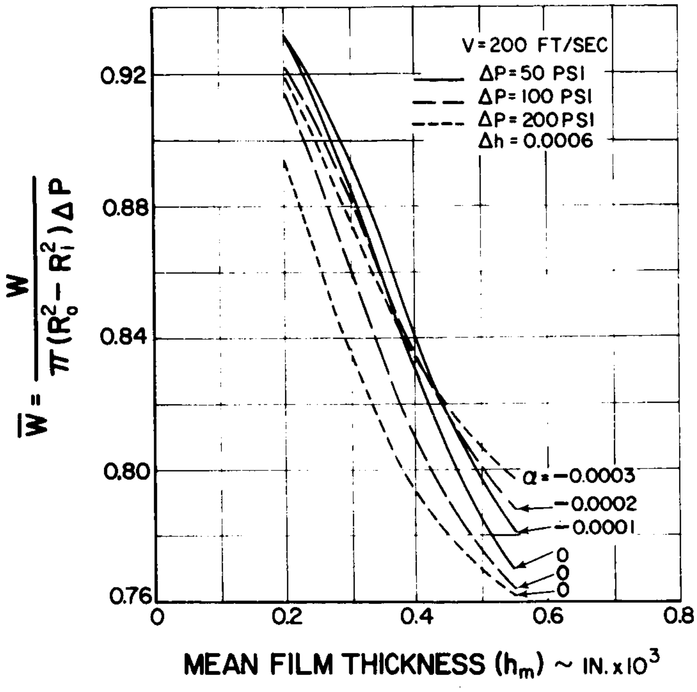

Figure 99 Analytical Prediction of Dimensionless Load for a Groove Depth of 0.6 Mils and a Speed of 200 ft/sec

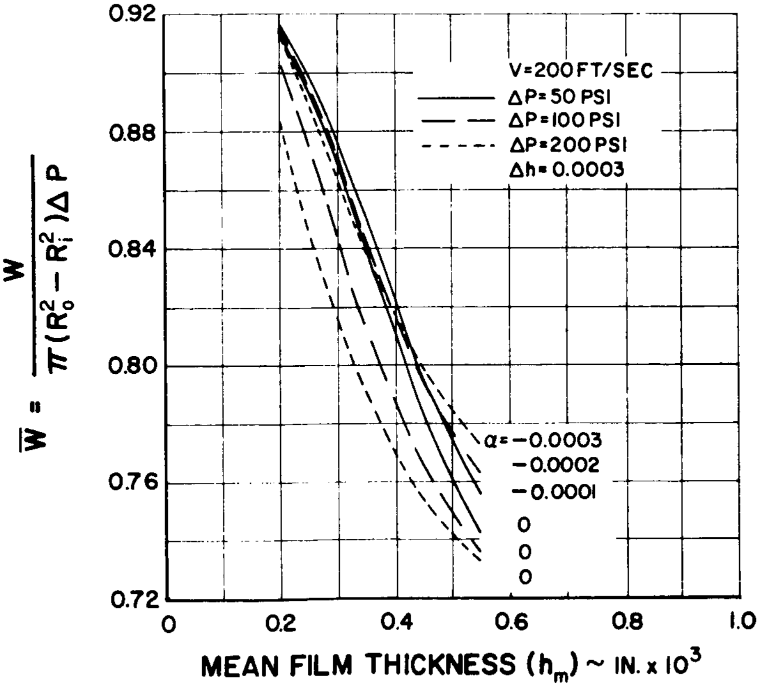

Figure 100 Analytical Prediction of Dimensionless Load for a Groove Depth of 0.3 Mils and a Speed of 200 ft/sec

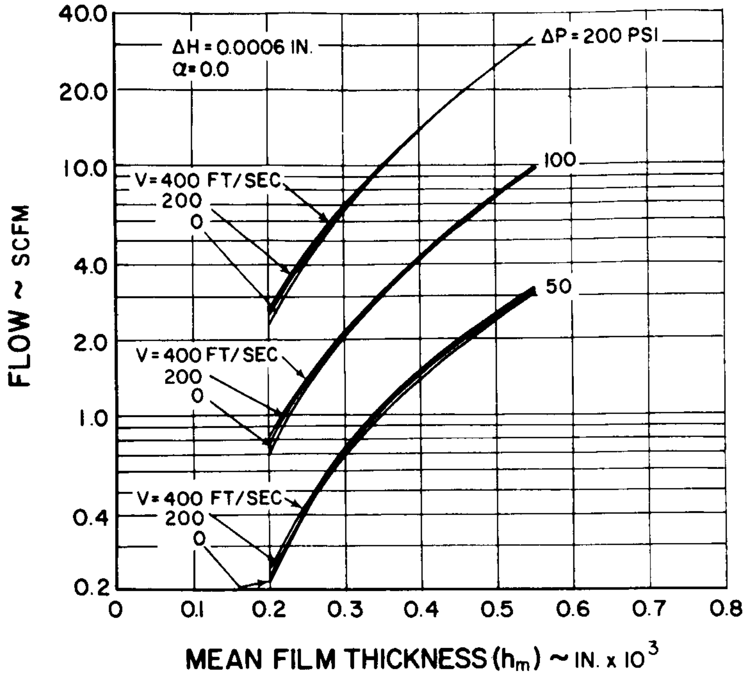

Figure 101 Analytical Prediction of Static Leakage with a Groove Depth of 0.6 Mils

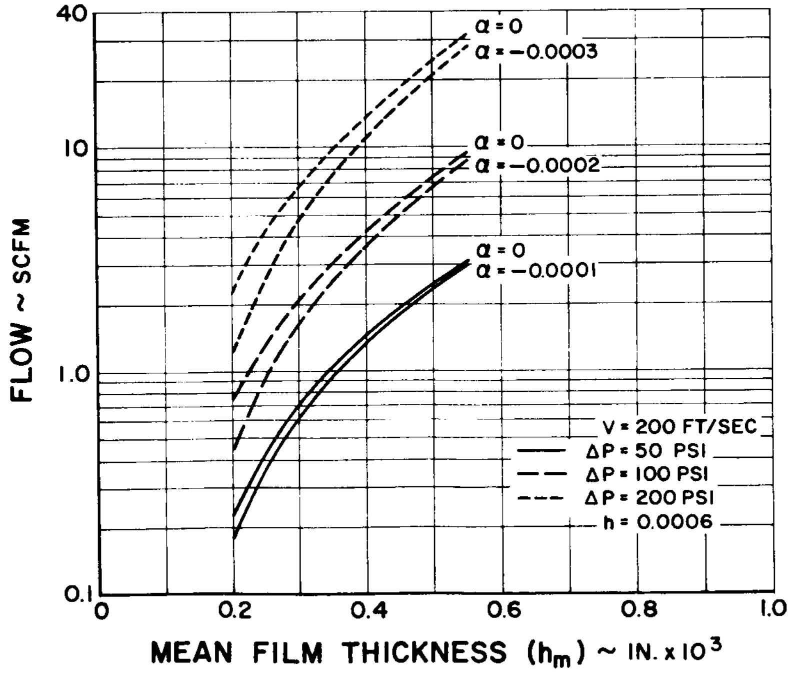

Figure 102 Analytical Prediction of Leakage with a Groove Depth of 0.6 Mils and a Speed of 200 ft/sec

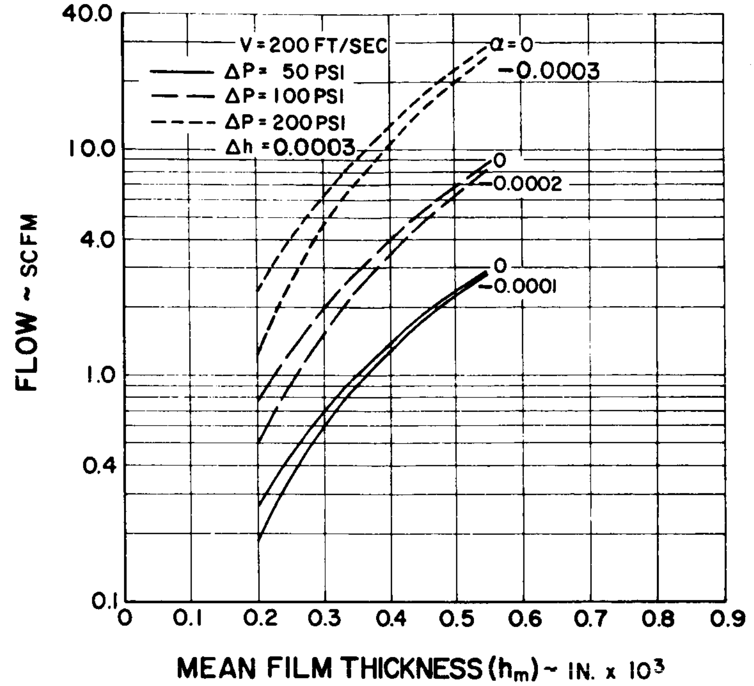

Figure 103 Analytical Prediction of Leakage with a Groove Depth of 0.3 Mils and a Speed of 200 ft/sec

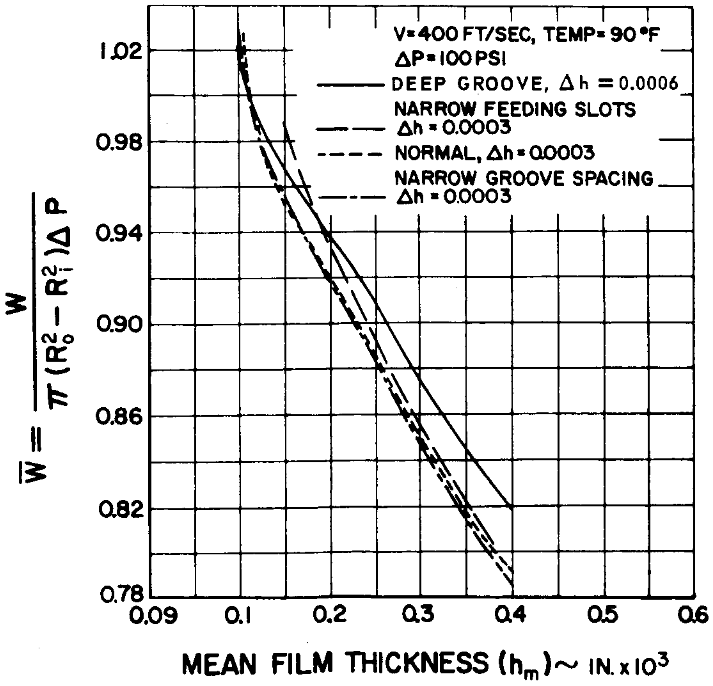

Figure 104 Dimensionless Load for Three Spiral-Groove Configurations at a Pressure Differential of 100 psi

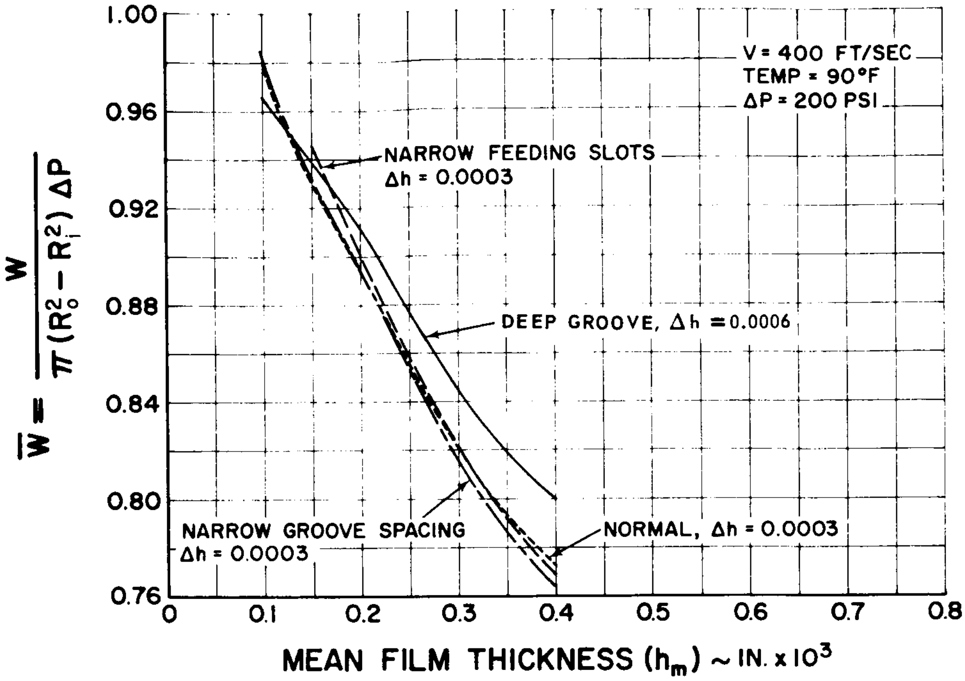

Figure 105 Dimensionless Load for Three Spiral-Groove Configurations at a Pressure Differential of 200 psi

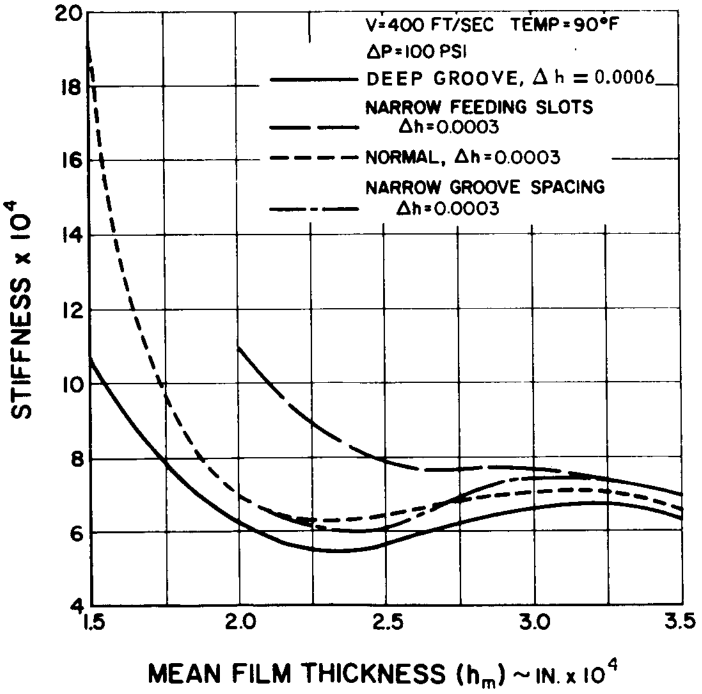

Figure 106 Film Stiffness for Three Spiral-Groove Configurations at a Pressure Differential of 100 psi

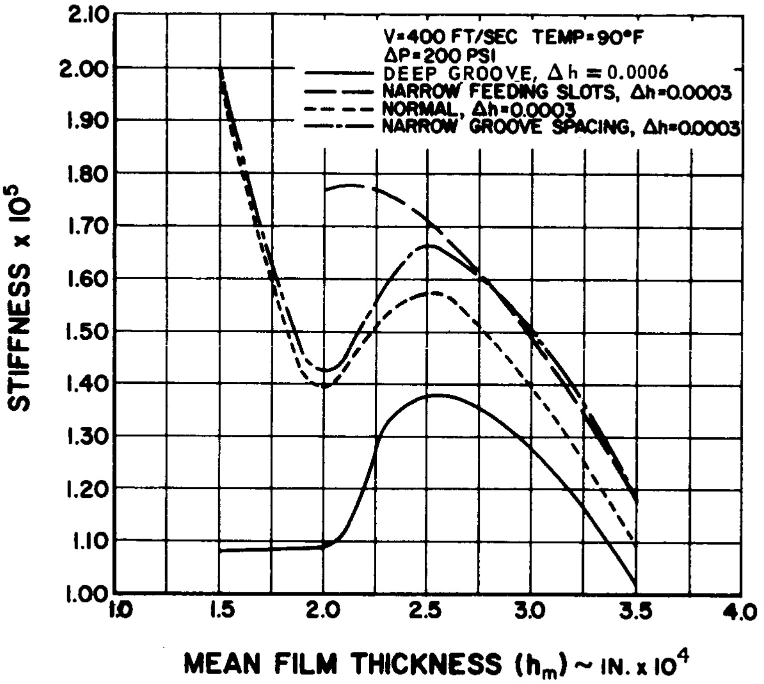

Figure 107 Film Stiffness of Three Spiral-Groove Configurations at a Pressure Differential of 200 psi

slot recess. The amount of variation of each geometrical parameter from the original design is tabulated below:

	Groove Depth Δh inch	Groove to Ridge With Ratio $A=Ag/Ar$	Width of Feeding Slots (inches)	Inner Radius of Feeding Slot (inches)
Normal	0.0003	3.0	0.094	3.369
Deep Groove	0.0006	3.0	0.094	3.369
Narrow Groove Spacing	0.0003	1.9	0.094	3.369
Narrow Feeding Slots	0.0003	3.0	0.047	3.416

By increasing the depth of the groove, a higher load-carrying capacity results, and the stiffness is slightly decreased. If the groove-to-ridge width ratio is decreased from 3.0 to the conventional optimum value of 1.9, no appreciable difference is observed for the load-carrying capacity or for the stiffness. The shortening of the width of the feeding slots provided a larger seal dam area, resulting in a high loading-carrying capacity and better stiffness characteristics.

The failure of Build 1 at 400 ft/sec and a pressure differential of 100 psi is primarily due to the stiffness characteristics of the present seal-geometry design. It is to be noted that the operating film thickness at this condition is equal to 0.31 mil. The stiffness for this design starts to decrease instead of increasing. For film thicknesses less than 0.3 mil, the load-carrying capacity and the stiffness will decrease. The analysis used here did not account for this effect.

A loss of stiffness at a pressure differential of 200 psig at the operating film thickness was also observed for this design, and the narrow feeding-slot design does show a positive increasing stiffness at the operating film thickness. If this configuration is to be pursued further, then the narrow feeding-slot design would be recommended.

3. ANALYSIS OF BUILD 2

Build 2 of the hybrid seal used the basic designs of the seal plate from Build 1 and the seal ring from Build 9 of the orifice-compensated hydrostatic seal. There were two major alterations in the design, however. In the seal plate the grooves were deepened from 0.3 mil to an average depth of 0.6 mil. Because of time limitations, the groove depth varied between 0.2 and 1.0 mil in Build 2. In the seal ring, the outer dam was shortened to gain better stiffness and to maintain a film thickness of 0.5 mil, resulting in an imbalance of 78 percent. Analytical predictions of dimensionless load and leakage are shown in Figures 108 through 119. They were derived by the same methods as were employed for the orifice-compensated hydrostatic seal.

As shown in Figures 108 through 111, with air at 90 degrees Fahrenheit, the maximum film stiffness for the configuration with given groove depth occurred at 0.45 mil for the static condition and shifted to 0.55 mil at 400 ft/sec. The converging film improves the situation, which implies that the maximum stiffness occurred at a smaller film thickness. A diverging film gives the reverse effect, which promotes early failure if not corrected. Increasing the air temperature improves the stiffness characteristics in general, but only a small amount. This design's inherent weakness in stiffness characteristics promoted the failure of Build 2 during a dynamic test at 600 degrees Fahrenheit.

The same procedures were used to estimate the operating film thickness and seal tilt angle as were used for the orifice-compensated hydrostatic seal. Curves of mean film thickness and leakage for operation at temperatures of 90 and 400 degrees Fahrenheit are shown in Figures 120 through 124. The data for the tests at 90 and 400 degrees Fahrenheit are plotted in Figures 125 and 126, respectively. The data for the test at 400 degrees Fahrenheit were modified by subtracting the difference between the two room-temperature static calibrations in order to minimize the effects of the changes which occurred within the seal during the testing. It should be noted that the seal's face had a larger variation in flatness during the high-temperature test than during the initial room-temperature test. This discrepancy may be accredited to thermal creep or to possible rubbing at low-pressure high-speed conditions prior to the final high-temperature test.

Matching the measured leakage ratio in Figures 125 and 126 to the analytical results of Figures 122 through 124, we have the operating film thicknesses and tilt angles shown in Tables XVI and XVII. Results of room-temperature testing (Table XVI) demonstrate three significant points:

- The operating mean film thickness is equal to 0.5 mil with an approximately parallel film for moderate and high pressure gradients.

- At moderate and high pressure gradients, the operating mean film thickness is equal to 0.625 mil at sliding speeds of 200 to 400 ft/sec. At those speeds, the film is converging at an angle of 0.2 milliradian (for 200 ft/sec) to 0.15 milliradian (for 400 ft/sec).

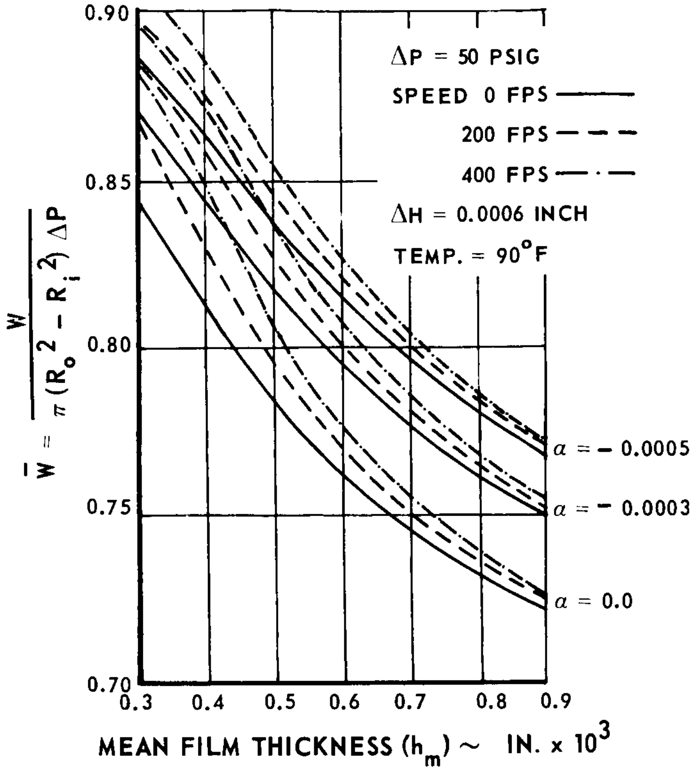

Figure 108 Analytical Prediction of Dimensionless Load for a Pressure Differential of 50 psi and a Temperature of 90 Degrees Fahrenheit

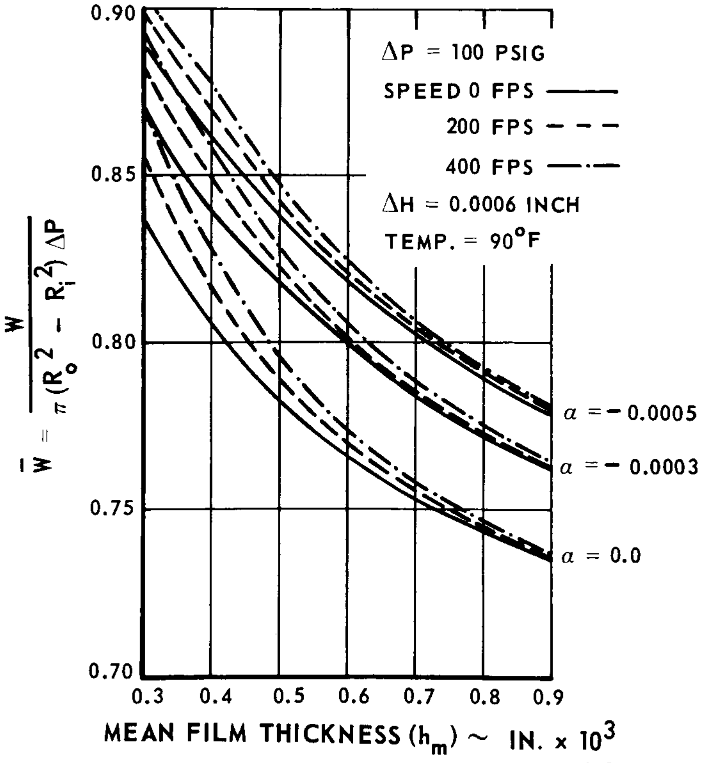

Figure 109 Analytical Prediction of Dimensionless Load for a Pressure Differential of 100 psi and a Temperature of 90 Degrees Fahrenheit

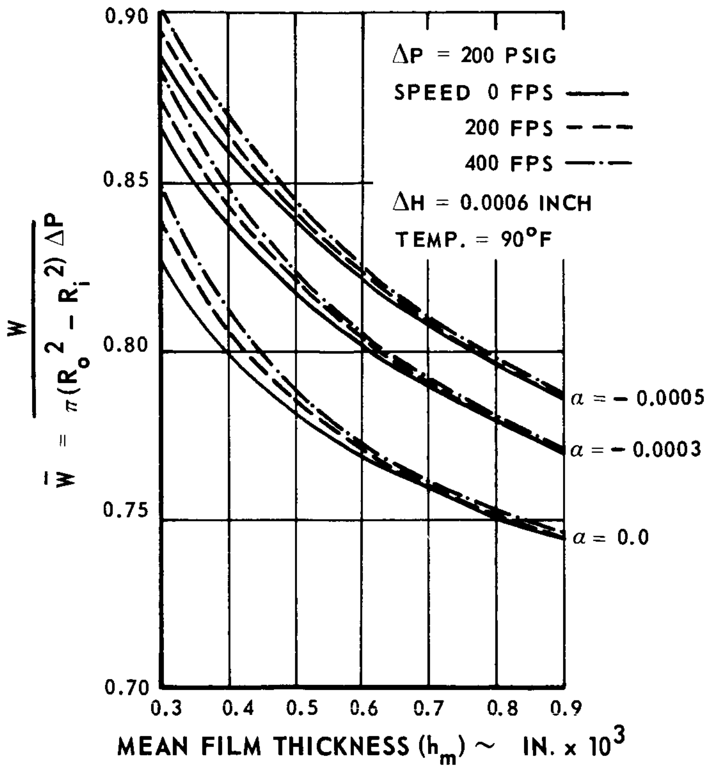

Figure 110 Analytical Prediction of Dimensionless Load for a Pressure Differential of 200 psi and a Temperature of 90 Degrees Fahrenheit

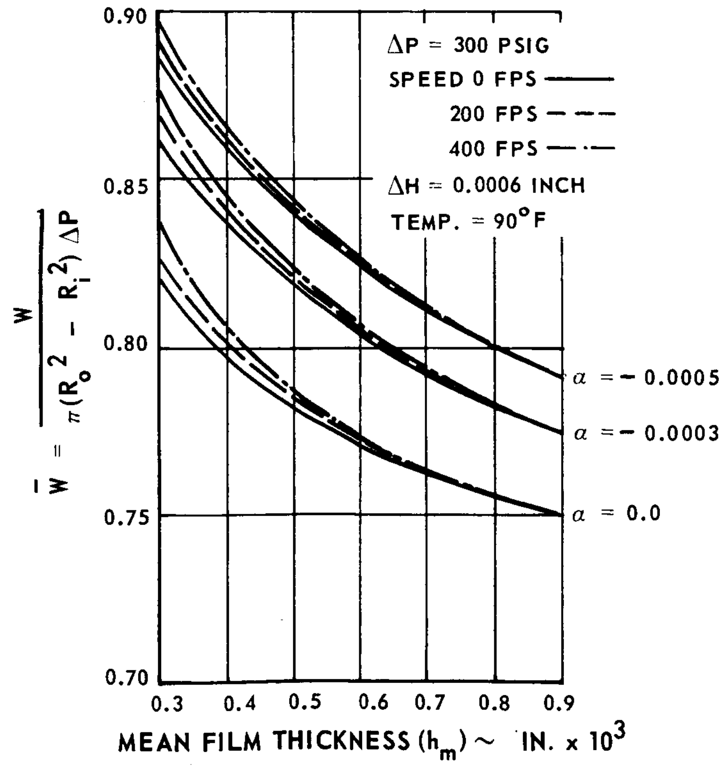

Figure 111 Analytical Prediction of Dimensionless Load for a Pressure Differential of 300 psi and a Temperature of 90 Degrees Fahrenheit

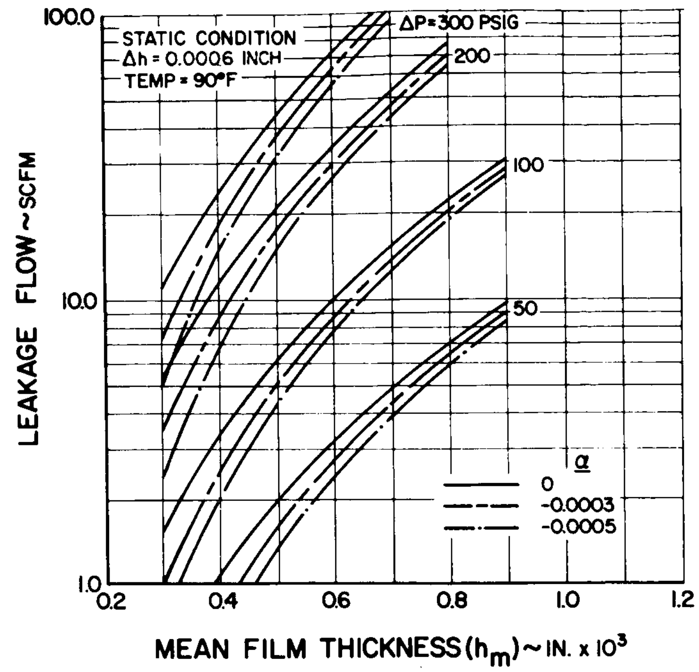

Figure 112 Analytical Prediction of Leakage at Static Conditions with a Temperature of 90 Degrees Fahrenheit

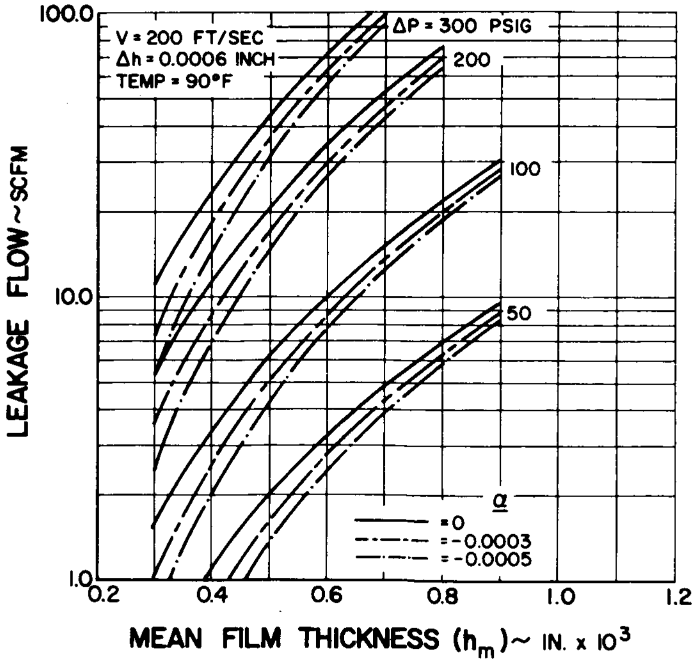

Figure 113 Analytical Prediction of Leakage at a Speed of 200 ft/sec and a Temperature of 90 Degrees Fahrenheit

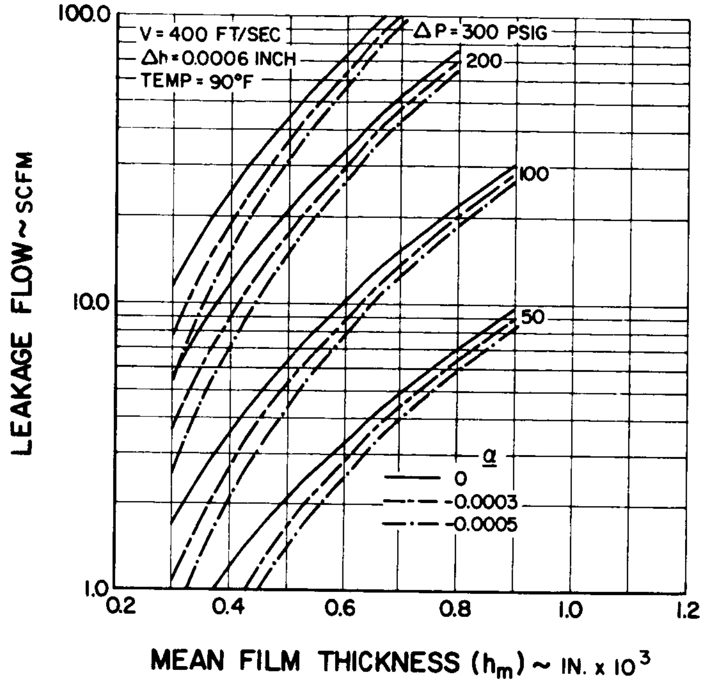

Figure 114 Analytical Prediction of Leakage at a Speed of 400 ft/sec and a Temperature of 90 Degrees Fahrenheit

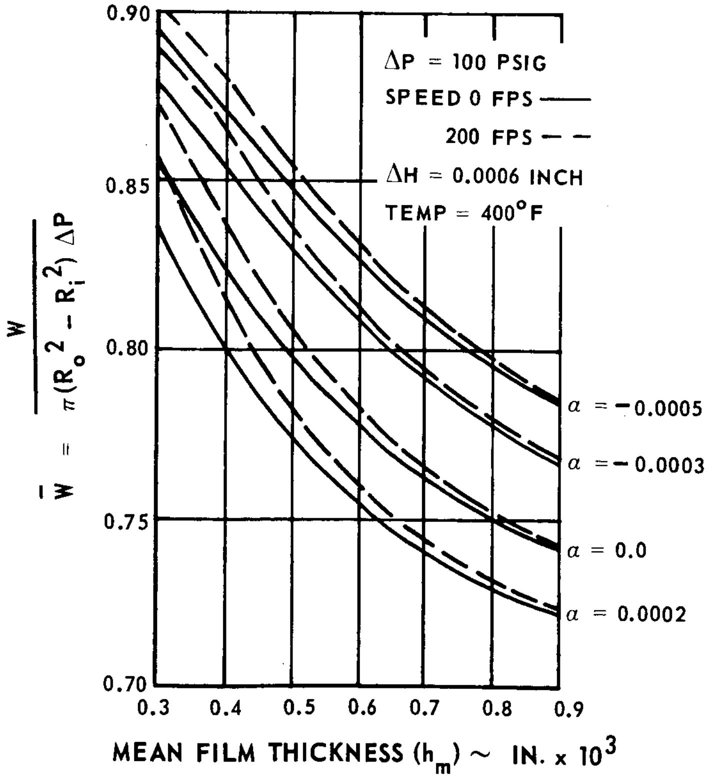

Figure 115 Analytical Prediction of Dimensionless Load at a Pressure Differential of 100 psi and a Temperature of 400 Degrees Fahrenheit

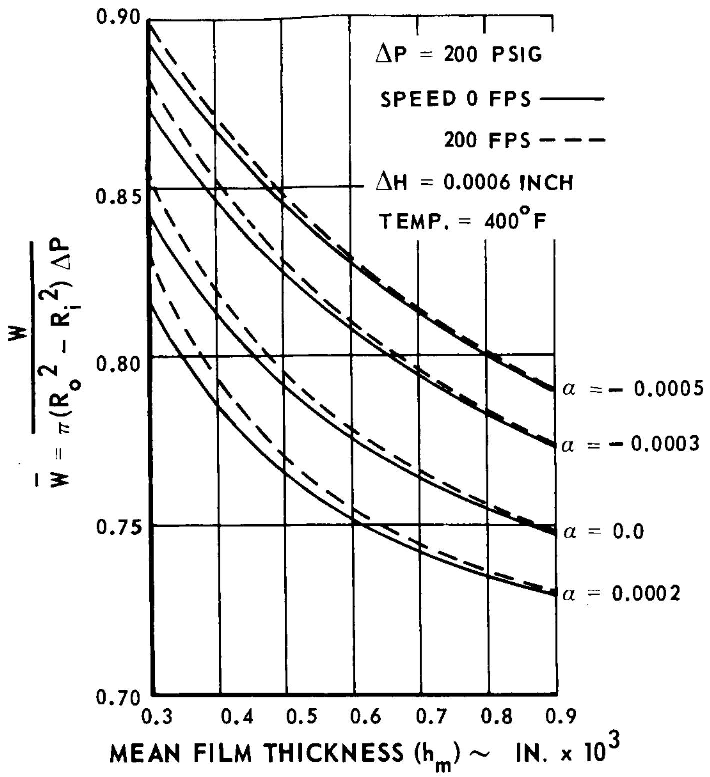

Figure 116 Analytical Prediction of Dimensionless Load at a Pressure Differential of 200 psi and a Temperature of 400 Degrees Fahrenheit

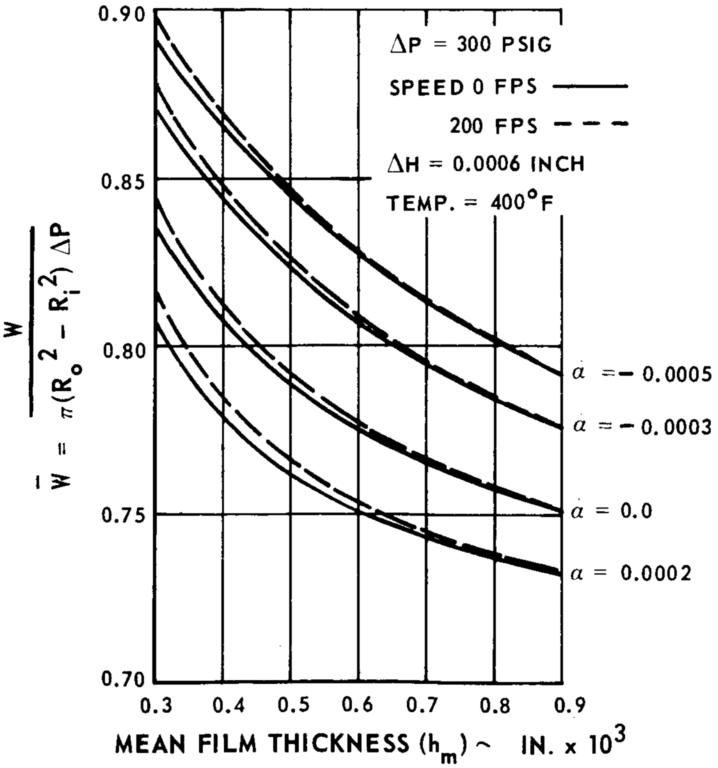

Figure 117 Analytical Prediction of Dimensionless Load at a Pressure Differential of 300 psi and a Temperature of 400 Degrees Fahrenheit

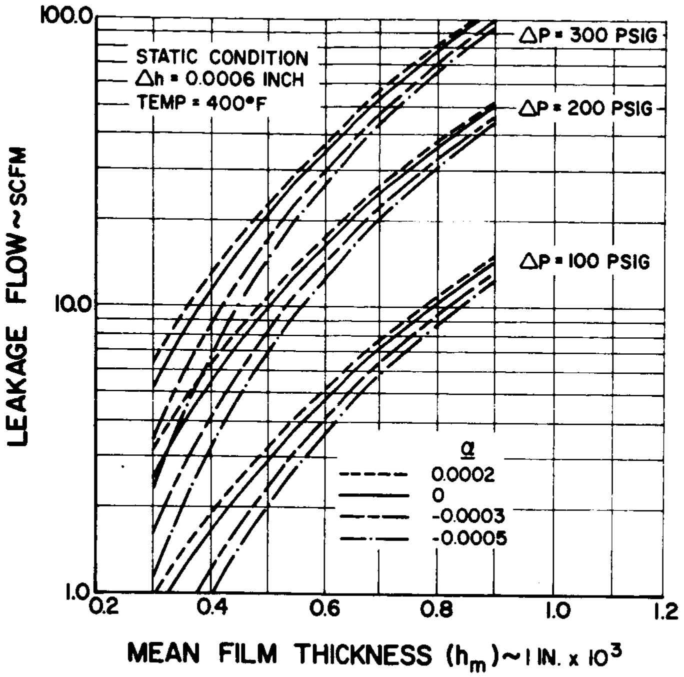

Figure 118 Analytical Prediction of Leakage at Static Conditions with a Temperature of 400 Degrees Fahrenheit

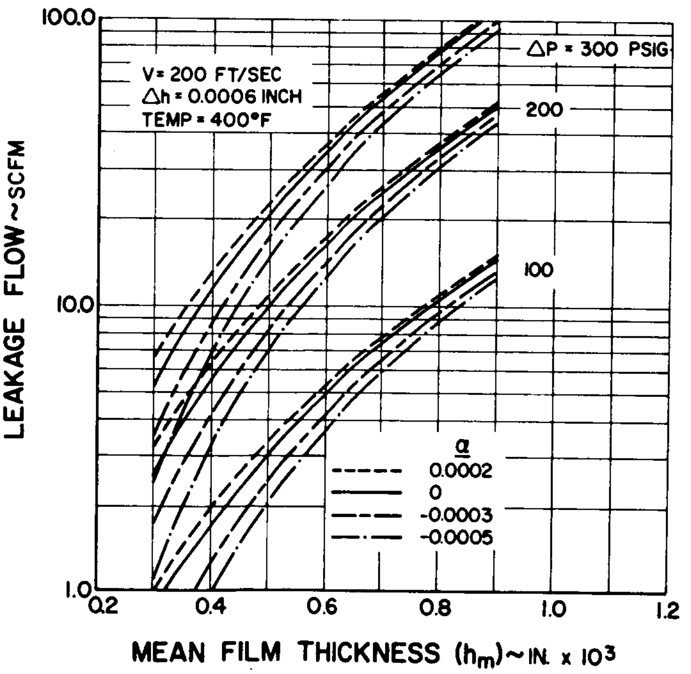

Figure 119 Analytical Prediction of Leakage at a Speed of 200 ft/sec and a Temperature of 400 Degrees Fahrenheit

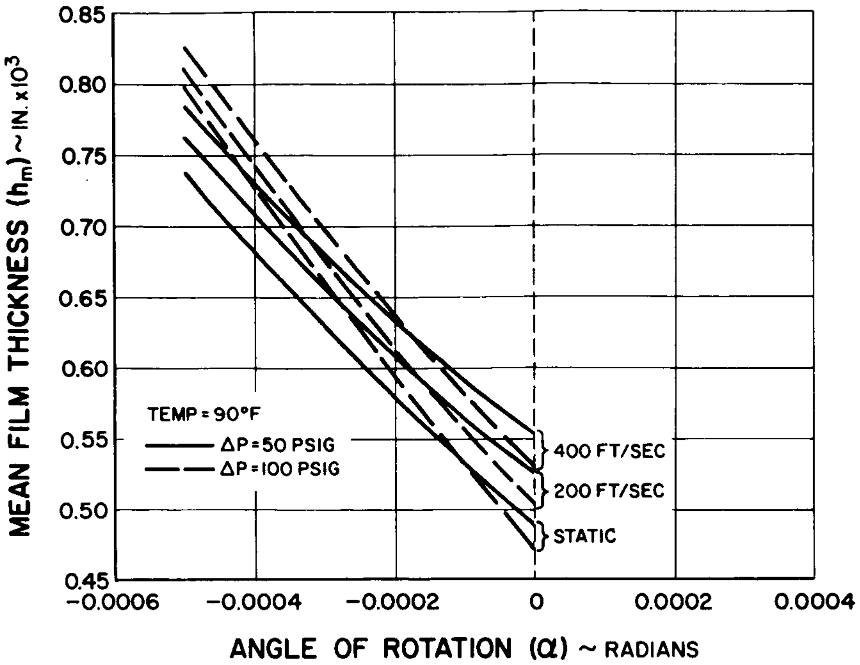

Figure 120 Mean Film Thickness at a Temperature of 90 Degrees Fahrenheit and Pressure Differentials of 50 and 100 psi

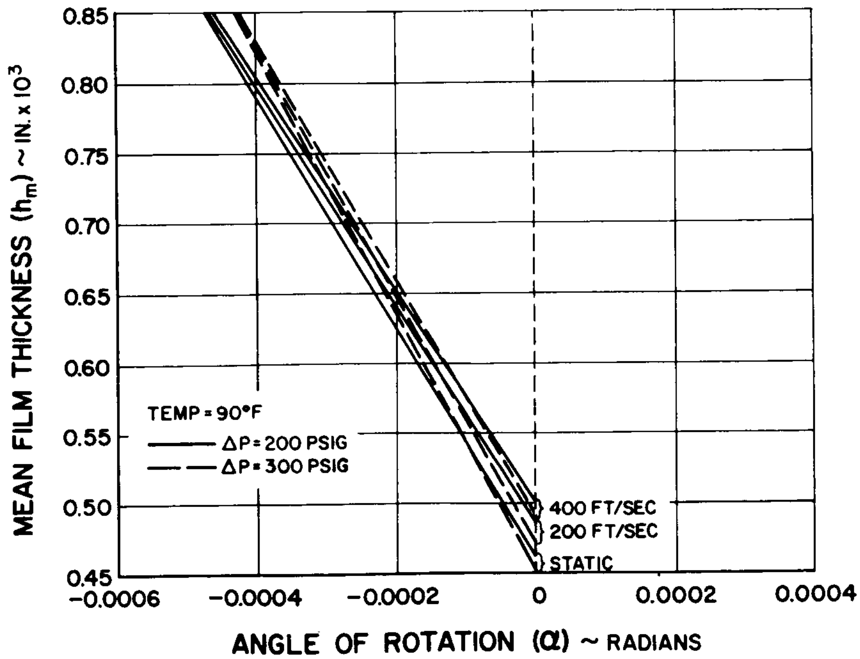

Figure 121 Mean Film Thickness at a Temperature of 90 Degrees Fahrenheit and Pressure Differentials of 200 and 300 psi

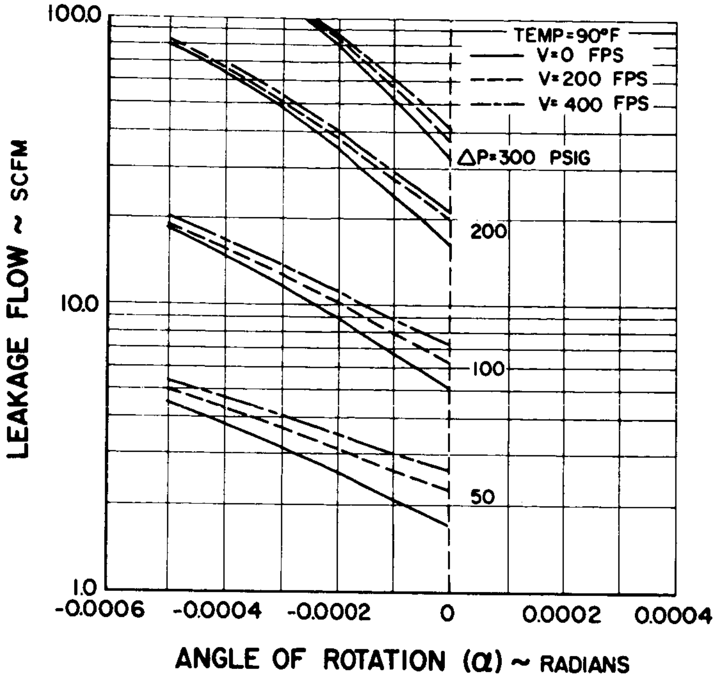

Figure 122 Leakage at a Temperature of 90 Degrees Fahrenheit

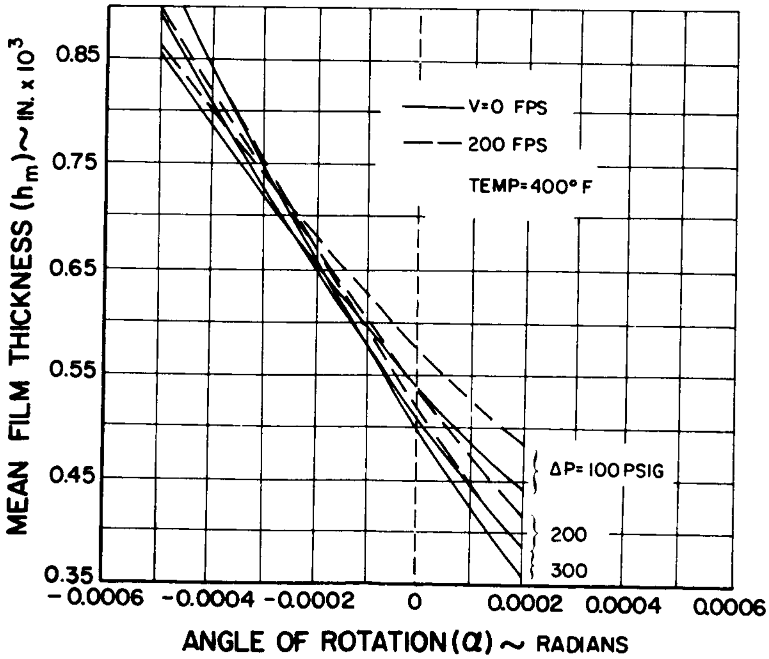

Figure 123 Mean Film Thickness at a Temperature of 400 Degrees Fahrenheit

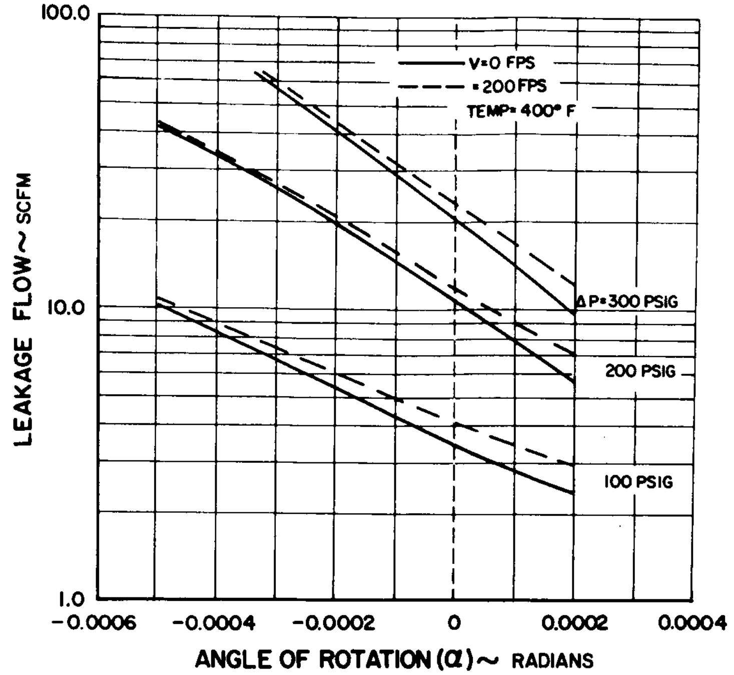

Figure 124 Leakage at a Temperature of 400 Degrees Fahrenheit

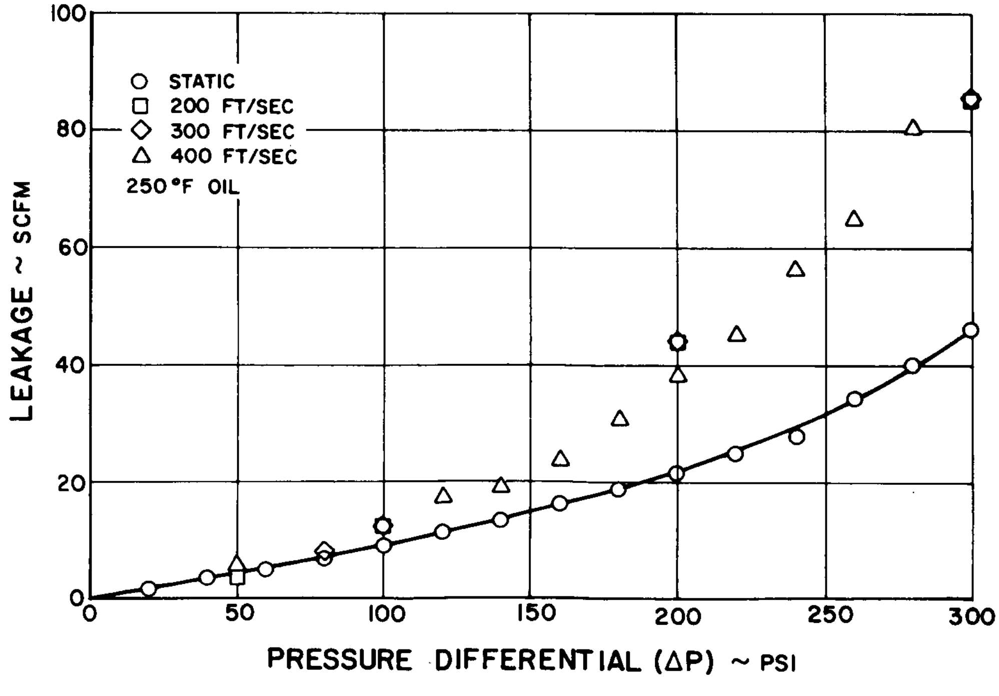

Figure 125 Measured Leakage with Room-Temperature Air

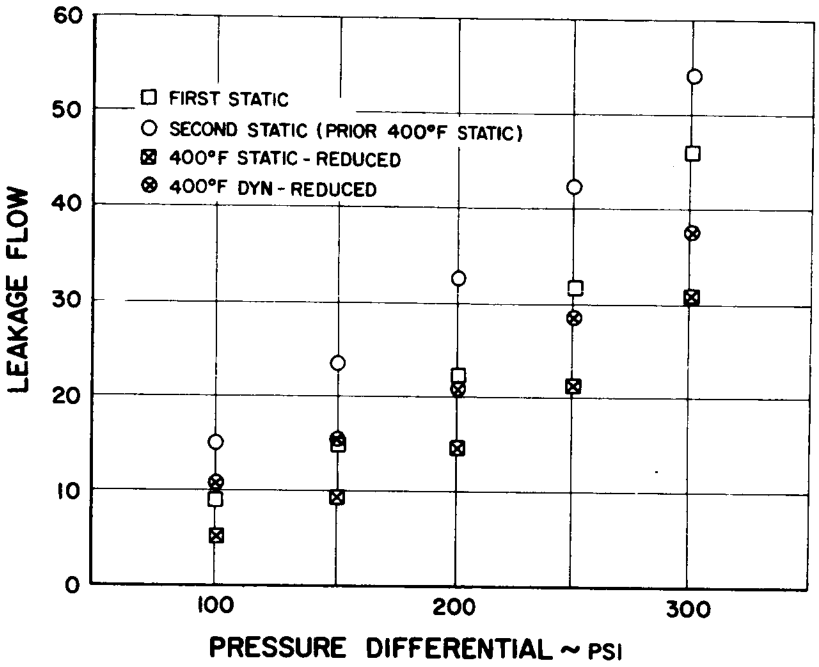

Figure 126 Modified Leakage with Air at 400 Degrees Fahrenheit

- At low pressure gradients, a severely converging film was observed for both the static and dynamic runs. Experimental observation indicates that the outer lip began to rub slightly during the low-pressure portion of the testing. The poor performance of this seal may be accredited to its inability to tolerate the seal plate's waviness at low pressure gradients.

Results of the high-temperature tests gave the following indications:

- The operating mean film thickness increased from 0.5 mil at 90 degrees Fahrenheit to 0.525 mil at 400 degrees Fahrenheit. The film was again parallel for moderate and high pressure gradients.
- The mean film thickness was approximately the same as it was at 90 degrees Fahrenheit, while the convergence of the gas film was slightly reduced at pressure differentials of 200 and 300 psi.
- At a pressure differential of 100 psi, the convergence of the gas film has the same effect as the convergence observed at 90 degrees Fahrenheit and 50 psi. This can be accounted for by the film's lower stiffness at high temperatures.

It was observed that the hybrid seal failed at 600°F with the inner lip severely worn, thus indicating that the cooling scheme in the oil-cooled seal plate design was inadequate. Furthermore, the hybrid seal failed at a larger nominal film thickness and leakage than its counterpart hydrostatic seal because the hybrid seal has an inferior stiffness value than the hydrostatic seal under divergent film operating conditions.

In conclusion, these recommendations are suggested:

- Major development efforts should be directed towards minimizing the thermal distortion of the seal plate or incorporating some conforming capability into the design of the seal plate and seal.
- Better combinations of materials for the seal and seal plate should be selected to withstand momentary high speed rubbing over the full range of operating conditions.
- The geometrical design of the hybrid seal should be chosen to avoid the divergent film completely under all operating conditions.

TABLE XVI

OPERATING MEAN FILM THICKNESS AND SEAL TILT ANGLE AT 90°F

Velocity (ft/sec)	Pressure Gradient (psig)	Total Leakage Rate (scfm)	Secondary Leakage Rate (scfm)	Net Leakage Rate (scfm)	Seal Tilt Angle (Radians x 10^3)	Mean Operating Film Thickness (in x 10^3)
0	50	4.5	1.2	3.3	-0.33	0.645
0	100	9.2	2.1	7.1	-0.12	0.54
0	200	22.0	4.0	18.0	-0.02	0.48
0	300	46.1	5.8	40.3	-0.045	0.49
200	100	12.4	2.1	10.3	-0.21	0.62
200	200	44.0	4.0	40.0	-0.21	0.65
200	300	85.6	5.8	79.8	-0.19	0.64
400	50	5.7	1.2	4.5	-0.37	0.72
400	100	12.0	2.1	9.9	-0.15	0.61
400	200	38.2	4.0	34.2	-0.14	0.605
400	300	85.6	5.8	79.8	-0.175	0.64

TABLE XVII

OPERATING MEAN FILM THICKNESS AND SEAL TILT ANGLE AT 400°F

Velocity (ft/sec)	Pressure Gradient (psig)	Total Leakage Rate (scfm)	Secondary Leakage Rate (scfm)	Net Leakage Rate (scfm)	Seal Tilt Angle (Radians x 10^3)	Mean Operating Film Thickness (in x 10^3)
0	100	5.4	1.7	3.7	-0.02	0.545
0	200	14.5	3.2	11.3	-0.02	0.525
0	300	30.4	4.6	25.8	-0.05	0.535
200	100	10.9	1.7	9.2	-0.42	0.81
200	200	20.9	3.2	17.7	-0.15	0.635
200	300	37.9	4.6	33.3	-0.11	0.6

I. TEST RIGS

A new test rig was designed for use with the seals developed under this contract. This design was similar in general to many of the test rigs currently in use at Pratt & Whitney Aircraft. The design objectives of the rig included the use of as many turbine parts as practical, interchangeability between the four seal types tested, and the duplication of engine environmental conditions. Flightweight parts used in the rig were:

- Duplex-ball thrust bearings
- Inner and outer bearing supports
- Thrust-bearing support mount
- Roller bearing, inner race and support mount
- Seal plate*
- Carbon seal assembly

All seals were compatible with the test rig, and were capable of being tested without any special adapters. In this respect, all seal designs had the same bolt circle and the same axial length.

The pressure dome was insulated to cut heat losses during testing. Pressurized and heated air entered the conical manifold attached to the inside of the pressure dome. In this fashion, the test seal was subjected to test temperature and pressures. Air temperatures at the seal were continually monitored and adjusted by means of a bleed valve.

Oil was introduced to the thrust bearings by means of a calibrated jet and scoop arrangement. Oil was introduced to the test seal area from a jet, via a scoop and passageways which allow under-race cooling of the roller bearing. This oil was centrifugally thrown out of the seal plate through radially drilled holes. This procedure also provided cooling for the seal plate. Lubrication of the roller bearing was from mist and spray in the seal compartment.

---

*Rubbing-contact face seal with piston-ring secondary seal

1. RIG INSTRUMENTATION

Figure 127 shows the method which was to be used to measure the generated torque at the seal-seal plate interface. This method was never fully proven out on the instrumentation validation rig, however, and was not used on the test rigs.

A proximity pickup was mounted internally in each of three hydraulic loading pistons mounted in the rig to monitor the distance to the back end of the piston. When a wear measurement was desired, the air pressure was slowly increased, moving the piston forward. This movement changed the output voltage of the pickup. When the voltage change stopped, the piston was bottomed on the seal carrier. At that time, the voltage reading was recorded. Calibration curves were generated for voltage versus distance, in order to provide a means of measuring wear over predetermined periods of time.

Two accelerometers, 90 degrees apart, were mounted on the seal-retaining ring. A third accelerometer was mounted on the rig to measure background vibration.

2. INERT GAS TEST

Figure 128 represents the changes made to the rig in order to test the seals under a layer of nitrogen. It involves the addition of a double labyrinth seal and a scavenge system.

3. RIG ANALYSIS

a. Pressure-Vessel Analysis

Stresses in the high-pressure and high-temperature region of the rig were calculated, and material and geometry selected as shown in the pressure-vessel summary, Figure 129.

In calculating stresses, a pressure of 300 psi was assumed. Thermal stresses were based on a temperature of 1300 degrees Fahrenheit at the piston ring housing flange and 500 degrees Fahrenheit at a distance of 3.5 inches in the direction of the bearing. A description of the analysis is given below.

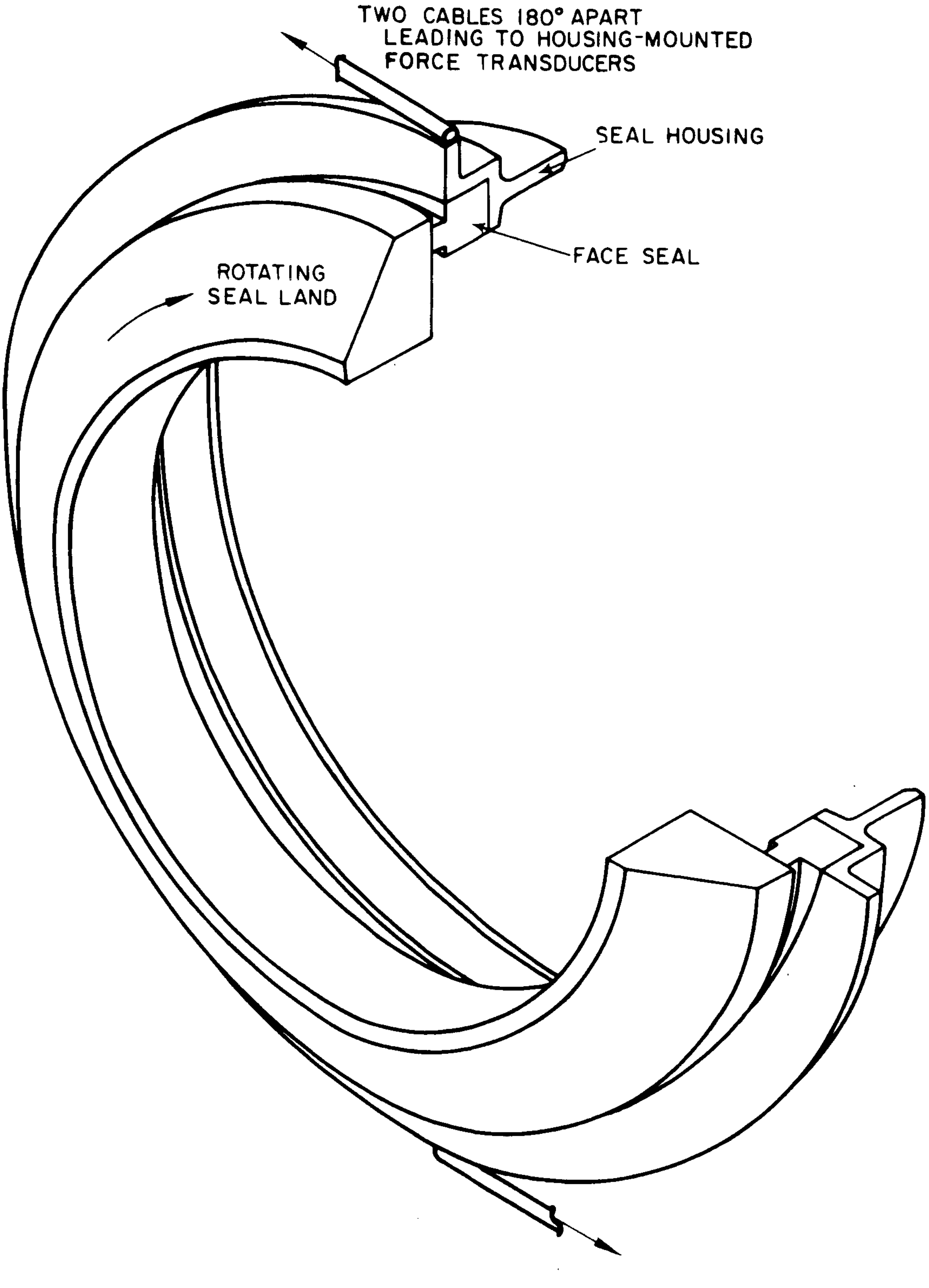
TWO CABLES 180° APART
LEADING TO HOUSING-MOUNTED
FORCE TRANSDUCERS
SEAL HOUSING
FACE SEAL
ROTATING
SEAL LAND

Figure 127 Method of Measuring Generated Torque at Seal Interface

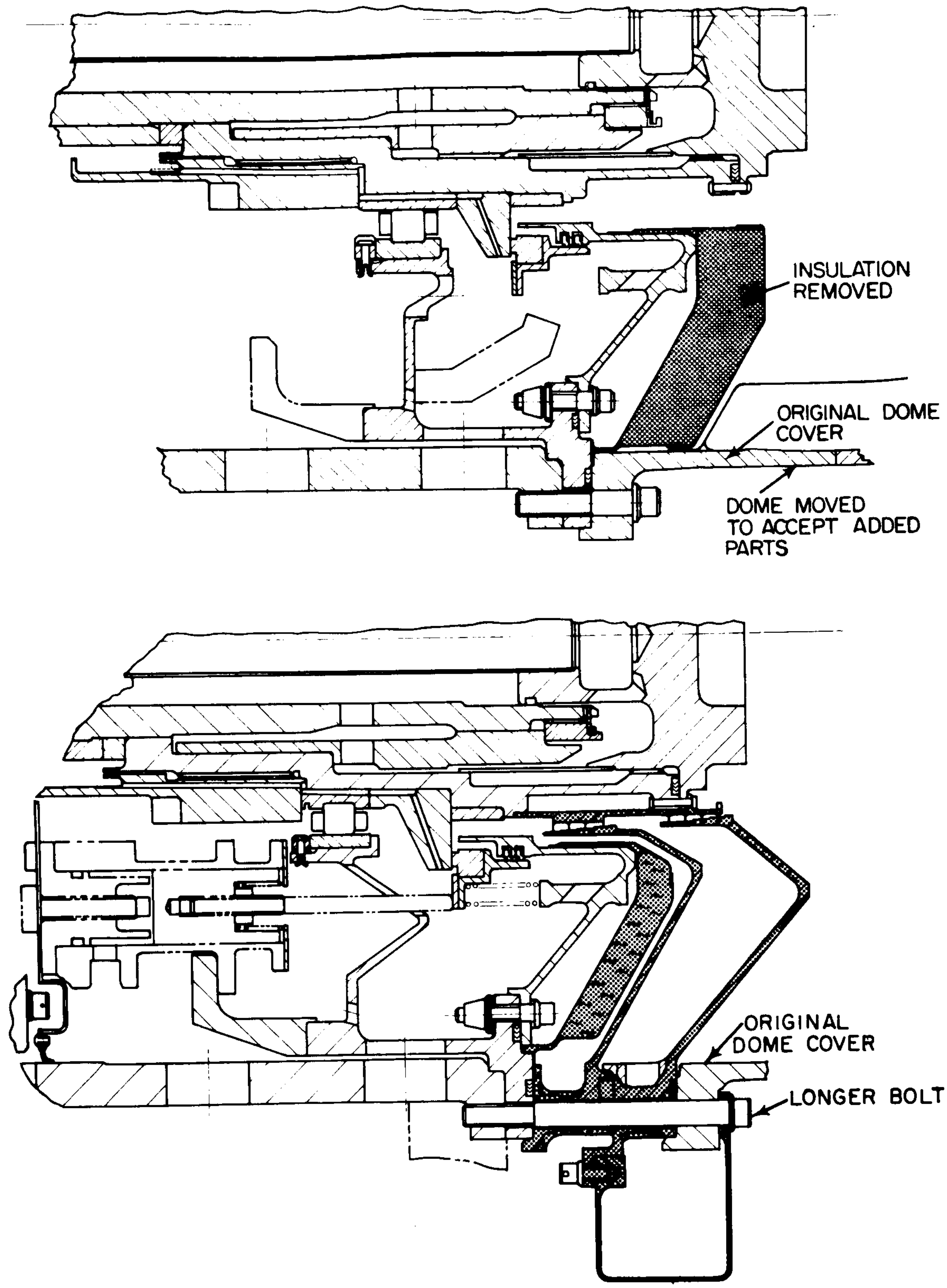
INSULATION REMOVED
ORIGINAL DOME COVER
DOME MOVED TO ACCEPT ADDED PARTS
ORIGINAL DOME COVER
LONGER BOLT

Figure 128 The Shaded Areas Illustrate the Changes to the Rig which Permitted Testing the Seals with a Layer of Nitrogen on the Oil Sump

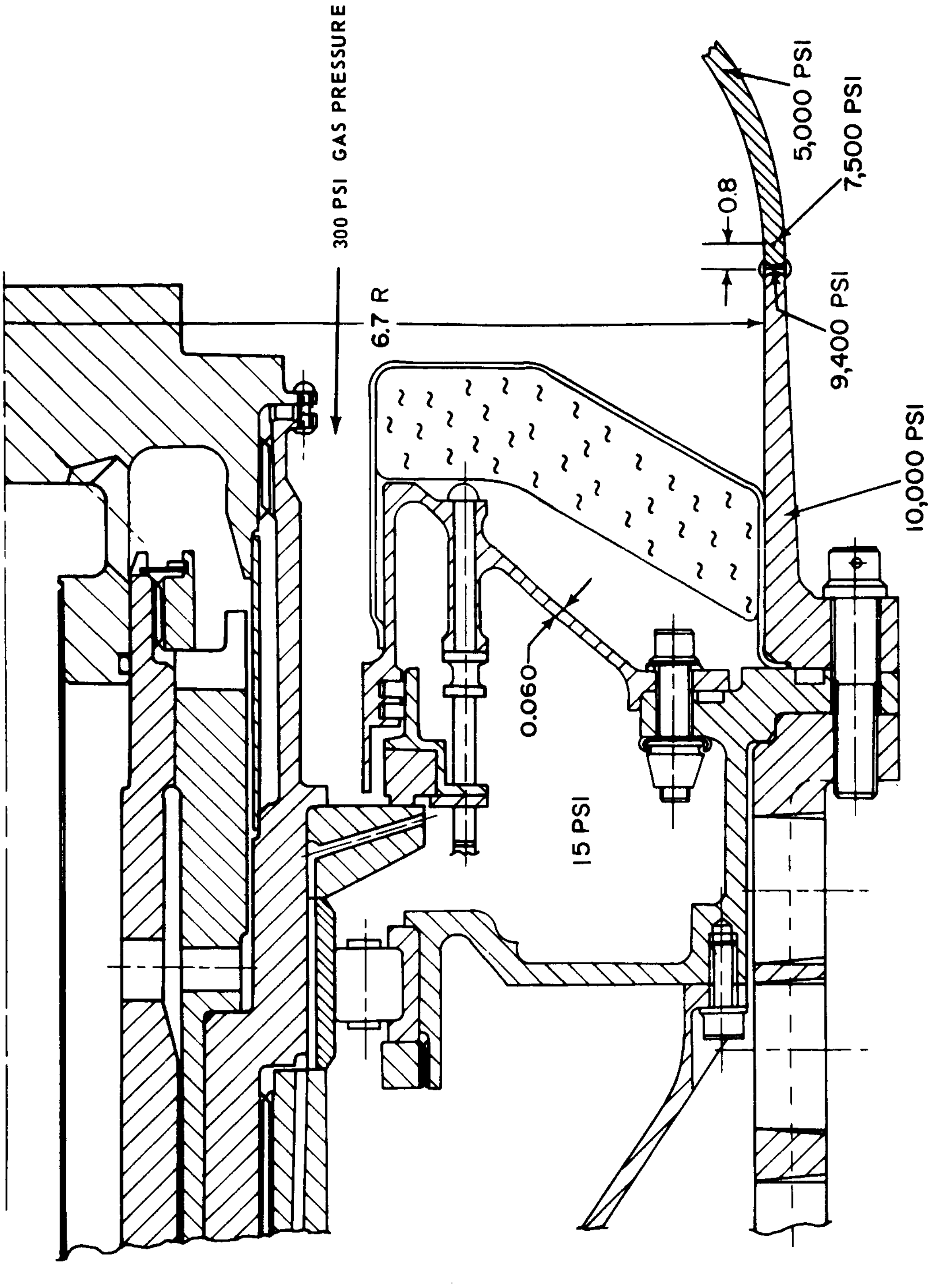
300 PSI GAS PRESSURE
6.7 R
5,000 PSI
7,500 PSI
0.8
9,400 PSI
10,000 PSI
0.060
15 PSI

Figure 129 Pressure-Vessel Summary

The cylinder membrane stress is defined as -

$$\sigma_2 = \frac{PR}{t}$$

where $P \equiv$ uniform pressure = 300 psi
$R \equiv$ mean radius of circum. - 6.7 in.
$t \equiv$ wall thickness = 0.2 in.

$\therefore \sigma_2 = 10{,}000$ psi

The sphere membrane stress is defined as

$$\sigma_1 = \frac{PR}{2t}$$

$\sigma_1 = 5{,}000$ psi

If flange stresses are not to interfere with discontinuity stresses, the parameter βx must be greater than or equal to three ($\beta x \geq 3$). β , a discontinuity parameter, for a cylinder is defined as

$$\beta = \sqrt[4]{\frac{3(1-\nu^2)}{R^2\,t^2}}$$

where ν = Poisson's ratio = 0.3
$\therefore \beta = 1.0\ \text{in}^{-1}$

Since the distance from flange to discontinuity is larger than 3 inches and $\beta = 1\ \text{in}^{-1}$, there is no interference between flange and discontinuity stresses.

The radial displacements due to pressure for a cylinder are defined as

$$\delta_1 = \frac{PR^2}{Et}\ (1 - \nu/2)$$

where E = modulus of elasticity = 23×10^6 psi

$$\therefore \delta_1 = 2.5 \times 10^{-3} \text{ in.}$$

and for a sphere

$$\delta_1 = \frac{PR^2}{2Et}(1-\nu)$$

$$= 1.02 \times 10^{-3} \text{ in.}$$

Thus the shear force acts radially inward on the cylinder.

With equal thickness for cylinder and sphere, the moment at the junction is zero. Consequently, the transverse shear normal to the wall becomes -

$$V_o = \frac{P}{8\beta}$$

$$= 37.5 \text{ lb/linear in.}$$

The meridional bending stress in the cylinder, defined as

$$\sigma_1^1 = -\frac{6M}{t^2}$$

is zero since the moment is zero. Consequently, the circumferential bending stress,

$$\sigma_2^1 = \nu\sigma_1^1$$

is zero.

The hoop stress in the cylinder is defined as

$$\sigma_2 = \frac{-2Vo}{t}(\beta R e^{-\beta x} \cos \beta x)$$

Since X is zero,

$$\sigma_2 = \frac{-2Vo}{t} \beta R$$

$$= -2,500 \text{ psi}$$

Therefore, the total stresses are:

$\sigma_1 = 5,000$ psi

$\sigma_2 = 10,000 + (-2,500) = 7,500$ psi

The maximum discontinuity stresses occur at $X = 0.8$.

$\therefore \beta x = 0.8$

Consequently, the cylinder bending moment due to edge shear, defined as

$$M = \frac{1}{\beta} \text{ Vo } e^{-\beta x} \sin \beta x$$

is equal to 12 lb-in/linear in.

The meridional bending stress in the cylinder,

$$\sigma_1^1 = 1,800 \text{ psi}$$

The circumferential bending stress,

$$\sigma_2^1 = 540 \text{ psi}$$

The hoop stress in the cylinder,

$$\sigma_2 = -1,120 \text{ psi}$$

Therefore, the total stresses at $X = 0.8$ are:

$$\sigma_1 = 5,000 + 1,800 = 6,800 \text{ psi}$$

$$\sigma_2 = 10,000 + 540 + (-1120) = 9,420 \text{ psi}$$

b. Thermal Stresses

The free thermal expansion of the cylinder at the hot side and the cold side at an axial distance of 3.5 inches was calculated.

The radial displacement was calculated to be:

$$\delta_1 = \text{Ra } \Delta T$$

where $\alpha \equiv$ coefficient of thermal expansion $= 8.7 \times 10^{-6}$

$\Delta T = 1,300° - 70° = 1230°F$

$R = 6.6$ in.

$\therefore \delta_1 = .071$ in.

and $\delta_2 = 6.6\ (8.0 \times 10^{-6})\ (500-70) = 0.023$ in.

$\Delta\delta = \delta_1 - \delta_2 = 0.048$ in.

The angular displacement is then,

$$\theta = \frac{\Delta \delta}{X}$$

$$= 0.0138 \text{ rad.}$$

If the continuity is maintained by either rolling or cylinder bending, the resulting stresses are respectively:

$$\sigma_{\text{rolling}} = \frac{\theta E c}{R}$$

where $c \equiv$ distance from the centroid to the point under stress = 1.5

$$\therefore \sigma_{\text{rolling}} = 72,400 \text{ psi}$$

$$\sigma_{\text{bending}} = 1.515 E \theta \left(\frac{t}{R}\right)^{1/2}$$

$$= 103,000 \text{ psi}$$

Actually both situations occur simultaneously and the actual stress is lower than either.

However, if the stress is 72,400 psi, then the strain is calculated to be

$$e = \frac{\sigma}{E}$$

$$= 0.3 \text{ percent}$$

The material selected has a one-way cyclic life greater than 6,000 cycles at e = 40 percent.

c. Buckling of Piston-Ring Housing

From design curves, the thickness required to prevent buckling is determined to be 0.054 in.

d. Thermal Analysis

A heat balance was performed on the rig assuming that the shaft rotates in 1300-degree Fahrenheit air, and a calculated heat input from the bearing and seal. A convective heat-transfer coefficient (from standard equations) was found for the shaft. Assuming shaft temperatures, the amount of heat transferred was determined. This heat is conducted through the shaft to the groove and transferred by convection to the oil. The bearing and seal heat rejection was transferred in the same manner to the groove.

A heat balance was required in setting a shaft temperature that would yield a metal temperature next to the groove whereby the heat input to the shaft is equal to the heat input to the groove. The results of this analysis are shown in Figure 130 where the various rig component temperatures are indicated.

e. Critical Speed Analysis

A critical speed analysis was made of the rig plus the drive system to determine whether or not any critical speed exists within the operating range of the rig. The analysis is an iterative solution where the actual vibration system is reduced to lumped masses which are linked together by flexible connections which, in turn, are elastically supported. This system (Figure 131) can be extended by adding one or more levels and again lumping masses.

The method is based upon assuming a frequency and, after working across the shaft or beam, determining a residual function, such as bending moment. If this function is zero, the assumed frequency is a natural one. A remainder curve for the function may be plotted similar to the torque remainder curve of the Holzer method. It is more complicated than the Holzer method, since four integrations are involved rather than two, and additional complications arise in dealing with the boundary conditions.

The differential equation at the natural frequency is

$$\frac{d^2}{dx^2}\left(EI\ \frac{d^2y}{dx^2}\right) = \mu\omega^2 Y \qquad (17)$$

where μ is the mass per unit length.

From the elementary beam theory,

$$EI\ \frac{d^2y}{dx^2} = M \qquad (18)$$

Hence,

$$\frac{d^2M}{dx^2} = \mu\omega^2 Y \qquad (19)$$

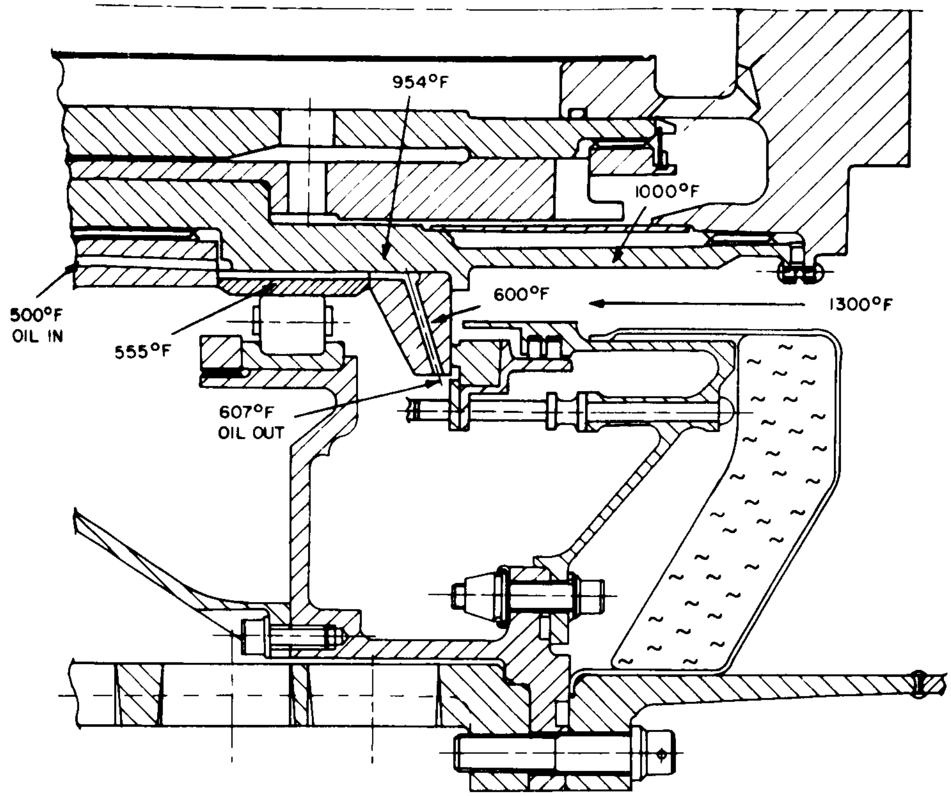
954°F
1000°F
600°F
1300°F
500°F OIL IN
555°F
607°F OIL OUT

Figure 130 Rig Temperatures at an Oil Flow of 24 ppm

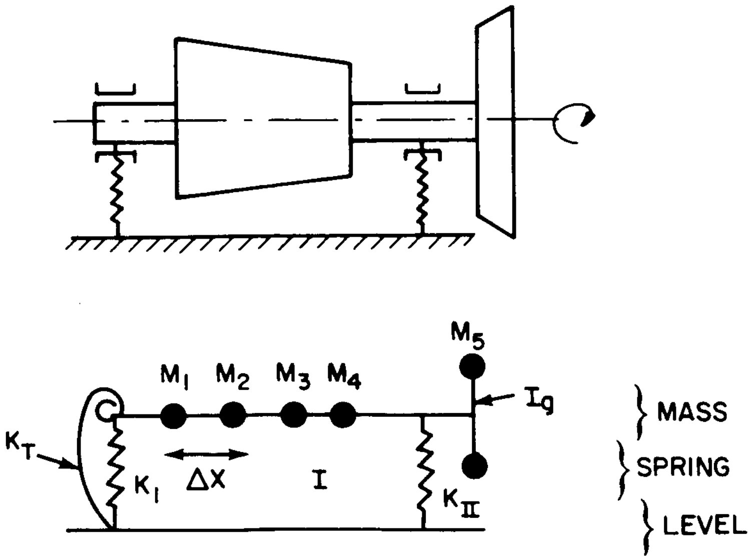
M5
M1
M2
M3
M4
Ig
MASS
KT
SPRING
K1
ΔX
I
KII
LEVEL

Figure 131 System Model for Analysis of Critical Speeds

Since Equation 17 is of the fourth order, four boundary conditions must be satisfied. Any frequency that satisfies these four boundary conditions is a natural one. Equations (18) and (19) may be transformed to permit tabular integration and thus form the basis for constructing the M and y diagrams. Then,

$$\Delta \left(\frac{dy}{dx}\right) = \left(\frac{\Delta X}{EI}\right) M_{avg} \tag{20}$$

$$\Delta \left(\frac{dM}{dx}\right) = \left(\mu \omega^2 \Delta X\right) Y_{avg} \tag{21}$$

where Δx is the length of a given section and M_{avg} and Y_{avg} are the average values of bending moment and deflection for that section.

Equation (20) states that the change in slope of the deflection curve at a given section equals $\Delta x/EI \times M_{avg}$. Equation (21) states that the change in slope of the moment curve at a given section equals $\mu \omega^2 \Delta X Y_{avg}$.

For any assumed frequency, the M and Y diagrams can be constructed to satisfy three of the four boundary conditions. By plotting the fourth boundary condition against frequency, the natural frequency will occur when this remainder equals zero. The actual calculation method is based upon the following series of equations.

The shaft or beam is transformed into a number of point masses connected by weightless springs. The moment diagram has a constant slope in each section, since

$$\frac{dM}{dx} = V$$

The change in shear at a mass is

$$\Delta V = mY\omega^2$$

The deflection curve is smooth, since the body is continuous. Assume that V_o, M_o, θ_o and Y_o are known (refer to Figure 131).

$$V_1 = V_o + m_o Y_o \omega^2$$

$$M_1 = M_o + V_1 \ (\Delta X)$$

$$M = M_o + \frac{M_1 - M_o}{\Delta X} X \qquad (22)$$

$$\Theta = \frac{1}{(EI)_1} \int_o^x M dx + C \qquad (23)$$

where C is a constant of integration. When the distance x is zero, the slope Θ becomes Θ_o; hence, the constant $C = \Theta_o$

Substituting Equation (22) in Equation (23) and integrating,

$$\theta = \frac{1}{(EI)_1} \left[M_o x + \frac{M_1 - M_o}{(\Delta X)_1} \frac{X^2}{2} \right] + \theta_o \qquad (24)$$

$$Y = \int_o^x \theta dx + C^1 \qquad (25)$$

where C^1 is another constant of integration. When the distance x is zero, the deflection Y becomes Y_o; hence, the constant $C^1 = Y_o$.

Substituting Equation (24) in Equation (25) and integrating,

$$Y = \frac{1}{(EI)_1} \left[M_o \frac{X^2}{2} + \frac{M_1 - M_o}{(\Delta X)_1} \frac{X^3}{6} \right] + \theta_o X + Y_o \qquad (26)$$

It is only necessary to know θ and y at the end of the section (that is, at point 1). Substituting $(\Delta x)_1$ for x, and β_1 for $(\Delta x/EI)_1$ in Equations (24) and (26) gives

$$\theta_1 = \beta_1 \left(\frac{M_o}{2} + \frac{M_1}{2} \right) + \theta_o$$

$$Y_1 = \beta_1 \left(\frac{M_o}{3} + \frac{M_1}{6} \right) (\Delta X)_1 + \theta_o (\Delta X)_1 + Y_o$$

$$V_2 = V_1 + m_1 Y_1 \omega^2$$

$$M_2 = M_1 + V_2 (\Delta X)_2$$

By repeating these steps across the body, the moment and deflection diagrams shown in Figure 132 can be calculated and drawn.

Generalizing the preceding equations, we find that

$$V_n = V_{n-1} + m_{n-1} \omega^2 Y_{n-1}$$

$$M_n = M_{n-1} + V_n (\Delta X)_n$$

$$\theta_n = \beta_n \left[\frac{M_{n-1}}{2} + \frac{M_n}{2} \right] + \theta_{n-1}$$

$$Y_n = \beta_n \left[\frac{M_{n-1}}{3} + \frac{M_n}{6} \right] (\Delta X)_n + \theta_{n-1} (\Delta X)_n + Y_{n-1}$$

where

$$\beta_n = \left(\frac{\Delta X}{EI} \right)_n$$

It can be demonstrated that V, M, , and Y at any point in the span are linear functions of the four assumed quantities at the starting end (that is, point O). Hence, Y, for example, at point n may be expressed as

$$Y_n = A_n V_o + B_n M_o + C_n \theta_o + D_n Y_o$$

where A_n, B_n, C_n, and D_n represent numerical coefficients to be computed. Since two boundary conditions must be known at point O, only two need be evaluated.

The boundary conditions for the usual cases are:

Fixed end:

$$Y_o = O \qquad \theta_o = O$$

Simple supported end:

$$Y_o = O \qquad M_o = O$$

Free end:

$$V_o = O \qquad M_o = O$$

At a common point on adjacent spans: Θ and y are the same for both.

The entire analysis is computerized, with the main input data describing physically the shaft or rotor, casing, and rotor support. The rotor and casing configurations must be broken up into spans ranging from one bearing to another. Each span, in turn, must be broken up into sections of finite length. From station to station, there are five physical quantities which are defined as follows:

1. Δ_x - length between stations (inches)
2. Wt - weight at station (lb)
3. β_{bend} - bending flexibility (radians/in-lb)
4. β_{shear} - shear modulus (in/lb)
5. I_{gyro} - gyroscopic moment of inertia (lb-in^2)

Figure 133 shows an example of how a section of shaft might be broken up. The shaft weight is concentrated at the stations so that we have a shaft without mass with the exception of the weight concentration at the stations. β_b and β_s describe the flexibility and shear characteristics of the shaft between the stations. I_{gyro} describes the gyroscopic effect, if any, at the station. Usually I_{gyro} will be neglected unless a large mass such as a compressor or turbine disc exists in which case the station will be located to coincide with the center of gravity of the disc.

Figure 134 is a schematic drawing of the rig analyzed. The system consists of a driveshaft, a coupling consisting of two splines on an intermediate shaft, the main span of the rig, and an overhang. The spring constants K_3 and K_4 were calculated analytically and were found to be 9.22×10^6 and 7.85×10^6 lb/in, respectively.

Three critical speeds were determined, all of which are well outside the operating range of the rig (up to 21,000 RPM). The critical speeds are as follows:

Critical	Position	RPM	% Total Energy*
N_1	Coupling	31,887	97.43
N_2	Overhang	60,521	60.20
N_3	Coupling	64,269	62.27

*Percent of total energy of shaft deflection which is concentrated in the section.

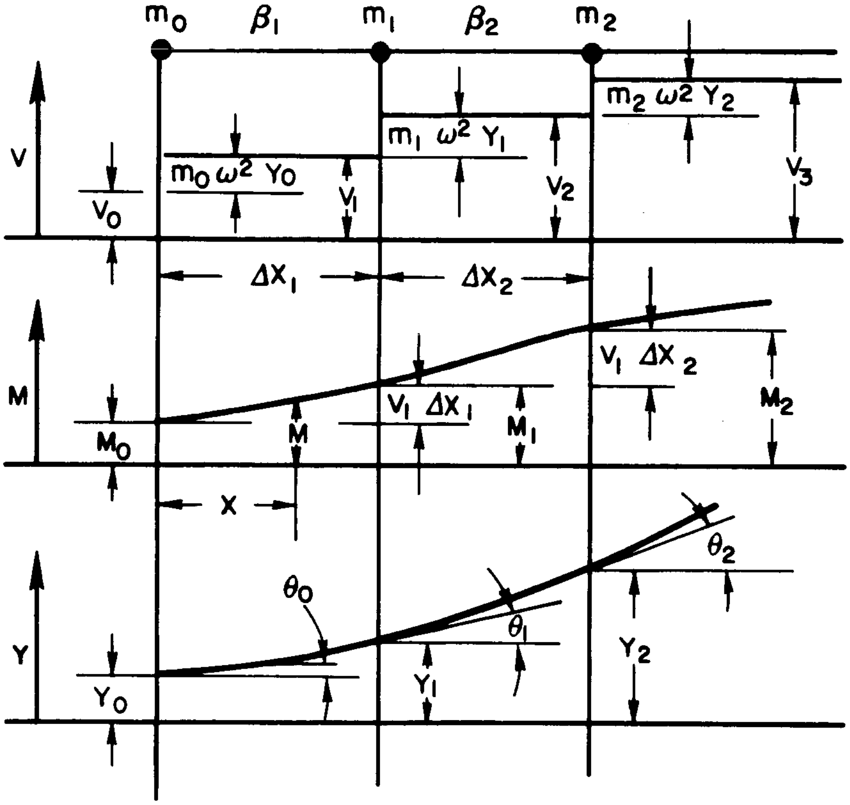
m0
β1
m1
β2
m2
V
V0
m0 ω2 Y0
V1
m1 ω2 Y1
V2
m2 ω2 Y2
V3
ΔX1
ΔX2
M
M0
M
V1 ΔX1
M1
V1 ΔX2
M2
X
Y
Y0
θ0
Y1
θ1
Y2
θ2

Figure 132 Moment and Deflection Diagrams

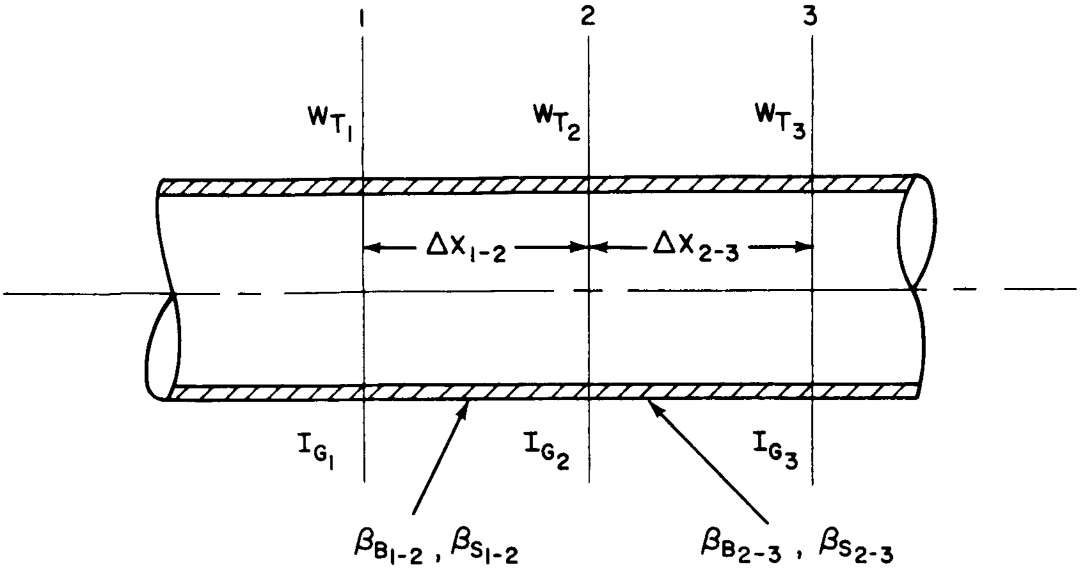
1
2
3
W_{T_1}
W_{T_2}
W_{T_3}
ΔX_{1-2}
ΔX_{2-3}
I_{G_1}
I_{G_2}
I_{G_3}
$\beta_{B_{1-2}}$, $\beta_{S_{1-2}}$
$\beta_{B_{2-3}}$, $\beta_{S_{2-3}}$

Figure 133 Method of Dividing Shaft for Vibration Analysis

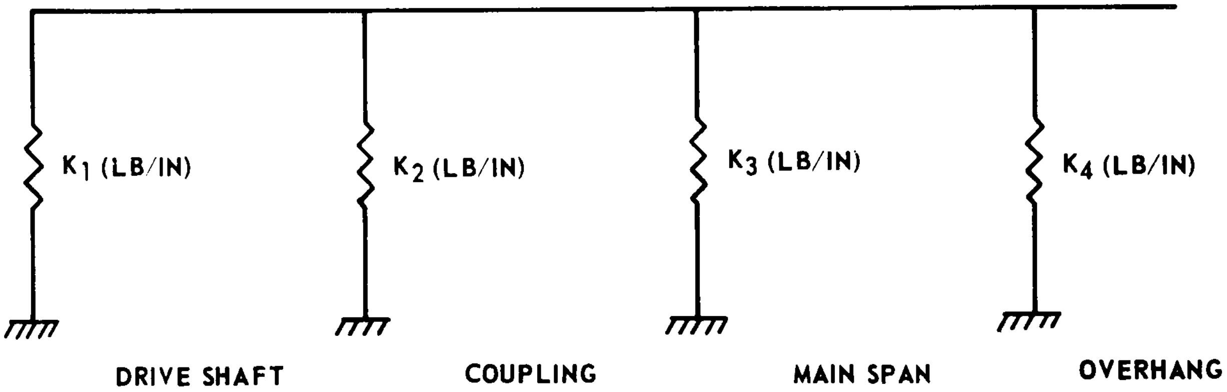
K_1 (LB/IN)
K_2 (LB/IN)
K_3 (LB/IN)
K_4 (LB/IN)
DRIVE SHAFT
COUPLING
MAIN SPAN
OVERHANG

Figure 134 Schematic of Analytical Model for Rig

In order to evaluate the influence of the support spring constants, which are difficult to determine precisely, the analysis was also made using two other sets of values for K_3 and K_4 , to compare with the results for the calculated spring rates. For one, these spring constants were taken to be 0.8 of their calculated values; for the other, K_3 was taken to be 5 x 10^6 lb/in and K_4 was taken to be 3 x 10^6 lb/in. K_1 and K_2 were assumed to be 1 x 10^{12} lb/in since these bearings were connected directly to ground and could be considered to be supported by infinitely stiff springs. K_1 and K_2 were not varied for the three analyses. The three analyses run for the three different sets of values for K_3 and K_4 indicated a difference of less than 400 rpm at the first critical point.

For a comparison with the results for the calculated spring rates K_3 and K_4:

K_3, K_4 = 0.8 Calculated Values

Critical	Position	RPM	% Total Energy
N_1	Coupling	31,819	97.34
N_2	Overhang	55,597	72.51
N_3	Coupling	63,695	74.22

K_3 = 5 x 10^6 lb/in, K_4 = 3 x 10^6 lb/in

Critical	Position	RPM	% Total Energy
N_1	Coupling	31,492	95.16
N_2	Overhang	40,900	73.22
N_3	Coupling	61,792	73.72

4. INSTRUMENTATION VALIDATION RIG

An existing Pratt & Whitney Aircraft seal test rig was modified to develop the instrumentation techniques necessary to measure the torque generated at the seal face, the seal wear, the hydraulic loading, and the seal's vibrational modes.

Initial attempts to use the torque measuring device revealed that the load range of the transducers being used was too large. The transducers selected had a range of 0 to 100 pounds, whereas the measured loads were on the order of 3 pounds. This large difference apparently came from the fact that the face-contact seal was not operating at a constant rubbing condition but instead was partially riding on an air film available from the air leakage. In addition, vibration of the torque arms introduced errors in the transducer readings. An attempt was made to eliminate the vibration problem by deadweight loading the force arms. Testing, however, revealed that the deadweight loads had not been distributed equally between the two force transducers and the vibration was still excessive.

The program was rerun on 28 December 1967. Tapping the hanging dead weights to reduce the static friction of the cable system improved the load split between the force arms. However, the loads due to torque generated at the carbon seal lip and seal plate interface were too small to be accurately detected with the present 0-100 pounds range force transducers.

Smaller transducers were procured, but additional redesign of the transducer mounting system is required to eliminate the vibrational problems in the torque arms induced by the shaft rotation and motion of the seal assembly.

Testing was conducted to develop instrumentation for measuring seal wear without disassembling the rig. The method studied to measure seal wear involved measuring the displacement of the seal-loading pistons with Bently probes. For the first test, the rig was run for 16.75 hours at a rubbing speed of 300 ft/sec and a pressure differential of 20 psi, with the air at ambient temperature. The probe data indicated zero wear, within an accuracy of 1 mil because of piston vibration. The actual wear was 0.2 mil. After running for 14.50 hours at a rubbing speed of 400 ft/sec and the same pressure differential and air temperature, one probe indicated a seal wear of 3.4 mils, the second indicated 10.3 mils, and the third was inoperative. Actual wear was 0.2 mils. The inconsistencies were caused by vibration of the pistons when they were in contact with the seal. The vibrations varied in amplitude to a maximum of 10 mils at frequencies considerably below the rig speed. Increasing the spring preload reduced the peak vibration amplitude to 6 mils and increased the vibration frequency to rig speed.

The rig was then run at a rubbing speed of 200 ft/sec with ambient air temperature and pressure differentials ranging from 20 to 200 psi. It was found that the total displacement of the cylinders was dependent on the seal air pressure, apparently because of axial displacement of the rig bearing with changing thrust load. With a seal pressure differential of 20 psi, the average travel was 27.6 mils, whereas with a seal pressure differential of 200 psi, the average travel was 20.0 mils. The movements of the three pistons, however, were within 1 mil of each other at all times. Considerable additional experimentation is required to develop this technique to an acceptable level of accuracy.

The hydraulic loading measurements were not effective when obtained under dynamic conditions. The seal air leakage increased gradually when the three piston push rods were moved to a position of contact with the seal. The loading required to increase the seal's air leakage was barely above the pressure loading required to overcome the piston preload. The Bently probe readout revealed the pistons to be subjected to vibration.

The static hydraulic loading results were considerably higher than the dynamic, and compared favorably with the analytically calculated values of the hydraulic force due to the seal's unbalance.

The test seal was instrumented with two accelerometers 90 degrees apart to record the axial vibrational modes of the seal (Figure 135). The test rig housing was also instrumented with an accelerometer to record the background vibration.

The seal was tested at rubbing speeds of 200, 300 and 400 feet per second using ambient air at pressures from 20 to 200 psig. The program was completed 16 February 1967 with the accelerometer output signals recorded at each condition. Analysis of the recorded data revealed high-frequency noise superimposed on the output of the two seal accelerometers and the external background accelerometer, making the data difficult to interpret accurately.

The program was repeated with the accelerometer output signals filtered to eliminate frequencies below 80 cycles per second and above 600 cycles per second. The recorded data still contained noise making it difficult to analyze.

The program was again repeated using a wave analyzer at each condition to pick out the predominant accelerometer output signal frequencies to see whether frequencies above 300 cycles per second could be filtered without losing any significant portion of the output signal.

Analysis of the accelerometer data revealed that for the rubbing-contact seal being tested in the validation rig, output signal frequencies above 300 cps and below 60 cps could be filtered without losing any significant portion of the output signal.

The program was rerun with the accelerometer output signals filtered to eliminate frequencies below 60 cps and above 300 cps. The analysis revealed that the overall acceleration level of the axial accelerometers (mounted 90 degrees apart on the seal) was more dependent on shaft speed than on the air pressure at the seal. The overall acceleration level at 200 fps (6,550 rpm) varied from ±1 g's to ±2 g's; at 300 fps (9,800 rpm) from ±2.8 g's to ±4.3 g's; and at 400 fps (13,100 rpm) from ±5.7 g's to ±7.2 g's for the pressures tested. The lag angle between the two axial accelerometer output signals varied from 90 to 180 degrees. They were never recorded in phase.

Further accelerometer work was continued on the main seal test rigs.

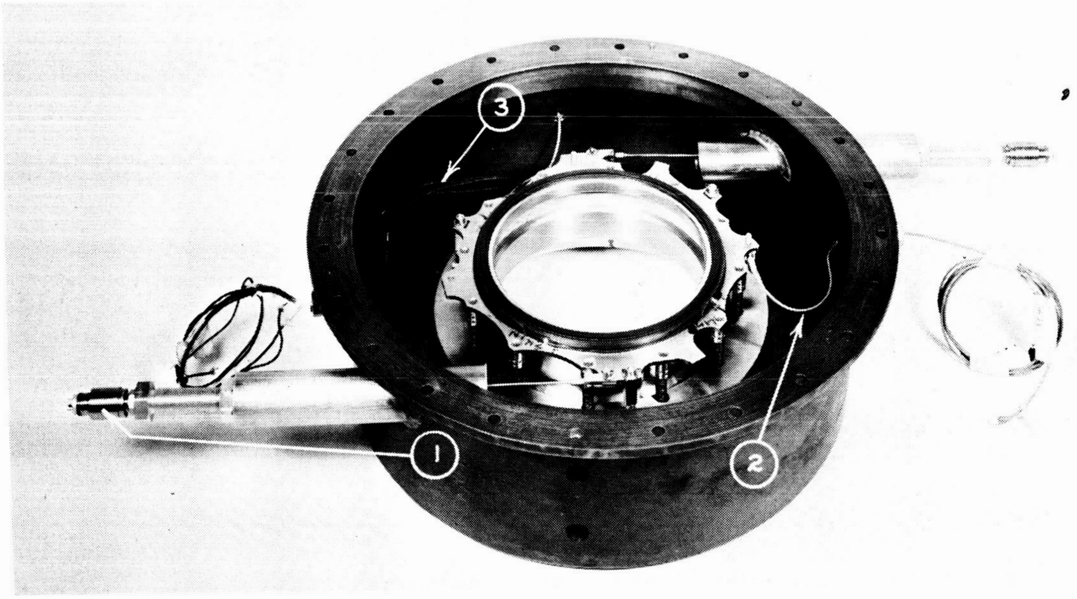

Figure 135 Test Seal Assembled in the Instrumentation Validation Rig Cover.
1. Transducers to Measure Torque Generated at Seal Face
2. Accelerometer 3. Seal Housing and Carbon
Thermocouples (XP-66908)

APPENDIX A

DEFLECTION ANALYSIS OF SEAL HOUSING FOR RUBBING - CONTACT SEALS

It was desired to be able to determine the deflections of the seal-housing assembly. A detailed analysis was performed yielding eight equations with eight unknowns. These equations were solved simultaneously on the IBM 1620 computer. The equations are arrived at by equating the slopes and deflections of contiguous members to ensure continuity of structure. For example, referring to Figure 136, the deflection of cylinder (3) at A is equal to the deflection of cylinder (2) at A, and the slope of (3) is equal to the slope of (2) at A.

The following is a detailed description of the analysis. The equations are based on material given in Roark's "Formulas for Stress and Strain", (Reference 1). A free body diagram of the seal design is sketched in Figure 137. Bodies 1, 2, and 3 comprise the carrier; body 4 the seal; body 5 the carbon retention ring; P refers to pressure; M refers to moment; V refers to shear; L refers to horizontal length; h refers to vertical length; and R refers to radius.

1. DEFLECTION OF BODY 1

The radial displacement of body 1 (see Figure 138) at point A (δA_1) and the corresponding angular displacement Θ, are given by the following equations:

$$\delta_{A_1} = \frac{P_o R_1^2}{E h_1} - \frac{V_1 R_1^2}{E L_1 h_1} - \frac{V_3 (R_1 + d) R_1}{E L_1 h_1}$$

$$\Theta_1 = \frac{R_1^2}{E I_1} \left[M_1 - M_3 + 1/2\, L_1 V_1 - 1/2\, L_1 V_3 \left(\frac{R_1 + d}{R_1} \right) - P_5 d \left(\frac{R_1 + d}{R_1} \right) + M_4 \left(\frac{R_1 + d}{R_1} \right) \right]$$

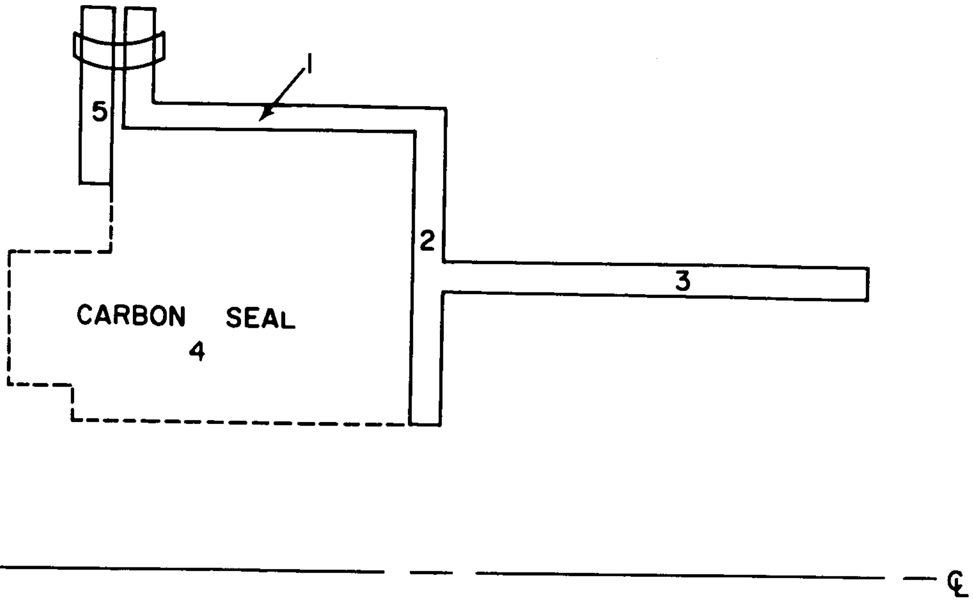
1
5
2
3
CARBON SEAL
4
℄

Figure 136 Division of the Seal and Housing Assembly

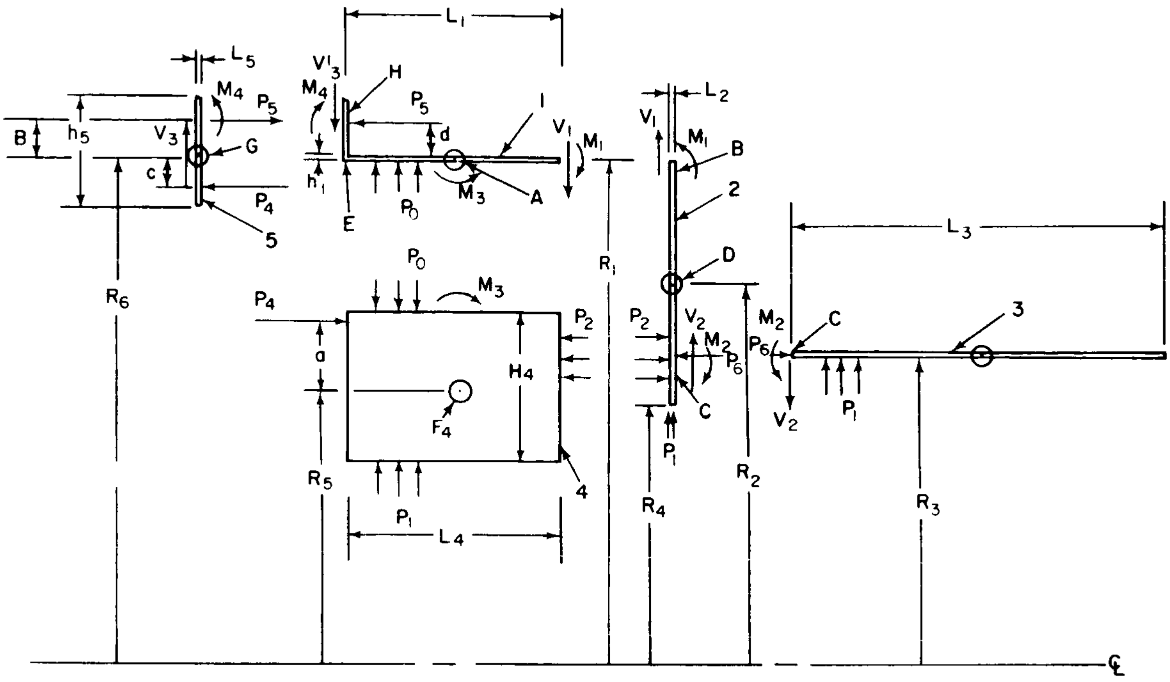
L_5
M_4
P_5
B
h_5
V_3
G
c
P_4
5
R_6
L_1
V'_3
H
M_4
P_5
1
V_1
M_1
d
h_1
E
P_0
M_3
A
L_2
V_1
M_1
B
2
D
R_1
P_0
M_3
P_4
P_2
a
H_4
F_4
R_5
P_1
L_4
4
P_2
V_2
M_2
P_6
C
P_1
R_4
R_2
M_2
C
P_6
3
L_3
V_2
P_1
R_3
℄

Figure 137 Freebody Diagram of the Seal

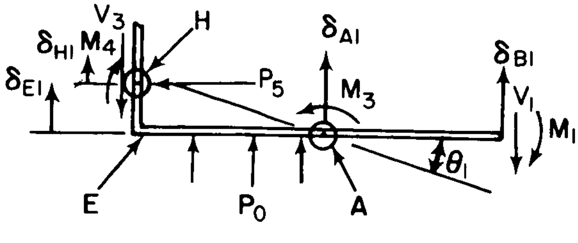
V_3
H
δ_{H1}
M_4
δ_{E1}
P_5
δ_{A1}
M_3
δ_{B1}
V_1
M_1
θ_1
E
P_0
A

Figure 138 Freebody Diagram of Body 1

The radial displacements of body 1 with respect to points B, E, and H are represented below:

$$\delta_{B_1} = \delta_{A_1} - 1/2\ L_1 \theta_1$$

$$\delta_{E_1} = \delta_{A_1} + 1/2\ L_1 \theta_1$$

$$\delta_{H_1} = \delta_{A_1} + 1/2\ L_1 \theta_1$$

where E = modulus of elasticity
(Flange contribution is insignificant to torsional stiffness since it is scalloped.)

2. DEFLECTION OF BODY 2

The radial displacement of body 2 (see Figure 139) with respect to point D (δ_{D2}) and the corresponding angular displacement θ_2 are given below:

$$\delta_{D_2} = \frac{P_1 R_4 R_2}{Eh_2} + \frac{V_1 R_1 R_2}{Eh_2 L_2} + \frac{V_2 R_2 R_3}{Eh_2 L_2}$$

$$\theta_2 = \frac{R_2^{\ 2}}{EI_2} (M_2 - M_1)$$

The radial displacement of body 2 at point B, $\delta_{B2} = \delta_{D2}$
The radial displacement of body 2 at point C, $\delta_{C_2} = \delta_{D_2}$
(Moment due to pressure P_2 is assumed negligible)

3. DEFLECTION OF BODY 3

The radial displacement of body 3 (see Figure 140) at points C (δ_{C3}) and the corresponding angular displacement θ_3 are given below:

$$\delta_{C_3} = \frac{P_1 R_3^{\ 2}}{Eh_3} - V_2 \left(\frac{C_3}{2D\lambda^3}\right) - M_2 \left(\frac{C_5}{2D\lambda^2}\right)$$

$$\theta_3 = - V_2 \left(\frac{C_4}{2D\lambda^2}\right) - M_2 \left(\frac{C_6}{\lambda D}\right)$$

where $D = \frac{Eh_3^{\ 3}}{12(1-\kappa^2)}$; $\lambda = \left(\frac{3(1-\nu^2)}{R_3^{\ 2} h_3^{\ 2}}\right)^{1/4}$

and C_3, C_4, C_5, C_6 are constants dependent on λL_3 and are given in Reference 1, p. 297.

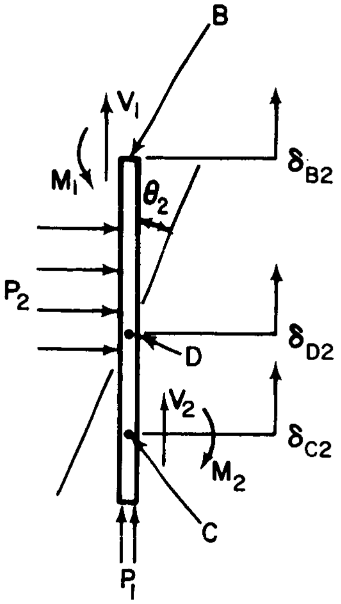
B
V_1
M_1
θ_2
δ_{B2}
P_2
δ_{D2}
D
V_2
δ_{C2}
M_2
C
P_1

Figure 139 Freebody Diagram of Body 2

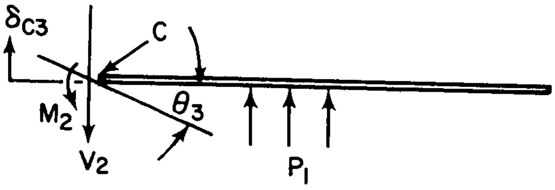
δ_{C3}
C
M_2
V_2
θ_3
P_1

Figure 140 Freebody Diagram of Body 3

4. DEFLECTION OF BODY 4

The radial displacement of body 4 (see Figure 141) at point F (δ_{F_4}) and the corresponding angular displacement Θ_4 are given below:

$$\delta_{F_4} = \frac{P_1 R_5 (R_5 - 1/2\, h_4)}{E_1 h_4} - \frac{P_o R_5 (R_5 + 1/2\, h_4)}{E_1 h_4} + R_5 \beta \Delta T$$

$$\Theta_4 = \frac{R_5^2}{E_1 I_4} (M_3 + P_4 a)$$

where

$\beta = (\alpha_1 - \alpha)$

α_1 = coefficient of thermal expansion of carbon

α = coefficient of thermal expansion of housing material

E_1 = Young's modulus of carbon

ΔT = operating temperature - room temperature

5. DEFLECTION OF BODY 5

The radial displacement of body 5 at point G (δ_{G_5}) and the corresponding angular displacement Θ_5 are given below:

$$\delta_{G_5} = \frac{R_6 (R_6 + b)}{E L_5 h_5} V_3 \qquad \text{(}V_3\text{ acts at bolt circle radius)}$$

$$\Theta_5 = \frac{R_6^2}{E\, I_5} \left[P5 \left(\frac{R_6 + b}{R_6} \right) b + P_4 \left(\frac{R_6 - C}{R_6} \right) C - M_4 \left(\frac{R_6 + b}{R_6} \right) \right]$$

The radial displacement of (5) at point H, $\delta_{H_5} = \delta_{G_5}$

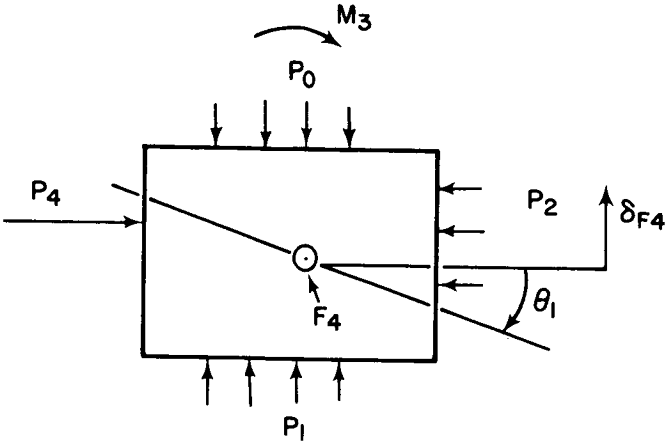
M3
P0
P4
P2
δF4
θ1
F4
P1

Figure 141 Freebody Diagram of Body 4

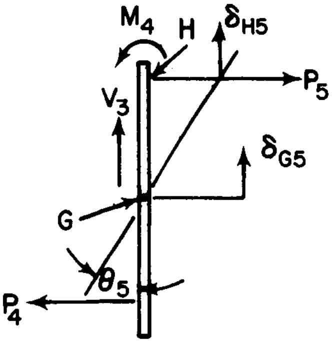
M4
H
δH5
P5
V3
δG5
G
θ5
P4

Figure 142 Freebody Diagram of Body 5

6. RELATIONS BETWEEN P_2, P_4, AND P_5

From lateral equilibrium,

$$P_2R_5h_4 = P_4\,(R_5 + a)$$

$$P_4\,(R_5 + a) = P_5\,(R_6 + b)$$

$$P_4 = \frac{P_2R_5h_4}{R_5 + a}\ ,\quad P_5 = \frac{P_2R_5h_4}{R_6 + b}$$

7. SLOPES AND DEFLECTIONS

Slopes and deflections were equated to insure continuity of structure:

$$\delta_{B1} = \delta_{B2} \qquad \theta_1 = \theta_2$$

$$\delta_{C2} = \delta_{C3} \qquad \theta_2 = \theta_3$$

$$\delta_{F4} = \delta_{A1} \qquad \theta_1 = \theta_4$$

$$\delta_{H5} = \delta_{H1} \qquad \theta_1 = \theta_5$$

There exist 8 unknowns (P_o, V_1, M_1, V_2, M_2, V_3, M_3, M_4) and 8 simultaneous equations. Consequently, the problem is solvable. The desired results are δ_{E1}, and θ_1, which represent the radial displacement and rotation of point E.

The moments of inertia are approximated for this analysis to be

$$I_n = 1/12\ h_n\ L_n^3 \text{ where } n = 1, 2, \ldots 5$$

The simultaneous equations that were solved on the IBM 1620 computer are as follows -

$$\delta_{B1} = \delta_{B2} :\ P_o\,\frac{R_1^2}{h_1} - V_1\,\frac{R_1^2}{L_1\,h_1} - V_3\,\frac{R_1(R_1 + d)}{L_1\,h_1} - \frac{R_1^2\,L_1}{2\,I_1}$$

$$\left\{M_1 - M_3 + 1/2\, V_1 L_1 - 1/2\, V_3 L_1\left(\frac{R_1 + d}{R_1}\right) - P_5\left(\frac{R_1 + d}{R_1}\right)d + M_4\left(\frac{R_1 + d}{R_1}\right)\right\}$$

$$= P_1 \frac{R_2 R_4}{h_2} + V_1 \frac{R_1 R_2}{h_2 L_2} + V_2 \frac{R_2 R_3}{h_2 L_2}$$

$$\delta_{C_2} = \delta_{C_3} : P_1 \frac{R_3^2}{h_3} - V_2 \frac{C_3 E}{2D\lambda^3} - M_2 \frac{C_5 E}{2D\lambda^2} = P_1 \frac{R_2 R_4}{h_2} + V_1 \frac{R_1 R_2}{L_2 h_2}$$

$$+ V_2 \frac{R_2 R_3}{L_2 h_2}$$

$$\delta_{F_4} = \delta_{A_1} : P_o \frac{R_1^2}{h_1} - V_1 \frac{R_1^2}{L_1 h_1} - V_3 \frac{R_1 (R_1 + d)}{L_1 h_1} = P_1 \frac{ER_5 (R_5 - 1/2 h_4)}{E_1 h_4}$$

$$- P_o \frac{ER_5 (R_5 + 1/2\, h_4)}{E_1 h_4} + R_5 E\beta\Delta T$$

$$\delta_{H_5} = \delta_{H_1} : V_3 \frac{R_6 (R_6 + b)}{L_5 h_5} = P_o \frac{R_1^2}{h_1} - V_1 \frac{R_1^2}{L_1 h_1} - V_3 \frac{R_1 (R_1 + d)}{L_1 h_1}$$

$$+ \frac{R_1^2 L_1}{2 I_1} \left\{M_1 - M_3 + 1/2\, V_1 L_1 - 1/2\, V_3 L_1 \left(\frac{R_1 + d}{R_1}\right) - P_5 \left(\frac{R_1 + d}{R_1}\right) d\right.$$

$$\left. + M_4 \left(\frac{R_1 + d}{R_1}\right)\right\}$$

$$\Theta_1 = \Theta_2 : \frac{R_1^2}{I_1} \left\{M_1 - M_3 + 1/2\, V_1 L_1 - 1/2\, V_3 L_1 \left(\frac{R_1 + d}{R_1}\right) - P_5 d\right.$$

$$\left.\left(\frac{R_1 + d}{R_1}\right) + M_4 \left(\frac{R_1 + d}{R_1}\right)\right\} = \frac{R_2^2}{I_2} (M_2 - M_1)$$

$$\Theta_2 = \Theta_3 : \frac{R_2^2}{I_2} (M_2 - M_1) = -V_2 \frac{C_4 E}{2D\lambda^2} - M_2 \frac{C_6 E}{D\lambda}$$

$$\theta_1 = \theta_4 : \frac{R_1^2}{I_1} \left\{ M_1 - M_3 + 1/2\ V_1 L_1 - 1/2\ V_3 L_1 \frac{R_1 + d}{R_1} - P_5 d \frac{R_1 + d}{R_1} + M_4 \left(\frac{R_1 + d}{R_1} \right) \right\} = \frac{E}{E_1} \frac{R_5^2}{I_4} (M_3 + P_4 a)$$

$$\theta_1 = \theta_5 : \frac{R_1^2}{I_1} \left\{ M_1 - M_3 + 1/2\ V_1 L_1 - 1/2\ V_3 L_1 \left(\frac{R_1 + d}{R_1} \right) - P_5 d \left(\frac{R_1 + d}{R_1} \right) + M_4 \left(\frac{R_1 + d}{R_1} \right) \right\} = \frac{R_6^2}{I_5} \left\{ P_5 \left(\frac{R_6 + b}{R_6} \right) b + P_4 \left(\frac{R_6 - C}{R_6} \right) C - M_4 \left(\frac{R_6 + b}{R_6} \right) \right\}$$

APPENDIX B

THERMAL ANALYSIS

For the purpose of thermal analyis, the critical components of the seal assembly or the seal itself, the seal plate, seal carrier, shaft, and any other structure near the seal or seal plate, such as the heat shields. Proper evaluation of the temperature distribution is dependent on knowledge of the following quantities: power generated at the interface of the seal and the seal plate, heat-transfer coefficients on all surfaces (including the mating surfaces of the seal and seal plate), and heat-transfer coefficients of coolants. The coefficients can be closely approximated from existing empirically derived data. However, assigning a value to the heat generation at the interface is more difficult. For the rubbing contact seal, heat generation due to friction as well as continuous film shear was analyzed. However, since the torque on the seal could not be measured accurately, and it was felt that a continuous film of air existed between the carbon and the seal plate, further analyses were conducted using a continuous air-film shearing concept which was developed for the gas-film seal analysis.

The uncertainty in the value of the heat generation for film shear is due to uncertainty of film-thickness, and local velocity gradient within the film. The local velocity gradient is complicated by the existence of two components of velocity: the tangential velocity due to shaft rotation and the radial velocity due to the air leakage.

Temperature distributions within critical components of the mainshaft seal were obtained by dividing the components into a finite mesh of nodes. The mesh geometry was then input on the TØSS Computer Program from the SHARE General Program Library. The TØSS program employs a method whereby an initial guess for the temperature distribution is "relaxed" in a cyclic order and a new temperature distribution is obtained after each cycle or iteration. Termination of the iteration is determined by a preset temperature tolerance. The reliability of the analytical model was demonstrated by comparing experimentally determined temperatures with analytically predicted temperatures.

1. HEAT-TRANSFER COEFFICIENTS

In this section, the coefficients of heat transfer which were used on various surfaces will be described.

a. Rotating Disks in Free Air

The correlation which was used to calculate the heat-transfer coefficient on rotating disks is found in Cobb and Saunders (Reference 10). They define the Reynolds Modulus as

$$R_{COBB} = \frac{\rho \omega r^2}{\mu}$$

where,

ρ = density of fluid in which the disk is rotating $\left(\frac{\text{lb mass}}{\text{ft}^3}\right)$

μ = viscosity of fluid (lb mass/foot hour)

r = radius of revolution (feet)

ω = angular velocity, (radians/hour)

For the laminar range, Cobb and Saunders recommend

$$Nu_{COBB} = \frac{hr}{k} = 0.36 \left(R_{COBB}\right)^{0.5} \tag{27}$$

where,

$$1 \times 10^5 \leq R_{COBB} \leq 2 \times 10^5$$

h = heat transfer coefficient (Btu/hour $ft^2 F°$)

k = thermal conductivity of fluid, (Btu/hour ft°F)

In the turbulent range, Cobb and Saunders recommend

$$\frac{hr}{k} = 0.015 \left(R_{COBB}\right)^{0.8} \tag{28}$$

Equation (28) is applicable for $R_{COBB} \geq 2.4 \times 10^5$.

Wagner, (Reference 11), predicts theoretically for the laminar regime when the fluid is air

$$\frac{hr}{k} = 0.335 \left(R_{COBB} \right)^{0.5} \tag{29}$$

Equation (27), which is empirical, and Equation (29), which is theoretical, agree fairly well. It should be pointed out that various authors employ different definitions of the Reynolds modulus in rotational heat transfer; hence, the subscript COBB.

b. Rotating Cylindrical Surfaces in Free Air

The correlation which was used to calculate the heat transfer from rotating cylindrical surfaces is due to Etemad's correlation (Reference 12). He recommends

$$\frac{2hr}{k} = 0.11 \left(0.5 \, R^2_{ETEMAD} \, Pr \right)^{0.35} \tag{30}$$

where,

$$R_{ETEMAD} = 2 \, R_{COBB}$$

Pr = Prandtl modulus

Equations (28) and (30) are in close enough agreement so that where disk and cylindrical surfaces form a continuous surface, a smooth transition exists in the coefficients of heat transfer.

c. Stationary Surfaces

The heat-transfer coefficients for the stationary surfaces were calculated using the standard free-convection correlation in Reference 3. It should be noted that the free-convection coefficient on the high-pressure side of the seal is much greater than on the low-pressure side because of air density.

d. Oil Flowing within Coolant Passages

Figure 143 is a design graph for oil flowing in coolant passages. The graph can be used to determine the heat-transfer coefficient and the pressure drop of the oil if the passage's diameter and the oil's flow rate are known. The graph was derived on the assumption that the oil filled the passage. The physical properties of the oil were evaluated within the 500- to 600-degree Fahrenheit range. If the locus of $\frac{W}{n}$ and D lies below the dashed line marked "LAMINAR", then the oil flow is laminar, and the heat-transfer coefficient is given by the single solid line marked "LAMINAR" which is independent of passage diameter. The coordinates of this line are $\frac{W}{n}$ and $hA/L^{0.67}$. If the locus of $\frac{W}{n}$ and D lies above the dashed line marked "LAMINAR", then the heat transfer coefficient is given by the lines labeled $(hA/L)_{\text{TURBULENT}}$. Interpolation between lines is to be made logarithmically. The pressure drop in psi per inch of flow length is determined by the locus of W/n and D. The quantity A on the graph is the heat transfer area. The two lines marked (hA/L) = 0.5 and 1.0 are not parallel to the other (hA/L) lines because these two lines correspond to the transition-regime flow and the latter group of lines correspond to the turbulent regime.

The Sieder-Tate empirical equation was used for Reynolds numbers less than 2100 to determine heat-transfer coefficients. For Reynolds numbers greater than 10,000, the Dittus-Boelter equation was used for the heat-transfer coefficient. These equations may be found in Reference 13, pages 137 and 132, respectively.

e. Surfaces Rotating Near Other Surfaces in the Gas-Film Seals

The heat-transfer coefficients for cylindrical and disk surfaces rotating close to other surfaces were calculated from References 4 and 5. These correlations were applied to the following three locations: cylindrical surface of the seal plate rotating within the fixed guard; the disk surface of the seal plate rotating within the rotating guard; and the windback seal mating surfaces. For these three locations, the correlation given in Reference 5 was applied, namely,

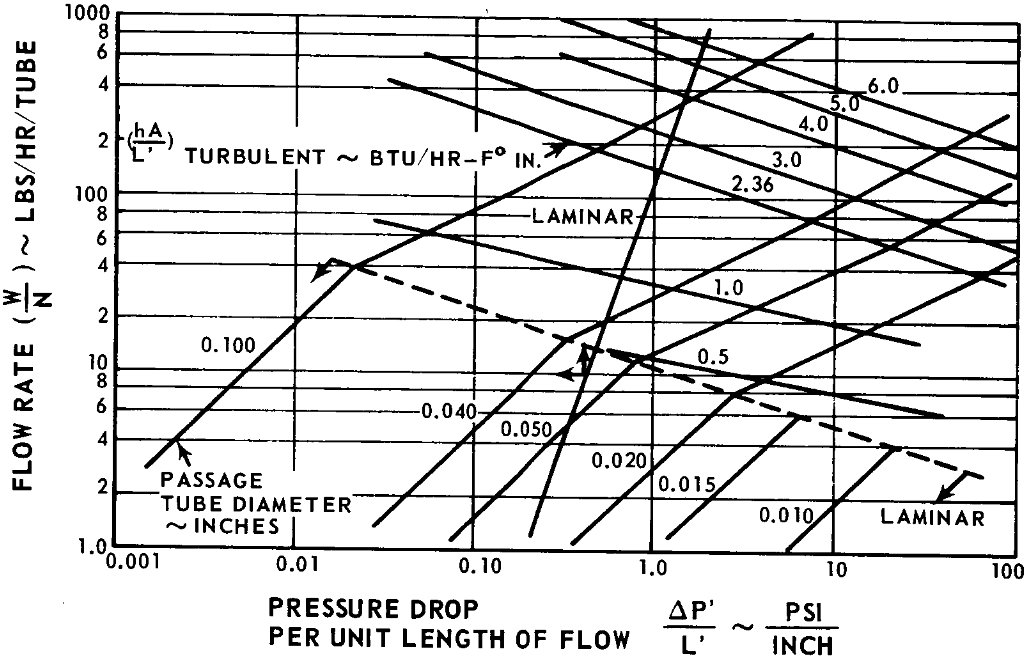

Figure 143 Oil Flow in Coolant Passages

$$\frac{h\,\Delta r}{k} = 0.175\ \frac{\omega\,(\Delta r)^{3/2}\ \rho\,R^{1/2}}{\mu} \qquad (31)$$

where

h = heat transfer coefficient (But/hour - ft$^{2\circ}$F)

k = thermal conductivity of air (Btu/hour - ft°F)

ρ = density of air (lbs-mass/ft^{3})

Δr = radial clearance between cylinders (feet)

ω = rotation of cylinder (radians/second)

μ = viscosity of air (lbs mass/ft-hour)

R = radius of cylinder (feet.)

When applying Equation 31 to the rotating disk portion of the seal plate within the rotating guard, Δr was replaced by the average axial clearance and R was replaced by the average radius of revolution. In order to reduce the number of internal thermal connections in the analytical program, the heat-transfer coefficients for these three locations were converted to equivalent thermal conductivities of the air between each pair of surfaces.

f. Exterior Surface of the Disk Portion of the Fixed Guard in the Gas-Film Seal

Since the leakage air exiting from the windback partially scrubs the disk portion of the fixed guard, the resulting heat transfer from that surface is certainly greater than for free convection. To account for this effect, the following equation from page 268 of Reference 3 was used.

$$\frac{\bar{h}\,\Delta r}{k} = 0.664 \left(\frac{\Delta r}{\mu}\ \rho\,\overline{V}\right)^{1/2} \mathrm{Pr}^{1/3}$$

where $\bar{h}$ = heat transfer coefficient averaged over distance Δr (Btu/hour-ft^{2}F°)

Δr = length of flat portion of fixed guard (feet)

k = thermal conductivity of air, (Btu/hour-ft°F)

μ = viscosity of air (lbs-mass/ft-hour)

ρ = density of air (lbs mass/ft^3)

$\bar{V}$ = free stream velocity of air (ft/hour)

Pr = Prandtl modulus of air

2. Energy Balance at Interface of Seal and Seal Plate for Sheared-Film Concept

The temperatures within the leakage air and at the interface of the seal and seal plate were determined from the following analysis.

Consider a control element (Figure 144) into which a fluid enters with enthalpy rate WC_pT_o and out of which a fluid leaves with enthalpy rate WC_p $\left[T_o+(dT_o/dx)dx\right]$ Total power generation within the element is defined as PLdx. The heat-transfer rates from the element to surfaces 1 and 2 are $h_1\ (T_o-T_{s1})$ Ldx and $h_2\ (T_o-T_{s2})$ Ldx, respectively.*

At steady-state conditions, the rates that energy enters and leaves the element are equal. Therefore,

$$WC_pT_o+PLdx = WC_p(T_o+\frac{dT_o}{dx}dx) \quad + \quad (h_1(T_o-T_{s1})Ldx + h_2(T_o-T_{s2})Ldx$$

Rearranging,

$$\frac{dT_o}{dx} + (h_1 + h_2)\frac{L}{WC_p}T_o - (h_1T_{s1} + h_2T_{s2})\frac{L}{WC_p} - \frac{PL}{WC_p} = 0 \qquad (32)$$

---

*The convective potentials should be written as $(T_{aw1} - T_{s1})$ and $(T_{aw2} - T_{s2})$ for surfaces 1 and 2 respectively; where T_{aw} is the adiabatic wall temperature. It has been assumed that $T_{aw} = T_o$.

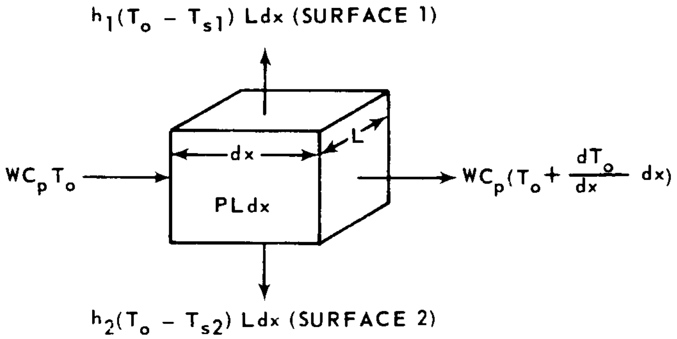
$h_1(T_o - T_{s1})$ Ldx (SURFACE 1)
WC_pT_o
dx
L
PLdx
$WC_p(T_o + \frac{dT_o}{dx} dx)$
$h_2(T_o - T_{s2})$ Ldx (SURFACE 2)

Figure 144 Analytical Element for Seal-Temperature Calculations Based on Film-Riding Assumption

where:

W = Mass fluid flow (lb/hr)

C_p = Specific heat at constant pressure of fluid (Btu/lb-°F)

T_o = Total Temperature of fluid (function of x), (°F)

h_1, h_2 = Heat transfer coefficients at surfaces 1 and 2 respectively, But/hr-ft^2-°F, not necessarily equal.

Ldx = Surface area on either side of fluid (ft^2)

P = Uniform power generation per surface (Btu/hr-ft^2)

T_{s1}, T_{s2} = Temperature of surfaces 1 and 2 respectively, (°F) (assumed to be constant within the element dx)

x = Coordinate in direction of fluid flow (ft)

By defining:

$$K = \frac{L}{WCp} \quad (h_1 T_{s1} + h_2 \, T_{s2} + P)$$

and substituting into Equation 32,

$$\frac{dTo}{dx} + (h_1 + h_2) \left(\frac{L}{WC_p} \; T_o \right) -K = 0$$

Rearranging:

$$\frac{dT_o}{T_o - \left[\dfrac{KWC_p}{(h_1 + h_2)L} \right]} + \frac{(h_1+h_2)}{WC_p} Ldx = 0 \qquad (33)$$

Equation 33 can be integrated directly if everywhere within the limits of integration the denominator of the first term does not equal zero. Also, to justify the assumption that T_{s1} and T_{s2} are constants within dx, the range of integration should be small. In terms of applying the solution of Equation 33 to a finite-difference program on a digital computer, the assumption presents no obstacle because temperatures must be taken as constant for finite distances. Integrating Equation 33 for

$$0 \leq x \leq w$$

$$T_{o1} \leq T_o \leq T_{o2}$$

Yields:

$$\ln\left[\frac{T_{o2} - \dfrac{KWC_p}{(h_1 + h_2)L}}{T_{o1} - \dfrac{KWC_p}{(h_1 + h_2)L}}\right] + \frac{(h_1 + h_2)Lw}{WC_p} = 0 \qquad (34)$$

Defining:

$$\frac{h_1\ Lw}{WC_p} = NTU_1 \quad \text{and} \quad \frac{h_2\ Lw}{WC_p} = NTU_2 \qquad (35)$$

Substituting Equations 34 and 35 and rearranging yields:

$$T_{o1} - \frac{KWC_p}{(h_1 + h_2)L} = \left(e^{NTU_1 + NTU_2}\right)\left(T_{o2} - \frac{KWC_p}{(h_1 + h_2)L}\right) \qquad (36)$$

Equation 36 is the solution to the differential Equation 32, but its form cannot be used in the TØSS computer program. The following analysis was, therefore, required to alter Equation 36 to a form suitable for the TØSS program. To simplify the algebraic manipulations, Equation 36 was written in the form

$$T_{o1} - Y = Z\ (T_{o2} - Y) \qquad (37)$$

where:

$$Y = \frac{KWC_p}{(h_1 + h_2)L}$$

$$Z = e^{NTU_1 + NTU_2}$$

Multiplying both sides of Equation 37 by WC_p and rearranging yields:

$$YWC_p\ (Z-1) = WC_p\ (ZT_{o2} - T_{o1}) \qquad (38)$$

Adding and subtracting $WC_p\ T_{o2}$ to the right-side of Equation 38 and rearranging yields:

$$WC_p\ (T_{o2} - T_{o1}) = WC_p\ (Z-1) \quad (Y-T_{o2}) \qquad (39)$$

The left side of equation 39 is recognizable as the rate of change of fluid enthalpy. To facilitate the identification of the right side of Equation 39, the parameter Y is written in terms of its constituents. Equation 39 becomes

$$WC_p(T_{o2} - T_{o1}) = WC_p(Z-1) \left(\frac{h_1T_{s1} + h_2T_{s2} + P}{h_1 + h_2} - T_{o2} \right)$$

or,

$$WC_p\ (T_{o2} - T_{o1}) = WC_p \frac{(Z-1)P}{h_1+h_2} + WC_p(Z-1) \left(\frac{h_1}{h_1+h_2} (T_{s1}-T_{o2}) + \frac{h_2}{h_1+h_2} (T_{s2}-T_{o2}) \right) \qquad (40)$$

Multiplying the numerator and denominator of the right side of Equation 40 by the surface area, Lw, and substituting Equation 35 into the result yields

$$WC_p(T_{o2}-T_{o1}) = \frac{Q(Z-1)}{NTU_1 + NTU_2} + \frac{(Z-1)}{NTU_1 + NTU_2} \left(h_1\ A(T_{s1} - T_{o2}) + h_2A(T_{s2} - T_{o2}) \right) \qquad (41)$$

where:

$Q = PLw$ = Total power generation in the fluid (Btu/hr)

$A = Lw$ = Area of either surface (ft^2)

Finally, Equation 41 may be written as

$$WC_p(T_{o2} - T_{o1}) = Q + Q\left(\frac{Z-1 - NTU_1 - NTU_2}{NTU_1 + NTU_2}\right) + \frac{(Z-1)A}{NTU_1 + NTU_2}\left(h_1(T_{s1}-T_{o2}) + h_2(T_{s2}-T_{o2})\right) \tag{42}$$

The sum of the second and third terms on the right side of Equation 42 is seen to be the effective convective heat transfer between the surfaces and the fluid. The sum of the first and second terms is the effective power generated within the fluid. The electrical analogue sketch shown in Figure 145 demonstrates the internal connections made in the TØSS program. The conductance connection between fluid nodes is WC_p. The conductance connection between the surface and fluid nodes is H_EA. An amount of power equal to $1/2\ (Q_E-Q)$ is removed from each surface via a dummy boundary node. An amount of power equal to Q_E is added to the downstream fluid node via another dummy boundary node. Note that the net influx of power to the system is equal to Q.

The power generated within the fluid is calculated from

$$Q = \frac{4\pi^2 \mu A N^2 r^2}{g\ Js} \tag{43}$$

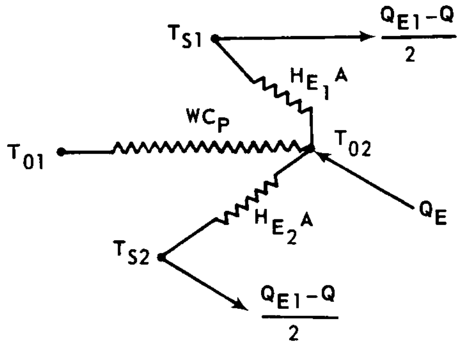
T_{S1}
$\frac{Q_{E1}-Q}{2}$
$H_{E_1}A$
WC_P
T_{01}
T_{02}
Q_E
$H_{E_2}A$
T_{S2}
$\frac{Q_{E1}-Q}{2}$

$$H_{E_1} = \frac{h_1\,(Z-1)}{NTU_1 + NTU_2}$$

$$H_{E_2} = \frac{h_2\,(Z-1)}{NTU_1 + NTU_2}$$

$$Q_E = \frac{Q\,(Z-1)}{NTU_1 + NTU_2}$$

Figure 145 Electrical Analog of Heat-Transfer Analysis

where,

Q = Heat generated (Btu/hr)

μ = Viscosity of the fluid (lb mass/ft-sec)

g = Gravitational constant

A = Area of rubbing surface (ft^2)

N = Rotational speed of seal plate relative to seal (rpm)

J = Mechanical equivalent of heat (778 ft-lb/Btu)

r = Mean radius of revolution (ft)

s = Separation distance (thickness of fluid) between seal and seal plate (ft)

Equation 43 includes only the tangential component of velocity when calculating fluid shear.

The heat-transfer surface coefficients were determined from forced convection considerations. The Reynolds modulus of the fluid is:

$$Re = \frac{DW}{\mu A_{flow}}$$

where:

A_{flow} = Flow area (ft^2)

The characteristic flow dimension used is the hydraulic diameter, D. At any radius, r:

$$D = \frac{4\ A_{flow}}{P_W} = \frac{4\ (2\ \pi\ rs)}{2\ (2\ \pi\ r)} = 2s$$

where:

P_W = Wetted perimeter of the flow passage (ft)

Consequently, at any radius

$$Re = \frac{W}{\pi r \mu} \tag{44}$$

Finally, h_1 and h_2 are determined from the appropriate Nusselt modulus:

$$Nu = \frac{hD}{K} = \frac{2hs}{K} \tag{45}$$

where:

K = Thermal conductivity of the air (Btu/hr-ft-°F)

The relationship between Equations 44 and 45 depends, of course, on whether the flow is laminar, transitional, or turbulent.

A typical example is discussed in this paragraph. Assume that the air is at 1200 degrees Fahrenheit, K = 0.0402 Btu/hr-ft-°F, average film thickness is 0.5 mil, and width of the seal face is 0.4 inch. Then, for a typical value of Reynolds number of 600., calculated from Equation 44 and a typical ratio of flow length of hydraulic diameter of 400, flow of air at the interface is laminar and in a "very long tube" condition. The appropriate asymptotic Nusselt modulus of 8 may therefore be used at the interface in Equation 45. A typical resulting value of h is 4000 Btu/hour-ft^2F° at the interface from Equation 45. The plausibility of this very high coefficient may be rationalized by calculation of a "pure conduction" coefficient. Namely, h (conduction) $= K/(s/2) = 2000$ Btu/hour-ft^2F°.

REFERENCES

1. Roark, R. T., Formulas for Stress and Strain, Third Edition, McGraw-Hill, New York, N.Y., 1954.

2. Whitley, S. and Williams, L. G., Principles of Gas-Lubricated Shaft Seals, Journal of Mechanical Engineering Science, Volume 4, No. 2, 1962.

3. Kreith, Frank, Principles of Heat Transfer, First Edition, p. 305, International Textbook Co., Scranton, Penna., 1959.

4. Becker, K. M. and Kaye, Joseph, Measurements of Diabatic Flow in an Annulus with an Inner Rotating Cylinder, Transactions of the ASME, Journal of Heat Transfer, p. 97-105, May, 1962.

5. Bjorklund, I. S. and Kays, W. M., Heat Transfer Between Concentric Rotating Cylinders, Transactions of the ASME, Journal of Heat Transfer, p. 175-186, August, 1959.

6. Bupara, S. S., Geer, T. E., and Allen, C. M., Experimental Evaluation of Orifice-Compensated Hydrostatic Mainshaft Seal under Static Condition, Third Quarterly of Cartriseal Corp. by Battelle Memorial Institute, April, 1967.

7. Kalnins, A., Analysis of Shell Revolution Subject to Symmetrical and Non-symmetrical Loads, Journal of Applied Mechanics, Transactions of the ASME, Volume 86E, September, 1964.

8. Whipple, R. T. P., The Inclined Groove Bearing, AERE T/R 622 (Revised), Atomic Energy Research Establishment, Horwell, Berkshire, 1958. (Available from H. M. S. O.)

9. Muijderman, E. A., Spiral Groove Bearings, Springer Verloy New York Inc., New York, N.Y., 1966.

10. Cobb, E. C. and Saunders, O. A., 1956 Proceedings of the Royal Society, 236A, p. 343-351.

11. Wagner, Carl, Journal of Applied Physics, Volume 19, p. 837-839, September, 1948.

12. Etemad, G. A., Transactions of the ASME, Volume 77, p. 1283-1289, November, 1955.

REFERENCES (Cont'd)

13. Badger and Banchero, Introduction to Chemical Engineering, McGraw-Hill, New York, N.Y., 1955.

14. J. W. Lund, R. J. Wernick, and S. B. Malanaski, Analysis of the Hydrostatic Journal and Thrust Gas Bearing for the NASA AB-5 Gyro-Gimbal Bearing, MT1 Report 627R26, Mechanical Technology, Inc., Latham, N. Y., 1962.

BIBLIOGRAPHY

Bupara, S. S., Walowit, J. A., and Allen, C. M., Gas-Lubrication and Distortion of High Pressure Mainshaft Seals for Compressors, Paper B-3, BHRA, Third International Conference in Fluid Sealing, Cambridge, England, April, 1967.

Hudelson, J. C., Dynamic Instability of Undamped Bellows Face Seals in Cryogenic Liquid, NASA TMX-52157, May 3, 1966.

Heinrich, G., Theory of Externally Pressurized Bearings with Compressible Lubricant, Proceedings of First International Symposium of Gas-Lubricated Bearings, ONR/ACR-49, U. S. Government Printing Office, p. 251-265, 1959.

R. P. I. and M. T. I., Design Manual of Gas Bearings, Volume 1, 1966

Whitley, S., The Design of the Spiral Groove Thrust Bearing, Paper 13, Bi-annual Gas Bearing Symposium, University of Southampton, Southampton, England, April 1967

Vohr, J. H. and Chow, C. Y., Design Handbook on Gas Bearings for Gyroscopes - Interim Report, M. T. I. Report 66TR15, ONR Contract Nour 4867(00), September 1966, AD 803539

Semiannual Reports

Distribution List
NAS3-7609

To:	Number of Copies
NASA-Lewis Research Center Air-Breathing Engine Procurement Section Attention: John H. DeFord	2
NASA-Lewis Research Center Air-Breathing Engine Division Attention: J. Howard Childs M.S. 60-4	1
W. H. Roudebush M.S. 60-6	1
D. P. Townsend M.S. 60-6	4
Lawrence E. Macioce M.S. 60-6	1
NASA-Lewis Research Center Technology Utilization Office Attention: John Weber	1
NASA-Lewis Research Center Report Control Office	1
NASA-Lewis Research Center Attention: Library	1
NASA-Scientific and Technical Information Facility P.O. Box 33 College Park, Maryland 20740 Attention: NASA Representative	6
NASA-Lewis Research Center Fluid System Components Division Attention: I. I. Pinkel	1
E. E. Bisson	1
R. L. Johnson	1
W. R. Loomis	1
L. P. Ludwig	1
M. A. Swikert	1
T. B. Shillito	1
NASA Headquarters Washington, D. C. 20546 Attention: N. F. Rekos (RAP)	1
A. J. Evans (RAD)	1
J. Maltz	1
NASA-Langley Research Center Langley Station Hampton, Virginia 23365 Attention: Mark R. Nichols	1
FAA Headquarters 800 Independence Avenue, S. W. Washington, D. C. Attention: J. Chavkin, SS/120	1
M. Lott, FS/141	1
Air Force Materials Laboratory Wright-Patterson Air Force Base, Ohio 45433 Attention: MANL, R. Adamczak	1
MANE, R. Headrick & J. M. Kelble	1
MAAE, P. House	1
Air Force Systems Engineering Group Wright-Patterson Air Force Base, Ohio 45433 Attention: SESHS, J. L. Wilkins	1
SEJPF, S. Prete	1
Air Force Aero Propulsion Laboratory Wright-Patterson Air Force Base, Ohio 45433 Attention: AFAPL (APFL), K. L. Berkey & L. DeBrohum	1
AFAPL (APTC), C. Simpson	1
APTP, I. J. Gershon	1
U. S. Naval Air Material Center Aeronautical Engine Laboratory Philadelphia 12, Pennsylvania Attention: A. L. Lockwood	1

To:	Number of Copies
U. S. Naval Research Laboratory Washington, D. C. Attention: Charles Murphy	1
Department of the Navy Bureau of Naval Weapons Washington, D. C. Attention: A. D. Nehman, RAAE-3	1
C. C. Singletorry, RAPP-4	1
Department of the Navy Bureau of Ships Washington 25, D. C. Attention: Harry King, Code 634A	1
U. S. Navy Marine Engineering Laboratory Friction and Wear Division Annapolis, Maryland Attention: R. B. Snapp	1
Department of the Army U. S. Army Aviation Material Labs. Fort Eustis, Virginia 23604 Attention: John W. White, Chief Propulsion Division	1
U. S. Army Ordnance Rock Island Arsenal Laboratory Rock Island, Illinois Attention: R. LeMar	1
AVCOM AMSAVEGTT Mart Building 405 South 12th Street St. Louis, Missouri 63100 Attention: E. England	1
Aerojet-General Corporation 20545 Center Ridge Road Cleveland, Ohio 44116 Attention: W. L. Snapp	1
Avco Corporation Lycoming Division Stratford, Connecticut Attention: R. Cuny	1
Battelle Memorial Institute 505 King Avenue Columbus 1, Ohio Attention: C. M. Allen	1
Bendix Corporation Fisher Building Detroit 2, Michigan Attention: R. H. Isaacs	1
B. F. Goodrich Company Aerospace & Defense Products Division Troy, Ohio Attention: L. S. Blalkowski	1
Boeing Aircraft Company 224 N. Wilkinson Dayton, Ohio 45402 Attention: H. W. Walker	1
Borg-Warner Corporation Roy C. Ingersoll Research Center Wolf and Algonquin Roads Des Plaines, Illinois	1
Carbon Products Division of Union Carbide Corporation 270 Park Avenue New York, New York 10017 Attention: J. Curran	1

Semiannual Reports

Distribution List (Cont'd)
NAS3-7609

To:	Number of Copies
Cartiseal Corporation 3515 West Touhy Lincolnwood, Illinois Attention: R. Voltik	1
Chicago Rawhide Manufacturing Company 1311 Elston Avenue Chicago, Illinois Attention: R. Blair	1
Clevite Corporation Cleveland Graphite Bronze Division 17000 St. Clair Avenue Cleveland, Ohio 44110 Attention: Thomas H. Koenig	1
Continential Aviation & Engineering 12700 Kercheval Detroit 15, Michigan Attention: A. J. Follman	1
Crane Packing Company 6400 W. Oakton Street Morton Grove, Illinois Attention: Harry Tankus	1
Douglas Aircraft Company Holiday Office Center 16501 Brookpark Road Cleveland, Ohio 44135 Attention: J. J. Pakiz	1
Durametallic Corporation Kalamazoo, Michigan Attention: H. Hummer	1
E. I. duPont de Nemours & Company 1007 Market Street Wilmington 98, Delaware Attention: G. Finn R. J. Laux A. J. Cheney	1 1 1
Fairchild Engine and Airplane Corporation Stratos Division Bay Shore, New York	1
Fairchild-Hiller Corporation Republic Aviation Division Farmingdale, Long Island New York 11735 Attention: D. Schroeder	1
Franklin Institute Laboratories 20th & Parkway Philadelphia 3, Pennsylvania Attention: J. V. Carlson Otto Decker	1
Garlock, Inc. Palmyra, New York 14522 Attention: E. W. Fisher	1
General Dynamics Corporation 16501 Brookpark Road Cleveland, Ohio 44135 Attention: George Vila	1
General Electric Company Advanced Engine and Technology Department Cincinnati, Ohio 45215 Attention: L. B. Venable G. J. Wile C. C. Moore H-25 W. McCarty	1 1 1 1
General Motors Corporation Allison Division Plant #8 Indianapolis, Indiana Attention: E. M. Deckman	1
Hercules Powder Company, Inc. 900 Market Street Wilmington, Delaware	1
Hughes Aircraft Company International Airport Station P. O. Box 90515 Los Angeles 9, California	1
Huyck Metals Company P. O. Box 30 45 Woodmont Road Milford, Connecticut Attention: J. I. Fisher	1
I. I. T. Research Foundation 10 West 35th Street Chicago, Illinois 60616 Attention: Dr. Strohmeier	1
Industrial Tectonics Box 401 Hicksville, New York 11801 Attention: J. Cherubin	1
Kendall Refining Company Bradford, Pennsylvania Attention: F.I.I Lawrence	1
Koppers Company, Inc. Metal Products Division Piston Ring and Seal Department Baltimore 3, Maryland Attention: F. C. Kuchler	1
Koppers Company, Inc. Monrosville, Pennsylvania Attention: Billy D. Pfoutz J. Heck	1 1
Lockheed Aircraft Company 16501 Brookpark Road Cleveland, Ohio 44135 Attention: L. Kelly	1
Martin Company 16501 Brookpark Road Cleveland, Ohio 44135 Attention: Z. G. Horvath	1
Mechanical Technology Incorporated 968 Albany-Shaker Road Latham, New York Attention: Donald F. Wilcock	1
Metal Bellows Corporation 20977 Knapp Street Chatsworth, California Attention: Sal Artino	1
Midwest Research Institute 425 Volker Blvd. Kansas City 10, Missouri Attention: V. Hopkins	1
Monsanto Chemical Company 800 North Lindbergh Blvd. St. Louis, Missouri 63166 Attention: K. McHugh R. Hatton	1 1
Morganite, Inc. 33-02 48th Avenue Long Island City 1, New York Attention: S. A. Rokaw	1

Semiannual Reports

Distribution List (Cont'd)
NAS3-7609

To:	Number of Copies
North American Aviation Inc. 16501 Brookpark Road Cleveland, Ohio 44135 Attention: George Bremer	1
Northrop Corporation 1730 K Street N. W. Suite 903-5 Washington 6, D. C. Attention: S. W. Fowler, Jr.	1
Pesco Products Division Borg-Warner Corporation 24700 N. Miles Bedford, Ohio	1
Pressure Technology Corporation of America 453 Amboy Avenue Woodbridge, New Jersey Attention: A. Dobrowsky	1
Rocketdyne 6633 Canoga Avenue Canoga Park, California Attention: M. Butner	1
Sealol Inc. P. O. Box 2158 Providence 5, Rhode Island Attention: Justus Stevens	1
Sinclair Refining Company 600 5th Avenue New York, New York 10020 Attention: C. W. McAllister	1
Sinclair Research Incorporated 400 E. Sibley Blvd. Harvey, Illinois Attention: M. R. Fairlie	1
SKF Industries, Inc. 1100 First Avenue King of Prussia, Pennsylvania Attention: L. B. Sibley	1
Socony Mobil Oil Company Research Department Paulsboro Laboratory Paulsboro, New Jersey Attention: E. Oberright	1
Director Government Research Laboratory Esso Research & Engineering Company P.O. Box 8 Linden, New Jersey 07036	1
Southwest Research Institute 8500 Culebra Road San Antonio, Texas Attention: P. M. Ku	1
Stanford Research Institute Menlo Park, California Attention: R. C. Fey	1
Stein Seal Company 20th Street & Indiana Avenue Philadelphia 32, Pennsylvania Attention: Dr. P. C. Stein	1
Sun Oil Company Automotive Laboratory Marcus Hook, Pennsylvania Attention: J. L. Griffith	1
Union Carbide Chemicals Company Division of Union Carbide Corporation Tarrytown, New York Attention: W. H. Millott & J. C. Haaga	1
United States Graphite Company 1621 Holland Saginaw, Michigan Attention: F. F. Ruhl	1
Westinghouse Electric Corporation 55 Public Square Cleveland, Ohio 44113 Attention: Lynn Powers	1
Wright Aeronautical Division Curtiss-Wright Corporation 333 West 1st Street Dayton 2, Ohio Attention: S. Lombardo	1
Pennsylvania State University Department of Chemical Engineering University Park, Pennsylvania Attention: Dr. E. E. Klaus	1
The University of Tennessee Department of Mechanical and Aerospace Eng. Knoxville, Tennessee Attention: Professor W. K. Stair	1 1

Pratt & Whitney Aircraft DIVISION OF UNITED AIRCRAFT CORPORATION

5 February 1968

In reply please refer to
AJP:RTD:lpk - Eng. 3S-4

To: National Aeronautics and Space Administration
Lewis Research Center
Airbreathing Engine Division
21000 Brookpark Road
Cleveland, Ohio 4413

Attention: John H. DeFord

Subject: Errors in Phase I Final Report on Development of Main-Shaft Seals for Advanced Air Breathing Propulsion Systems, PWA-3161

Reference: Contract NAS3-7609

1. Since the publication of the subject report, several errors have been discovered. The errors and their corrections are listed below.

2. Cover:
   - As reads: "...R. H. McKibbin,..."
   - Should read: "...A. H. McKibbin,..."

3. Page ii, line 14:
   - As reads: "... and H. L. Northurp,..."
   - Should read: "...and H. L. Northup,..."

4. Page iii, line 13:
   - As reads: "3. Post inface deformation test analyses..."
   - Should read: "3. Posttest interface deformation analyses..."

5. Page iii, line 27:
   - As reads: "...up to 550 OSP at..."
   - Should read: "...up to 550°F at..."

6. Page iii, line 30:
   - As reads: "...film at 100 SP and..."
   - Should read: "...film at 100°F and..."

EAST HARTFORD, CONNECTICUT 06108

✓ 7. Page iii, line 31:

- As reads: "365 SP and..."
- Should read: "365°F and..."

✓ 8. Page iv, line 1:

- As reads: "...created a severly divergent..."
- Should read: "....created a severely divergent..."

✓ 9. Page 5, line 18:

- As reads: "...with Linde LC1C coating (chrome corbide). Twenty-four..."
- Should read: "...with Linde LA2 coating (aluminum oxide). Twenty-four..."

✓ 10. Page 11, 5th line from bottom:

- As reads: "...land or sea "dam". ..."
- Should read: "...land or seal "dam". ..."

✓ 11. Page 52, 2nd line from bottom:

- As reads: "...high temperatare, and..."
- Should read: "...high temperature, and..."

✓ 12. Page 94, 2nd line from bottom:

- As reads: "...lip was severly scored..."
- Should read: "...lip was severely scored..."

✓ 13. Page 100, 5th line from bottom:

- As reads: "...and $b + \alpha R_c/H_o$"
- Should read: "...and $b = \alpha R_c/H_o$"

✓ 14. Page 200, Equation 34:

- As reads: $\left[\frac{T_{02}-\ldots}{T_{01}-\ldots}\right] + \ldots$
- Should read: $\ln\left[\frac{T_{02}-\ldots}{T_{02}-\ldots}\right] + \ldots$

UNITED AIRCRAFT CORPORATION
Pratt & Whitney Aircraft Division

A. J. Parks
Project Manager